Dark Matter Annihilation in the Epoch of Reionisation

Sarah Schön

Doctor of Philosophy
2017

School of Physics
The University of Melbourne

Submitted in Total Fulfillment

of the Requirements of the Degree of Doctor of Philosophy

Abstract

Dark matter constitutes about 26% of the Universe's mass-energy content, compared to the 5% that make up the familiar matter described by the Standard Model of particle physics. Besides the ubiquitous gravitational effects, astrophysical observations have also shown dark matter to be at most weakly interacting with ordinary matter. Furthermore the fundamental particle nature of dark matter remains unclear though a number of potential models have been proposed, many of which arise naturally as part of theoretical frameworks beyond the Standard Model. In addition dark matter plays an instrumental role in the evolution of observable structure and fully situating dark matter within the Standard Models of both particle physics and cosmology remains a critical pursuit of modern physics.

Amongst the most promising of dark matter models are those that self-annihilate to Standard Model particles. In astrophysical settings, the presence of annihilating dark matter could be inferred from either the presence of high energy annihilation products or through the modification of standard astrophysical phenomenology, an in particular events such as the Epoch of Reionisation, by the additional heating and ionisation provided by dark matter annihilation. In this thesis, the potential impact of self-annihilating dark matter on early structure is investigated. A vital aspect of this calculation is the detailed treatment of the energy transfer. To this end, a Monte Carlo code was written to track the full evolution of the injected particles and the subsequent secondary particle cascades and record the energy deposited in and around dark matter halos. Since there is considerable uncertainty as to the precise dark matter density distribution of high redshift objects, a range of profiles and mass-concentration relations are compared. A number of different dark matter particle masses and annihilation models are also considered. Besides the self-heating of the halos, the impact of the escaped particle on circumgalactic medium is investigated as well as how the additional heating can suppress the infall of gas onto the halo. Lastly the power from the halo itself is compared to that from others sources such as the diffuse dark matter background and CGM.

Declaration

This is to certify that:

- This thesis entitled "Dark matter annihilation in the Epoch of Reionisation" comprises only my original work towards the PhD, except where indicated otherwise.
- Due acknowledgement has been made in the text to all other material used.
- This thesis is no longer than 10^5 pages in length, exclusive of tables, figures, bibliographies and appendices.

.....

Sarah Schön

Acknowledgements

My first few months in Melbourne I frequently spent in a delighted panic while coming to terms with the idea that what had been a somewhat inevitable final step in my schooling had acquired a very real deadline. Four of the most illuminating years later, and I would like to thank the people who helped me to not only finish my thesis but convinced me that I could in the first place.

Foremost thanks must go to my supervisors Katie Mack and Stuart Wyithe about whom not enough good things can be said. I will always be grateful to them for allowing me this opportunity, as well as for their patience, good humour and unfailing generosity when it came to both their time and vast expertise.

I would also like to acknowledge all those individuals who not only enriched my understanding of the universe but also the academic world (the latter of which can at times appear far more daunting than the former). Special thanks go to Jonathan McDowell, Carmelo Evoli and Andrea Ferrara for not only their assistance and but also for being wonderful hosts in far off lands and to Tracy Slatyer for amongst other things, the invaluable discussion on the finer points of Inverse Compton scattering. Last but not least, I'm immensely grateful to Elisabetta Barberio for her ongoing support, and to her Masters student Cassandra Avram for the tremendous company along the way.

I've never been the most sociable person in the world but the astrophysics department at the University of Melbourne has been one of the most welcoming and positive communities I have ever had the good fortune to be a part of and you are some of the kindest, smartest and supportive people I have ever had the pleasure of knowing.

Thanks to my wonderful sisters, Melanie (as well as her boys) for always making me smile and Sophia, my best friend, for her unconditional support. Finally there will never be enough words of thanks for my mother, who is the embodiment of grace and resilience.

Contents

List of Tables

List of Figures

Constants and units

Astrophysical		
c	speed of light in vacuum	$2.99792458 \times 10^{10}$ cm s^{-1}
G	gravitational constant	$6.67428 \times$ m^3 kg^{-1} s^{-2}
T_0	CMB temperature at z=0	2.725 K
$M_\odot$	solar mass	1.98855×10^{33} g
Atomic		
m_e	electron mass	0.510999 MeV
h	Planck constant	4.13567×10^{-15} eV s
k_b	Boltzmann constant	$1.38065 \times$ J K^{-1}
α	fine structure constant	7.297352×10^{-3}
Ry	Rydberg constant	13.6 eV
σ_T	Thomson cross section	6.65246×10^{-25} cm^2
r_e	classical electron radius	2.81794×10^{-13} cm
a_0	Bohr radius	5.291772×10^{-9} cm
Conversion Factors		
erg	erg	10^{-7} J
pc	parsec	3.085678×10^{16} cm
eV	electron-Volt	$1.6021765 \times 10^{-12}$ erg
u	atomic mass unit	1.660539×10^{-24} g

Chapter 1

Searches for Dark Matter I; A brief introduction informed by astrophysics

1.1 A New Kind of Matter

The 19th and 20th centuries saw the sciences undergo remarkable paradigm shifts on almost all fronts. A major driving factor behind this was the development and overhaul of scientific instrumentation which allowed unprecedented access to new physical scales and phenomena, many of which flew in the face of accepted scientific canon. While in large part the plethora of these newly identified phenomena have been brought together into cohesive models, a number of the questions raised since then remain open. Perhaps one of the most significant and curious of these unresolved mysteries regards the simple, physical make up of the universe.

One of the great ideological shifts undertaken by the astronomical community began with the ongoing discussion of where the physical boundaries of our universe could be found. In 1920 Harlow Shapley and Heber Curtis took part in the so called Great Debate (Shapley and Curtis, 1921) in which they each put forth an argument as to whether what were then identified as distant "spiral nebula" were simply small gas clouds located within the Milky Way or large, distant structures and galaxies in their own right. While the issue of the accurate classification of distant nebula was certainly important in a sense that it is in the scientific spirit to aim at making good measurements, the answer had consequences far beyond being able to quote a correct distance.

This became evident when a crucial part of the debate was settled by Edwin Hubble. From 1922-1923, Hubble spent his time at California's Mt Wilson Observatory where he used the recently completed Hooker telescope to make the first observations of Cepheid variable stars located within the Andromeda Nebula (Hubble, 1926). The identification of these standard candles allowed Hubble to confirm that the "spiral nebula" in question were indeed distant galaxies beyond the confines of the Milky Way. Even more strange was the realisation that the spectra of these new galaxies were redshifted (Hubble, 1929), and the galaxies themselves were moving away from the Milky

Way. This discovery in conjunction with the theoretical work stemming from Albert Einstein's general relativity, was to lay the foundations of modern cosmology. It also signalled a profound shift from a world view that had consisted of a (relatively) small, eternal and unchanging universe to one that was not only far more vast than previously thought but also vastly more dynamic in its evolution.

With this brave new view of the Universe came a whole slew of questions. These covered everything from the obvious task of developing a functional cosmological framework, to the highly esoteric debate on the validity of platonic realism (including the odd existential crisis), as well as the seemingly straightforward matter of recording and cataloguing the objects found in this newly expanded cosmic backyard. Not for the first time it was to be the latter task that posed a seemingly innocuous question which was to cause physicists headaches for decades to come. What started off with a simple exercise in trying to match the visible mass component of a distant cluster to that predicted by its dynamics, led to the realisation that the lion's share of the universe's matter was not accommodated by the meticulously cultivated theory of what matter was expected to be.

1.1.1 Early Discoveries

The first suggestions that the universe could possibly contain a significant, hitherto unseen and un-detected mass component came around the same time Hubble made his groundbreaking discoveries. While there had been some suggestions (Kapteyn, 1922; Jeans, 1922) that the motion of stars in the Milky Way were indicative of missing mass, the first such indication from observation of extra-galactic bodies was made in 1933 courtesy of Fritz Zwicky. The Swiss born Zwicky was conducting a study into the characteristics of the Coma cluster and its galaxies, including the methods of calculating their distance and redshift. In a concluding remark, Zwicky used the velocity dispersion of the individual galaxies in conjunction with the virial theorem to deduce the total mass of the cluster. Rather unexpectedly, the mass derived from that argument was about 400 times of that indicated by the luminous mass of the cluster (Zwicky, 1933). Zwicky followed up this discrepancy with a more rigorous calculation (Zwicky, 1937), again finding a deficit in the visible mass component compared to that given by the motion, albeit by a revised value of 160.

It should be noted that at this point in time astronomers did in fact already expect galaxies to contain a non-luminous matter component which was thought to consist of ordinary gas and faint stars and Zwicky's report of a mass deficit was thus in itself not considered unusual. However according to the work conducted on the stellar kinematics within the Milky Way (Oort, 1932), this unseen mass component was also assumed to be sub-dominant to that of the visible stellar population which was in stark conflict with the results from the Coma cluster. At the time the scientific community turned out to

be reluctant to fully embrace the notion that galaxies contained a massive "dark matter" component, largely driven by the concern that the dynamics of large scale structures were simply not well enough understood to come to any satisfactory conclusion on the issue[1]. Over the next decades evidence steadily amassed in support of "'dark matter', including credible work on the behaviour of galaxy rotation curves and the mass of the Local Group (Kahn and Woltjer, 1959), but it wasn't until the 1980s that these findings became part of the widely accepted astrophysical narrative.

1.2 The Missing Mass Problem and Galaxy Rotation Curves

While the debate regarding the existence, abundance and make-up of "dark matter" within galaxies and galaxy clusters had come to somewhat of an impasse, the rest of the astrophysical community continued on its merry way of progress and discovery. One of the instrumental advancements which allowed for the mass problem to be revisited in earnest was that of new, sensitive spectrographs and their subsequent use in measuring the rotation curves of galaxies.

The radial velocities of galaxies' outlying regions had previously been measured amongst others by Babcock (1939) and Oort (1940). Both found that the periphery regions of the spiral galaxies they studied rotated considerably faster than would be expected from Keplerian laws. These findings were interpreted to be due to either strong dust absorption or again the result of elevated mass-to-light ratios. As with previous data this was not enough to sway the case either for or against the existence of a dominant dark matter galaxy component.

1.2.1 Extended Galaxy Rotation Curves

Up until the very early 1970s the rotation curves at hand were limited by the optical data available to the inner parts of the galaxy. Fortunately at this point advances in observation techniques allowed these limitation to be overcome through radio measurements of the 21cm line (Roberts and Rots, 1973; Bosma, 1978) and highly sensitive spectrographs (Rubin and Ford, 1970). Extended galaxy rotation curves could now be observed and the evidence overwhelmingly confirmed that the flattening far beyond the visible galaxy component was a nigh universal feature. These results presented by Vera Rubin in the late 70s (Rubin et al., 1978, 1980) were critical in finally establishing the presence of a massive non-light emitting component that extended far beyond the visible galaxy structure.

Galaxy Rotation Curve of NGC6503

Figure 1.1 shows the galaxy rotation curve of NGC6503 taken from Begeman et al. (1991). Also shown are the different contributions to the stars' motion including the

[1] Zwicky was famously disgruntled with this treatment and felt that his colleagues were unfairly dismissive of his claims.

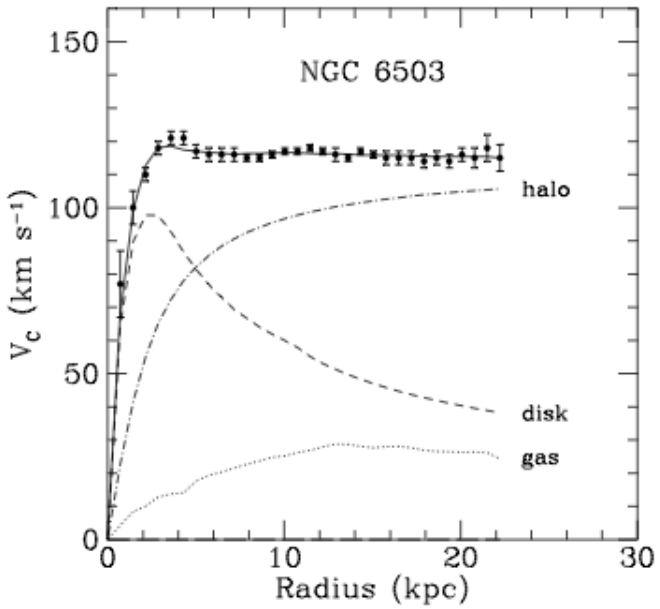

Figure 1.1: The rotation curve of NGC6503 taken from (Begeman et al., 1991), showing the different mass contributions from the gas, stellar disk and dark matter halo.

galactic disk, gas and the dark matter halo. Simple Newtonian mechanics suggests that the circular velocity of the stars as they travel around the centre of the galaxy to be,

$$v_c = \sqrt{\frac{GM(r)}{r}}. \tag{1.1}$$

If the total mass content of the galaxy would in large correspond to the luminous component then the circular velocity would be expected to decrease with radius (as is shown by the dashed disk line). However, the data clearly shows a close to flat rotation curve far beyond the main galaxy bulge. In order to recover the motion an added mass component beyond the contribution of gas (which also extends beyond the visible parts of the galaxy) has to be postulated. In this case it is the presence of dark matter, as shown by the dot-dashed halo line in Figure 1.1.

1.3 Brief Foray into Cosmological Matters

As is often the case, scientific progress is rarely straightforward and determined to frustrate attempts to turn it into a clean, linear narrative. Taking a few temporal steps back brings matters back to Einstein and the theoretical foundations of modern cosmology. The following briefly outlines some of the key aspects that led to the present picture of the universe and the role dark matter plays in the formation of structure.

1.3.1 Theoretical Background

Take the starting point to be the assumption that the universe can be treated as a gravitating fluid that is both homogeneous and isotropic (and at least at this point neglects pressure) and is governed by the laws of General Relativity generally expressed by the

Einstein Field Equations

$$R_{\mu\nu} - \frac{1}{2}g_{\mu\nu}R = -\frac{8\pi G}{c^4}T_{\mu\nu} + \Lambda g_{\mu\nu}, \tag{1.2}$$

where $R_{\mu\nu}$ and R are the Ricci tensor and Ricci scalar obtained from the Riemann curvature tensor, $g_{\mu\nu}$ represents the metric tensor, G is the gravitational constant, $T_{\mu\nu}$ is the energy-momentum tensor, and lastly, Λ is the cosmological constant. The energy-momentum tensor $T^{\mu\nu}$ for a uniform, ideal fluid is given by

$$T^{\mu\nu} = (c^2\rho + P)\frac{U^\mu U^\nu}{c^2} - Pg^{\mu\nu}, \tag{1.3}$$

with $U^\mu = c\mathrm{d}x^\mu/\mathrm{d}s$ the four-velocity of the fluid, ρc^2 the energy density and P the pressure. In the case of a homogenous and isotropic universe,

$$T^\mu{}_\nu = \mathrm{diag}(c^2\rho, -P, -P, -P). \tag{1.4}$$

The appropriate metric that describes the universe's structure is given by the

Robertson Walker Metric

$$\mathrm{d}s^2 = c^2\mathrm{d}t^2 - a(t)^2\left(\frac{\mathrm{d}r^2}{1-kr^2} + r^2\mathrm{d}\Omega^2\right) \tag{1.5}$$

where $\mathrm{d}s$ describes an infinitesimal space-time interval, k is a parameter dependent on space curvature and $a(t)$ a scale factor necessitated by the conditions of isotropy and homogeneity.

Friedmann Equations Solving the Einstein field equation in conjunction with the Robertson Walker metric yields the Friedmann equations,

$$\left(\frac{\dot{a}}{a}\right)^2 + \frac{k}{a^2} = \frac{8\pi G}{3}\rho \tag{1.6}$$

$$\frac{2\ddot{a}}{a} + \frac{\dot{a}^2 + k}{a^2} = -8\pi G P \tag{1.7}$$

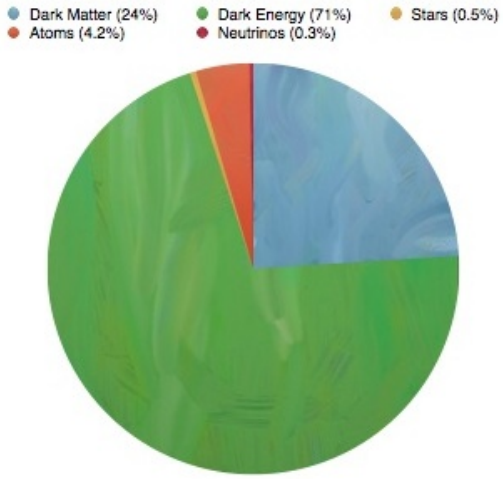

Figure 1.2: Mass-energy content of the current universe from WMAP2009

Here ρ and P refer to the density and pressure respectively. Taking $k = 0$ equation 1.4 can be written as

$$H(t) = \left(\frac{\dot{a}}{a}\right)^2 = \frac{8\pi G}{3}\rho. \tag{1.8}$$

The critical density corresponding to a flat-space time geometry can then be defined as

$$\rho_c = \frac{3H^2}{8\pi G} \tag{1.9}$$

where H is the Hubble parameter. If in addition the assumption holds that each of the mass-energy components has an equation of state that can be written in the form of $p_i = w_i\rho_i$ and the density of each component is parameterised in the following way

$$\Omega_i = \sum_i \Omega_i = \sum_i \frac{\rho_i}{\rho_c} \tag{1.10}$$

the Friedmann equation can be cast as

$$H^2(z) = H_0^2[\Omega_r(1+z)^4 + \Omega_m(1+z)^3 + \Omega_k(1+z)^2 + \Omega_\Lambda] \tag{1.11}$$

Ω_m, Ω_k, Ω_r and Ω_Λ are the density parameters for mass, spatial curvature, radiation, and dark energy respectively, today. For recent measurements of these parameters see for instance the Planck survey (Planck Collaboration et al., 2015). Figure 1.2 shows the density parameters as well as a more detailed breakdown of baryonic matter components and illustrates the remarkable bias towards dark matter and energy. The dominance of dark matter over the familiar atomic content in particular has important consequences

for structure formation, especially during the early stages in which the evolution of matter was dominated by gravitational effects.

1.3.2 Dark Matter and Structure Formation

In a universe that is strictly homogeneous and isotropic, structures such as the Milky Way should not exist, and as such the above equations do not explain how the complex and varied array of structures that can be observed comes to pass. Within the standard paradigm it is assumed that minuscule, quantum fluctuations were responsible for the first in-homogeneities in the energy-mass density field. These seeds grew first through inflation and then gravitational effects until eventually collapsing to form the precursors of familiar galaxies and galaxy clusters.

Starting with the field of overdensities

$$\delta(\mathbf{x}) = \frac{\rho(a\mathbf{x})}{\bar{\rho}} - 1 \tag{1.12}$$

the growth of the field of density perturbations can first be described in the linear regime by a growth function

$$D(a) \propto H(a) \int_0^a \frac{\mathrm{d}a'}{a^3 H^3(a')}. \tag{1.13}$$

Once the overdensities grow beyond unity, a full non-linear treatment becomes necessary which in the most general cases requires some form of numerical solution. However in some cases an analytic solution can be reached giving the statistical distribution of the halo population in the form of the halo-mass function.

Halo-mass Function A halo-mass function (Murray et al., 2013) using the model by Sheth, Mo and Tormen(Sheth et al., 2001) is given in Figure 1.3 at redshifts from 0-30 over a range of 10^3-$10^{15}\mathrm{M}_\odot$. Within the hierarchical growth scheme of dark matter halos, small structure collapses first and then undergoes numerous merger events to form the high mass halo population.

Luminous Structure

Despite the pivotal role played by dark matter in bringing forth structure formation, it is the luminous content that has historically occupied the immediate attention of astronomers. The theory of galaxy formation (Cole, 1991; White and Frenk, 1991; Croton et al., 2006; Benson, 2010) is a complex and ongoing[2] discipline which will here only be touched upon briefly.

Central to the theory of galaxy formation is that the baryonic content should achieve

[2]Purely as a note of historical interest; one of the earliest proponents to popularise the existence of galaxies beyond the Milky Way as distant *island universes* was Immanuel Kant (Kant, 1755) in 1755. In the same work he also questions, albeit on philosophical rather than observational grounds, whether the Universe is finite and has a beginning and end.

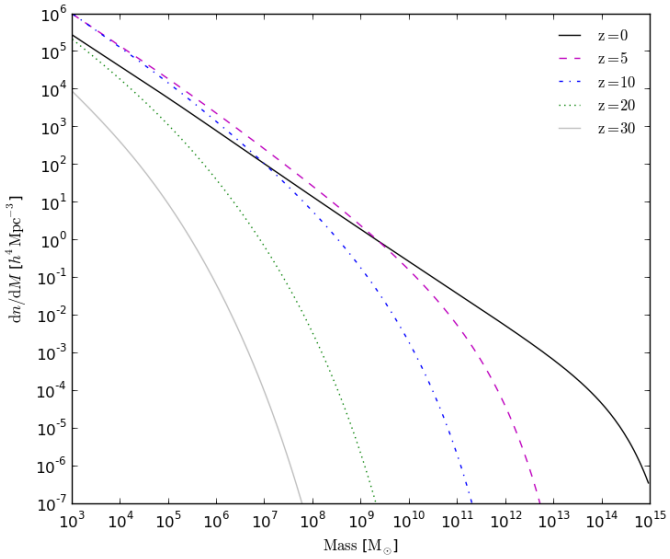

Figure 1.3: Halo-mass function from (Murray et al., 2013) at redshift $0, 1, 2$ and 5 using a fitting function from Sheth-Mo-Tormen and a Planck cosmology.

densities sufficiently high to allow for nuclear fusion and therefore star formation. During the early stages of the Universe, the baryonic mass content follows that of its dark matter counterpart. Once dark matter structure starts to form, primordial gas collapses onto halos to form the earliest galaxies. However the evolution of the baryonic fluid is now complicated by pressure terms which oppose the gravitational forces. The scale at which the sound-crossing time becomes greater than the gravitational free fall-time is called the Jeans mass and gives a measure of the smallest baryonic objects able to form (for further discussion of miminal baryonic objects see the beginning of Chapter 6). The gas then undergoes cooling and fragmentation, eventually leading to star formation. Of course modern galaxy formation incorporates a broad range of elements including the dynamics merger evolution of the underlying dark matter halos, complex gas cooling and feedback schemes, as well as star formation models.

The details of star formation (McKee and Ostriker, 2007; Krumholz and Tan, 2007) within galaxies is an equally complex topic. The first stellar objects (Bromm et al., 2009), categorised as Population III stars[3], are believed to have formed around $z \simeq 30$. These massive objects, around $100\mathrm{M}_{\odot}$ are responsible for the first metals as well as starting the process of ionising the hitherto neutral intergalactic medium (IGM). This gradual ionisation is denoted the Epoch of Reionisation and marks an important change

[3]Historically, stellar populations were first classified as metal rich Population I and metal poor Population II stars (Baade, 1944). To explain the presence of metals in the observed populations, the existence of Population III stars, made from primordial gas, was proposed. At this time, this population of stars is yet to be observed.

in state of the Universe as well as an exciting prospect for future study of early structure formation.

1.4 Epoch of Reionisation

The Epoch of Reionisation signals a significant phase transition the Universe underwent in its latter stages. Figure 1.4 shows a schematic of the history of the Universe up to present day. Following nucleosynthesis during which protons and neutrons fused to form light elements (including helium with small fractions of deuterium, helium isotopes and lithium), the Universe baryonic matter content mainly consisted as a hot plasma coupled to the photon field. As the Universe continued its expansion, it cooled eventually leading to recombination of hydrogen and the decoupling from the photon field (leading to the cosmic microwave background). What followed were the cosmic dark ages during which dark matter continued to form structure until eventually the first luminous sources appeared. At this point the IGM still consisted of neutral hydrogen however, radiation from the first stars soon started to ionise the gas surrounding their host halos. As structure continued to grow, the ionised bubbles grew with them and eventually merged with surrounding bubbles. Reionisation is believed to have been completed by $z \simeq 6$ at which point the gas of the IGM had been fully ionised and the Universe became optically transparent.

1.4.1 21-cm Cosmology

The 21-cm line refers to the hyperfine spin-flip transition of neutral hydrogen in its ground state which is caused by the interaction of the magnetic moments of the proton and electron. The energy difference of the electron spin states has a wavelength of approximately 21 cm, ergo the name. T_S is the so called spin temperature

$$T_S = -\frac{T_*}{\ln(\frac{n_1}{3n_0})} \tag{1.14}$$

where n_1 and n_0 are the occupation states of the spin flip states. T_* is defined as temperature equivalent to the transition energy so that

$$T_* = \frac{h\nu_{21}}{k_b}. \tag{1.15}$$

Collisional interactions with other hydrogen atoms as well as thermal coupling to the CMB photon field will pump electrons into the excited spin state. In the presence of the CMB field alone the spin temperature rapidly reaches equilibrium with the CMB temperature $T_{CMB} = 2.75(1+z)$ K and the 21-cm is undetectable. Fortunately collisional interaction with Lyα photons, known as the Wouthusen-Field effect couple the spin flip temperature to the gas instead so that the neutral hydrogen becomes visible against

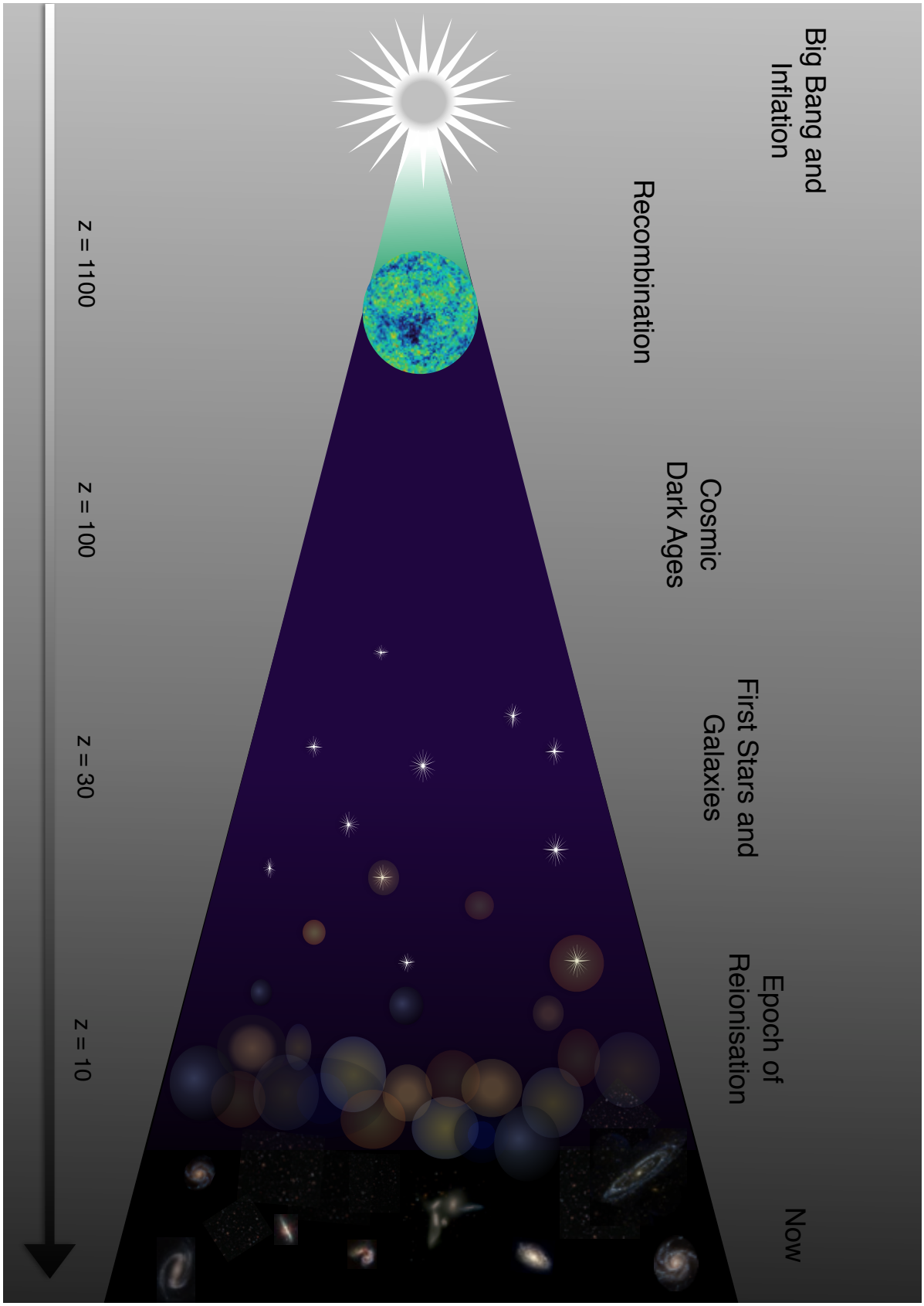

Figure 1.4: Overview of cosmic history leading up to the Epoch of Reionisation and finishing in present day.

the CMB background. (Whether the signal manifests as emission or absorption is set by the difference in gas and CMB temperature).

Photons produced during the energy transition are redshifted due to the expansion of the Universe, so that

$$\nu_{21} = \frac{\nu_{21}}{1+z}. \tag{1.16}$$

The redshifting of the 21-cm line can therefore be exploited to observe the Epoch of Reionisation (Furlanetto et al., 2006a; Barkana, 2009). The relevant observable is the 21-cm brightness temperature contrast and can be thought of as the contrast between a neutral cloud of hydrogen in the observer's line of sight and the CMB background. Solving the radiative transfer equation

$$I_\nu = \frac{2k_B}{\lambda^2} T_b \tag{1.17}$$

where T_b is the brightness temperature and λ the 21-cm wavelength gives the brightness temperature contrast δT_b,

$$\delta T_b = \frac{T_S - T_{CMB}}{1+z}(1 - e^{-\tau_\nu}). \tag{1.18}$$

In the above expression τ_ν is the optical depth, or the path integral of the photon along the line of sight, multiplied by the absorption coefficient α_ν, of the medium it travels through. The average optical depth for the cloud considered here is

$$\tau_\nu \equiv \int_{\Delta_S} \alpha_\nu \mathrm{d}s \approx \frac{3}{32\pi} \cdot \frac{hc^3 A_{10} \bar{n}_H(z)}{k_B \nu_{21}^2 T_S} \cdot \frac{(1+\delta)\bar{x}_{HI}}{H(z)} \tag{1.19}$$

where δ is the cosmic matter overdensity, A_{10} is the spontaneous emission of the 21-cm transition, $\bar{n}_H$ is the average number density of hydrogen, $\bar{x}_{HI}$ is the average fraction of neutral hydrogen and $H(z)$ is the Hubble constant. Provided $\tau_\nu \ll 1$ the above simplifies to

$$\delta T_b = \frac{3}{32\pi} \cdot \frac{A_{10} c^3 h \bar{n}_H^0}{\nu_{21}^2 k_b} \cdot \frac{T_S - T_{CMB}}{T_z} \frac{(1+z)^2}{H(z)} (1+\delta)\bar{x}_{HI}. \tag{1.20}$$

Here $\bar{n}_H^0$ is the average hydrogen number density at redshift 0. The 21-cm power spectrum is given by

$$P_{21}(k,z) \equiv \langle |\delta\tilde{T}_b(\mathbf{k},z)|^2 \rangle_k = \frac{1}{m} \sum_{i=1}^{m} |\delta\tilde{T}_{b,i}(k,z)|^2 \tag{1.21}$$

where k refers to the wavenumber and $\delta\tilde{T}_b$ denotes the Fourier transform of δT_b.

A number of radio frequency experiments probing the Epoch of Reionisation using

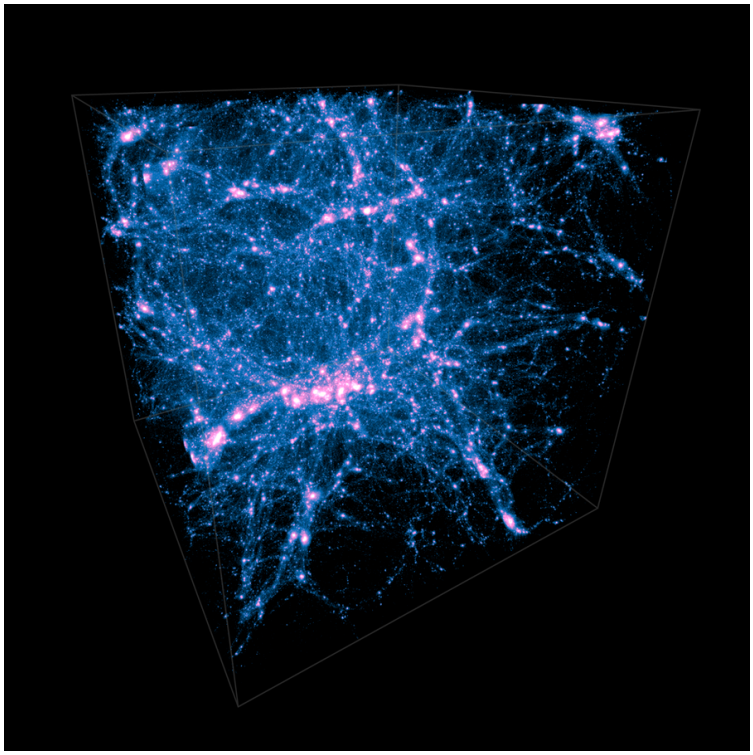

Figure 1.5: External view of the full dark matter Illustris box (Genel et al., 2014).

the 21-cm signal (Mesinger et al., 2014) are currently ongoing or in the planning stages. These include the SKA[4] (Mellema et al., 2013) and its pathfinder the MWA[5] (Tingay et al., 2013), PAPER[6] (Pober et al., 2013) and LOFAR[7] (Chapman et al., 2012). These experiments make use of massive arrays of antennae as radio interferometers to try and detect 21-cm emission. A number of key challenges need to be faced before the prospect of successful detection can be realised. These include man-made signal pollution from radio and television and the successful removal of foregrounds both of terrestrial origin and perhaps most importantly from astrophysics sources.

1.5 N-Body Simulations

One of the pivotal methods of investigating the growth and evolution of structure is through N-body simulations. Groundbreaking work employing dark matter simulation such as the Millennium (Springel et al., 2005), MillenniumII (Boylan-Kolchin et al., 2009) and Bolshoi simulations (Klypin et al., 2011) as well as the full hydrodynamical suite (Genel et al., 2014), show dark matter acts as the effective backbone facilitating the formation of stars and galaxies. Figure 1.5 shows the so called cosmic web in the

[4]http://www.skatelescope.org/
[5]http://www.mwatelescope.org/
[6]w.astro.berkley/edu/ dbacker/eor
[7]http://lofar.org/

external view of the dark matter box from the Illustris simulation. The bright, high density regions are indicative of dark matter halos hosting galaxies and galaxy clusters. The statistical distribution of the simulated halos is in very good agreement with the distribution of observed structure.

Uncertainty in the Dark Matter Model

Dark matter plays a vital role in the emergence and behaviour of stars and galaxies which begs the question whether the fact that the fundamental nature of dark matter is as of yet undetermined has any potential implications for the evolution of galactic structure. In general an N-body dark matter simulation will make certain assumptions about the fundamental nature of dark matter, for instance that it only interacts gravitationally, is non-collisional, can be treated as cold (i.e. being constituent of low velocity particles). However, changing these assumptions by, for example, swapping out the cold dark matter with a warm model can lead to noticeable changes in the final halo population. In this case warm dark matter will tend to suppress small-scale structure due to the particles increased free streaming length. Similarly the existence of high density cusps at the centre of halos is somewhat contingent on the precise dark matter model used, though realistically constraints from observations do restrict how much variation is allowed in the underlying dark matter model[8].

1.6 Further Evidence

Even though the works of Zwicky and Rubin are conventionally cited as forming the cornerstones of the discovery of dark matter (Roos, 2012), there is further evidence which not only supports the existence of dark matter but contains valuable information regarding its relative abundance and make-up.

1.6.1 Gravitational Lensing

Weak and strong (Markevitch, 2006; Clowe et al., 2006) gravitational lensing have also offered compelling evidence in support of dark matter. Both types of lensing are relativistic phenomena caused by the distortion of light due to gravitational effects. The two techniques are distinct insofar as strong lensing features the clear distortion of a single source by a massive lens, while in the case of weak lensing the lens is lighter and only causes mild shearing of the source image. Both can be used to measure the masses of objects (generally galaxy clusters) independent of their dynamics. Mass-to-light ratios, as well as mass distributions found from such measurements are in support of results derived from dynamical studies indicating an invisible mass component.

[8] As a rule uncertainties in the baryonic effects tend to outweigh those from dark matter.

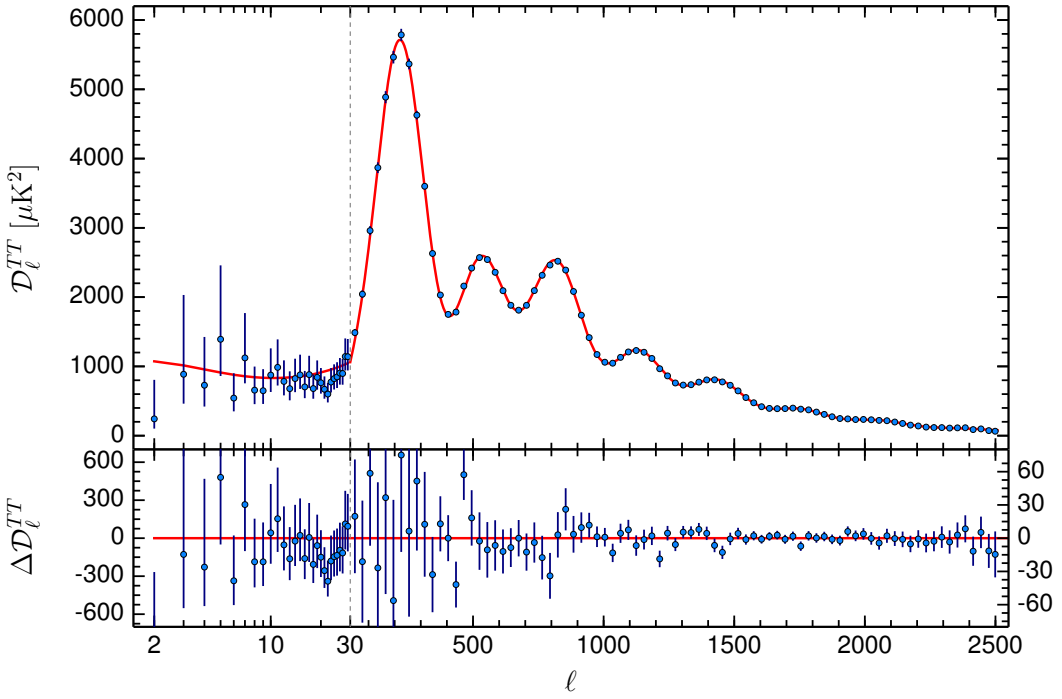

Figure 1.6: Planck 2015 CMB temperature power spectrum with best fit spectrum from ΛCDM cosmology and residuals shown in lower plot (Planck Collaboration et al., 2016).

1.6.2 CMB

The cosmic microwave background is a thermal radiation relic due to plasma recombination in the early universe. It is of great cosmological interest as it provides support not only for the Big Bang paradigm, but gravitationally driven anisotropies in the CMB also contains information on the dark matter abundance relative to the universe's baryonic content. In the early Universe, the radiation and matter components were strongly coupled leading to in-phase oscillations in the primordial adiabatic perturbations. These acoustic oscilations are imprinted observables in the baryon-photon fluid after decoupling, see Figure 1.6. What is critical to the question of the make-up of dark matter is that baryonic matter, in addition to being self-gravitating, is pressure supported while the proposed dark matter component is pressure-less. The peaks in the CMB power spectrum depend on the total matter content while the troughs are driven by the baryonic pressure only. Fitting cosmological models to the power spectrum allows for the relative abundance of baryonic and dark matter to be established. Measurements from the Wilkinson Microwave Anisotropy Probe (WMAP) (Komatsu et al., 2009) and Planck satellite (Planck Collaboration et al., 2016) show that the dark matter mass density parameter $\Omega_{DM} = 0.268$ while the contribution form baryonic matter is $\Omega_B = 0.042$. Careful analysis of the CMB spectrum has greatly contributed to the

Figure 1.7: Composite image of the bullet cluster showing mass distribution after collision (Markevitch, 2006; Clowe et al., 2006). The pink distributions, taken from data provided by the Chandra X-ray telescope, show hot gas and are indicative of the majority of the baryonic content of the two clusters. The blue shows the actual concentration of mass of the clusters and was determined using gravitational lensing. The optical image on which these are superimposed was taken from the Magellan and Hubble Space Telescope.

understanding of the mass-energy content of the Universe, including the presence of the "dark energy" component.

1.6.3 Bullet Cluster

A particularly striking example that not only supports the existence of dark matter but underlines its non-baryonic nature is the Bullet Cluster (Clowe et al., 2004; Markevitch et al., 2004). The composite image in Figure 1.7 shows the Bullet cluster which has just undergone a major merger. The image shows that the distribution of the mass component consisting of majority of the two clusters' baryons does not align with the mass of the system (determined using weak lensing and x-ray maps.)

1.7 Towards the Fundamental Nature of Dark Matter

Despite the presence of dark matter only being inferred indirectly through its gravitational interaction with astrophysical objects, a number of inferences can be made about its fundamental nature. While not able to give an exact picture, these observations offer invaluable constraints for any potential model put forth. While today it is widely accepted that dark matter is non-baryonic in nature, the first dark matter models proposed were baryonic, with most eventually ruled out on the basis on insufficient abundance.

1.7.1 MOND

While a new dark matter particle sector is taken as the concordance solution to the unexpected observed galaxy and cluster dynamics, there is an alternative explanation in the form of Modified Newtonian Dynamics (MOND). First proposed by Mordehai Milgrom in three papers in 1983 (Milgrom, 1983a,b,c), the theory proposes that if Newton's second law is modified so that $F_N = ma^2/a_0$ in the low acceleration limit $a \ll a_0 \sim 1.2 \times 10^{-10}$ ms^{-2}, then the shape of galaxy rotation curves can be explained without the introduction of a dark matter component.

In order to provide a credible alternative to the dark matter paradigm, MOND had to be made compliant with general relativity. This was achieved in steps (Bekenstein and Milgrom, 1984; Bekenstein, 1988; Bekenstein and Sanders, 1994; Sanders, 1997), culminating in Tensor-Vector-Scalar gravity or TeVeS (Bekenstein, 2004; Skordis, 2008). The latter has been able to show compliance with a wider range of the "missing mass" phenomenology in part due to the presence of additional fields and free parameters though these in turn limit the predictive power of the theory, as well as general practicality. Furthermore, while MOND has shown agreement with the observation of galaxy rotation curves (Sanders, 1996; Milgrom and Sanders, 2005, 2007), the theory has been less successful in describing dynamics at cluster scales (including the collision behaviour demonstrated by the Bullet cluster) and the CMB doppler peaks, both of which are well described by Λ- CDM (Sanders, 2003; Skordis et al., 2006; Dodelson and Liguori, 2006; Sanders, 2007; Famaey and McGaugh, 2012).

1.7.2 Baryonic Dark Matter Candidates

When Fritz Zwicky first proposed the existence of dark matter within the Coma cluster, his concept of "dark matter" would have been rather different than today's notion of an exotic, hitherto undiscovered particle. Considering that during this time the Standard Model of particle physics was itself still under development, it is perhaps not surprising that the initial solutions to the dark matter problem were of baryonic origin.

MACHOS MACHOs or massive astrophysical compact halo objects such as black

holes, planets, brown and white dwarfs and neutron stars, were a once popular explanation for dark matter. Ultimately MACHOS were ruled out as the dominant component of dark matter by two key observations.

Gravitational microlensing (see §1.6.1) was first proposed as a useful tool to search for compact objects within the Milky Way in the 1980s (Chang and Refsdal, 1979; Paczynski, 1986). While initial measurements seemed to be consistent with a MACHO dark matter solution (Alcock et al., 1993; Aubourg et al., 1993), more precise studies later put the upper limit of the fraction of the MACHO Milky Way halo mass at around 8% (Lasserre et al., 2000; Tisserand et al., 2007).

As mentioned in §1.6.2, analysis of the CMB's baryonic acoustic oscillations provided further evidence that the bulk of the dark matter component was not baryonic. Another line of reasoning that puts an upper limit of the total abundance of baryons in the universe comes from Big Bang nucleosynthesis calculations. Using the abundance measurements of light elements such as deuterium, allowed the total baryon contribution to be set at about $\Omega_b h^2 = 0.02 \pm 0.002$ (Fukugita et al., 1998; Burles et al., 2001). Both these measurements effectively rule out MACHOS as the principal component of dark matter.

Primordial Blackholes One particular type of MACHOS worth a separate mention are primordial blackholes. By forming before Big Bang nucleosynthesis took place with masses below the microlensing sensitivity, it allows both the baryon limits set by CMB measurements and nuclesynthesis, as well as the microlensing MACHO limits to be circumvented (Carr and Hawking, 1974; MacGibbon, 1987; Yokoyama, 1998; Kim et al., 1999). However the viability of primordial black holes as dark matter candidates is hampered by the efficiency with which primordial black holes would have formed. The low number of objects is difficult to avoid without potentially infringing on other cosmological constraints (Ali-Haïmoud and Kamionkowski, 2017).

Neutrinos On the particle side, neutrinos were considered to fit a number of requirements for a viable dark matter candidate since they only interacted weakly as well as having mass as was shown thanks to the discovery of neutrino oscillations (Doroshkevich et al., 1980a,b; Zeldovich et al., 1980). Neutrinos also fall into the category of hot dark matter in which particles travel with relativistic velocities[9] (Peebles, 1982; Schramm and Steigman, 1981).

The latter quality turns out to have important consequences for structure formation. In the case of hot dark matter, massive structures are formed first while in

[9]This is due to the fact that neutrinos are very light particles and thus their thermal relics are extremely energetic after falling out of equilibrium.

contrast cold dark matter undergoes hierarchical structure formation from small masses up. Numerical simulations show that the structure formed in a hot dark matter universe to be incompatible with observed clustering scales of large structure (Davis et al., 1982; White et al., 1983), ruling out neutrinos and hot dark matter as a satisfactory candidate. Other neutrino particles, such as the sterile neutrino, have been proposed as dark matter candidates though the existence of these additional species are in part constraint by cosmological observations (Albiński and Michel, 1982; Dodelson and Widrow, 1994a). While in the end neutrinos fell short of the mark, the proposal of neutrinos as dark matter marked an important practical step towards placing dark matter within the context of particle physics, as well as developing the WIMP paradigm.

Towards New Physics

The culmination of astrophysical observations over the last decades has produced a compelling case for the presence of a significant dark matter component. More over while a small fraction of dark matter does indeed reside in the form of the familiar baryonic matter listed above, the evidence also suggests that the lion's share is in the form of a as of yet unspecified new particle. In order to fully answer the question of the fundamental nature of dark matter, particle physics must be invoked. In the next chapter the possible particle nature of dark matter is presented, including how weakly interacting models can motivate new ways of detecting dark matter.

Chapter 2

Searches for Dark Matter II: A brief introduction informed by particle physics

At this point it is expedient to make the leap from the massive scales of galaxies to the realm of the fundamental particles. The study of the most elemental building blocks of nature matured as a discipline alongside astrophysics during the last century, cumulating in the formulation of its own concordance paradigm in the form of the Standard Model (SM). Having resigned oneself to the existence of dark matter, the question of how this unanticipated matter component is to be understood against the backdrop of the fundamental particles must eventually be answered.

As it turns out dark matter also poses a significant challenge within the context of particle physics. In a sense this is not unexpected considering the body of evidence indicating its presence comes exclusively from astronomical observations and then only through the gravitational effects due to galaxy scale masses. In contrast there is no sign of any such particle in known particle interactions, and the theoretical framework of the SM does not naturally suggest a viable dark matter candidate. On the other hand, dark matter underpinning problems in both astro and particle physics also opens up unique opportunities to further both fields on a quite fundamental level, as well as potential avenues of investigation into dark matter.

In the following chapter, a brief summary of the role that particle physics plays in the search for dark matter is presented, beginning with the current state of the Standard Model and how its shortcomings can inform searches for potential dark matter candidates. A number of the leading possibilities are outlined[1] as well as experiments making use of these models when searching for evidence of dark matter particle interactions. Lastly is the summary of the remainder of this thesis which will focus on the role annihilating dark matter plays during early structure formation and how astrophysical observations could offer valuable constraints for this kind of dark matter.

[1] Including a description of how self-annihilating candidates can be modelled.

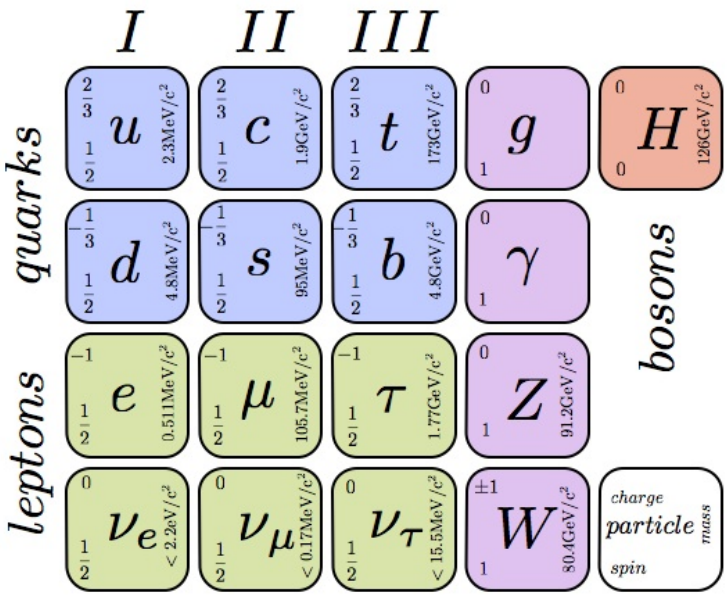

Figure 2.1: Table of the constituent particles of the Standard Model

2.1 The Standard Model

Modern particle physics and its related phenomena are described by a gauge quantum field theory commonly referred to as the Standard Model (SM). It distinguishes between half-spin fermions which make up conventional matter and the integer spin bosons which mediate the forces acting between them. (For a general overview of the Standard Model and its various components see for example Salam (1968); Glashow et al. (1970); Abers and Lee (1973); Renton (1990); Novaes (2000); Pich (2007).)

Counted amongst the fermions are quarks and leptons occupying the blue and green boxes respectively in Figure 2.1 (Yao et al., 2006). Amongst the leptons (Weinberg, 1967) are the electrically charged electron e, muon μ, and the tau τ particles as well as their neutral respective neutrino counterparts ν_e, ν_μ, ν_τ whilst quarks come in six different flavours, namely up, down, charm, strange, top and bottom (u, d, c, s, t, b). In addition to their electric charge, quarks also carry a so called colour charge which has three different types, often called red, green and blue (Fritzsch et al., 1973). Since the colour charge does not manifest itself in nature it suggests that some form of confinement criterium exists that stipulates that quarks only exist in colour-neutral composites called hadrons. For example, three quarks each carrying different colour charge will form a colour neutral triplet. These are called baryons and make up particles such as protons

(uud) and neutrons (ddu). Alternatively a quark and anti-quark pair (meson) will also be colour neutral and these include particles such as the pions and kaons.

In contrast the gauge bosons, red in Figure 2.1 (Yao et al., 2006), are considered force carriers and mediate the fundamental forces between particles (with the exception of gravitational interactions). Of these the massless, changeless photon γ is perhaps the most recognisable, being exchanged during electromagnetic interactions. The weak force is mediated by the $W^{\pm}, Z$, the massive intermediate vector bosons and lastly the colour or strong force has eight gluons g_{α}, which themselves carry colour charge and are therefore self-interacting. The last two forces, while stronger than electromagnetism only work over short range since their force carriers are either massive or colour confined[2].

Underlying the SM are a number of symmetries, including but not limited to:

- Charge conjugation (C), Parity transformation (P) and Time reversal (T) which are all discrete symmetries. While not all SM interactions preserve these individually, the CPT Theorem states that the combined symmetry is conserved (Schwinger, 1951).

- Continuous symmetries (these are generally described by Lie groups) such as space-time rotations and translations, and the internal isospin symmetry.

Symmetries are used to generate the algebraic group structure of the theory. Three of the four fundamental interactions (strong and electroweak) are accounted for by the standard model gauge theory which undergoes the following spontaneous symmetry breaking:

$$SU(3)_C \otimes SU(2)_L \otimes U(1)_Y \longrightarrow SU(3)_C \otimes U(1)_{em} \tag{2.1}$$

Here $SU(3)_C$ corresponds to the strong force (colour interactions) and $SU(2)_L \otimes U(1)_Y$ to that of the electroweak interactions. The electromagnetic group $U(1)_{em}$, is a subgroup of the electroweak symmetry group and manifests itself as a separate force after symmetry breaking (Weinberg, 1967).

2.2 Physics Beyond the Standard Model

The SM does a remarkable job of explaining the near complete span of recognised particle physics phenomenology though a handful of outstanding issues remain that indicate the theory to be still incomplete (Bertone et al., 2005). Some of the most pressing of these issues include:

Hierarchy Problem Perhaps the most pertinent is the Hierarchy Problem that arises due to the Higgs field (responsible for giving mass to particles). In its presence arise

[2]Not surprisingly the range of interaction for the atomic strong and weak force is comparable to that of the smallest hadrons and also sets an effective limit for the size of stable atoms

the massive discrepancy between the weak and the Planck energy scales which requires an arguably contrived level of fine-tuning to solve(Zee, 2003).

The fine-tuning problem On a similar note is the fact that the SM contains a considerable number of tuneable parameters. These have been determined to high accuracy experimentally however there is no theoretical explanation as to why the parameters in question have the values they do (Schwartz, 2013). One instance of this fine-tuning arises in QCD to describe hadronization, the process in which quarks and gluons split to form hadrons.

Flavour Problem The flavour problem addresses fundamental questions related to the origin of quark and lepton masses, the existence of three generation of leptons and particulars of the Yukawa couplings and colour mixing matrix (Volkas, 1996).

Gravity Another point of contention is that the standard model does not incorporate gravitational interactions into its framework. This has led to the conjecture that there exists a more fundamental theoretical description which would solve the problem of unification and to which the current SM merely presents a low energy limit (Nagashima, 2013).

Neutrino mass The experimental evidence for neutrino oscillation (involving the mixing of neutrino mass and flavour states) requires the particles to have mass while within the SM they are decidedly mass-less (Maltoni et al., 2003).

Dark Matter and Dark Energy As already mentioned, the absence of a dark matter particle is the prime motivator behind this work. While the neutrino has some qualities of a potential dark matter candidate, they are not abundant enough to explain the total observed dark matter content. In a similar vein the Standard Model also fails to explain the proportion of Dark Energy that makes up the total mass-energy content of the universe (see Chapter 1).

The points at which the SM fails are important road markers on the way to building new, more comprehensive theoretical frameworks to describe particle physics. Of particular interest here are the cases in which a proposed theory describing physics beyond the Standard Model also yields a potential dark matter candidate. On occasion these theoretical dark matter particles will also have extra-gravitational interactions with the standard physics sector, giving an ansatz for wider experimental methods aimed at detecting dark matter. In turn the empirical knowledge we have of dark matter works to constrain new theories which is generally challenging as they describe energy scales difficult if not impossible to reproduce in a laboratory setting.

2.3 Potential Dark Matter Candidates

The following gives a short description of some of the leading dark matter candidates. Most are naturally part of a theoretical frameworks beyond the Standard Model.

2.3.1 Supersymmetry

Motivated by the Coleman-Mandula Theorem (Coleman and Mandula, 1967) Supersymmetry, commonly abbreviated to SUSY postulates that each boson has a supersymmetric fermion counterpart and vice versa. In order to explain why these particles have not been detected, it is assumed that SUSY deals with a spontaneously broken symmetry which comes with the added benefit of removing a number of problems that have been plaguing the Standard Model for some time. This includes solving the Hierarchy Problem and gauge coupling unification. In addition, it offers an attractive dark matter candidate in the form of the SUSY neutralino which offers astrophysically compatible masses and interaction cross-sections. The neurtralino has the interesting quality of being its own anti-particle which means it self-annihilates which in turn might offer another way to detect dark matter. For further details see Bagger (1996); Martin (1998); Peskin (2008). See Appendix A for a detailed derivation of neutralino properties in the context of the minimal supersymmteric model (MSSM).

2.3.2 Extra-dimensions

The idea of our observable universe being imbedded in extra dimensions goes back to the 1920s (Kaluza, 1921) when physicists first attempted to unify electromagnetism with gravity. In the case of Universal Extra Dimensions (UED) where all SM fields are allowed to propagate in the full set of dimensions[3] a dark matter candidate also arises. One of the best studied of these is the Lightest Kaluza-Klein particle (Servant and Tait, 2003).

2.3.3 Axions

Proposed as part of Peccei-Quinn Theory as a solution to the Strong CP Problem, axions present another potential cold dark matter candidate. The theory works by introducing a new, spontaneous broken symmetry with axions acting a the boson associate with the field. (The axion acquires its mass due to QCD vacuum interactions.) It was shown that axions in the presence of a strong magnetic field can be converted to photons which also opens up the possibility of future detection (Rosenberg and van Bibber, 2000).

2.3.4 Sterile Neutrino

Sterile neutrinos share many qualities of their SM counterpart with the exception that their weak interactions are restricted to mixing. While sterile neutrinos would make

[3]This is opposed to models in which the Standard Model interactions except gravity are confined to the brane, which comprises the familiar space-time dimensions.

a viable dark matter candidate and are well motivated theoretically based on chirality arguments they are more challenging to detect than the weakly interacting WIMPs (Dodelson and Widrow, 1994b).

The list presented above encompasses a number of leading theoretical particle dark matter candidates. These are not taken to be an exhaustive list, though they do demonstrate a lot of the general qualities that are desirable in a dark matter particle given the constraints from astrophysical observations. Models such as those from SUSY and Kaluza-Klein can be generally classified as a WIMP or weakly interacting massive particles. To date they have been some of the most favoured dark matter models due to the fact that they naturally arise in theoretical frameworks with other desirable qualities as well as having well motived mass ranges and interaction cross-sections. However failure to detect any evidence for either WIMPs or supersymmetry at the most recent run of the LHC is beginning to encroach on the potential WIMP candidate parameter space.

2.4 Modelling Dark Matter

Self-annihilating models are some of the most promising potential dark matter candidates. However in order to make use of these in an experimental setting the annihilation power as well as the nature of the annihilation products must first be determined. Here self-annihilating refers to a majorana type dark matter matter candidate that acts as its own anti-particle. This is in contrast to models where the dark matter sector contains a distinct anti-particle. The precise nature of the annihilation processes impact the annihilation products as in the latter case the subsequent particles don't necessarily carry the conserved quantum numbers of the original particles.

2.4.1 Effective Dark Matter Models

One of the most straightforward ways to model a generic annihilating (decaying) dark matter particle is via an effective field theory which reduces the number of operators by re-parameterising the complete interactions (Dreiner et al., 2013). In most cases this results in a four particle interaction with effective coupling between the incoming and outgoing particles set by the annihilation cross-sections. This is shown in the upper left part of Figure 2.2 where the original dark matter particles annihilate to pairs of leptons, quarks or bosons.

2.4.2 Annihilation Cross-Section

The interaction strength between dark matter particles is set by the velocity averaged annihilation cross-section. A natural choice of cross-section is close to that of the weak interaction as this gives the correct present day density if dark matter is assumed to be a thermal relic. In this work it is assumed that dark matter is cold and thus the velocity averaged annihilation cross-section is taken as constant regardless of environment. More

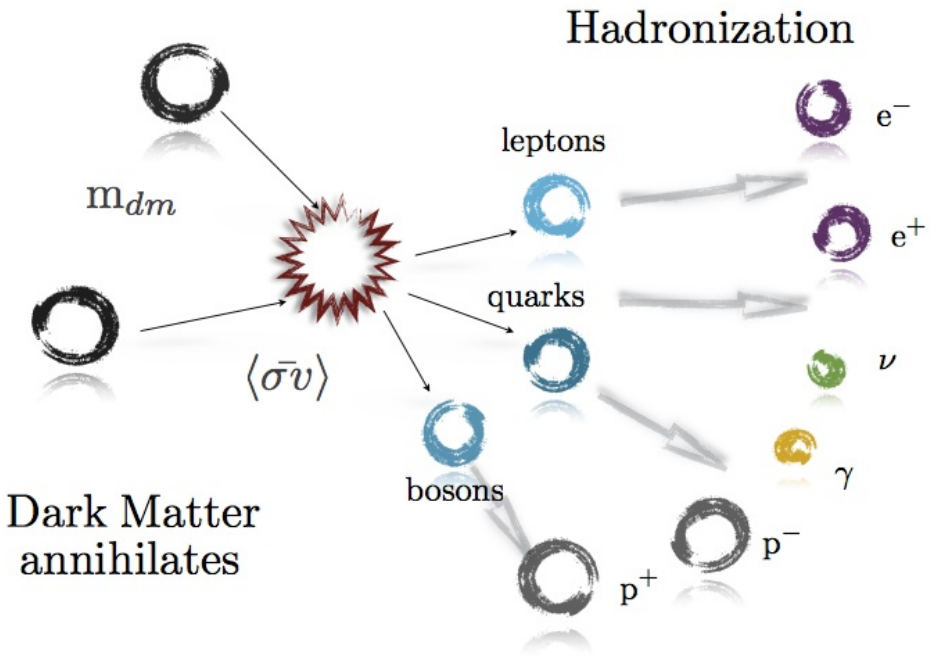

Figure 2.2: Schematic of dark matter particles annihilation via unstable standard model quarks, leptons and bosons which, if unstable, continue to hadronize until only stable SM particles (electrons, positrons, photons, neutrinos, protons and anti-protons) remain.

realistically the bulk motion of dark matter within halos may need to be taken into consideration when calculating the annihilation rates within collapsed structure (this, as well as the dynamics structure of halos in general, is not addressed directly in this thesis but instead left for future work)[4].

2.4.3 Annihilation Channel

In general the direct annihilation products of dark matter particles are here taken to be in the form of unstable SM particles (see Figure 2.2). As a whole if the annihilation products are not stable they tend to have lifetimes very much shorter than the scales associated with halo processes and are so allowed to further decay until only stable particles remain. Depending on what the intermediate annihilation product was, the final distribution of stable products can vary vastly in terms of the type of particle and energy distribution of the different products.

2.4.4 PYTHIA Modeling

In order to produce a realistic spectrum of annihilation products, the final particle distribution is modelled using the PYTHIA code (Sjöstrand et al., 2006, 2008). PYTHIA is a Monte Carlo event generator for particle physics. To simulate the annihilation event a electron/positrons proxy is used, where the centre of mass energy of the event sets the mass of the dark matter particle. The intermediate annihilation product is preset to the dark matter model's annihilation channel. The code was allowed to run until only electrons, positron, photons and neutrinos remain[5]. Figure 2.3 shows the spectrum of stable annihilation products for different dark matter masses and annihilation channels. In each plot, blue/green curves show electrons/positrons while red curves show photons. From top to bottom the annihilation channel changes from muons, quarks, tau leptons and W bosons with different line styles showing different masses as indicated in each plot. The figure clearly illustrates that both the energy distribution as well as relative abundance of annihilation products can vary significantly both with mass and the annihilation channel. As will be shown throughout this work, the energy transfer process can vary markedly with particle energy making the realistic modelling of the annihilating products an important part of the following analysis.

PYTHIA Tunes and Hadronization

As mentioned above the process of hadronization which allows quarks to form stable products does not naturally arise within the Standard Model. PYTHIA employs the phenomenological Lund String model (Andersson et al., 1979, 1983) when implementing

[4]To further muddy the waters, processes such as the Somerfeld Enhancement (Feng et al., 2010) exist that can further undermine the assumption of a constant annihilation cross-section.

[5]Protons and anti-protons were also produced but in such small numbers that they were neglected in the subsequent energy transfer treatment

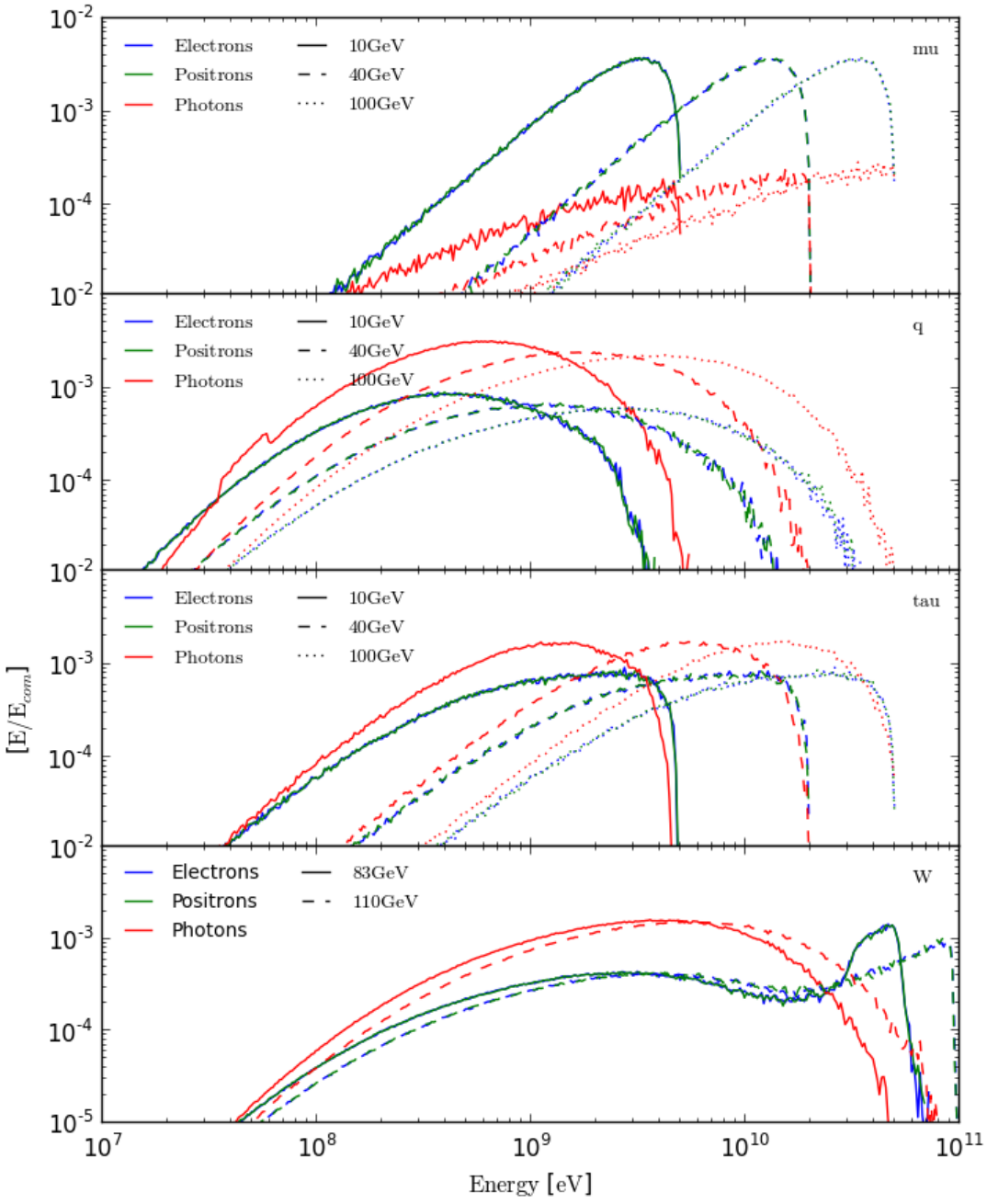

Figure 2.3: Outputs for an electron/positron dark matter proxy simulation in PYTHIA, showing the energy distribution of stable particles for different annihilation channels. Blue and green lines show electrons and positrons respectively while the red denotes photons. From top to bottom the annihilation channels shown are via muons, quark, tau and W boson. In each of the lepton cases, dark matter masses of 5(5.5), 20 and 50GeV were employed while the heavy vector boson case assumes a 83 or 110 GeV particle.

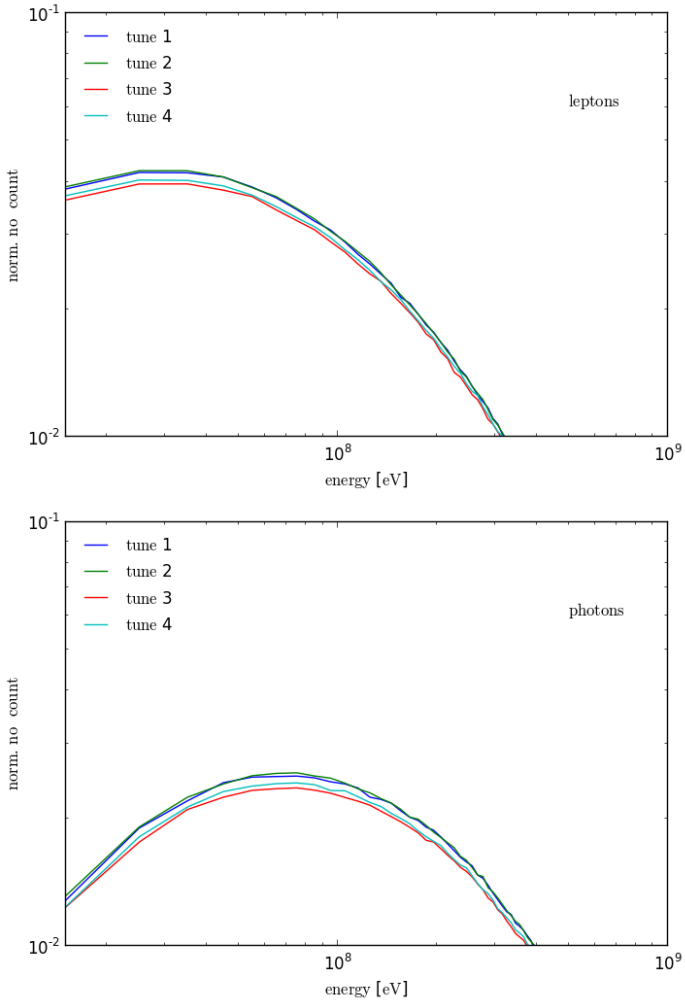

Figure 2.4: The variation in the normalised number count for a 20GeV dark matter particle annihilating via the μ channel. The top panel shows the results for leptons and the lower photons, in both case the annihilation was simulated 100000 times.

hadronization while the user can select different tunes for the model's free parameters. While in principal the various free parameters can be set independently, in reality there exist correlations and anti-correlations between different sets that arise from experimental constraints. PYTHIA tunes provide correlated settings for the appropriate groups of parameters. Depending on the tune the final distribution of stable particles will vary subtly, however in comparison to uncertainties in the rest of the underlying dark matter model these variations are deemed negligible. Figure 2.4 shows the difference in annihilation products for different PYTHIA tunes (different coloured curves), where the top plot show electrons/positrons and the lower photons. It is evident that the variation due to the tune is very small. In particular the change due to the hadronization tune is strongly subdominant to other uncertainties that arise when modelling both the halo and the energy transfer and not taken further into account.

2.5 Searches for Dark Matter Particles

The existence of dark matter as well as its empirical characterisation as massive, collisionless and at most weakly interacting have been well established through a range of astrophysical observations. However, in order to reveal more of dark matter's fundamental nature, experiments that look for particle interactions are in order. Over the years a number of avenues searching for experimental of dark matter have been explored (Bergström, 2000; Bertone et al., 2005; Bertone and Hooper, 2016) and can to a degree be summarised in Figure 2.5 (Feng, 2016), where the red and black particles indicate Standard Model and dark matter respectively and the interaction is left open, depending on the underlying theoretical model employed.

Searches are somewhat dependent on the kind of WIMP dark matter particle under investigation. In the case of other dark matter models such as axions or non-WIMP candidates searches differ significantly due to their contrasting phenomenologies.

2.5.1 Collider Experiments

The production of new particles in colliders has long proven fertile grounds in the expansion of the particle zoo and is perhaps the most straightforward when it comes to methods to identify dark matter particles. Attempts to discover new physics at colliders (Csáki et al., 2003) entail the acceleration of fundamental particles to highly relativistic energy scales. Experiments conducted at facilities such as the Large Hadron Collider (Baer et al., 2003) are planning runs of up to 14TeV as soon as 2017/2018.

The idea behind these experiments is that if Standard Model particle are smashed into each other at sufficiently high energies new particles, perhaps even a dark matter particle maybe created. While the dark matter particle will not be detectable directly at the LHC, keeping track of the remaining collision products will allow scientists to determine the presence of any "missing mass" which maybe indicative of a new particle.

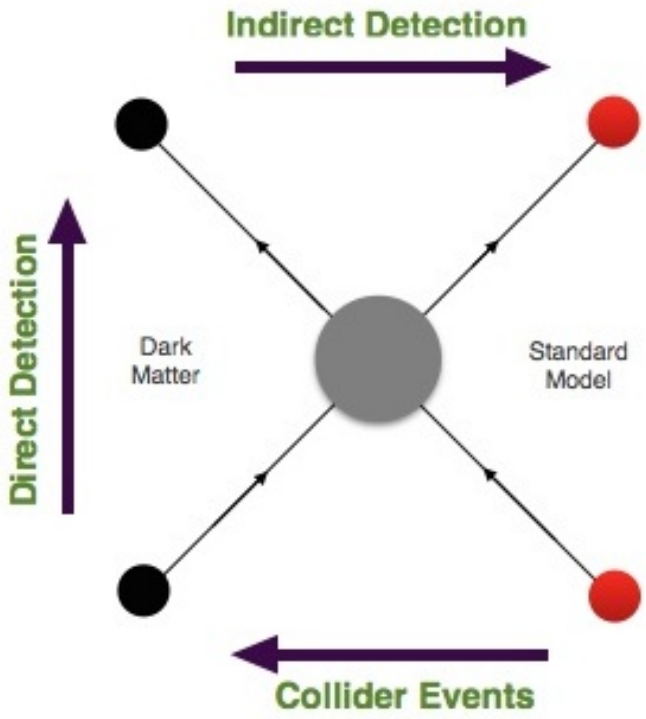

Figure 2.5: Summary of current dark matter searches with the format taken from (Feng, 2016)

2.5.2 Direct Detection Experiments

Alternatively if one works under the assumption that the Galaxy and therefore the Solar System sit within a dark matter halo, then there should be a steady flux of dark matter particles passing through the Earth as it orbits the Sun. In practice the collision between an incoming WIMP-like particle and an atomic nuclei should be detectable through the nucleus recoil energy. In addition there are expectations of seasonal variations in any potential signal due to the Earth's relative motion against or with the dark matter background at different points on its journey around the Solar System.

There have been quite a few direct detection experiments conducted over the years such as DAMA/Na (Bernabei et al., 2003) and then later DAMA/LIBRA (Bernabei et al., 2008, 2010), CRESST-II (Angloher et al., 2012), EDELWEISS (EDELWEISS Collaboration et al., 2011) LUX (Akerib et al., 2014) and XENON100 (Aprile et al., 2012). Experiments have so far produced conflicting results. In particular the DAMA/LIBRA collaboration reported the detection of seasonal modulations compatible with dark matter interactions. However these results are inconsistent with results from LUX. This suggests that either the detection made by DAMA are due to seasonal environmental effects or that dark matter has some complex, unexpected phenomenology that causes particles to interact differently depending on the atomic target within the detector. Overall direct detection experimental techniques remain some of the most promising to date with more collaborations planned for the near future.

2.5.3 Indirect Searches

In the case of annihilating and decaying dark matter models the detection of the highly energetic annihilation products maybe used to infer the existence of the parent particle. These tend to be astrophysical searches as any non-gravitational interaction such as annihilation have to be at or around the weak scale. As such it requires high density regions, preferable as close as possible such as found at the centre of Milky Way to conduct searches of particle excesses (Cohen et al., 2012).

While the Galactic Centre presents a relatively accessible over-dense region of dark matter, it is also home of one of the most astrophysically rich regions in the Milky way. This highlights an ongoing complication with these kind of experiments as they rely on meticulous treatment of the underlying astrophysics in order to disentangle a potential dark matter signal. A major issue is that often that underlying physics is not yet fully understood or the signal may even be degenerate with a standard process. Similarly, uncertainty in the underlying dark matter structure makes for further complications, though non-detections from spheroidal dwarf galaxies occupying the Milky Way's sub-halos have been used to constrain the annihilation cross-section for different dark matter masses.

2.5.4 Global Impact Searches

Instead of focusing on a single, dense and sufficiently near region of dark matter to detect an excess in the associated annihilation products, another possibility is to look for the potential global impact dark matter annihilation may have on standard cosmic evolution. One of the most exciting is the potential modification of the 21cm signal associated with the Epoch of Reionsation. There are a number of ways in which the additional injected energy from dark matter annihilation and decay could produce these changes including direct heating and ionisation of the intergalactic medium (IGM) (Evoli et al., 2014; Poulin et al., 2015). A related effect is suppression of star formation due to heating of the IGM.

2.6 Outline of the Following Work

Having given a brief summary of the state of dark matter searches to date, it now remains to outline the remaining content of this thesis. The following work is motivated by the idea of using global signals such as the 21cm line of neutral hydrogen to constrain annihilating dark matter models. One of the pivotal aspects of this is the integration of dark matter annihilation into standard astrophysical processes, such as star formation and the heating of the intergalactic medium, as well as potential complex feedback mechanisms between forming structure and the injected annihilation products.

Figure 2.6 shows a schematic overview of the way structure formation can complicate the way dark matter annihilation can modify the Epoch of Reionsiation.

- The emergence of structure in the form of dense halos both boosts the total annihilation power, compared to that of a uniform dark matter density field, and changes the distribution of the injected energy. The first poses a challenge because the precise structure of the smallest halos is not well constrained. These tiny halos, depending on their density concentration and minimum mass, can significantly alter the total annihilation power so that even when making the assumption that dark matter annihilation only leads to uniform heating of the IGM, careful treatment of the collapsed structure in the cosmic web is necessary. In the case where heating and ionisation are treated as non-uniform, the spatial distribution of halos need to be taken into consideration in addition to the power boost afforded by structure. On one hand this is an attractive prospect as the topology of ionised bubbles is imprinted into the power spectrum of the 21-cm signal. A dark matter annihilation signature could then potentially be distinguishable from that of stars due to their different lower halo mass cut-off and spectrum of ionising particles. On the other hand the full evolution of the high energy annihilation products is non-trivial and incorporation of in-situ dark matter annihilation into a cosmological simulation would face a number of challenges related to the calculation of a

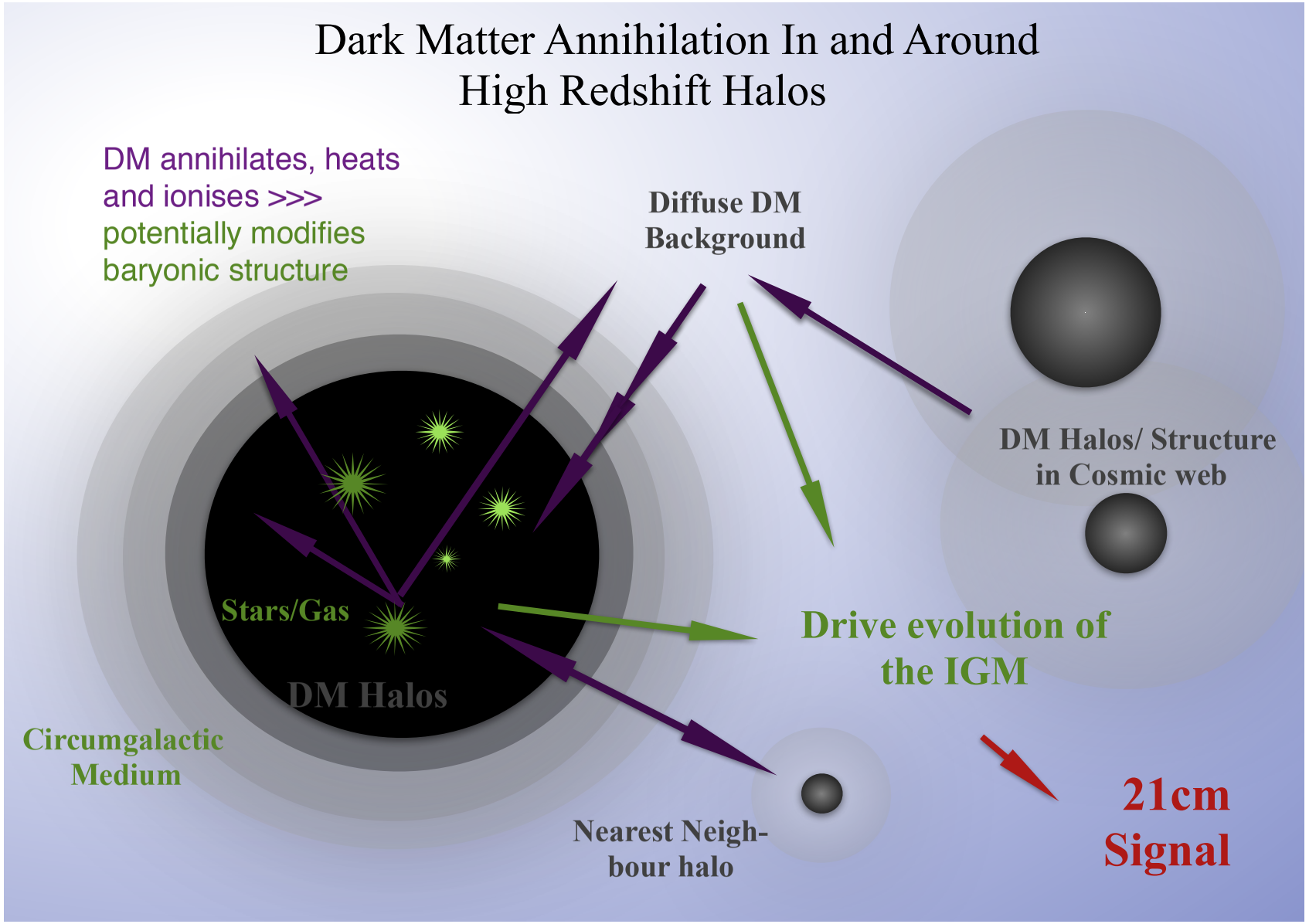

Figure 2.6: Overview of dark matter annihilation in and around high redshift structure.

non-uniform ionising field from dark matter annihilation.

- The relativistic nature of the annihilation products means that as a whole energy loss is facilitated over long distances. However halos are also the site of both elevated dark matter and gas densities in addition to hosting baryonic structure making them excellent candidates for producing modified astrophysical phenomenology. In order for stars to form, gas has to cool sufficiently to be allowed to collapse. Dark matter annihilation transfers energy to the gas in and around the halo and if the heating is efficient enough it could suppress structure formation. In contrast, the particle cascades produced by annihilation could also affect the chemical evolution of the gas. When it comes to the formation of Population III stars, metal cooling is not yet possible and instead occurs via radiative, molecular and atomic hydrogen cooling and therefore the presence of annihilating dark matter could impact the cooling processes within the halo as well. The production of Lyman-Werner photons as a result of dark matter annihilation inside the halo could also aid in the formation of direct-collapse black holes (Bromm and Loeb, 2003; Begelman et al., 2006; Wise et al., 2008).

- Besides the annihilation power coming from the halo or circumgalactic medium itself, there are a number of other heating sources that should be considered. The dark matter from the IGM (including the boost from collapsed structure) provides the most prominent secondary energy input, though nearby structure and sub-halos could also contribute. The fraction of total matter contained in structure increases at lower redshift while the average gas density decreases which can change the respective energy transfer efficiency of the different annihilation sources. Thus the relative importance of these secondary sources will also change with redshift. A further issue that is raised when dealing with halos as part of a wider cosmic background is the matter of mergers. Halos, especially at high redshifts undergo a rapid series of mergers as part of hierarchical structure formation, disrupting both its dark matter and baryonic content. How this affects dark matter annihilation rates and energy transfer should also be taken into account.

- Lastly there is the prospect of astrophysical feedback mechanisms being modified by dark matter annihilation and especially by dark matter structure. For instance consider heating from annihilation disrupting the formation of the first stars and galaxies. The change in luminous structure will provide modification to heating and ionising radiation from stars (on top of the heating directly from dark matter annihilation) and change the evolution of the circumgalactic medium (CGM) and IGM. This will in turn feedback into the inner evolution of the halo while at the same time the IGM is also heated by the diffuse dark matter background as is

the CGM. It is not a priori clear how these accumulating, non-linear interactions would impact Reionisation or modify the 21-cm signal. Integrating dark matter annihilation into a cosmological simulation will help in clarifying these issues.

While the full realisation of such a model is beyond the scope of this work, it will focus on the impact dark matter annihilation may have on critical, early structure formation, as well as lay the groundwork for a fully integrated model[6]. The key points are given below

2.6.1 Outline of Thesis

This chapter described the employment of a range of realistic dark matter models, including different masses, annihilation cross-sections and channels. The motivation for different annihilation candidates as well as the use of PYTHIA to model of the final annihilation spectrum of stable particles.

Chapter 3 presents the energy transfer code especially written to realise the electromagnetic cascades produced by the high energy annihilation products. The code includes the interaction processes expected for gas consisting of atomic Hydrogen and Helium, in addition to the CMB photon field. It allows the user to inject an electron, positron or photon into an arbitrary gas density field and record the heating, ionisation and Lyman-alpha photons deposited in pre-defined spatial bins. In the case were the gas field has a boundary (such as the edge of a dark matter halo) the code is also able to record the energy distribution of escaped particles.

Chapter 4 is a first order look at the impact dark matter annihilation has on structure formation. Instead of the full particle code it uses a simplified analytic model to calculate the energy transfer from injected particles, which allows the exploration of the parameter space of different dark matter particle and halo models. In this chapter the energy input from the annihilation process over the Hubble time is compared to the total gravitational binding energy of the halo.

Chapter 5 presents a follow-up on Chapter 4 but focusing on the most promising halo parameter space, namely small, high redshift structures which may host the first stars. Here the full energy transfer code is used to calculated the radial-dependent heating and ionisation fractions as well as a comparison with the gravitational binding energy of each shell.

Chapter 6 uses the escaped particle spectrum from the previous chapter to investigate to which the degree the escaped annihilation energy heats the circum-galactic

[6] A crucial part of this will be determining which and when processes have the potential to make observable changes to standard astrophysics.

medium. If the heating process is efficient enough it may lead to suppression of gas accreting onto the halo and a subsequent raising of the Jeans mass.

Chapter 7 examines the validity of treating halos as isolated objects by comparing the heating of the gas from within the halo to that coming from the photon bath produced by the diffuse dark matter background. It also considers whether annihilation in the nearby circumgalactic medium can effect the local object.

Chapter 8 presents a summary of outcomes and how these results can contribute to improving the modelling of dark matter annihilation and testable predictions.

Chapter 3

Atomic Physics

Dark matter models such as described in the previous chapter give a measure of the total number of particles and energy produced during the annihilation and decay process. In general the immediate annihilation products are unstable on time scales well below those relevant to the astrophysical phenomena considered here, and are taken to hadronize until only stable particles remain. These stable particles, including electrons and positrons, photons, protons and anti-protons as well as neutrinos, ultimately go on to interact with and potentially deposit their energy into the surrounding medium. In order to give a meaningful measure of how annihilating and decaying dark matter can modify the evolution of observable phenomena, a rigorous treatment of the coupling between the injected particles and the surrounding matter field is mandatory.

For dark matter models with masses on order of GeV the final annihilation products will generally comprise particles with relativistic energies. This means that rather than depositing their energy directly into the gas, the original particle will lose energy through the production of secondary particles. In the case where the initial energy of the original particle is high enough, these secondaries will initiate similar particle cascades, and so on, until the energies have been lowered sufficiently to allow direct energy transfer to the gas. On the whole the injected particles undergo a wide range of interactions depending on the energy of the particle, while the relative importance of each interaction will vary with the associated medium's density, ionisation state and the energy of the particles comprising the interaction medium(Slatyer et al., 2009; Evoli et al., 2012) .

Needless to say, following these high energy electromagnetic cascades in detail is challenging. Not only does it require keeping track of a great number of particles, but also their trajectories and how these change as the particle interacts with the surrounding media, and of course most importantly the interactions they undergo and the energy deposited at each point of the particle's evolution. The relative likelihoods of the interactions are themselves path-dependent and so need to be calculated along the particles' trajectories as appropriate. The following chapter first presents the relevant interactions for each particle species and then outlines the Monte-Carlo code used to keep track of the injected particles.

Interaction Mediums

The work presented in later chapters concerns un-evolved structure at high redshift ($z = 10 - 50$). It is thus assumed that the injected particles only interact with a pristine gas field consisting of Hydrogen and Helium (in their unexcited, atomic state) and the CMB photon field. The energy distribution of CMB photons is taken to be that of a perfect black-body where the CMB temperature is given by,

$$T_{CMB}(z) = T_0(1 + z) \tag{3.1}$$

with $T_0 = 2.275$K.

3.1 Photons

3.1.1 Lyman Photons

Photons with energy below the Lyman limit (13.6eV) are assumed to cease direct interaction with their surrounding medium. However their production through dark matter annihilation is still important as in reality photons below this limit can play an important role, especially when taking into account more complex environments than are under consideration here. For instance photons with energies between 11.2 and 13.6eV are classified as Lyman-Werner photons. These photons maybe absorbed by molecular Hydrogen and through excitation and subsequent radiative decay lead to its disassociation. Before the production of metals, the formation and destruction of H_2 plays an important role in molecular cooling at high redshifts (Abel et al., 1997) and are thus vital for early star (Abel et al., 2002) and galaxy formation (Bromm et al., 2009).

In addition Lyman-α photons facilitate the Wouthuyen-Field effect (Wouthuysen, 1952; Field, 1959). Here, by undergoing continuous collisional interactions with the Lyman-α photons, the spin temperature of the gas becomes coupled to its kinetic temperature as opposed to rapidly reaching thermal equilibrium with the CMB temperature. Ultimately this allows for the neutral Hydrogen to become observable relative to the CMB temperature in either absorption or emission.

Due to these important effects it is thus of interest to keep a record of the production of Lyman photons when calculating the energy transfer from dark matter annihilation products.

3.1.2 Photo-ionisation

Photons with energy above 13.6 eV can ionise Hydrogen atoms. During the photo-ionisation process the incident photon passes on all its energy, minus that required to overcome the relevant binding energy, to the newly freed electron. Different photo-ionization cross-sections can be found in the literature and are shown in Figure 3.1. An

	E_{th}	$E_0(eV)$	$\sigma_0(Mb)$	y_a	P	y_w	y_0	y_1
H	1.360e1	4.298e−1	5.475e4	3.288e1	2.963e0	0.000e0	0.000e0	0.000e0
He	2.459e1	-1.361e1	9.492e2	1.469e0	3.188e0	2.039e0	4.434e1	0.136e0
He^+	5.442e1	1.72e0	1.369e4	3.288e1	2.963e0	0.000e0	0.000e0	0.000e0

Table 3.1: Fitting parameters for the electro-ionisation cross-section fits.

empirical fit to laboratory data is given by Verner et al. (1996)

$$\begin{aligned} \sigma_{ion}(E) &= \sigma_0 F(y) \text{ Mb}, \quad x = \frac{E}{E_0} - y_0, \quad y = \sqrt{x^2 + y_1^2} \\ F(y) &= \left[(x-1)^2 + y_w^2\right] y^{0.5P-5.5} \left(1 + \sqrt{y/y_a}\right)^{-P}, \end{aligned} \tag{3.2}$$

where E denotes the energy of the photon in eV and the fit parameters σ_0, E_0, y_w, y_a, P, y_0 and y_1 are given in Table 3.1. Alternatively the cross-section for H and He^+ have analytic expressions (Zdziarski and Svensson, 1989),

$$\begin{aligned} \eta &= \frac{1}{\sqrt{E/E_{ion} - 1}} \\ \sigma_{ion} &= \frac{2^9 \pi^2 r_0^2}{3\alpha^3} (E_{ion}/E)^4 \frac{\exp(-4\eta \arctan(1/\eta))}{1 - \exp(-2\pi\eta)}, \end{aligned} \tag{3.3}$$

where r_0 is the classical electron radius and E_{ion} = 13.6 eV in the case of neutral Hydrogen and E_{ion} = 54.4 eV for once ionised Helium. The authors give the cross-section for neutral Helium is given by the fit,

$$\sigma_{He} = -12\sigma_{ion,H} + 5.1 \times 10^{-20} \text{cm}^2 \begin{cases} \left(\frac{E}{250\text{eV}}\right)^{-2.56}, & 50\text{eV} < E < 250\text{eV} \\ \left(\frac{E}{250\text{eV}}\right)^{-3.30}, & E > 250\text{eV} \end{cases} \tag{3.4}$$

In the above expression $\sigma(ion, H)$ denotes the earlier analytic expression for the photo-ionisation cross-section of neutral Hydrogen.

3.1.3 Compton Scattering

Photons also lose energy through scattering of off free electrons (Heitler, 1954; Chen and Kamionkowski, 2004) (where for the purpose of Compton interactions, all electrons are taken to be free). The Compton scattering differential cross-section is given by the Klein-Nishina equation.

$$\frac{\mathrm{d}\sigma}{\mathrm{d}E'_\gamma} = \pi\alpha^2 r_c^2 \frac{1}{E_\gamma} \left\{ \frac{E'_\gamma}{E_\gamma} + \frac{E_\gamma}{E'_\gamma} - 1 + \left[1 - \left(\frac{1}{E'_\gamma} - \frac{1}{E_\gamma}\right)\right]^2 \right\} \tag{3.5}$$

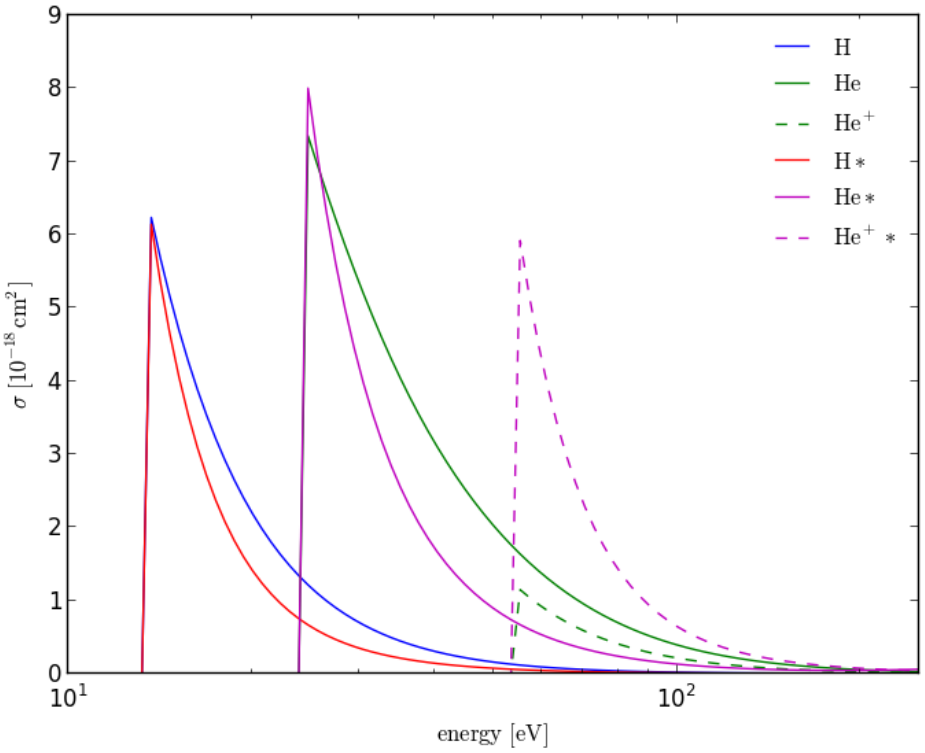

Figure 3.1: Photo-ionization cross-section for Hydrogen and Helium.

$$\frac{E_\gamma}{1+2E_\gamma} < E'_\gamma < E_\gamma.$$

Here the energies are again taken to be in electron masses (m_{e^-} = 511 keV), E_γ is the incoming photon's energy and E'_γ the energy after scattering, while r_c is the Compton radius of the electron.

3.1.4 Pair-Production

Pair Production on the CMB

Photons with energy above the critical energy of 2 m_{e^-} undergo electron/positron pair creation. In order to satisfy conservation of momentum, pair-creation occurs off a background field of particles such as the CMB photon field (Agaronyan et al., 1983; Ferrigno et al., 2004). The differential spectrum of the electrons produced during pair-creation is given by

$$\frac{\mathrm{d}N}{\mathrm{d}E\mathrm{d}\epsilon\mathrm{d}t} = \sigma_T c \frac{3}{64}\frac{1}{\epsilon^2 E_\gamma^2}\left[\frac{4A^2\ln(4\epsilon E_\gamma(A-E)/A)}{E(A-E)} - 8\epsilon A + \frac{2(2\epsilon A-1)A^2}{E(A-E)} - \left(1-\frac{1}{\epsilon A}\right)\frac{A^4}{E^2(A-E)^2}\right] n(\epsilon) \quad (3.6)$$

$$\frac{A}{2}\left(1-\sqrt{1-\frac{1}{E\epsilon}}\right) < E < \frac{A}{2}\left(1+\sqrt{1-\frac{1}{E\epsilon}}\right)$$

$$A = E_\gamma + \epsilon$$

and the spectrum for positrons is taken to be identical. In the above expression all energies are again given in units of electron mass, E is the energy of the created lepton, E_γ the energy of the pair producing photon, ϵ and $n(\epsilon)$ the energy and energy distribution of the CMB photons. σ_T is the Thomson cross-section.

Pair Production on Hydrogen and Helium

Pair production is also facilitated by interaction with the gas component of the medium (Zdziarski and Svensson, 1989; Motz et al., 1969), and this process dominates pair-production off of CMB photons in the following calculations. In the case of neutral Hydrogen and Helium the relevant cross-sections are respectively given by

$$\sigma_H(E_\gamma) = 5.4\alpha r_e^2 \ln\frac{513E_\gamma}{E_\gamma+815} \quad (3.7)$$

$$\sigma_{He}(E_\gamma) = 8.76\alpha r_e^2 \ln\frac{513E_\gamma}{E_\gamma+815}. \quad (3.8)$$

For ionized species including both singly and doubly ionized Helium,

$$\sigma_+(E_\gamma) = \alpha r_e^2 \left(\frac{28}{9} \ln(2E_\gamma) - \frac{218}{27} \right) \tag{3.9}$$

Pair Production on Free Electrons

For pair-production off of free electrons, the following fitting function is employed (Joseph and Rohrlich, 1958)

$$\sigma_+(E_\gamma) = \alpha r_e^2 \left(\frac{28}{9} \ln(2E_\gamma) - \frac{100}{9} \right) \tag{3.10}$$

In all of the above, α is the fine structure constant and r_e the classical electron radius.

3.1.5 Photon Splitting

Photons also lose energy through scattering off of CMB photons (Svensson and Zdziarski, 1990). In this case the energy of the original photon is almost evenly split by the two particles after collision. The precise final spectrum of photons is given by:

$$\frac{\mathrm{d}N}{\mathrm{d}E\mathrm{d}t} = R(20/7)\frac{1}{E_\gamma}\left[1 - \frac{E}{E_\gamma} + \left(\frac{E}{E_\gamma}\right)^2\right], \tag{3.11}$$

where R is total scattering rate

$$R = 1.83 \times 10^{-27} h_{50}^{-1} T_0^6 H_0 (1+z)^6 E_\gamma$$

and $h_{50} = H_0/(50\mathrm{km/s/Mpc})$. However, since at the redshift of interest for this work this process is highly subdominant, it is omitted.

3.2 Electrons and Positrons

3.2.1 Electro-ionization

Like photons, electrons with sufficient energy may ionise their surrounding medium (Shah et al., 1987, 1988; Kim and Rudd, 1994). The electo-ionisation cross-section fits are taken from Arnaud and Rothenflug (1985) and given by,

$$\sigma_{ele}(E) = 10^{-14}\mathrm{cm}^2 \frac{1}{u(I/eV)^2}\left[A\left(1-\frac{1}{u}\right) + B\left(1-\frac{1}{u}\right)^2 + C\ln u + D\ln u/u\right], \tag{3.12}$$

where $u = E/I$ and $I = 13.6, 24.6$ and 54.4eV are the ionising potentials for H, He and He^+ respectively. The coefficients A, B, C and D are given in Table 3.2.

As in the photon case, the ionising particle passes on some its energy to the newly released secondary electron. However unlike photons, the original electron may continue

Target	A	B	C	D
H	22.8	−12.0	1.9	22.6
He	17.8	−11.0	7.0	−23.2
He^+	14.4	−5.6	1.9	−13.3

Table 3.2: Fitting parameters for the electro-ionisation cross-section fits.

interacting provided it retains enough energy to either ionise or excite the gas. The energy of the secondary electron (where the electron with the lower energy is assumed to be the secondary particle) is well fitted by the distribution from Shull (1979) and Furlanetto and Stoever (2010),

$$p(\epsilon) \propto \frac{1}{1 + (\epsilon/\bar{\epsilon}_i)^{2.1}}. \tag{3.13}$$

Here $\bar{\epsilon}_i$ is equal to 8, 15.8 and 32.6eV for H, He and He^+ respectively.

The cross-sections and secondary electron energy distributions are shown in Figure 3.2. The electro-ionisation cross-section drops of less rapidly with energy compared to the photo-ionisation cross-section, and remains an efficient energy loss mechanism at energies > 10^2eV for electrons in a halo-like environment. The average secondary energy only increases logarithmically with that of the incident particle so that most secondaries will tend to be low energy electrons. Once an electron's energy drops below 10.2eV it is assumed to be thermalised locally and interacts no further with the gas.

3.2.2 Electron-excitation

Electron-excitation (Bransden and Noble, 1976; Fisher et al., 1997; Stone et al., 2002; Hirata, 2006; Chuzhoy and Shapiro, 2007) occurs when the incoming electron does not impart enough energy onto the atom to fully ionise it. Instead the shell electron will be raised to an excited atomic state from which it spontaneously decays later, emitting a photon. This process is an important source of Lyman photons. The fitting functions are taken from the above references and are given for atomic Hydrogen and Helium as

$$\sigma_{exc}(E_{kin}) = \frac{4\alpha_0^2 R_{ryd}}{E_{kin} + E_{ion} + E_{exc}}\left[A\ln(E_{kin}/R_{ryd}) + B + CR_{ryd}/E_{kin}\right] \tag{3.14}$$

and for ionised Helium,

$$\sigma_{exc}(x) = \frac{\pi\alpha_2}{16x}\left[A\ln(x) + B\ln(x)/x + C + D/x + E/x^2\right] \tag{3.15}$$

$$x = \frac{E_{kin}}{E_{exc}}$$

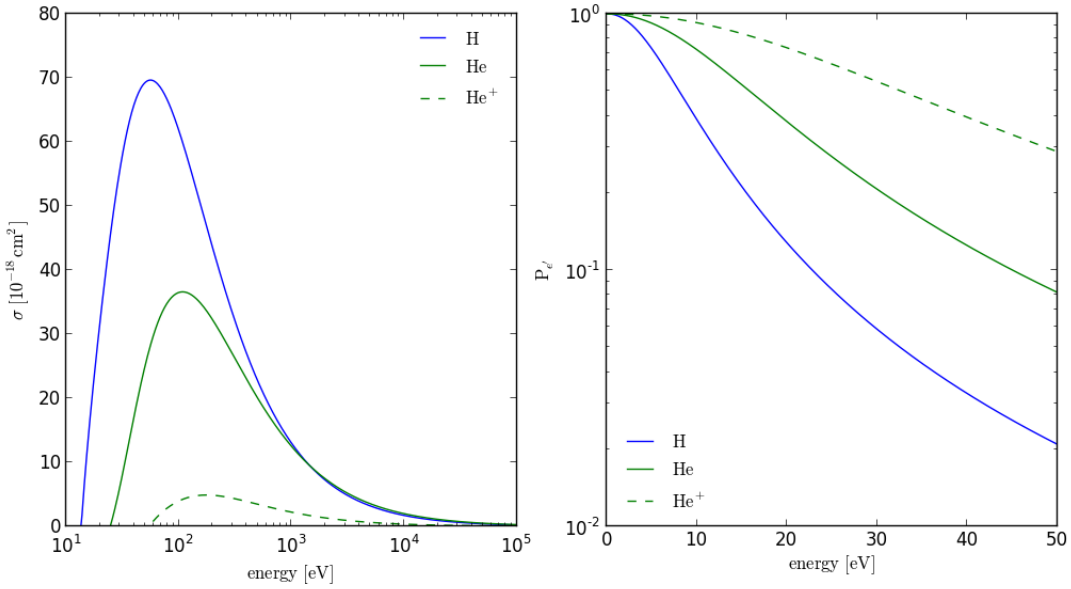

Figure 3.2: The electron ionisation cross-section for Hydrogen(blue), atomic and once ionised Helium (green solid and dashed lines) are shown in the plot on the left while the energy distribution of the secondary electrons produced during the ionisation process are shown on the right.

Target	A	B	C	D	E
H	0.5555	0.2718	0.0001		
He	0.1771	−0.0822	0.0356		
He^+	3.22	0.357	0.00157	1.59	0.764

Table 3.3: Fitting parameters for the electro-excitationtion cross-section fits.

In the above expression E_{kin}, E_{ion} and E_{exc} refer to the kinetic energy of the incoming electron, the ionisation energy of the respective target atom and the excitation energy. The fitting parameters for the excitations cross-sections are given in Table 3.3.

3.2.3 Coulomb Scattering

Coulomb scattering (Spitzer and Scott, 1969; Shull and van Steenberg, 1985; Furlanetto and Stoever, 2010) provides a source of collisional heating with a cross-section given for 100eV < E < 1000eV by,

$$\sigma(E) = (7.83 \times 10^{-11}) \ln(\Lambda) \frac{E}{eV}^{-2} \text{cm}^2 \tag{3.16}$$

where $\ln(\Lambda) = 10$. As the gas becomes ionised, Coulomb scattering off of free electrons supersedes electro-ionisation as the dominant energy loss mechanism. As a result of this, the partition of deposited energy becomes dominated by heating as opposed to

ionisation in the neutral gas scenario.

3.2.4 Recombination

Free electrons encountering ionised protons recombine to form atomic Hydrogen (Karzas and Latter, 1961). This process is also sub-dominant, in particular for non-ionised gas environments. The cross-section is given by

$$\sigma_{rec} = 3 \times 10^{10} \frac{g_f}{\nu n^3 v_e^2} \mathrm{cm}^2. \tag{3.17}$$

Here g_f is the Gaunt factor and approximately one, ν is the emitted radiation frequency, v_e the velocity of the electron and finally n the atomic level at which the atom recombines.

3.2.5 Inverse-Compton Scattering

By far the most important interaction that high energy electrons undergo is scattering off of photons, transferring some of their energy during Inverse Compton (IC) process (Blumenthal and Gould, 1970). In this case the injected electron scatters off the CMB photon field. The general doubly differentiated distribution of final photon energies is taken from Slatyer et al. (2009)

$$\frac{\mathrm{N}}{\mathrm{d}E_\gamma \mathrm{d}\epsilon \mathrm{d}t} = \frac{3}{4}\sigma_T c \frac{1}{\epsilon E_e^2}\left[2q\log(q) + (1+2q)(1-q) + 0.5(1-q)(\Gamma q)^2/(1+\Gamma q)\right] n(\epsilon), \tag{3.18}$$

$$\Gamma = 4\epsilon E_{ele}$$

$$q = \frac{E_\gamma}{E_{ele}} \frac{1}{\Gamma(1 - E_\gamma/E_{ele})}$$

Again all energies are given in units of electron mass and ϵ and $n(\epsilon)$ are the energies and energy density of the CMB photons respectively. Due to both the greater densities and average energy of the CMB photons, IC scattering is more efficient energy loss mechanism at high redshifts especially when considering heating of relatively small volumes such as dark matter halos.

3.2.6 Positrons

Positrons at high energies behave in the same manner as electrons. Similarly at lower energies they affect ionisation and excitation of the atomic field. However in addition positrons also undergo annihilation with free electrons as well as through the formation of positronium off the surrounding gas (Heitler, 1954; Guessoum et al., 2010). The

annihilation cross-section is

$$\sigma_{ann} = \frac{\pi r_e^2}{\gamma + 1}\left[\frac{\gamma^2 + 4\gamma + 1}{\gamma^2 + 1}\log(\gamma + \sqrt{\gamma^2 + 1} - \frac{\gamma + 3}{\sqrt{\gamma^2 - 1}})\right]. \tag{3.19}$$

The annihilation process both off of free electrons and through the formation of positronium creates two photons. For low energy impact positrons it is assumed that their final energy is simply the electron/positron rest-mass.

3.3 Other Particles

3.3.1 Neutrinos

Neutrinos only interact weakly with other particles and are here assumed to free-stream without having any significant interactions with the surrounding gas. It is however worthy of note that while not directly contributing to the energy transfer, different annihilation channels produce different fractions of stable particles. Thus models with annihilation channels favouring the production of neutrinos will overall be less efficient at transferring energy to the gas.

3.3.2 Protons and Anti-protons

Analysis of the energy spectra produced by PYTHIA shows that in addition of electrons, photons and positrons, a dark matter candidate with sufficient mass may also produce proton/anti-proton pairs. These interact in a similar manner as low energy electrons and positrons. However as for the dark matter models considered here these events constitute a negligible fraction of the total centre of mass energy, so they are neglected in this treatment.

3.4 Energy Transfer Code

Having outlined the main process particles undergo, it is now of interest to consider how to keep track of the interactions.

3.4.1 MEDEA

MEDEA (Valdes et al., 2007, 2010) and MEDEAII (Evoli et al., 2012) is a Monte Carlo code that uses random sampling of the relevant physical processes to produce a break-down of the injected energy into heating, ionisation and Lyman photons. The code was originally designed to calculate the contribution of dark matter annihilation to reionization. As such it assumes uniform spatial distribution of the injected energy and does not track the physical path of the particles as they cascade. For the work completed in Chapter 4, the outputs from MEDEAII are used to estimate the partition of energy transferred to dark matter halos for different ionisation fractions.

However in order to give a full account of the energy transfer in collapsed structure with a non-uniform gas field, the spatial evolution of the injected particles must be

tracked alongside the energy loss. For that purpose a new code has been developed that gives not only the energy breakdown of the injected particles but also the distribution of the energy for an arbitrary gas density background. In addition the new code allows for a physical boundary to be defined (for example, the virial radius of a halo) and the spectra of particles that escape that region to be recorded. This new code is used to refine the calculation of dark matter annihilation in small, high redshift halos, as well as the energy loss in the circumgalactic medium, taking into account the energy loss to the halo.

The new code also gives a correction to the lower cut-off of the IC process from MEDEAII, which made the assumption that IC can be neglected for

$$E < \left(\frac{1+z}{21}\right)^{-1/2} \text{MeV}.$$

Careful analysis by Slatyer (via private communication) shows that this is an overestimate, especially at high redshifts. For redshifts above 10, IC scattering should be taken to play an important role for energies as low as 35keV.

3.4.2 Halo Energy Transfer Code

We retain the Monte Carlo sampling method from MEDEAII to process the particle interactions in the new energy transfer code (NETC). The particle tracking follows a similar treatment to the one found in the GEANT4 (Allison et al., 2006; Agostinelli et al., 2003) suite.

Enviroment

The halo energy transfer code allows for the gas fields (atomic and ionised Hydrogen and Helium) to be set independently of each other, along with the free electrons and free photon field over some arbitrary environment in $\mathbb{R}^3$. For the purposes of this work, the gas density distributions are spherically symmetrical and follow the same profile up to normalisation, while the photon field is representative of the CMB and thus uniform. Particles (in this case electrons, positrons and photons, though the code could easily be augmented to include other particles and processes) can be injected at any point with a given energy and orientation, within the defined environment.

Particle Evolution

Given an input,

$$\text{Input} = [E_i, x_i, y_i, z_i, \theta_i, \phi_i, \text{id}] \tag{3.20}$$

where for i particles E_i denotes the energy, x_i, y_i and z_i the position and θ_i and ϕ_i the orientation, the particles are evolved step-wise. The actual step has to be of a size to allow the density across the step to be taken as constant. In the cases of halos and the

circumgalactic medium the density follows a power law and the step-size chosen for this work is of the form

$$S(\mathbf{x}) = \epsilon r(\mathbf{x}) \tag{3.21}$$

here ϵ is a free parameter. The particular form for the step-size $S(\mathbf{x})$ was chosen since the correct choice of ϵ allows the constant density approximation to be made across the step (see §3.4.4) as well making larger steps in the outer parts of the halos were the gas density is lower and fewer gas interactions take place. The latter means that fewer iterations need to be made for lower energy particle interacting with the gas, thus speeding up the code. A brief discussion about the convergence with number of iterations and step-size can be found at the end of the chapter. Given an initial position and the corresponding step-size $S(\mathbf{x})$, the end point of the step is given by,

$$\begin{aligned} x_f &= x_i + S(\mathbf{x}_i)\sin(\theta_i)\cos(\phi_i) \\ y_f &= y_i + S(\mathbf{x}_i)\sin(\theta_i)\sin(\phi_i) \\ z_f &= z_i + S(\mathbf{x}_i)\cos(\theta_i) \end{aligned} \tag{3.22}$$

Assuming the particle travels in a straight line from $\mathbf{x}_i$ to $\mathbf{x}_f$ the code then decides whether an interaction occurs. Depending on whether a boundary to the environment has been set a number of outcomes are possible. In the case where the particle doesn't interact and $\mathbf{x}_f$ is outside the boundary, the particle is removed from the input list and is added to the spectra count of escaped particles. Similarly if the particle interacts but the interaction radius is outside the boundary, the particle is just counted as having escaped. If no interaction takes place within the step, the end point $\mathbf{x}_f$ becomes the start point for the next step and the process is repeated until either the particle runs out of energy or escapes the environment. In the case where an interaction takes place within the step and within the boundary, the code runs the appropriate process on the particle, records any energy deposited and adds any new particles created during the process to the input with initial position at the interaction radius.

Particle Interaction Whether or not an interaction takes place is calculated via the mean free path, λ of each process.

$$\frac{1}{\lambda} = \sigma_i(l)\rho_i/m_i \tag{3.23}$$

The chance that a particle survives a distance l without interaction is given by

$$P(l) = e^{-n_\lambda}, \tag{3.24}$$

$$n_{\lambda_i} = \int_0^l \mathrm{d}l'/\lambda_i(l').$$

We note that in evolving the particle, the assumption is made that the density ρ_i is constant across the step. Since this is an approximation the density across the step is set by choosing a random point along the step-trajectory to avoid bias.

Using the above probability distribution for each interaction process i, a random number η in the range from $(0, 1)$ is chosen, such that

$$n_{\lambda_i} = -\ln \eta_i. \tag{3.25}$$

From this and the mean free path the distance to each interaction can be calculated and whichever interaction returns the shortest distance is the one that is assumed to take place (boundary conditions allowing).

3.4.3 Physics not Covered

The code described above does not keep track of the time it takes for the injected particle to deposit its energy. In the case of particles with very long mean free paths or very low energy loss to particle energy ratios this time can be substantial, spanning across non-negligible redshift ranges or in extreme cases even the age of the universe. The redshift dependence of deposited energy is particularly important when determining the energy input into the intergalactic medium (IGM).

For this work and unlike the IGM the environments under consideration are relatively small, pertaining to either compact early halos or the immediate area surrounding. This means that the particles with long mean free paths will readily escape the set boundaries and thus won't distort the energy deposition results. In addition the halos under consideration are both high density and high redshift objects meaning the energy loss rate is more efficient and allows for the temporal on the spot approximation to be made.

To quantify this, consider a first order calculation of the escape times of injected particles. At redshift 40, the virial radius of a $10^6 M_\odot$ halo is 2.34×10^{18}m. Assume a relativistic annihilation product traveling at a fraction f of the speed of light, moves in a straight line from one edge of the halo to the other to escape. For high energy electrons and positrons the dominant interaction is through IC scattering and thus they're evolution is strongly tied to the redshift dependent change of the CMB photon field. (High energy photons either escape the halo without interaction or pair-create off of the gas field to produce electrons and positrons in turn.) Then the escape time of the particle can be written as

$$\tau_{esc} = \frac{4.95 \times 10^4}{f} \text{yrs} \tag{3.26}$$

At this redshift and for $f = 0.1$ that corresponds to $\triangle z \lesssim 1$ (using a cosmological

calculator by Wright (2006)). Similar numbers hold for redshift 20.

For lower energy injected particles, as well as the secondary cascade products produced by the relativistic progenitors, interactions will occur predominantly with the gas of the halo. For this work the gas distribution and ionisation state of the halo is taken to be static (as is the CMB photon field) and therefore the precise redshifting of these particles is not incorporated into the calculation. At these redshifts and considering the physical size of the halo, low energy particles will be rapidly thermalised within the halo while those in the midrange (for example photons interacting via Compton scattering) will quickly escape the halo with limited gas interactions. However this approximation will not hold within the context of a cosmological simulation and redshifting will have to be taken into consideration as the energy transfer of interest continues beyond the bounds of a single micro-halo to surrounding structure as well as the IGM.

The code also simplifies the underlying gas field in that the code does not take into account any bulk motion of the gas and how this may subsequently affect the scattering angle of the particles. In general the injected particles are assumed to undergo random walks through the medium.

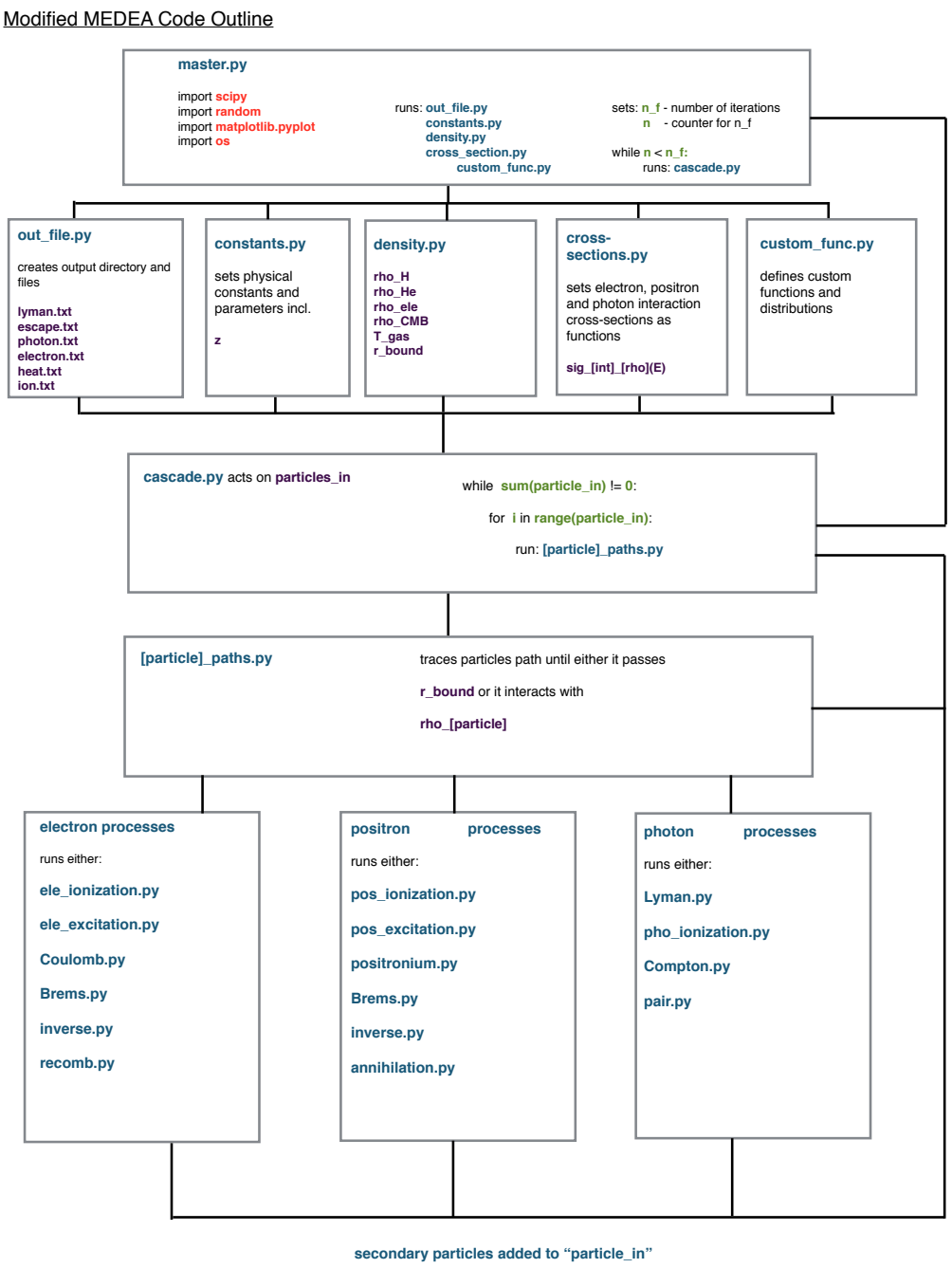

Figure 3.3: Schematic for the new energy transfer code.

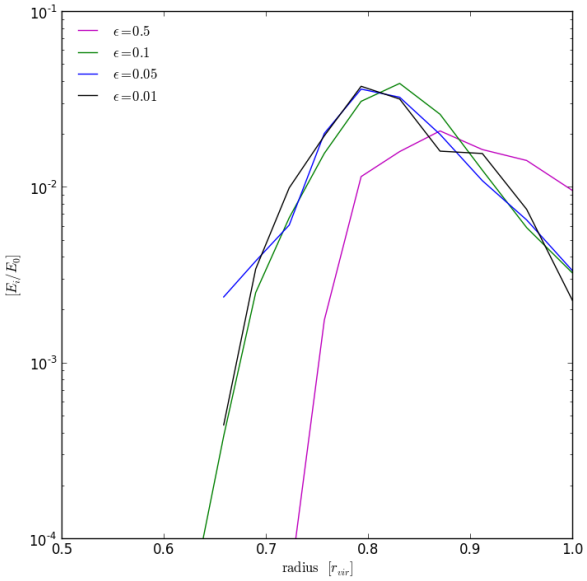

Figure 3.4: Convergence with different step-sizes for a 10^4 eV electron in a $10^5 M_\odot$ halo at redshift 20. Different coloured curves correspond to different ϵ with black, blue, green and magenta showing ϵ = 0.01, 0.05, 0.1 and 0.5 respectively.

3.4.4 Code Convergence

Lastly the convergence of the Monte-Carlo code is discussed in relation to the two free parameters governing the step-size and number of iterations. The convergence of the deposition fractions will vary with particle energy, interaction medium density and the type of particle in question.

Step-Size

For the work conducted in this thesis the step-size of the particle is proportional to the radial distance from the halo centre. The free parameter ϵ, as shown in equation 3.20, was set at 0.01 for all calculations. Figure 3.3 shows the change in the heating deposition curve for a 10^4 eV electron in a $10^5 M_\odot$ halo at redshift 20. Curves are shown for ϵ = 0.5, 01, 0.05 and 0.01 (magenta, green, blue and black respectively). ϵ has to be sufficiently small so that the change in gas density within each step does not distort the path of the particle[1]. In the case of both the halo and CGM where density decreases monotonically with radius, a too large choice of ϵ will result in a deposition curve shifted towards the edge of the halos as the random sampling within the step will either overestimate the density when oriented towards the inner halo or underestimate

[1] As the halos and the circumgalactic medium under consideration here are taken to have the same ionisation fractions as well as relative fraction of hydrogen to helium gas throughout, the choice of ϵ has minimal impact on the partition of energy into heating, ionisation and Lyman photons.

it when pointed outwards. This can be seen in the magenta $\epsilon = 0.5$ curve in Figure 3.3. Once $\epsilon < 0.1$ the position of the deposition curve becomes stable and the remaining variation is due to the number of iterations (in this case 200).

Number of Iterations

Figure 3.4 shows the change in deposition curves for different number of iterations for $5 \cdot 10^3$ eV electrons (left plot) and $5 \cdot 10^2$ eV photons (right plot) for different initial conditions. The uppermost row of plots shows the particle injected close to the edge of a $10^5 M_\odot$ halo at redshift 20. For the electrons curves show $N = 10$, 50, 100, 200 and 500 while the photons (due to their longer mean free path) show $N = 50$, 100, 200, 500 and 1000 in red, magenta, blue, green and black respectively. The row below shows the same halo at redshift 40, the next the same particles injected into a $10^7 M_\odot$ halo at redshift 20 and the bottom row show the same as the top but with the particles injected closer to the centre of the halo.

Electrons at the energies shown here rapidly transfer their energy to the gas and thus require relatively few runs to achieve a convergent final output for all the scenarios shown in Figure 3.3. In contrast the photons, which at this energy have a mean-free path comparable to the virial radius, show far greater variation even for $N = 1000$ though the curves do converge. It is worth noting that for the density distributions used in this work, the relative contribution to heating, ionisation and Lyman photons converges relatively quickly and it is the spatial distribution of the deposited energy that requires a large number of iterations to achieve a marked reduction in variability.

In order to allow for a more expedient running time, the code was used to hierarchically build up a library of deposition curves for particles injected into the halo. These results are then used to augment the high energy particles cascades.

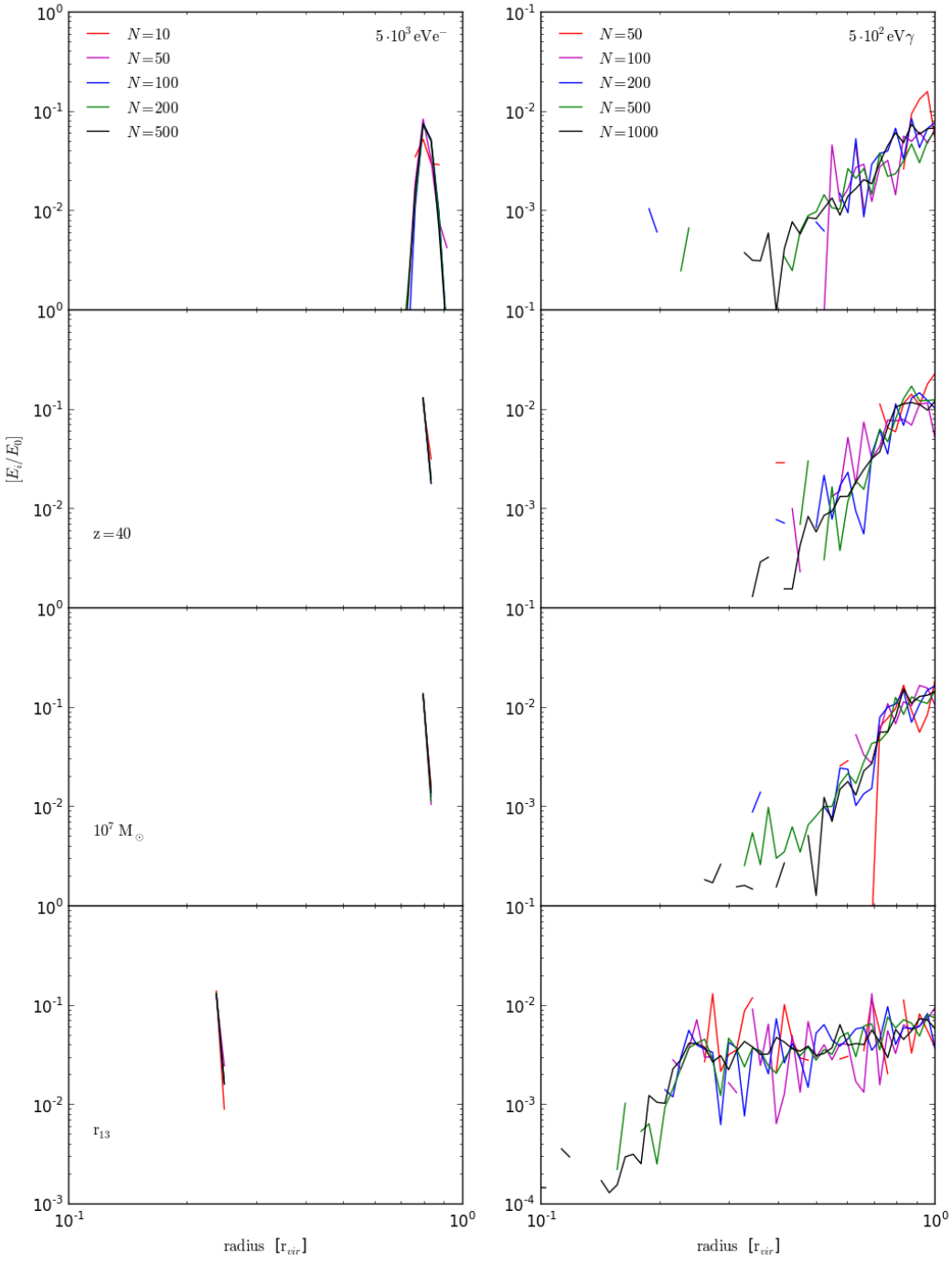

Figure 3.5: Convergence for number of evolutions for different parameters. Plots on the left show $5 \cdot 10^3$ eV electrons and plots on the right $5 \cdot 10^2$ eV photons. Top row shows a $10^5 M_\odot$ halo at redshift 20. The row below shows the same at redshift 40. Below that a $10^7 M_\odot$ halo at z=20. The last row shows the same as the top but for particle injected closer to the halo's centre.

Chapter 4

Self-heating Dark Matter Halos

To reiterate briefly, the emergence of astrophysical structure can be traced back to quantum scale fluctuation embedded in the matter-energy density field during the very early stages of the universe. These over densities proceed to grow until eventually undergoing gravitational collapse to form halos. Halos continue to accrete material, as well as undergoing numerous merger events leading to the hierarchical build up of a massive halo population. The underlying dark matter web also acts as the host for the first stars and galaxies and the evolution of the luminous structure is closely enmeshed with that of the halos.

In the context of searches for signals from dark matter annihilation, structure can pose an exceedingly complex problem. High density dark matter regions correspond to elevated sources of dark matter annihilation power, so that the precise distribution of the dark matter sets not only the total of the energy injected but also impacts on the way this energy is distributed. In order to derive robust constraints from any possible dark matter detection or non-detection, careful treatment of the uncertainties in the underlying dark matter structure is necessary as these can go so far as to lead to order of magnitude variations in the overall dark matter power (Mack, 2014). In addition the overlap with luminous matter can make disentangling a potential dark matter signature from standard astrophysical sources difficult as these can dominate or even mimic any potential dark matter signal as well as having their own idiosyncratic uncertainties associated with them.

On the other hand this overlap also opens up the possibility of modification of structure formation due to dark matter annihilation. For instance the additional injection of energy into halos has been proposed to impact star formation or even lead to exotic structure. Subsequently events closely tied to the emergence of stars and galaxies such as reionisation would also be effected. These changes to the evolution of standard astrophysical phenomena may be detectable and thus offer another possible avenue in the search for dark matter. As such it is important to give a full account of how (if at all) energy from dark matter annihilation modifies and is modified by halo hosted structure in order to make full use of observations to constrain dark matter models.

In this and the following chapter the ability of dark matter halos to "self-heat"

is explored. In particular there is a focus on un-evolved, high redshift objects[1], the treatment of energy transfer from the injected particles to the halo's gas, as well as the possible variations due to different dark matter halo and particle models.

4.1 Structure of a Dark Matter Halo

As a first order approach, dark matter halos are here characterised as fully virialised, stable and spherically symmetrical structures. The density profiles of halos with masses upwards from $10^8 - 10^9 M_\odot$ are well documented through the use of N-body simulations. In general the resolution of these simulations is set by the mass of their dark matter component-particles which are of order of $10^7 M_\odot$ so the nature of objects at that mass scale and below is less certain. To allow for these uncertainties a number of plausible halo models are considered and presented below.

4.1.1 Density Profiles

Three different dark matter density profiles are considered in this work, with their main point of difference being the distribution of mass at the centre of the halo.

NFW Profile

An interesting aspect of dark matter halos is that they appear to host universal density profiles (Navarro et al., 1996) up to a free parameter, the dark matter density profile of the halo can be determined entirely by its mass and redshift. The profile itself follows a broken power law and was originally and is still commonly fit by the NFW profile

$$\rho_{NFW}(r) = \frac{\rho_0}{\frac{r}{r_s}(1+\frac{r}{r_s})^2} \tag{4.1}$$

Einasto Profile

Further studies (Merritt et al., 2005; Graham et al., 2006) suggest that an improved fit over the NFW profile is provided by an Einasto profile. The Einasto profile (Einasto and Haud, 1989) describes a profile that follows the NFW profile closely in the outer halo but flattens towards its centre (with the added benefit of removing the mathematical singularity from the middle of the halo).

$$\rho_E(r) = \rho_0 e^{-\frac{2}{\alpha_e}[(\frac{r}{r_s})^\alpha - 1]} \tag{4.2}$$

The Einasto profile has an additional free parameter $\alpha_{ein} = 0.17$ which in this calculation is taken as constant over both mass and redshift. In this chapter the behaviour of the

[1]These halos, besides being the hosts of the first stars, are promising sites for dark matter annihilation to play a significant role as the greater densities at high redshifts naturally lead to higher dark matter annihilation rates and the lack of existing structure decreases the number of processes and interactions that could compete with, or swamp any potential modifications due to dark matter.

Einasto and NFW profiles closely resemble each other and thus only the results for the Einasto profile are shown for expedience.

Burkert Profile

Another alternative is the profile given be Burkert (Burkert, 1995) which was originally defined to fit the dark matter profiles of dwarf galaxies. In contrast to the fitting function of Einasto and NFW, Burkert profile becomes constant towards the centre of the halo.

$$\rho_B = \frac{\rho_0}{(1 + \frac{r}{r_s})(1 + \frac{r^2}{r_s^2})} \tag{4.3}$$

In all profiles, r_s is the scale radius, giving the radius at which the dark matter density profile's gradient breaks and is defined as

$$r_s = \frac{r_{vir}}{c}. \tag{4.4}$$

A range of profiles for different masses and redshifts are shown in the top plot in Figure 4.1. Overall, halos at higher redshifts (in this case the dashed lines) are more compact objects than those at lower. The different dark matter density profiles are illustrated in the bottom plot in Figure 4.1 with the NFW, Einasto and Burkert profiles shown in black, yellow and cyan respectively. It demonstrates the marked difference in density at the centre of the halo when comparing the profiles of the flat Burkert with those of the cusp-y Einasto and NFW. While these high density regions only make up a small fraction of the overall mass, they do contribute considerably to the total energy produced from dark matter annihilation.

From the above density profiles, the expression for the mass of the halo is then given by

$$M_{halo} = \int_{r=0}^{r=R} \rho(r) r^2 \mathrm{d}m \tag{4.5}$$

It is of note that the halo mass in the above expressions does not converge as $r \longrightarrow \infty$. Instead the halo mass is taken as the mass enclosed within the virial radius so that $R = r_{vir}$, which is commonly defined as denoting the radius at which the density contained within is Δ_c times that of the critical density ρ_c.

$$\bar{\rho}(< r_{vir}) = \Delta_c \rho_c \tag{4.6}$$

where critical density is defined in the usual manner and $\Delta = 200$.[2]

[2] All calculation assume cosmological parameters consistent with the latest Planck collaboration such that $h = 0.71$, $\Omega_{\Lambda,0} = 0.6825$ and $\Omega_{m,0} = 0.3175$.

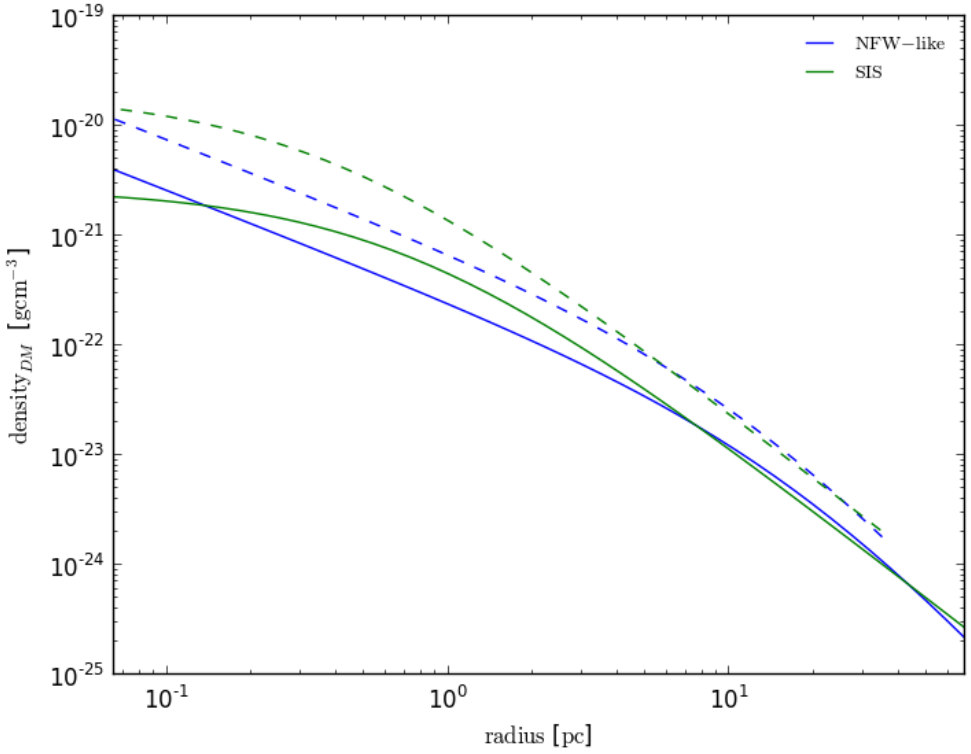

Figure 4.1: Density distribution of the gas content of the halo. The blue lines show a gas distribution that follows that of the underlying dark matter profile while the green shows the singular isothermal profile used in the examination of the first star forming halos. Solid lines show a $10^5 M_\odot$ halo at redshift 20, dashed halos at redshift 40.

4.1.2 Mass-Concentration Relation

The concentration parameter sets the radius r_s at which the density profiles turns over and as such regulates the density at the centre of the halo. Two contrasting, slightly modified expressions for the concentration-mass relation were chosen from Comerford and Natarajan (2007) eq. 4 and Duffy et al. (2010) eq. 5 which are both dependent on halo mass and redshift. The gradient of the relation from Comerford is considerably steeper than that of Duffy and both relations produce highly concentrated profiles for small mass halos at low redshift. Qualitatively, this behaviour persists to high redshifts, though the concentration parameter decreases overall (see Figure 4.2).

$$c_c(M,z) = \left(\frac{M}{1.3\times10^{13}M_\odot}\right)^{-0.15}\frac{22.5}{(1+z)} \tag{4.7}$$

$$c_d(M,z) = \left(\frac{M}{2\times10^{12}h^{-1}M_\odot}\right)^{-0.084}\frac{14.85}{(1+z)^{0.71}} \tag{4.8}$$

It is important to note that both concentration relations were fitted for galaxy-sized halos at low redshift and here are extrapolated considerably beyond their intended parameter space. As a check, a third mass-independent modification of the above relations is also considered:

$$c_f(z) = \frac{47.85}{(1+z)^{0.61}}. \tag{4.9}$$

A comparison of these mass-concentration relations is shown in Figure 4.2, where the dashed lines denote c at redshift 10 and the solid line at redshift 50. As already mentioned, the relation from Comerford produces extremely compact objects at the low end of the mass range and at high redshifts. The middle plot of Figure 4.1 shows how the profile of a halo varies with different mass-concentration parameters. In conjunction with the above density profiles these allow a range of different dark matter halo models to be investigated and demonstrates how halo morphology impacts dark matter annihilation effects.

4.1.3 Baryonic Content

Lastly the distribution of the halos' gas needs to be defined. In this case the assumption is made that the gas traces the profile of the dark matter component such that

$$\rho_B(r) = \frac{f_B}{f_{DM}}\rho_{dm}(r), \tag{4.10}$$

where f_B and f_{DM} are the mass fraction of gas and dark matter in the halo respectively. This approach was initially chosen for simplicity though realistically the gas distribution would not follow the dark matter profile due to the added pressure effects felt by baryonic

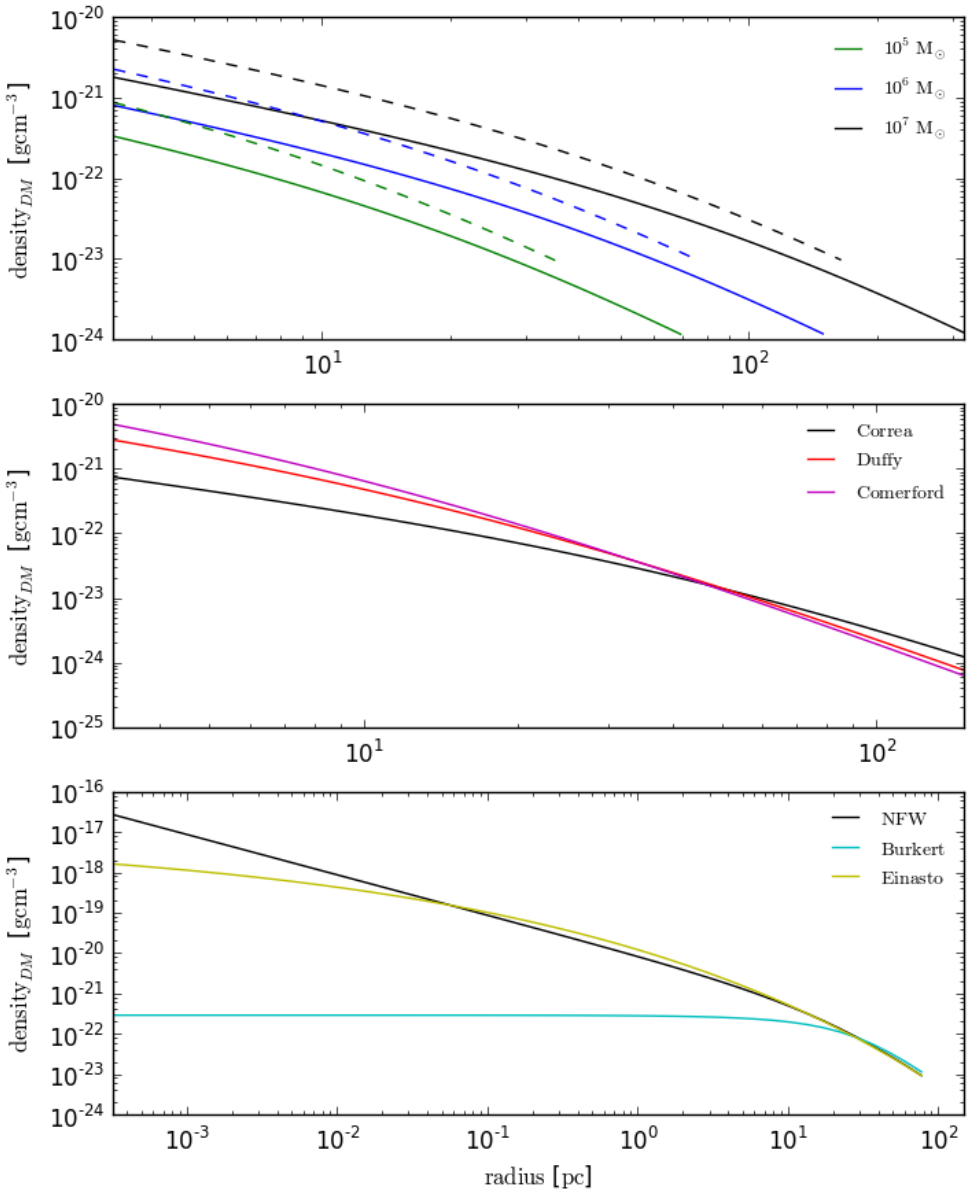

Figure 4.2: Dark matter density profiles as they vary with mass (10^5-$10^7 M_\odot$) and redshift (solid line - z = 20, dashed line - z = 40) is shown in the top figure. The middle shows the variations in the dark matter density profile in a $10^6 M_\odot$ halo at redshift 20 for a range of mass-concentration relations (black is the semi-analytic model from Correa, red from Duffy et al and magenta from Comerford). The bottom plot shows different density profiles, the black represents the NFW profile, yellow the Einasto and cyan a Burkert profile.

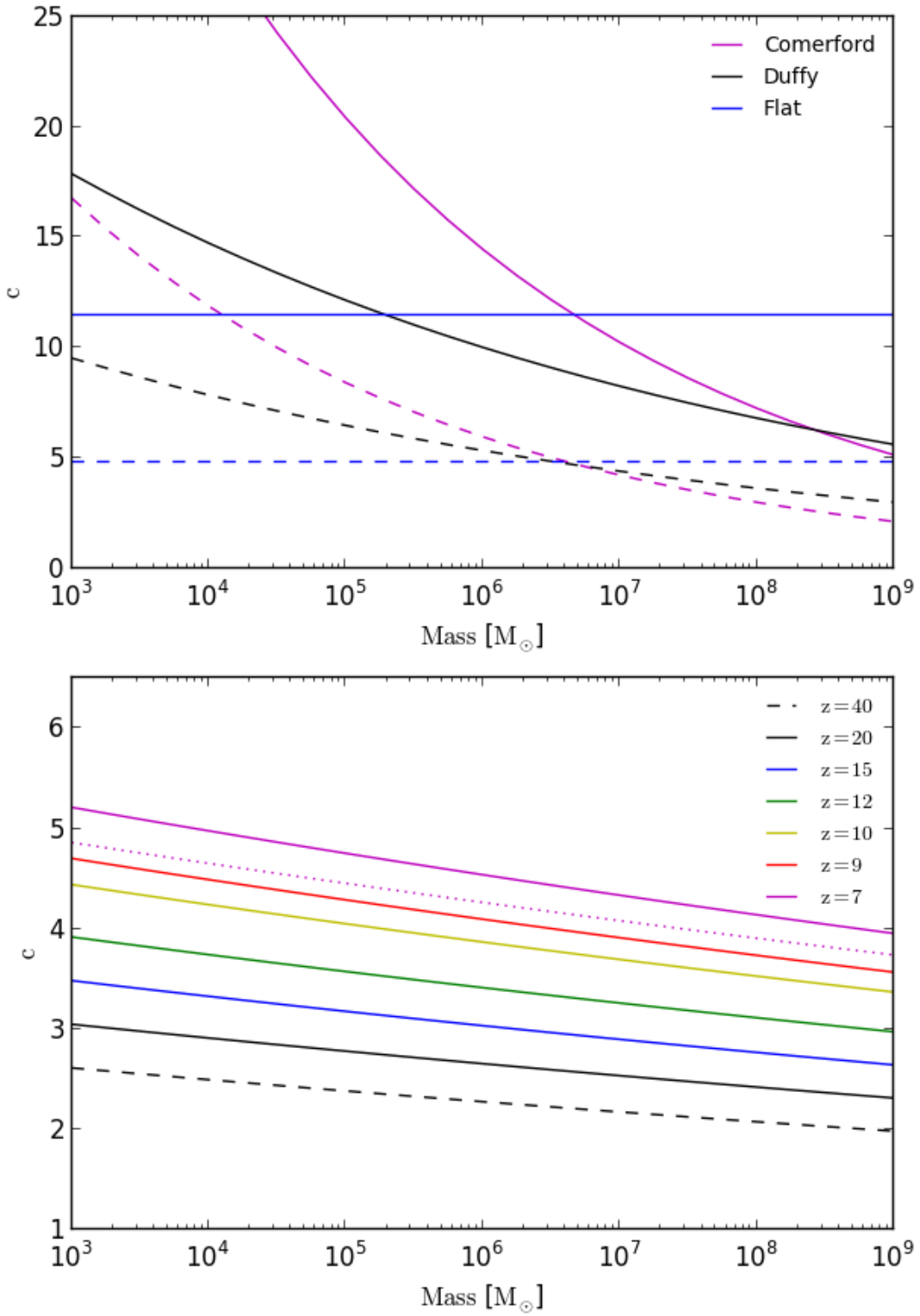

Figure 4.3: Mass-concentration relations used in this work. The upper plot shows mass concentration relations as given by Comerford and Duffy (magenta and black) as well as a mass independent intermediate model (blue). Solid lines show the relation at redshift 50 and the dash at redshift 10. The lower plot shows the semi-analytic model of Correa at various redshifts. The dashed line at z = 40 is extrapolated from the given model.

Halo Model	mass $\log_{10}[M_\odot]$	redshift [z]	c	dark matter profile	gas profile
Halo1	3 – 9	0 – 50	Flat	Einasto	NFW-like
Halo2	3 – 9	0 – 50	Duffy	Einasto	NFW-like
Halo3	3 – 9	0 – 50	Comerford	Einasto	NFW-like
Halo4	3 – 9	0 – 50	Flat	Burkert	NFW-like
Halo5	3 – 9	0 – 50	Duffy	Burkert	NFW-like
Halo6	3 – 9	0 – 50	Comerford	Burkert	NFW-like

Table 4.1: Summary of the different dark matter halo models considered in this chapter.

matter. Since the energy deposition will depend on the distribution of the gas, a more realistic model will be employed for the full energy cascade calculation. In the next chapter the profile of a singular isothermal sphere (SIS) is used and the two density profiles are shown in Figure 4.3 for comparison.

The halo models as well as redshift and mass ranges are summarised in Table 4.1.

4.2 Dark Matter Annihilation Power from Halos

A generic self-annihilating SUSY neutralino is chosen as the dark matter particle candidate spanning masses from 5 GeV to 110 GeV, with quark/anti-quark pairs, muons, tau, or W bosons as their immediate annihilation products. In practice, more exotic candidates that either annihilate or decay to inject energy in the form of standard model particles could also be used provided a sufficient compatibility with the assumed cosmology.

4.2.1 Dark Matter Annihilation Power

The power produced by dark matter annihilation per unit volume is given by:

$$P_{dm}(x) = \frac{c^2}{m_{dm}} \langle v\sigma \rangle \rho_{dm}^2(x), \tag{4.11}$$

where m_{dm} and ρ_{dm} are the dark matter particle mass and volume density respectively and $\langle v\sigma \rangle$ is the velocity averaged annihilation cross-section which we take to be $2 \times 10^{-26} \mathrm{cm}^{-3}\mathrm{s}^{-1}$. [3]

The dark matter models used in this chapter are summarised in Table 4.1. Spectra of the annihilation products are calculated as described in Chapter 2, using the electron/positron proxy and the PYTHIA code.

[3] While a cross-section constant across all our models is adopted here, note that $\langle v\sigma \rangle$ for some of the models proposed may already be subject to constraints in conjunction with the dark matter particle mass employed.

Dark Matter Model	m_{dm} [GeV]	$\langle v\sigma \rangle_{max}$ [$\mathrm{cm}^{-3}\mathrm{s}^{-1}$]	Annihilation Channel
DM1	5	2.0×10^{-26}	τ
DM2	5	2.0×10^{-26}	μ
DM3	5.5	2.0×10^{-26}	q
DM4	50	2.0×10^{-26}	τ
DM5	50	2.0×10^{-26}	μ
DM6	50	2.0×10^{-26}	q
DM7	83	2.0×10^{-26}	W

Table 4.2: Summary of the different dark matter annihilation models considered in this work.

4.3 Binding Energy Comparison

4.3.1 Over the entire Halo

As an initial estimate of the impact dark matter annihilation has on the gas, the total power produced through dark matter annihilation within the halo over the Hubble time is compared to the gravitational binding energy of the halo. The gravitational binding energy of the halo is given by,

$$U_G = \int_0^{r_{vir}} \frac{GM_{int}(r')m_{shell}(r')}{r'} \mathrm{d}r', \tag{4.12}$$

where G is the gravitational constant, $M_{int}(r')$ is the mass contained within radius r' and $m_{shell}(r')\mathrm{d}r'$ the mass in the infinitesimal spherical shell at r'.

The total power from dark matter annihilation from the halo is,

$$P_{tot} = \int_0^{r_{vir}} 4\pi P_{dm}(r) r^2 \mathrm{d}r \tag{4.13}$$

and the Hubble time (here taken as a proxy for the halo's age) is defined in the usual manner as

$$t_H = \frac{1}{H}. \tag{4.14}$$

Therefore the total energy produced within the halo over it's lifetime is,

$$U_{dm} = P_{tot} t_H. \tag{4.15}$$

The ratio of the energy from dark matter annihilation and the gravitational binding energy

$$R_{tot} = \frac{U_{dm}}{U_G} \tag{4.16}$$

is shown in Figure 4.4 for different halo models. The top left hand panel shows the fiducial model of the Einasto profile combined with the mass-concentration relation

from Duffy for a 5GeV particle annihilating via μ. Here grey regions denote halos for which the total energy produced within the halo over the Hubble time is greater than its gravitational binding energy. The other panels show the ratio between the fiducial and other dark matter halo models. Panels on the left show halos with an Einasto profile while those on the right show models with a Burkert profile. From top to bottom, the rows indicate a Duffy, Comerford and constant mass-concentration relation. The plots show that the more concentrated the object the greater the dark matter the total energy from dark matter annihilation. This is due to the high density at the centre of these objects.

Of course R_{tot} only gives a measure of the total energy produced rather than energy actually transferred to the gas of the halo. In order to calculate the fraction of the injected energy deposited into the halo, f_h, the energy loss along the various trajectories of particles produced during the annihilation process are summed over.

4.4 Energy Transfer

The energy transfer calculation performed for the work in this chapter includes the majority of the processes described in Chapter 3 (except photon pair-production off the gas and CMB fields and Coulomb scattering for electrons) but does not resolve the entire electromagnetic cascades. Instead, a first order, computationally light, approximation is employed which allows efficient exploration of the dark matter model parameter space. First off, collisions are neglected and particles are assumed to travel in a straight line in $\mathbb{R}^3$;

$$\mathbf{x}(t) = \mathbf{x}_f t + \mathbf{x}_f(1-t) \tag{4.17}$$

where $\mathbf{x}_i$ and $\mathbf{x}_f$ are the initial and final position of the particle respectively and $t \in [0,1]$. A particle specific, averaged energy loss rate S_α is integrated along that path to give the energy lost by particle of kind α, with initial energy E_i traveling form point $\mathbf{x}_i$ to $\mathbf{x}_f$.

$$L_\alpha(\mathbf{E}_i, \mathbf{x}_i, \mathbf{x}_f) = \int_0^1 S_\alpha(\mathrm{E}(t))\rho_g(\mathbf{x}(t))\mathrm{d}t. \tag{4.18}$$

Then the spherical symmetry of the halo is used in order to calculate the average energy lost by a particle of species α created at radius r_i (placed along the x-axis for convenience) while traveling to r_f

$$\bar{L}_\alpha(E_{in}, r_i, r_f) = \frac{\int_0^\pi \int_0^{2\pi} L_\alpha(E_{in}, \mathbf{x}(r_i), \mathbf{x}(r_f, \theta, \phi))\mathrm{d}\theta\mathrm{d}\phi}{4\pi r_f}. \tag{4.19}$$

The energy loss rate for a photon is driven by the total interaction cross-section which is heavily dependent on the photon energy. Figure 4.5 shows the number of

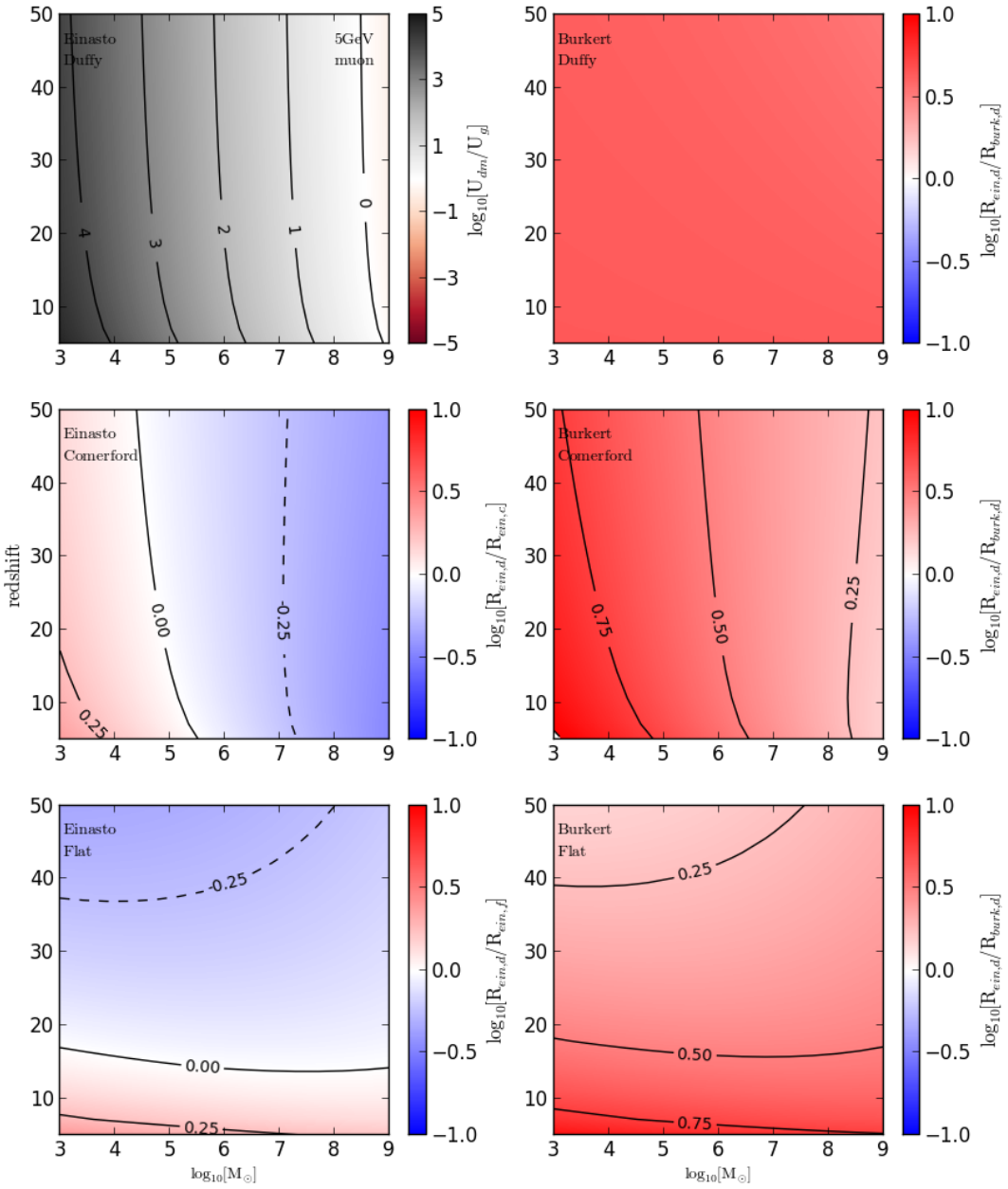

Figure 4.4: The ratio of the total energy from dark matter annihilation over the Hubble time and the halo's binding energy for 10^3-$10^9 M_\odot$ halos between redshifts 5 - 50. The top left panel shows the fiducial model of a halo with a dark matter Einasto profile and a mass-concentration relation from Duffy et al. The other panels show the residue of this fiducial model and halo with different density profiles and mass-concentration relations. All halos on the left show Einasto profiles and those on the right Burkert profiles, the mass-concentration relation from top to bottom are from Duffy, Comerford and a flat relation.

interactions the photons with different energies, injected at various radii, undergo before escaping the halo. We note that in the case of high energy photons that predominantly lose energy through electron/positron pair-creation, particles will largely escape the halo without significant interaction. In contrast, for photons with energy below the MeV range, the main energy transfer mechanisms moves to Compton scattering and photo-ionisation/excitation. These have a higher interaction cross-section than the pair-production process and so are considerably more efficient at depositing their energy into the gas. Overall only particles created very close to the core of the halo, and thus injected in a high density gas environment, contribute to the energy transfer in any notable form. Thus density profiles with a cusp and high mass-concentration parameters are considerably more efficient than the more relaxed models at depositing energy as they provide the high density core required for the photon energy-loss processes.

In contrast, electrons and positrons are assumed to lose energy continuously according to the particle's stopping power as well as in collisions via IC scattering off cosmic microwave background (CMB) photons. The latter process dominates in the high redshift regime. Figure 4.6 shows the fraction of the injected particle's initial energy that is lost as the particle reaches the virial radius, with the right hand side showing halos at redshift 30 and the left at redshift 0. From top to bottom the halo density profiles are ordered from least to most concentrated. We note that IC scattering is indeed shown to be the dominant energy-loss mechanism for high energy electrons at high redshift and the energy lost is independent of the halo profile. In contrast, energy loss through interactions with the halo gas is dominant for low-energy particles and is, as expected, more efficient in the highly concentrated models. While most of the injected electrons are high energy particles, and will therefore undergo IC scattering at high redshift, the lost energy will be transferred to the halo's gas through the up-scattered CMB photons created in the process. Thus while the energy loss of the injected electrons from IC scattering is independent of the halo profile, the amount of energy absorbed by the halo will still be dependent on its density distribution.

As a whole electrons and positrons are found to be the dominant source of dark matter annihilation energy being transferred to gas in the halo. However as mentioned before this does not take into account electron/positron pair creation off of the gas and CMB photon field through which high energy photons would be able to contribute to the energy deposition.

4.4.1 Total Energy Lost

Now the total fraction of the annihilation energy lost by the injected particles within the halo can be calculated which requires integration over the energy spectrum at each point in the halo volume:

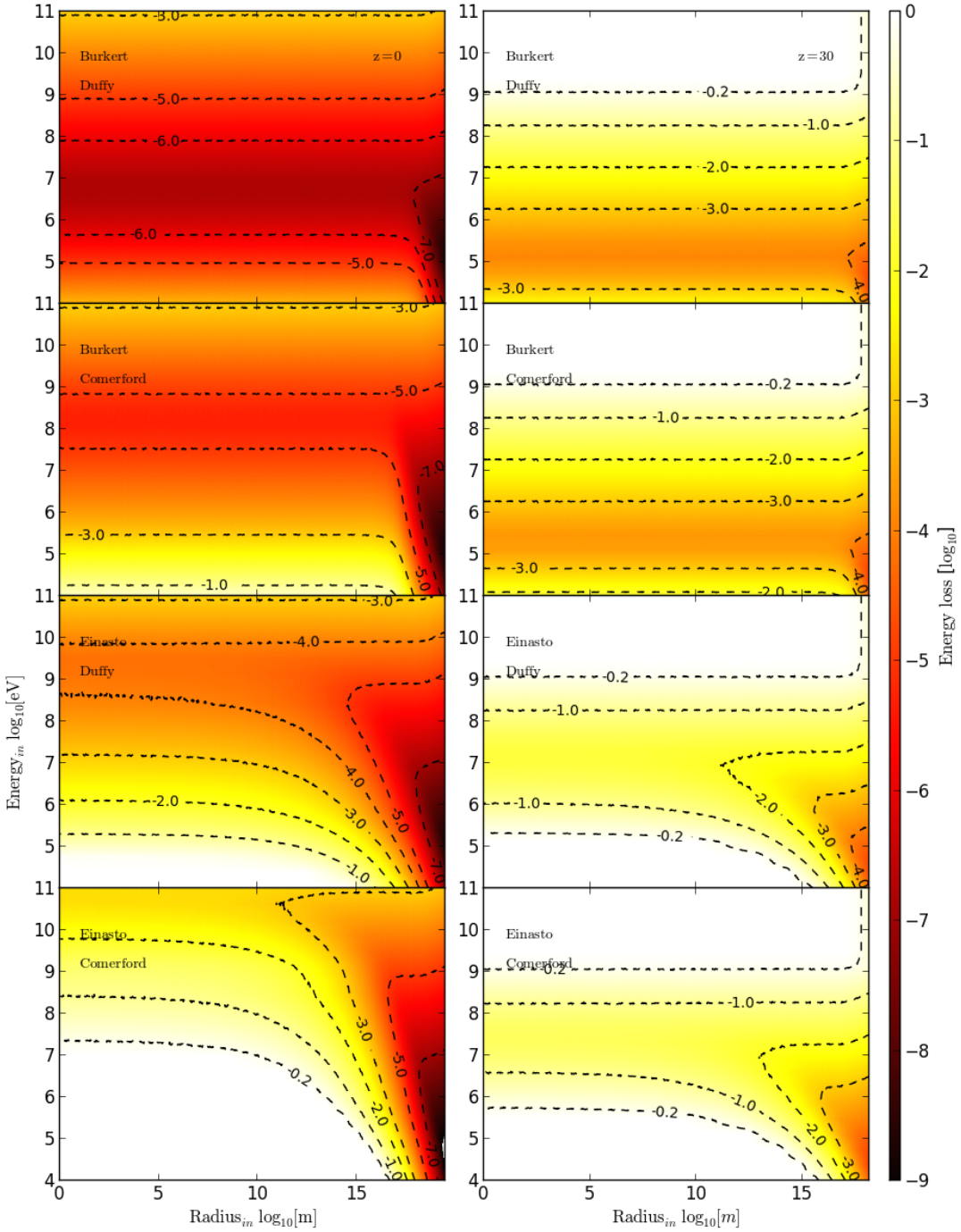

Figure 4.5: Energy lost by electrons injected at different radii and initial energies in the simplified energy transfer scheme. Different panels show various halo models with panels on left showing results at $z = 0$ and on the right at $z = 30$.

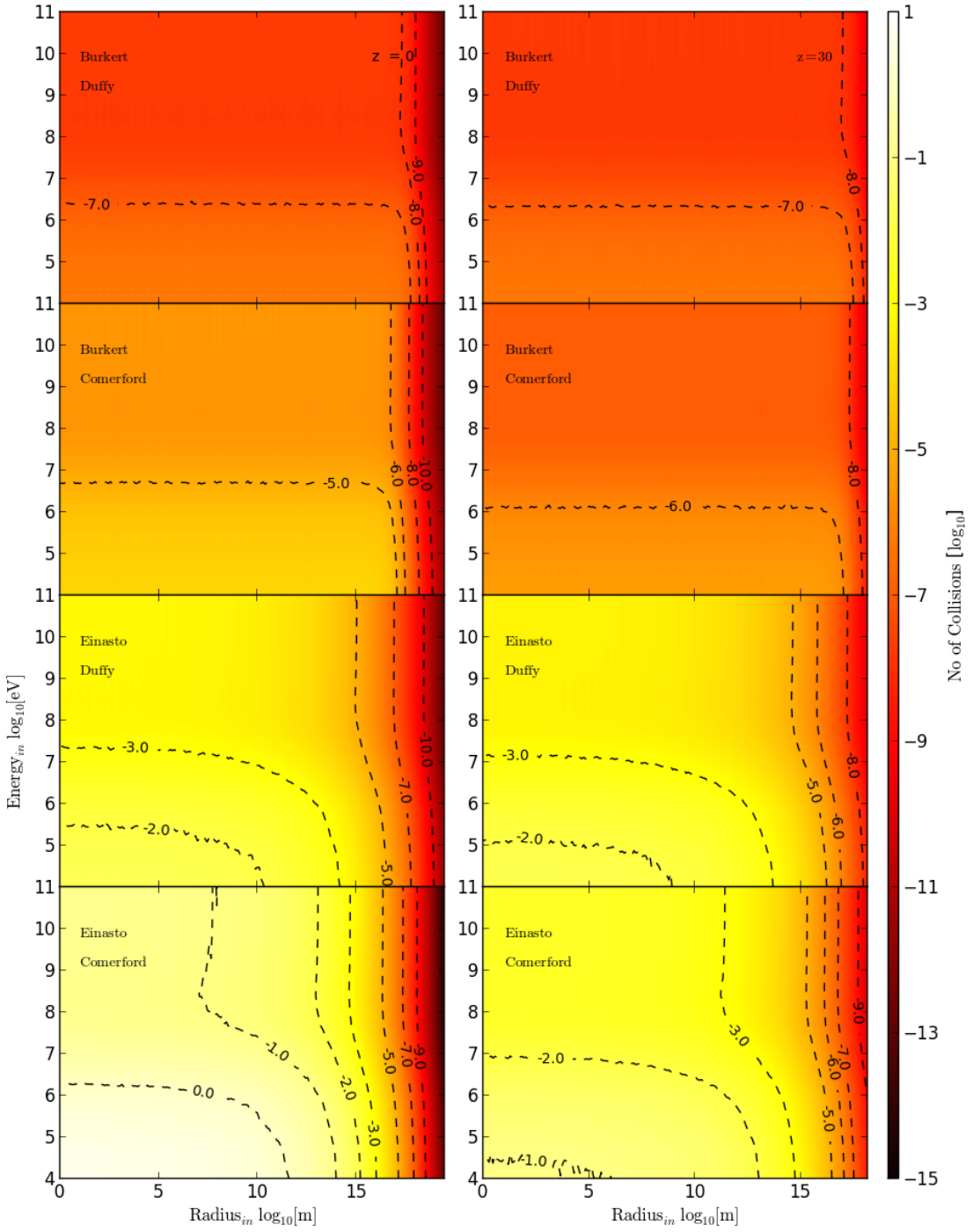

Figure 4.6: Energy lost by injected photon injected at different radii and initial energies in the simplified energy transfer scheme. Different panels show various halo models with panels on left showing results at $z = 0$ and on the right at $z = 30$.

$$U_{lost} = \sum_{\alpha=1}^{3} f_\alpha \int_0^\infty \int_0^{r_{vir}} 4\pi\mu_\alpha \bar{L}_\alpha(\epsilon_i, r, r_{vir}) P_{dm}(r) r^2 \mathrm{d}\epsilon \mathrm{d}r, \tag{4.20}$$

where α refers to the different injected particle species and μ_α the fraction of the total annihilation energy in form of that species. Given that the total energy produced through dark matter annihilation is given by equation 4.15, the fraction of the total energy from dark matter that is in turn lost in the halo is then simply

$$T(M, z) = \frac{U_{lost}}{U_{tot}}. \tag{4.21}$$

It should be noted that high-energy particles create a cascade of lower-energy particles as they lose energy. Following these secondary particles is beyond the complexity of this calculation and we thus set an energy absorption fraction for these secondary particles (see §4.5.1 for further detail). These secondary particles carry less energy[4] than the originally injected particles and thus interact more readily with the gas than their high energy progenitors.

4.5 Binding Energy Comparison

As an initial measure of the impact that dark matter annihilation has on the halo structure, we compare the total energy produced via annihilation to the halo's gravitational binding energy. The gravitational binding energy is given by

$$U_G = \int_0^{r_{vir}} \frac{G M_{int}(r') m_{shell}(r')}{r'} \mathrm{d}r', \tag{4.22}$$

and the total energy injected via dark matter annihilation over the Hubble time t_H (which is here taken as a proxy for the halos age) is

$$U_{dm} = \int_0^{r_{vir}} 4\pi P_{dm}(r) r^2 dr \cdot t_H. \tag{4.23}$$

The ratio and transfer fraction can then be combined to calculate the bulk energy fraction transferred to the halo over the Hubble time. As alluded to previously, the energy is transferred via the secondary particles created during the injected particle journey through the halo. While we here are not in the position to give rigorous treatment to the injection of the secondary particle, we do observe these to be of considerably lower energy than the original "parent" particle. This holds in particular for the dominant energy transfer process of electrons and positrons undergoing IC scattering and producing lower energy photons. We make the assumption that the secondary particles

[4]The precise spectrum of secondary particles produced will be dependent on the down-scattering process.

produced through inverse Compton scattering, transfer their energy more readily to the gas in the halo and subsequently set an energy absorption fraction of $f_{abs} = 0.1$ with the rest of the energy escaping [compare the photon escape fractions of ionising galaxies Mitra et al. (2013), Benson et al. (2013)], so that we have,

$$F_{eff} = R(M, z)T(M, z)f_{abs}. \tag{4.24}$$

The precise energy absorption fraction from secondary particles, as parameterised by f_{abs} in eq. 4.24, is critical in determining the impact dark matter annihilation may have on the halo's gas component. Since we don't rigorously treat secondary energy absorption in this work, it is difficult to accurately quantify the impact these particles have on the overall energy deposition into the halo. For example, Spolyar et al. (2008) in their analysis of GeV range neutralino type dark matter, found that in order for there to be efficient energy transfer from the injected particles (including secondaries) notably higher gas densities, such are found after collapse of the proto-stellar core, are required. It may however be worth noting that Spolyar's work does not take into consideration electrons and positrons losing energy through inverse Compton scattering off CMB photons. Instead high energy charged particles solely emit Bremsstrahlung radiation which in turn undergoes electron-positron pair-creation, thus triggering an electromagnetic cascade (Yao et al., 2006). While these cascades also down scatter the injected energy, the process produces secondary particles with high energies, particularly during the early stages of the cascade. When taking secondaries into account, electromagnetic cascades are perhaps not as efficient at energy transfer as the IC scattering mechanism at high redshifts, because the latter produces low energy secondaries more readily. These have interaction cross-sections bigger than those of the EM cascade secondaries, corresponding to a higher energy transfer rate. Inverse Compton scattering can also be thought of as producing an energy spectrum of secondaries comparable to that of particles injected by annihilation of much smaller (keV - MeV) dark matter candidates, which have been found to evacuate notable fractions of gas from small halos (Ripamonti et al., 2007). This further motivates the relatively high absorption fraction used here. We return to discuss different values of f_{abs} in §4.5.1.

Figures 4.7 and 4.8 show this effective energy transfer fraction, assuming $f_{abs} = 0.1$. In Figure 4.7 we utilise a 5 GeV dark matter particle annihilating to muon and show F_{eff} for various halo models. The left hand panel shows results for Einasto profiles, with our three mass-concentration models, and the right hand panel shows results for the Burkert model. While the overall behaviour is the same for all halo models, we find the cuspy Einasto model to be more efficient at self-heating. In a similar vein, the mass-concentration relation which produces the highest value for c produces the greatest F_{eff} at fixed redshift and halo mass, indicating that the more concentrated the

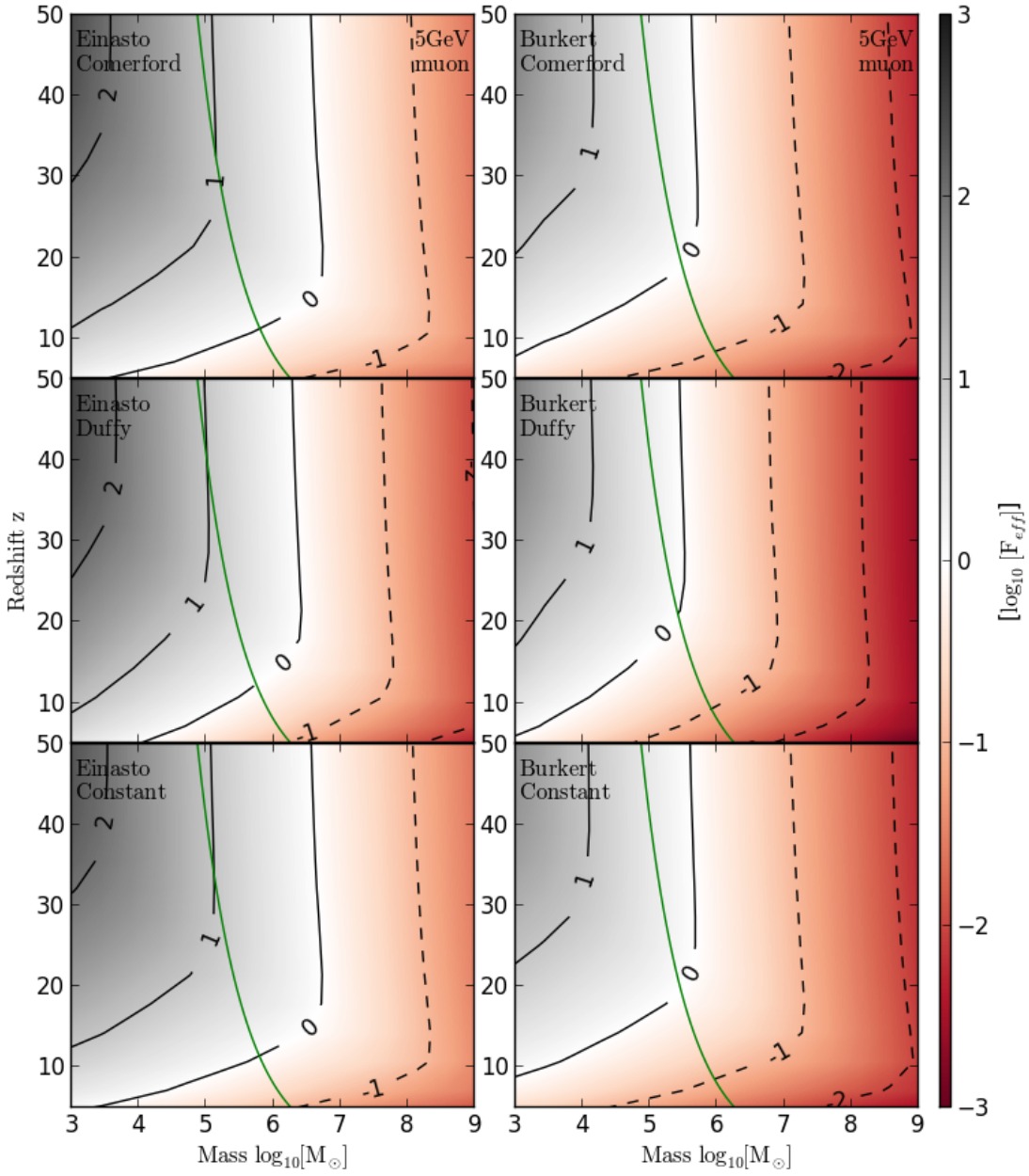

Figure 4.7: The ratio F_{eff} for a 5GeV particle annihilating via the μ annihilation channel with various halo models. The plots on the left show halos with and Einasto profile this on the right a Burkert profile. Plots in rows from the top to bottom make use of mass-concentration relations from Comerford, Duffy and the constant model respectively. The green contour shows the minimal mass of halo capable of from structure through molecular cooling.

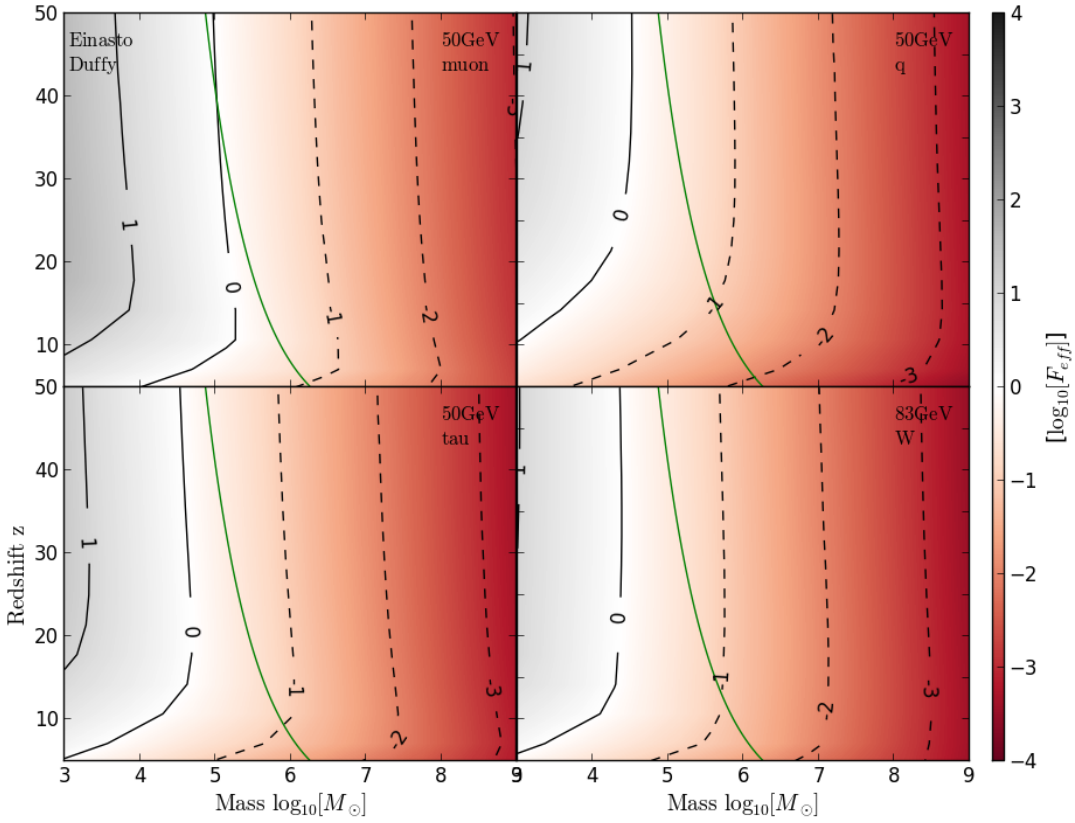

Figure 4.8: The ratio F_{eff} for a halo with an Einasto profile with Duffy mass-concentration relation. The plots show F_{eft} for different dark matter models, clockwise from the top right: 50GeV via μ, 50GeV via q, 83GeV via W and 50GeV via τ. The green contour shows the minimal halo that is able to cool through molecular cooling.

halo the more efficient is the energy transfer process.

At high redshifts, star formation has not yet disassociated molecular Hydrogen, providing a cooling channel in halos of $10^5 - 10^6 M_\odot$ (Haiman et al., 1997). Also included in Figure 4.7 is the critical mass above which halos undergo molecular hydrogen cooling (green curve) (Loeb, 2006). Halos to the left of the curve do not cool and therefore cannot collapse and form stars. We note that for all models there is a region between $z = 15 - 50$ and for halos $10^5 - 10^6 M_\odot$ in which molecular hydrogen cooling is possible but $F_{eff} > 1$. This opens the possibility that dark matter annihilation could have a significant impact on the gas chemistry in these systems and by extension on other internal structure formation.

Figure 4.8 shows similar plots for different annihilation channels and an Einasto profile with a Duffy mass-concentration relation. The tau, muon and quark cases all correspond to 50 GeV dark matter particles while the W boson case shows a 83 GeV

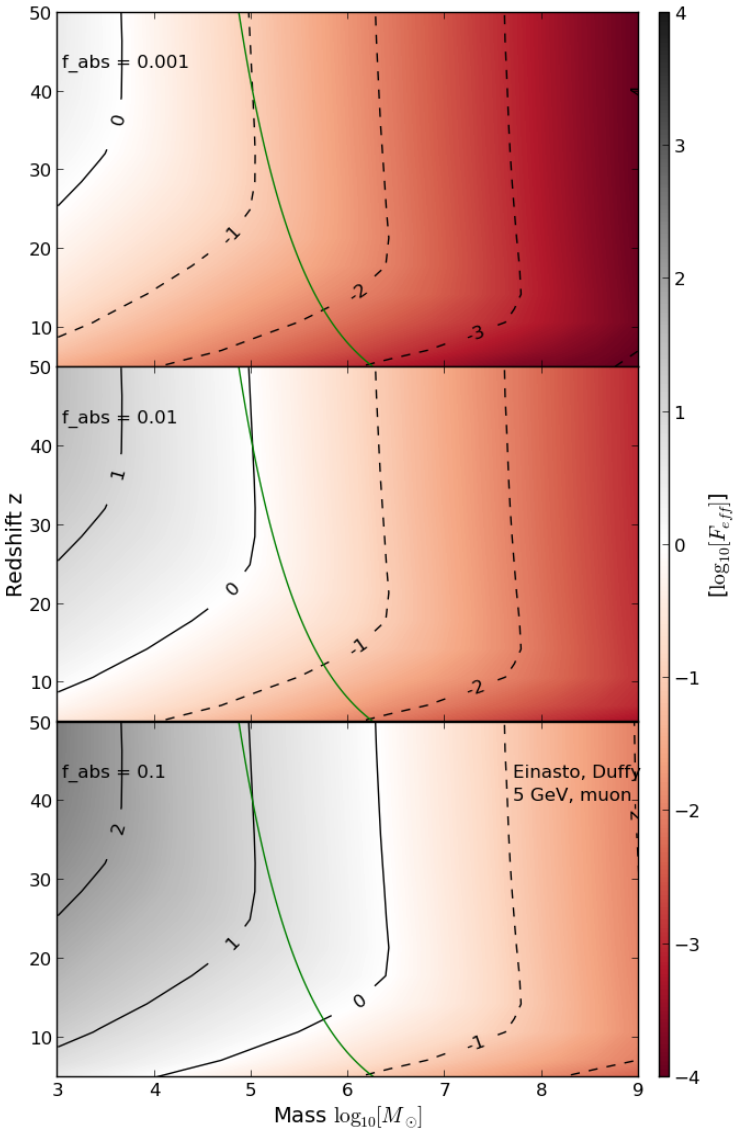

Figure 4.9: Ratio of energy produced by dark matter annihilation over the Hubble time deposited into the halo, to the halo's gravitational binding energy for different secondary particle absorption fractions. From top to bottom, $f_{abs} = 0.001, 0.01, 0.1$ In all cases we are considering a 5 GeV dark matter particle annihilating via the muon channel in a halo with an Einasto profile and Duffy mass concentration relation. Again the contour lines correspond to the plot's colourbar.

particle. In all cases we find that at high redshift, $F_{eff} \sim 1$ either coincides with the molecular cooling line or lies to the left of it, suggesting a smaller impact from larger dark matter particle candidates. At the same time, we note that while star formation may not be impacted in the largest halos for this dark matter model, they nevertheless act as both sources and sinks for ionising radiation. This should be taken into account when including annihilating dark matter in reionisation calculations.

Finally while we find that at high redshift the energy deposition behaviour is comparable between all four models (with the mu path being the most efficient), there is greater variation at low redshift. This is because as the mechanism with which the injected particles lose energy becomes less efficient, their sensitivity to the injected particle's initial energy increases and we see variation in F_{eff} due to the differences in their dark matter model's injected particle energy distributions.

4.5.1 Uncertainty due to f_{abs}

We consider the uncertainty in our estimate in the secondary particle energy absorption fraction by comparing the energy depositions plots for a range of f_{esc}, shown in Figure 4.9. From top to bottom, panels show $f_{abs} = 0.001, 0.01$ and 0.1, in all cases the halo hosts an Einasto profile with a Duffy mass-concentration relation. We note the impact f_{abs} has on the energy transfer into the halo's gas. In particular in the case in which only a $f_{abs} = 0.001$ of the energy carried by secondary particles is transferred to the halo, the impact dark matter annihilation has on heating the halo's gas becomes significantly reduced. This reaffirms the importance of careful future treatment of the secondary particles within the halo.

4.5.2 Choice of Baryonic Profile

In the work presented so far, the profile of the baryonic halo component is assumed to follow that of the dark matter distribution. While the dominant energy loss mechanism for high energy particles is through scattering off of the CMB photon field, secondary particles created in the subsequent cascade, as well as the actual energy transfer to the halo, is facilitated via interaction with the gas. Therefore changing the gas distribution can be expected to lead to changes in the overall heating of the halo. In Figure 4.10, the comparison between the ratio of energy produced by dark matter annihilation over the Hubble time and transferred into the halo, and the gravitational binding energy, for a case in which the baryonic profile traces that of the dark matter distribution (upper panel) and one for which the baryonic component forms a core (lower panel) is shown. The two models produce comparable results, with the baryonic core model being only marginally less efficient at high redshifts.

The strong similarity between the two baryonic models is predominantly due to the energy transfer mechanism employed here. For the dark matter models at the

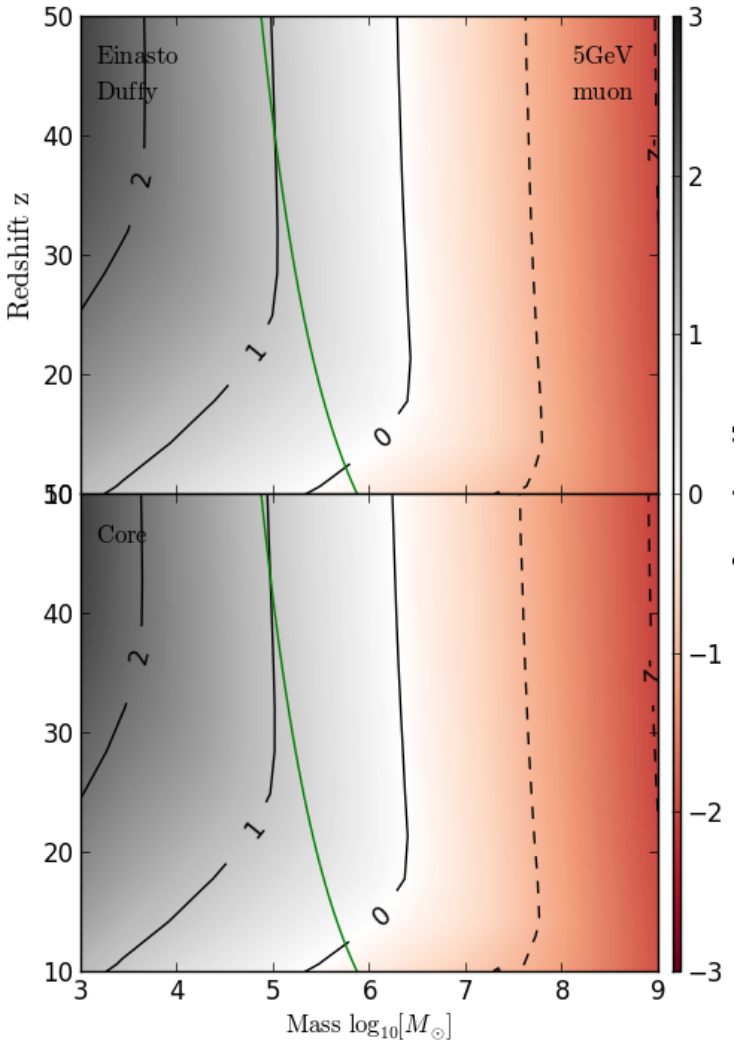

Figure 4.10: Ratio of energy produced by dark matter annihilation over the Hubble time deposited into the halo, to the halo?s gravitational bind- ing energy for a 5 GeV dark matter particle annihilating via a muon. The upper panel shows and Einasto-like baryonic profile with a Duffy mass- concentration relation and fabs = 0.1, while the lower shows the same with a baryonic core profile.

electroweak scale considered in this work, annihilation products will[5] primarily interact with the CMB photon field to produce secondary particle cascades. The secondary particles are not tracked in this treatment and their energy loss via interactions with the gas are included via f_{abs} and the energy partition calculated using the MEDEA code. Since both of these are here taken to be independent of the gas distribution, the two different gas models give close to exactly the same result. Small differences arise at high redshifts where the gas is sufficiently dense to allow for the low energy tail of the injected particles to deposit some energy before escaping the halo.

The inability to fully account for the energy loss to the gas due to secondary particles represents a significant shortcoming of this treatment. An updated gas density distribution, as well as full tracking of not only the primary injected particle but also the cascade products, is presented in the next chapter.

4.6 Potential for Modification of Structure Formation

The above calculation gives the gross efficiency of the energy transfer from the dark matter annihilation products to the halo. However there is a further partition of this deposited energy into heating, ionisation and the production of Lyman α photons which needs to be taken into consideration. A limitation of the energy transfer treatment here is that the full high energy particle cascades are not resolved and so this energy deposition partition cannot be given directly. However since the driving energy loss mechanism is IC scattering, the spectrum of the photons produced during this process can be calculated separately and then be used in conjunction with an energy deposition code such as MEDEA2 to give a first order approximation of the breakdown of the energy transferred to the halo.

As described in Chapter 3, MEDEA2 uses a Monte Carlo method and random sampling of relevant physical processes to give the energy partition of a given electron, photon or positron into heating, H and He ionisation and Lyman α photon production. It evolves the particle, including secondaries produced, in a homogeneous gas field and does this for a specifiable particle energy, redshifts (gas-density) and range of ionisation fractions of the gas (where H and He are always assumed to have the same ionisation fraction). Outputs from MEDEA2 are shown in Figure 4.11 where the plot on the left shows results for electrons/positrons with energies between 50 and 10^6 eV and the plot on the right for photons. In both figures, blue, green and red lines show the fraction of energy depositing into heat, ionisation and lyman photons respectively. Solid lines show results for a gas ionisation fraction of 10^{-4} while dashed lines indicate a fraction of 0.365. (The MEDEA code was run for 10 different ionisation fractions, spaced equidistant in

[5]The injected particle distribution does feature a low energy tail. While these particle occupy an energy regime in which they can interact directly with the gas, they largely free stream out of the halo and therefore represent only a subdominant contribution to the total energy transfer to the halo.

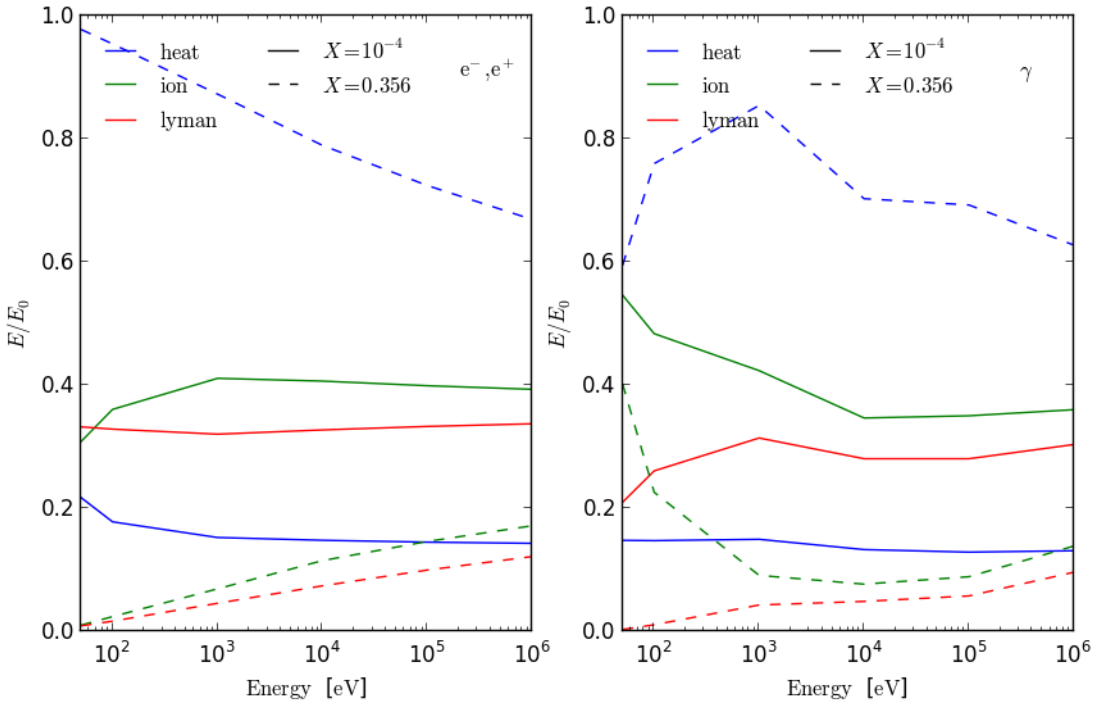

Figure 4.11: MEDEA outputs for electrons/positrons (left plot) and photons (right plot). Blue, green and red lines show the fraction of energy deposited into heating, ionisation and lyman photons respectively. Solid lines show results for an ionisation fraction of 10^{-4} and dashed lines for 0.356.

logspace between 10_{-4} and 1.)

MEDEA2 outputs were produced for the range of up-scattered IC photons at the average gas density of the halo. It is important to note here that these outputs do not take into account the variable density of the halo's gas component or the fact that particles traveling beyond the virial radius should be taken to have escaped and no longer contribute to the total energy deposition. In order to partially compensate for the first point[6], MEDEA2 outputs were also produced at different gas densities representative of those that may be found within the halo. At the high redshifts considered here this had little impact on the MEDEA2 output energy partitions as the high gas densities and CMB photon number densities mean high on the spot, energy transfer efficiency so few particles free stream. Subsequently, IC photon energy weighted averages of the outputs were used to produce energy deposition fractions.

Figure 4.12 shows the energy partition into heating (red), ionisation (green) and Lyman photons (blue) at different ionisation fractions of the halo gas using this method. The plot on the left shows a 10^5 and on the right a $10^6 M_\odot$ halo at redshifts 30 (solid

[6]The parameter f_{abs} is a measure of how much of the energy is actually absorbed by the halo and in part accounts for the particles that escape.

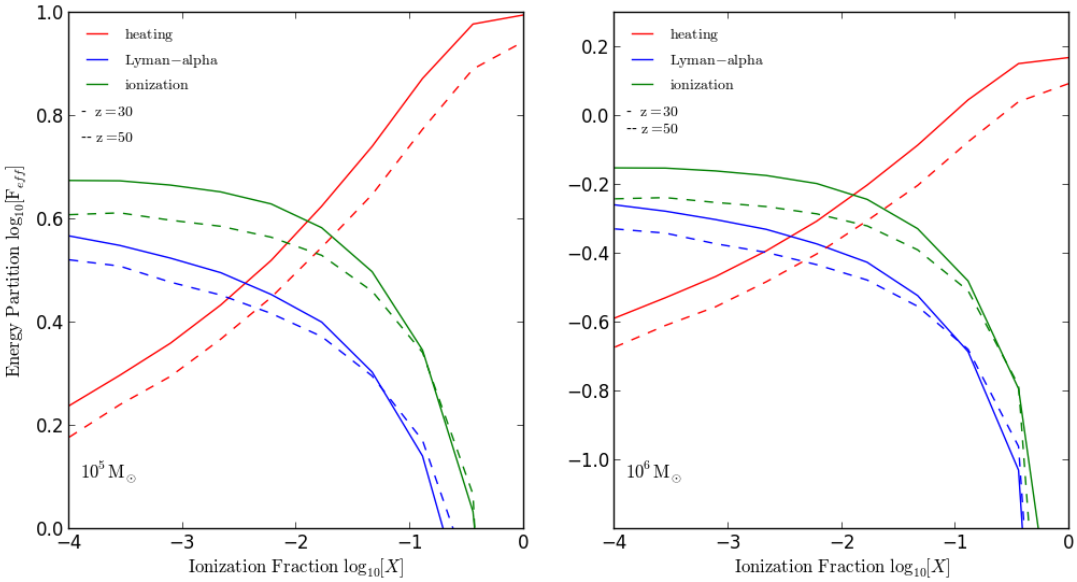

Figure 4.12: Plots show the MEDEA energy breakdown of energy deposited form dark matter annihilation for different ionisation fractions. The plot on the left shows a $10^5 M_\odot$ halo and $10^5 M_\odot$ on the right. Heating, Lyman-alpha photons and ionisation energy channels are respectively shown in red, blue and green with solid lines showing partitions at redshift 30 and dash at redshift 50.

line) and 50 (dashed line). In both cases the energy breakdown is given as a ratio to the gravitational binding energy over the Hubble time and the dark matter model consists of a 5GeV particle annihilating via μ. For an energy absorption fraction $f_{abs} = 0.1$, the $10^5 M_\odot$, enough energy is channelled into heating the halo to overcome the gravitational binding energy of the gas at any ionisation fraction. For the $10^6 M_\odot$ halo this holds for ionisation fractions greater than 0.1 but below a significant portion of the binding energy is still deposited within the halo over the Hubble time.

The above suggests that even when taking into account the critical mass from molecular cooling, there is a parameter space for which primordial gas inside $10^5 - 10^6 M_\odot$ halos above redshift 20 would cool and the energy injected from dark matter annihilation exceeds the binding energy of the gas. Potentially this could lead to the disruption of early star formation inside these halos and subsequently a delay in the formation of the first galaxies. This complements previous work (Ripamonti et al., 2007, 2010) which found that dark matter annihilation/decay can lead to significant evacuation of gas from halos with $10^6 M_\odot$ mass. While the authors of that work used dark matter models of lower mass than is used here, the full treatment of relativistic particles shows that halo disruption effects are still possible for dark matter models with masses in the GeV range.

This effect is more pronounced for low mass dark matter models and concentrated

halos that display some form of density cusp at their centre since these models naturally correspond to greater dark matter annihilation power. Overall dark matter models annihilating via muons produce the greatest annihilation effect as these produce the highest branching ratio into electrons and positrons. Regardless of model, the overall energy transferred to the halo gas drops off rapidly at low redshifts as the reduced gas and CMB number densities lead to increased mean free paths of the interaction processes and thus the injected particles readily escape the halo.

In order to explore a wide parameter space, a straightforward analytic energy transfer treatment was employed. However this did not give a complete description of the energy deposition and of the secondary particles created during interactions with the gas and CMB photons. The efficiency with which the particles transfer their energy to the halo is critical in determining the ability of dark matter annihilation to impact structure formation. With this in mind the updated energy transfer code introduced previously is used in the following chapter to further explore the parameter space identified here as being potential sites of modification of structure formation through dark matter annihilation.

Chapter 5

Self-heating Dark Matter Halos II A Closer Look

In the previous chapter, the potential impact dark matter annihilation has on early structure formation was explored. A simplified energy transfer scheme giving an approximation for the total energy deposited into the halo was implemented which allowed for a number of dark matter candidates to be compared over a wide range of redshifts and halo models. The overall results suggest that the most prominent, direct changes to the concordant astrophysical picture would be found in small, high-redshift structures, such as those that host the first stars.

Having narrowed the parameter space of interest, it is now expedient to improve on this calculation. In this chapter the full energy transfer code introduced in Chapter 3 is employed which follows the full evolution of not only the primary, injected particle but also that of any secondary particle cascades. This allows for a more accurate breakdown of the deposited energy, as well as its radial distribution throughout the halo. The latter would also provide a clearer indication of how precisely dark matter annihilation could effect the evolution of the halo.

As in the previous chapter the heating over the Hubble time due to dark matter annihilation is compared to the gravitational binding energy, though in this case this is done for radial shells rather than the total halo. In addition to the energy transfer treatment, the halo density profiles and dark matter candidate list are also partially revised to better reflect updated dark matter constraints and halo models.

5.1 Halo and Dark Matter Models

The changes made to the dark matter halo and particle models adopted in Chapter 4 are briefly outlined below.

5.1.1 Dark Matter Candidates

As well as the models considered in Chapter 4 (weak interaction annihilation cross-section, masses of 5, 50 and 83 GeV and muon, quark, tau and W boson annihilation channel), an additional dark matter model with an electron/positron annihilation channel, and masses of 130MeV, 1GeV, 10GeV and 100GeV is also taken into consideration.

Dark Matter Model	m_{dm} [GeV]	$\langle v\sigma \rangle_{max}$ [$\mathrm{cm}^{-3}\mathrm{s}^{-1}$]	Annihilation Channel
DM1	$0.13 - 100$	$1.0 \times 10^{-28} - 1.0 \times 10^{-26}$	e^-
DM2	$5, 20, 50$	$5.0 \times 10^{-27} - 1.0 \times 10^{-26}$	τ
DM3	$5, 20, 50$	$5.0 \times 10^{-27} - 1.0 \times 10^{-26}$	μ
DM4	$5.5, 20, 50$	$5.0 \times 10^{-27} - 1.0 \times 10^{-26}$	q
DM5	$83, 110$	$2.0 \times 10^{-26} - 1.0 \times 10^{-26}$	W

Table 5.1: Summary of the different dark matter annihilation models considered in this chapter.

This particular model is an attractive option because none of the annihilation power is lost via conversion to neutrinos which don't contribute to the energy deposition into the surrounding gas.

The fiducial annihilation cross-section has also been updated for the remainder of the dark matter candidates so that the total annihilation power of the halo matches that of the 130 MeV, $\sigma = 1.0 \times 10^{-28}\mathrm{cm}^{-3}\mathrm{s}^{-1}$ model. The dark matter particle parameter space is summarised in Table 5.1.

5.1.2 Density Profiles

Increases in dark matter densities mean increases in annihilation rates, while greater density gas regions will have greater interaction rates with the injected particles. Therefore the high density regions at the centre of the halo can have considerable effect on the total energy that is ultimately transferred to the halo. Uncertainties in the halo model, and in particular extrapolation to small mass and high redshifts, can lead to extremely concentrated structures and core densities. In order to give realistic estimates of the self-heating efficiency and avoid artificially high density structures, both the mass-concentration relation and baryon density distribution have been up dated. Besides that, the halo models used here retain much of the same general form as those used in the previous chapter's calculation and are summarised in Table 5.2. The key differences are in the mass concentration relation and gas profile which both were updated to produce a physically better motivated model and in particular to avoid overly concentrated objects.

Gas Distribution

For the initial halo model, the gas component of the halo was assumed to follow that of the dark matter distribution. From this point onwards, the profile of a pseudo-isothermal sphere is used as it makes a reasonable first order approximation for the mass distribution of halo-type objects (Binney and Tremaine, 1987) and avoids a divergent

Halo Model	mass $\log_{10}[M_\odot]$	redshift [z]	c	profile
Halo1	5 – 7	20, 40	Correa	Einasto
Halo2	5 – 7	20, 40	Correa	Burkert
Halo3	5 – 7	20, 40	High	Einasto
Halo4	5 – 7	20, 40	High	Burkert

Table 5.2: Summary of the different dark matter halo models considered in this chapter.

core density in the case of the NFW profile.

$$\rho_{SIS}(r) = \frac{\rho_0}{a + r^2}. \tag{5.1}$$

Figure 4.3 shows the comparison between the old gas profile (in blue), and the Singular Isothermal Sphere (SIS) profile used in this chapter (in green).

Mass-concentration

For galaxy-sized halos at low redshifts, simulations and theoretical studies have provided numerous models (Comerford and Natarajan, 2007; Duffy et al., 2010; Ludlow et al., 2016) of the mass-concentration relation. An issue that arises is the uncertainty in both the dark matter profile and the mass-concentration relation when considering smaller, high redshift structures. The upper panel in Figure 4.1 shows how different mass-concentration relations can diverge considerably when extrapolated to the parameter space of interest for this work.

For the follow up calculation in this chapter, the semi-analytic relation of Correa et al. (2015) was chosen (shown for different redshifts in the lower panel of Figure 4.1). The model combines an analytic description of the halo mass accretion history based on extended Press-Schechter theory with empirical fits from results of the OWLS (OverWhelmingly Large Simulation) numerical simulation. As a comparison, the mass-concentration fit from a high resolution N-body simulation (Angel et al., 2016) is shown by the pink dotted line at redshift 7. Lastly, another mass-concentration relation denoted High, is also used for reference and is simply double that of the Correa model.

Dynamic vs Fixed Halos

At this point a brief mention should be made about the assumption that the halos under consideration here are in a perpetual state of equilibrium and that both the underlying dark matter structure, as well as the baryonic content of the halo remain unchanged. More realistically, halos after collapse will grow through a combination of merger events and inflowing gas. At high redshifts especially, the rapid merger rate means that a significant fraction of halos are not relaxed and more over, recovery takes place over a number of dynamical times (Poole et al., 2016).

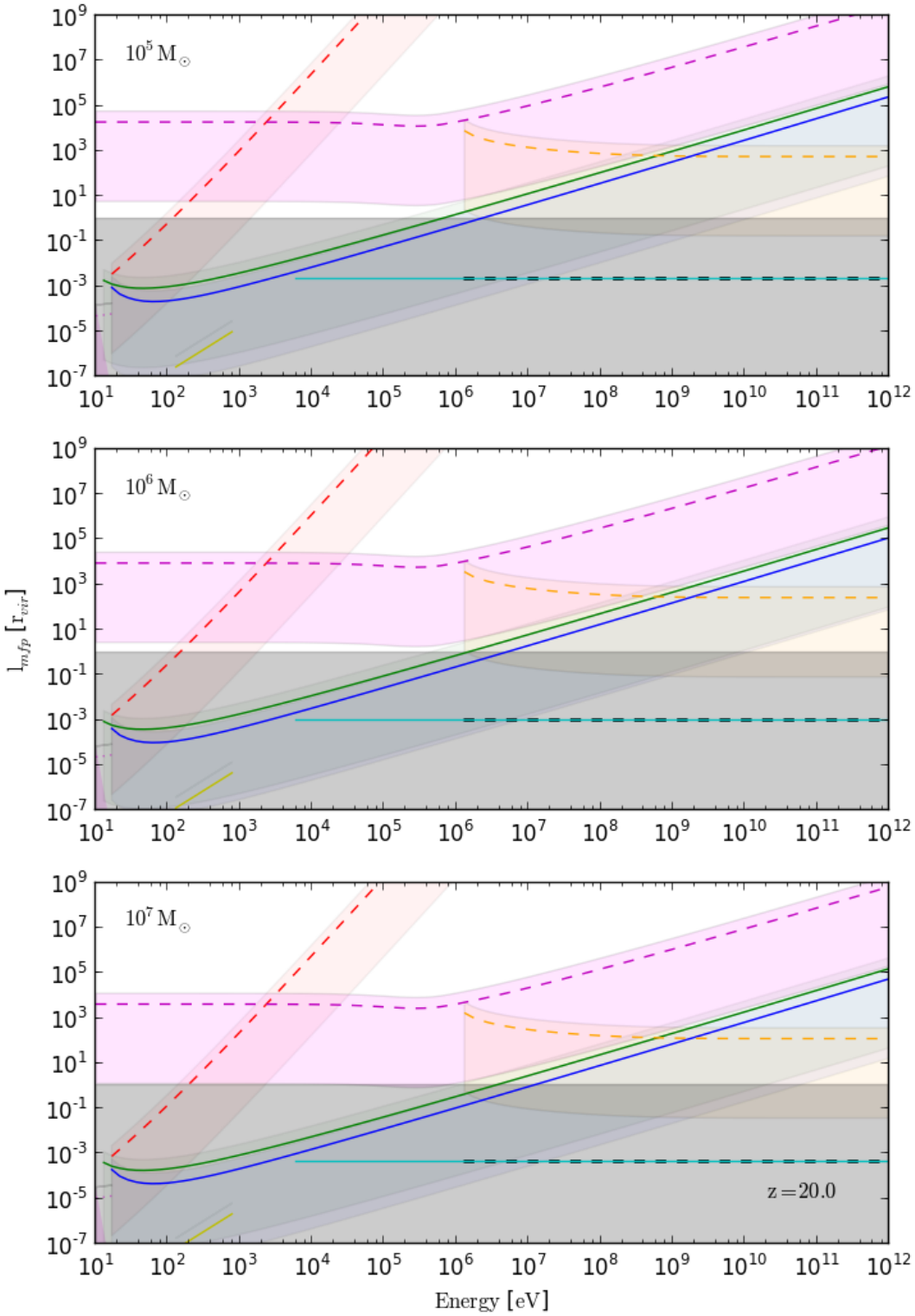

Figure 5.1: Summary of mean free paths normalised to r_{vir} of relevant atomic process within 10^5, 10^6 and $10^7 M_\odot$ halos at redshift 20. Solid lines denote electrons processes (blue - ionisation, green - excitation, yellow - coulomb scattering and cyan - inverse Compton scattering) and dashed lines denote photon processes (red- ionisation, magenta- Compton scattering, orange - pair production off the gas field and black- pair production off the CMB field). Positrons undergo the same process as electrons with the purple dotted line denoting annihilation via positronium. The grey shaded area shows the area inside of the halo.

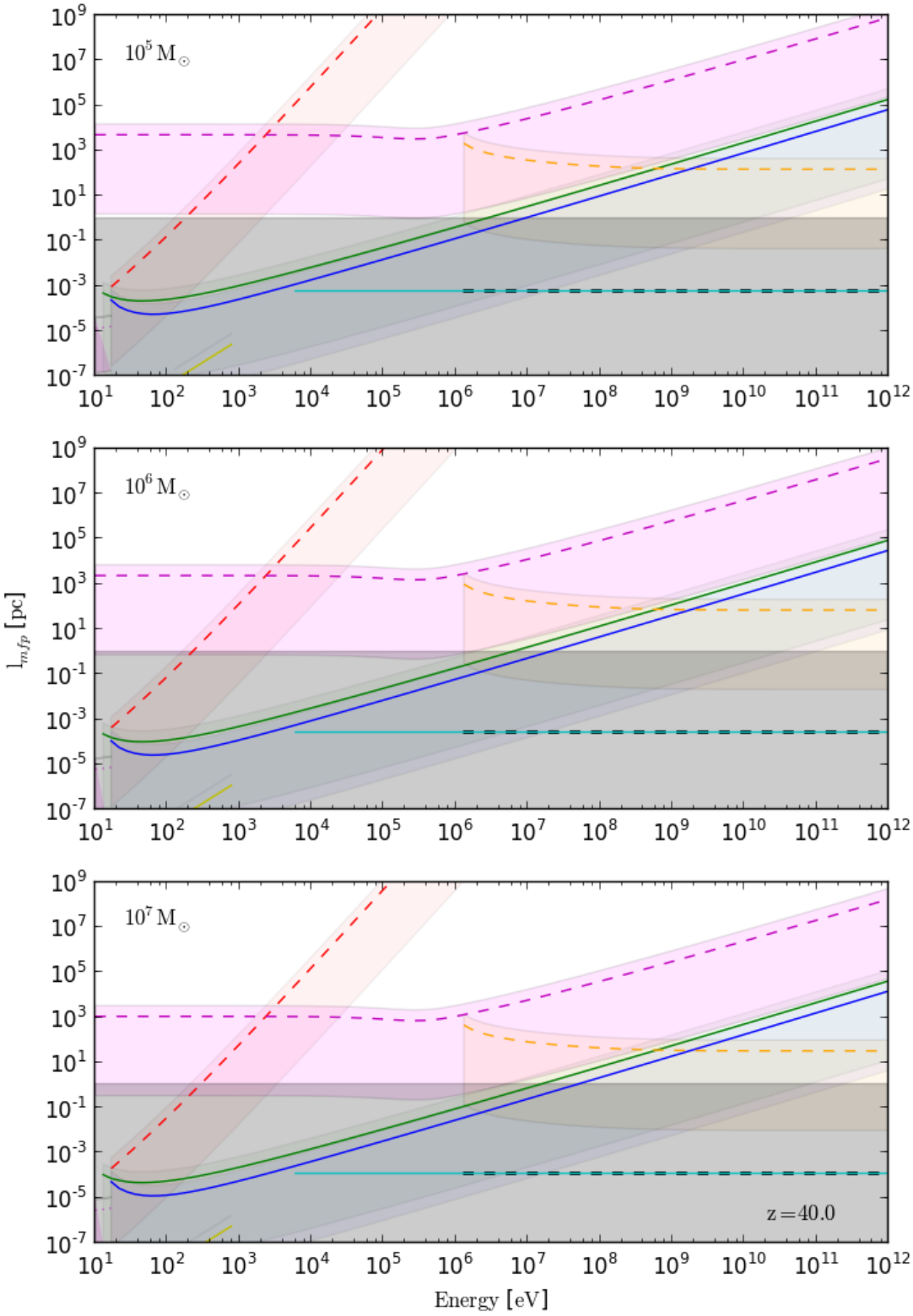

Figure 5.2: Same as previous figure but for halos at redshift 40.

The disruption of both the dark matter and gas density distributions associated with mergers could subsequently impact both the dark matter annihilation power and the absorption efficiency. In addition self-consistent modelling of the halo incorporating the potential ongoing effects due to the halo self-heating, such as expulsion of gas, is not accounted for. These concerns however are anticipated to be included in future work.

5.2 Energy Transfer

The efficiency of the energy transfer to the halo's gas is driven by the energy of the injected particle and the number density of the interaction medium. The mean free paths of the relevant particle interactions for different particle energies are shown in Figures 5.1 (for halos at redshift 20) and 5.2 (redshift 40). In all plots the grey shaded region denotes the radii up to the virial radius with dashed lines showing photon processes and solid lines lepton processes. The lines themselves show the mean free path for the relevant medium's average density within the halo, while the shading either side shows the mean free path at the virial radius r_{vir} and $r_{vir}/200$.

Inspection of Figures 5.1 and 5.2 shows that for low energy particles the dominant energy loss process is via ionisation (solid blue for electrons and positrons, dashed red for photons), excitation (solid green for electron and positrons) and annihilation (solid magenta for positrons)[1]. These processes are crucial in so far as they are the ones to actually facilitate the energy transfer to the halo. For high energy particles the dominant interactions processes are inverse Compton (cyan for electrons and positrons) and electron-positron pair creation off the gas and CMB photon fields for photons (dashed orange and black lines respectively), as well as Compton scattering (dashed magenta) for mid-range energy photons. These latter interactions don't contribute to the energy transfer directly, but create secondary, lower energy particles which (provided they don't escape the halo beforehand) eventually down-scatter sufficiently to directly interact with the gas.

In order for these processes to take place, their mean-free paths need to be smaller, or comparable to the size of the virial radius. For example the photon ionisation mean-free path grows beyond the halo's boundary for particles with energy greater than $\sim 10^3$ eV. Similarly the mean-free path for Compton scattering is generally just beyond or comparable to the virial radius, meaning that photons with energy between 10^3 eV and the threshold for pair-creation will mostly free stream out of the halo and only deposit a small fraction of their energy.

[1] Also shown in yellow is heating due to Coulomb interactions between injected and free electrons for a fully ionised halo. While this process does not contribute in the case of pristine, atomic gas, once the halo does become ionised Coulomb scattering rapidly becomes the dominant interaction for electrons. This also means that while the energy deposited due to interactions with neutral gas goes mostly into ionisation, the deposition partition becomes quickly skewed towards heating for only weakly ionised gas.

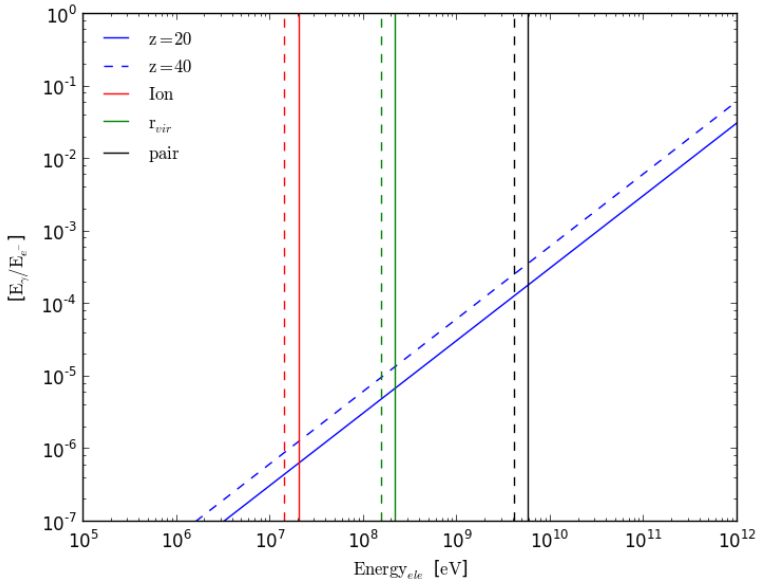

Figure 5.3: The average energy of the up-scattered CMB photon as a fraction of the original electron/positrons energy (blue). The vertical lines show thresholds at which the IC photons have enough energy to photo-ionise Hydrogen (red), the mean-free path becomes the size of the virial radius (green) and have sufficient energy to pair-created (black). In all cases solid lines show results at redshift 20 and dashed lines at redshift 40.

The initial point at which the particle is injected can also play an important role in determining whether any interaction takes place and mean-free paths can vary up to two orders of magnitude due to the high densities found at the halo's centre. On the other hand, the dense inner part of the halo subtends only a very small solid angle for any particle injected further out and thus the increased energy absorption is really only felt by particle created in or close to the centre. Overall it stands to reason that large, dense structures will be more efficient at facilitating the energy transfer process. When examining the first star-forming halos there is somewhat of a trade-off in that lower redshift structures are bigger but halos at higher redshifts denser.

5.2.1 Role of Inverse Compton Scattering

Before going on to present the outputs from the energy transfer code, it would be expedient to make a closer examination of the dominant mechanism via which the injected particles interact with their surroundings. High energy electrons and positrons[2] lose energy by up-scattering the CMB field photons via the inverse Compton process. Depending on the energy of the up-scattered photon, these will either go on to create an electron-positron pair and continue the cascade or deposit their energy into the gas

[2]Photons undergo electron/positrons pair-creation so this ultimately applies to them as well.

via either photo-ionisation or Compton scattering.

The final energy of the up-scattered photon is dependent on both the initial energy of the electron/positron and CMB photon (the final photon energy distribution is given by Equation 3.17). The nature of the electromagnetic cascade (and the associated energy transfer efficiency) will therefore vary with that initial energy. To illustrate this point the average energy of the up-scattered CMB photon is given by Blumenthal and Gould (1970) as

$$\bar{E}_{IC} = \frac{4}{3}\gamma_e^2 E_\gamma \tag{5.2}$$

and is plotted as a fraction of the original electrons's energy in Figure 5.3 (blue lines). Also shown are vertical lines indicating when the up-scattered photons have an average energy high enough to photo-ionise Hydrogen (red lines), have mean-free paths comparable to the halo's viral radius (green) and undergo electron/positron pair-production (black). In each case solid lines correspond to values at redshift 20 and dashed lines at 40.

These limits can give a useful first order indication as to how effective the energy transfer process is for the original electron/positron. For instance electrons producing IC photons with energy below the photo-ionisation limit but with energies high enough to make electro-ionisation and excitation inefficient will (unless produced in a particularly high density region) only contribute marginally to the heating of the halo. Energy transfer becomes efficacious once electrons have sufficient energy to produce photons above the ionisation limit[3]. In the case of heating a finite volume such as a halo, the overall effectiveness drops off once the mean-free path of the IC photons exceeds the virial radius and the particles escape instead. The next point of interest is the energy range in which the IC photons are energetic enough to produce electron/positron pairs themselves. At this point the overall energy loss compared to the original electron's energy also becomes significant, meaning that as the particle traverses through the halo, it will produce extensive particle cascades. The energy transfer efficiency of the cascade will in this case be dependent on the distribution of the cascade particles.

The cascades corresponding to the energy regimes described above are further illustrated in Figure 5.4, which shows snapshots of particle cascades produced by electrons with (from top to bottom) 1, 10, 100 and 1000 GeV of energy. In each case the particle was injected at a radius of $r_{vir}/100$ and allowed to travel the radial distance denoted by the thick black line. In each plot red, blue and green points denote photons, electrons and positrons respectively, while the grey vertical line shows the edge of the halo.

The top panel shows the cascade in the case of a 1 GeV electron. The IC photons

[3]The dark matter model annihilating to 130 MeV electron/positron pairs is motivated by the fact that they produce IC photons that fall into this regime.

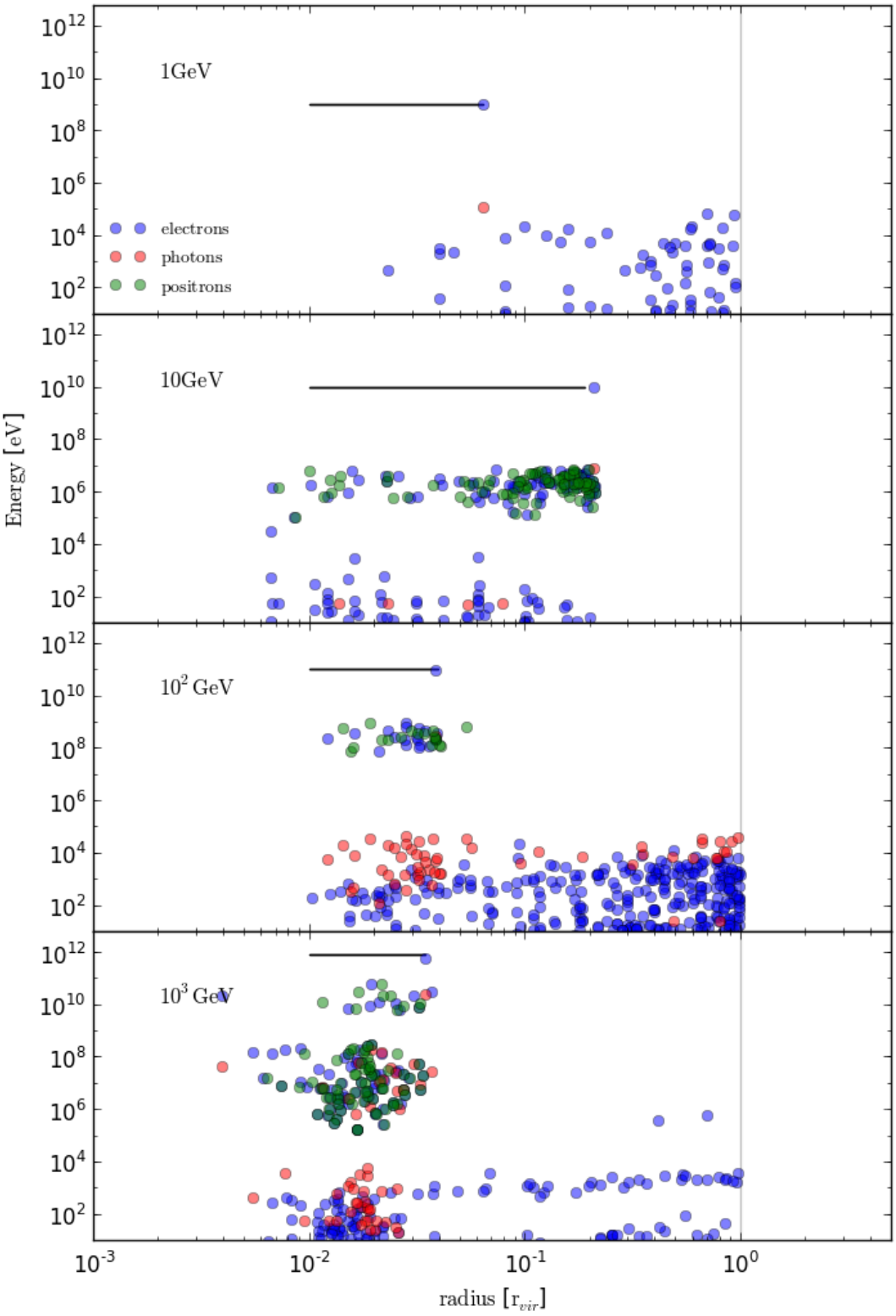

Figure 5.4: Snapshots of particle cascade induced by inverse Compton scattering for electrons injected at $r_{vir}/100$ in a $10^5 M_\odot$ halo at z = 20 with (from top to bottom) 1, 10, 100 and 1000 GeV of energy. Blue and green points denote electrons and positrons, while red denotes photons. The black horizontal line shows the radial path the original particle has traveled and the grey vertical the edge of the halo.

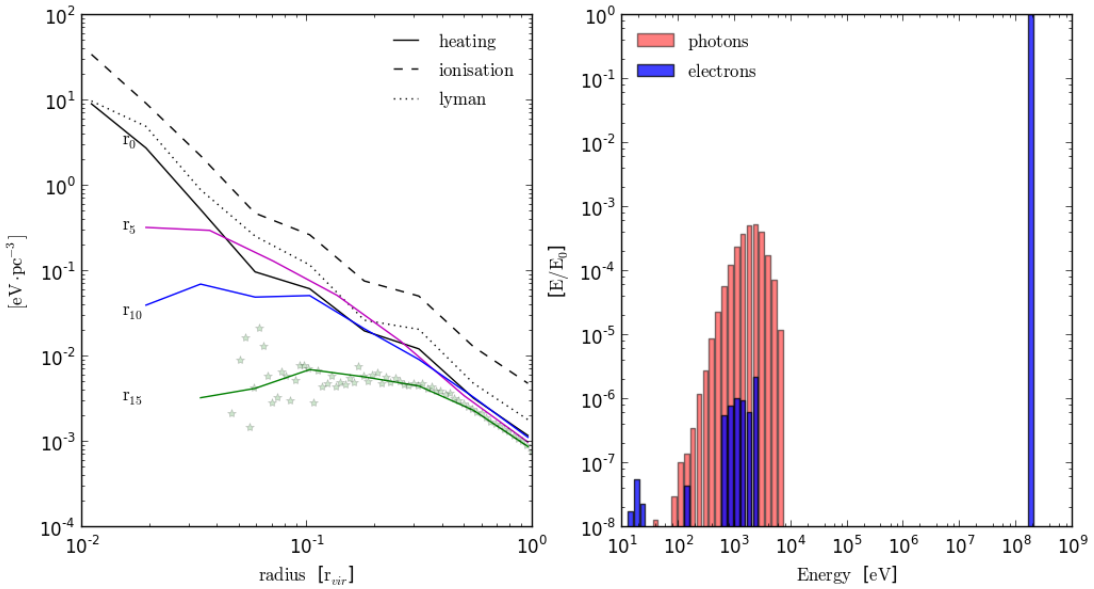

Figure 5.5: Energy transfer code outputs for 130 eV electrons injected at various radii. The left plot shows the smoothed, radial energy deposition curves for electrons injected into a $10^5 M_\odot$ Halo at redshift 20, where solid lines denote heating. For the r_0 case, ionisation (dashed) and lyman photons (dotted) are also shown, while for the green r_{15} curve, the stars show the raw-data. The plot on the right shows the energy distribution of the cascade-particles that escape the halo as a fraction of the original particle energy. Red columns show photons, while blue show electrons.

ionise the gas and produce secondary low energy electrons. However since the mean-free path of the photons is at this point larger than the virial radius, most of the electrons are created and deposit their energy in the outer parts of the halo. In the second panel the 10 GeV electron produces a steady trail of electron/positrons via its IC photons. In contrast to the plot above, the IC photons of the secondary leptons have large enough ionisation cross-sections to allow them to interact with the gas in situ. The third panel is similar to the second insofar as both display a secondary distribution of electron/positron pairs. However, as the energy of the original electron increase so does the energy range of the cascade particles, including the final distribution of IC photons. Finally the bottom plot shows 100 GeV electron where the secondary population of electrons/positrons produces a tertiary set of particles which only then produce the IC photons that ultimately deposit energy to the halo.

5.3 Code Output

To account for the wide range of potential particle interactions as well as to capture the full evolution of potentially complex particle cascades, the energy transfer code introduced in Chapter 3 is now employed. In order to determine the total energy transfer for each dark matter model, the deposition fractions for each particle species

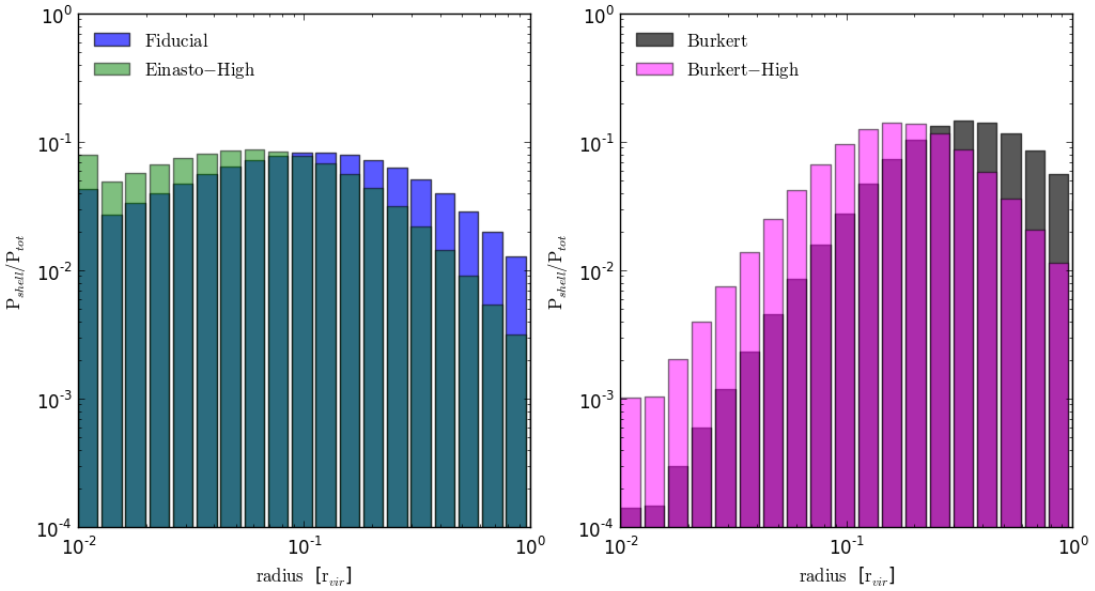

Figure 5.6: The fraction of the total annihilation power of different radial shells for different halo models. The left shows an Einasto profile with the Correa and High mass-concentrations in blue and green respectively, while the right shows a Burkert profile for the same mass-concentration relations in black and purple. All models are shown for a $10^5 M_\odot$ halo at redshift 20.

α, with energy E_j injected at radius r_i are first calculated,

$$\begin{matrix} \mathbf{h}^\alpha_{ijk}, & \mathbf{x}^\alpha_{ijk}, & \mathbf{l}^\alpha_{ijk} \\ \mathbf{e}^\alpha_{ijk}, & \mathbf{f}^\alpha_{ijk}, & \mathbf{p}^\alpha_{ijk} \end{matrix} \tag{5.3}$$

Here $\mathbf{h}$, $\mathbf{x}$ and $\mathbf{l}$ denote the fraction deposited as heating, ionisation and lyman photons at each radius r_k, and $\mathbf{E}$, $\mathbf{F}$ and $\mathbf{P}$ the energy distribution of escaped electrons, photons and positrons in energy bin E_k. These act as a kind of pseudo basis which are then weighted by the appropriate halo and dark matter models.

Figure 5.5 shows the output for a $10^5 M_\odot$ halo at redshift 20. The left shows the smoothed, heating curves (in units of $\mathrm{eV/pc^3}$) for a 130 MeV electron injected at different radii (see different coloured solid curves). For the black r_0 curve, the ionisation (dashed) and Lyman photon fractions (dotted) are also shown, as is the unsmoothed data for the green r_{15} curve. The plot on the right shows the distribution of the escaped particles for the r_{15} curve, where red shows photons and blue electrons.

The total, halo-summed energy deposition[4] for a particle α with energy E_j is then given by,

$$\mathbf{H}^\alpha_{jk} = \sum_i w_i \mathbf{h}^\alpha_{ijk}, \quad \chi^\alpha_{jk} = \sum_i w_i \mathbf{x}^\alpha_{ijk}, \quad \mathbf{L}^\alpha_{jk} = \sum_i w_i \mathbf{l}^\alpha_{ijk}, \tag{5.4}$$

[4]The summed escaped particle spectra will be revisited in greater detail in the next chapter.

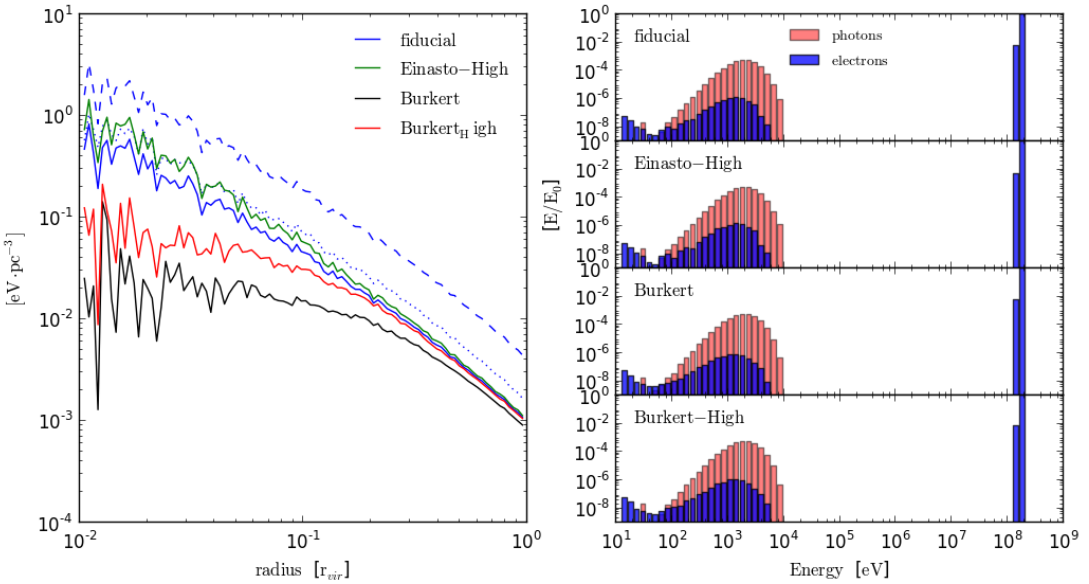

Figure 5.7: The energy deposited at different radii for different halo models for a 130 MeV dark matter particle is shown on the left, while the escaped spectra are shown on the right. The colour/line types are the same as in previous plots.

where w_i is the fraction of the total dark matter annihilation power produced within the shell at radius r_i. The coefficients w_i will naturally vary deepening on the halo model and are shown in Figure 5.6. The four different models compared here are the cuspy Einasto profile on the left and the flat-core Burkert profile on the right. For the Einasto profile the blue bars show the fiducial model (using the mass concentration from Correa et. al.) while the green is the high mass-concentration model. The same applies on the Burkert side with black and purple being the respective colours.

As expected, the majority of the annihilation power is produced in the inner parts of the halo for the Einasto profiles, while in the case of the Burkert model the outer parts of the halo dominate. In both cases having a high mass-concentration parameter shifts the contribution from the different shells towards the centre of the halo. This is significant because as was shown in Figure 5.5 particles injected at different radii will produce different deposition curves, so that different underlying dark matter models will not only change the total annihilation power but also how the deposited energy is distributed throughout the halo.

In Figure 5.7 the weighted total, un-smoothed deposition curves are shown for the same halo and particle type as in Figure 5.5 for the different dark matter halo models. On the left $\mathbf{H}^{\alpha}_{jk}$ is shown for the fiducial (blue), Einasto-High (green), Burkert (black) and Burkert-High (red) models, with the fiducial model also including curves for heating (dashed) and Lyman photons (dotted). The difference between the models is particu-

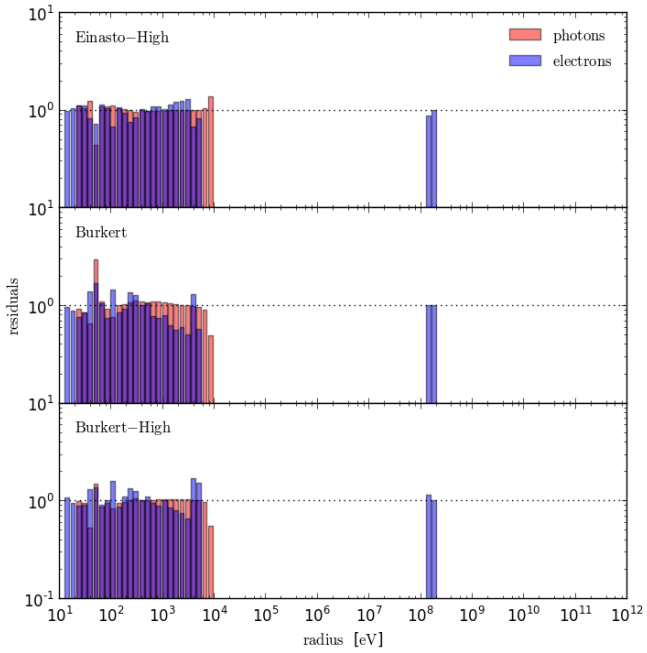

Figure 5.8: Comparison of the escaped particle spectra for different halo models. From top to bottom, panel show the ratio between the Einasto-High, Burkert and Burkert-High compared to the fiducial halo model.

larly striking in the inner parts of the halo, while the curves converge in the outer parts. A more concentrated dark matter, cusp-like halo model will in general be more efficient at transferring energy to the core of the halo. This is primarily because they produce most of their annihilation power near the centre of the halo, but also because in most case only particles injected into the inner shells will be able to deposit energy there. In contrast the energy transferred to the outer shells is nigh identical regardless of where the particle was originally injected, therefore the models converge in those parts of the halo.

The plot on the right of Figure 5.7 shows the escaped spectra for the different halo models (from top to bottom: fiducial, Einasto-High, Burkert and Bukert-High). These are qualitatively very similar in so far as they all show the original electron emerging from the halo only having lost a small fraction of its energy, as well as a distribution of IC photons along with the associated electrons from photo-ionisation. To highlight the differences the ratios between the fiducial and remaining models (from top to bottom, Einasto-High, Burkert and Burkert-High) are shown in Figure 5.8. The main difference can be observed in the Burkert ratios where there is a deficit in the high end electron distribution. This arises because the IC photons with energy above 10^3 only have a mean-free path comparable to the halo radius when injected close to the centre of the halo, otherwise they will free stream. The Einasto type profiles produce more of their

annihilation power in the inner regions and therefore are able to produce more high energy electrons than the Burkert models.

Summary of Code-Outputs for the Fiducial Halo Model

Below the code-outputs for 10^6, 10^8 and 10^{10} eV particles are summarised for the fiducial halo model. Figures 5.9 and 5.10 shows the output for 10^6 eV particles at redshift 20 and 40 respectively. In each figure the rows from top to bottom correspond to 10^5, 10^6 and $10^7 M_\odot$ halos. From left to right columns show electrons, photons and positrons. Each column shows on the left the radial energy deposition fractions (heating-blue, ionisation-green and Lyman photons-red) while the plot on the right shows the distribution of the escaped particles. Just as with the plots above, red columns show photons and blue and green show electron and positrons. The radial deposition curves and escaped spectra were calculated as in the example above.

The outputs for the 10^5, 10^7, 10^9 and 10^{11} eV particles can be found in section C1 of the Appendix. In order to fully resolve the annihilation spectra of the various dark matter models, 10 energy bins between those plotted outputs were also calculated but are not shown here for sake of brevity.

5.3.1 Heating and Ionisation

The code outputs can now be used to calculate the radially dependent heating $\mathfrak{H}$, ionisation $\mathfrak{I}$ and lyman photon $\mathfrak{L}$ production for different dark matter models,

$$\begin{aligned} \mathfrak{H}_k &= \sum_\alpha f_{j\alpha} \sum_j \mathbf{H}^\alpha_{jk} \\ \mathfrak{X}_k &= \sum_\alpha f_{j\alpha} \sum_j \chi^\alpha_{jk} \\ \mathfrak{L}_k &= \sum_\alpha f_{j\alpha} \sum_j \mathbf{L}^\alpha_{jk}, \end{aligned} \tag{5.5}$$

where $f_{j\alpha}$ is the fraction of the annihilation spectrum carried by particle α with energy E_j as shown in Figure 2.4.

Heating and Ionisation for different dark matter and halo models

The heating curves for the different dark matter models are shown in Figures 5.15 - 5.17 where each plot shows a different dark matter halo (5.15 - fiducial $10^5 M_\odot$ at z=20, 5.16 - fiducial $10^6 M_\odot$ at z=20 and 5.17 - Burkert $10^5 M_\odot$ at z=20). Each panel shows a different annihilation channel where top left is via muon, top right quarks, middle left tau, middle right W boson and bottom shows the electron/positrons pairs. Different coloured curves correspond to different dark matter masses while for the lightest candidate the energy partition into ionisation and Lyman photons are also shown (dashed and dotted lines.) In all cases the plots show the total energy transferred over the Hubble time in units of

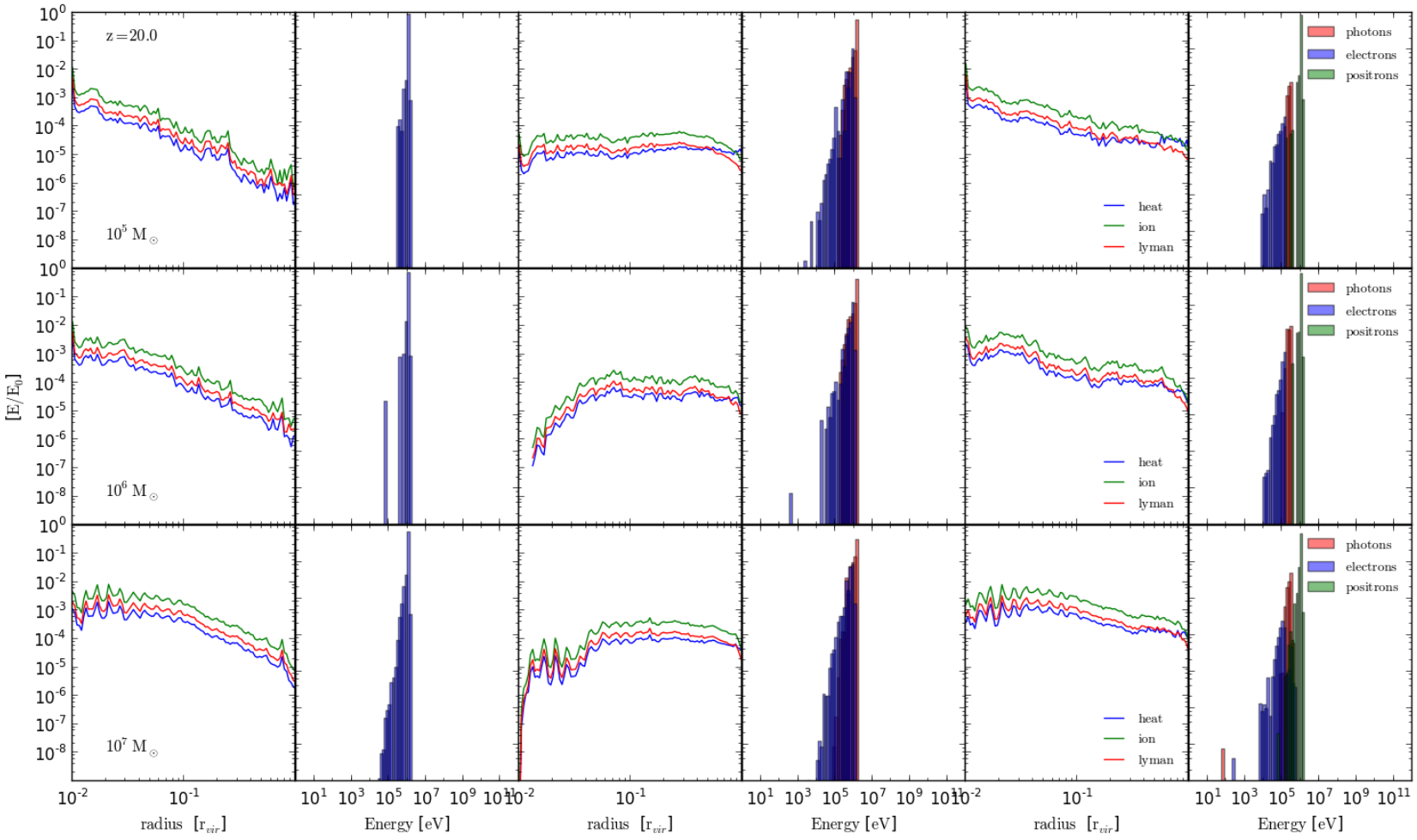

Figure 5.9: Energy transfer code output summary for 10^5, 10^6 and 10^7 $M_\odot$ (top, middle and bottom rows) halos at redshift 20. The columns from left to right show the outputs for electrons, photons and positrons. In each column the left plots shows the energy deposition fractions and the right plots the escaped particle energy distribution. For the deposition plots, curves show heating (blue), ionisation (green) and lyman photons (red), while the columns correspond to electrons (blue), positrons (green) and photons (red)/

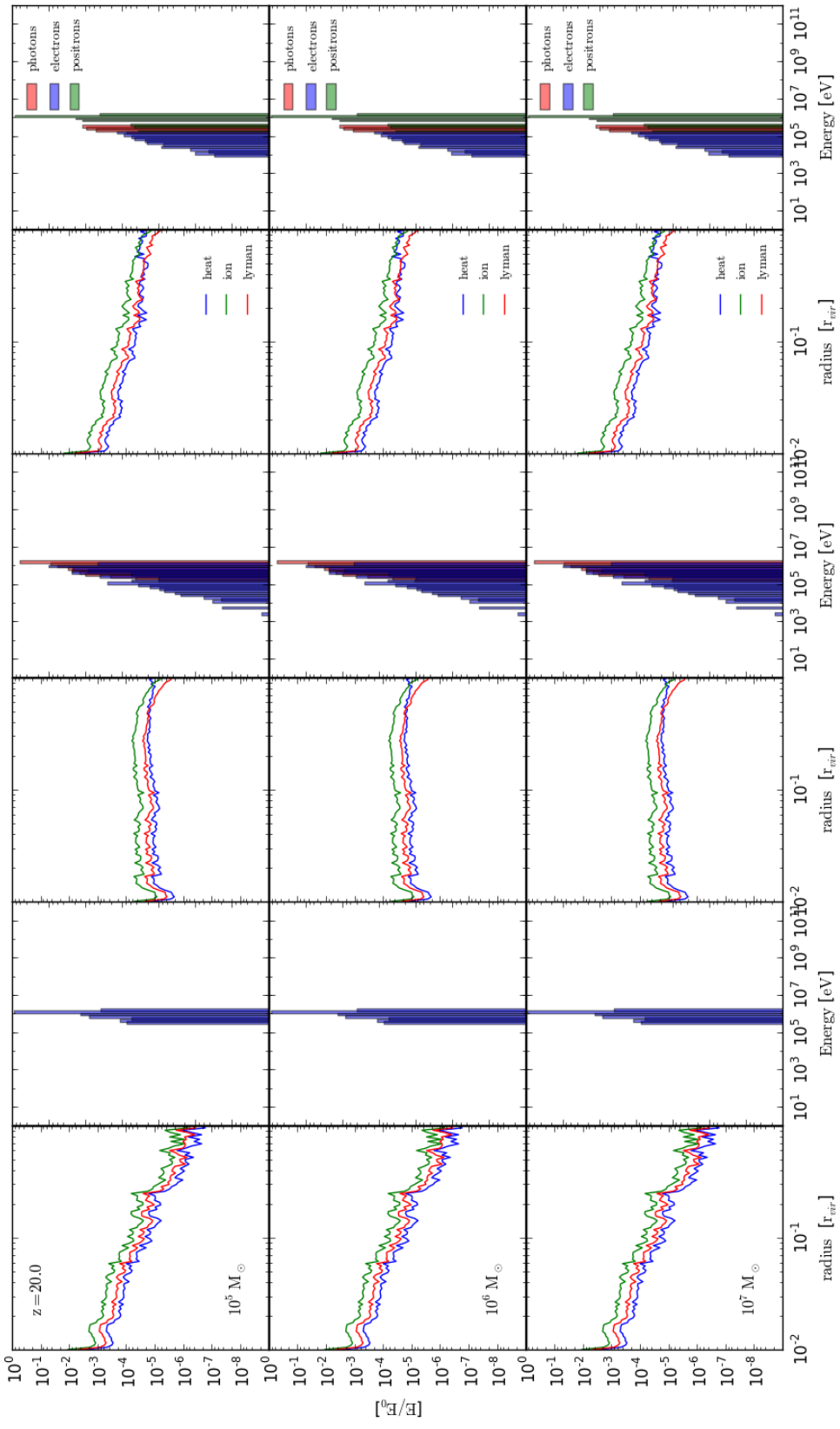

Figure 5.10: Code output for a 10^6 eV particle injected into 10^5 – $10^7 M_\odot$ halos at redshift 40.

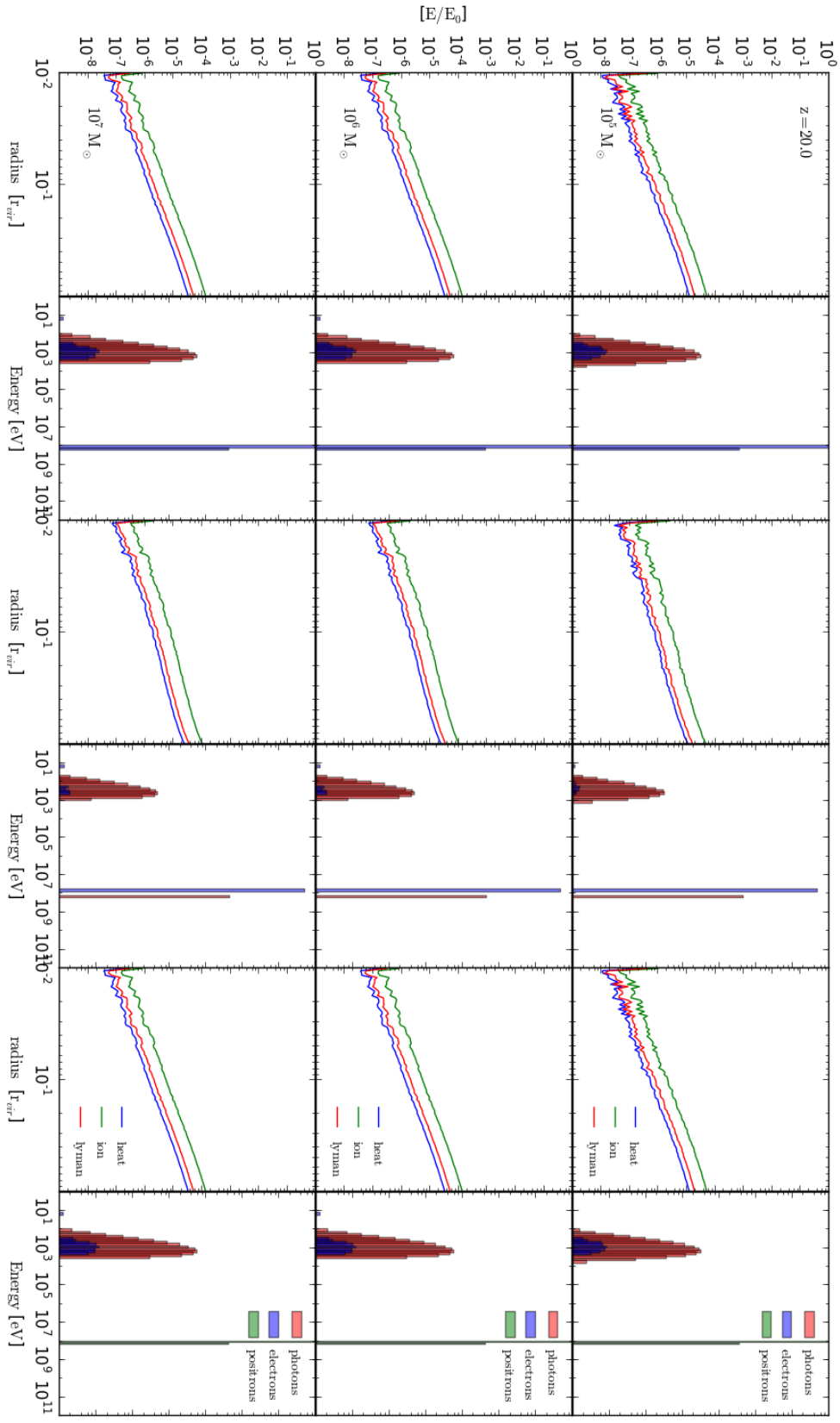

Figure 5.11: Code output for a 10^8 eV particle injected into 10^5 – $10^7 M_\odot$ halos at redshift 20

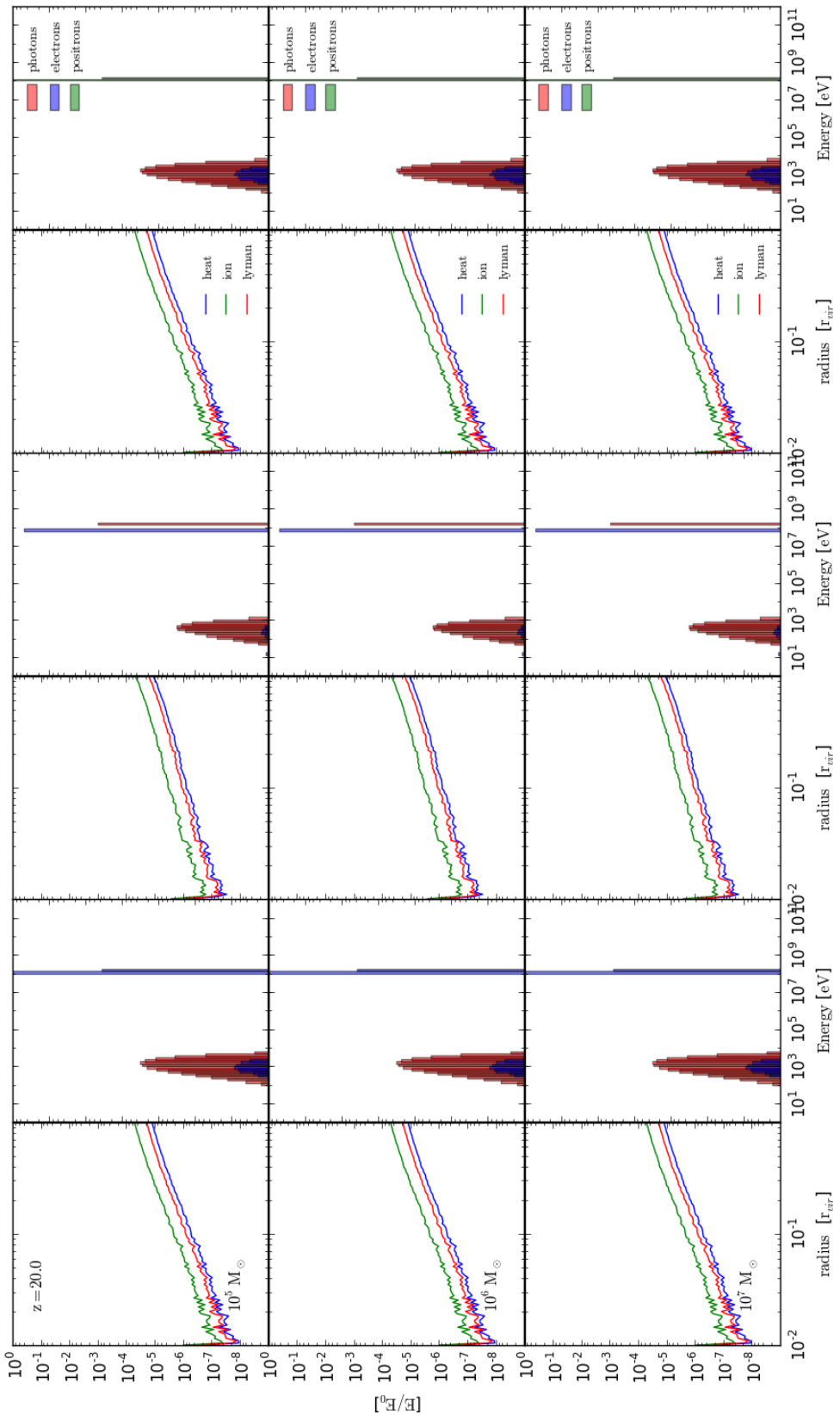

Figure 5.12: Code output for a 10^8 eV particle injected into 10^5 – $10^7 M_\odot$ halos at redshift 40.

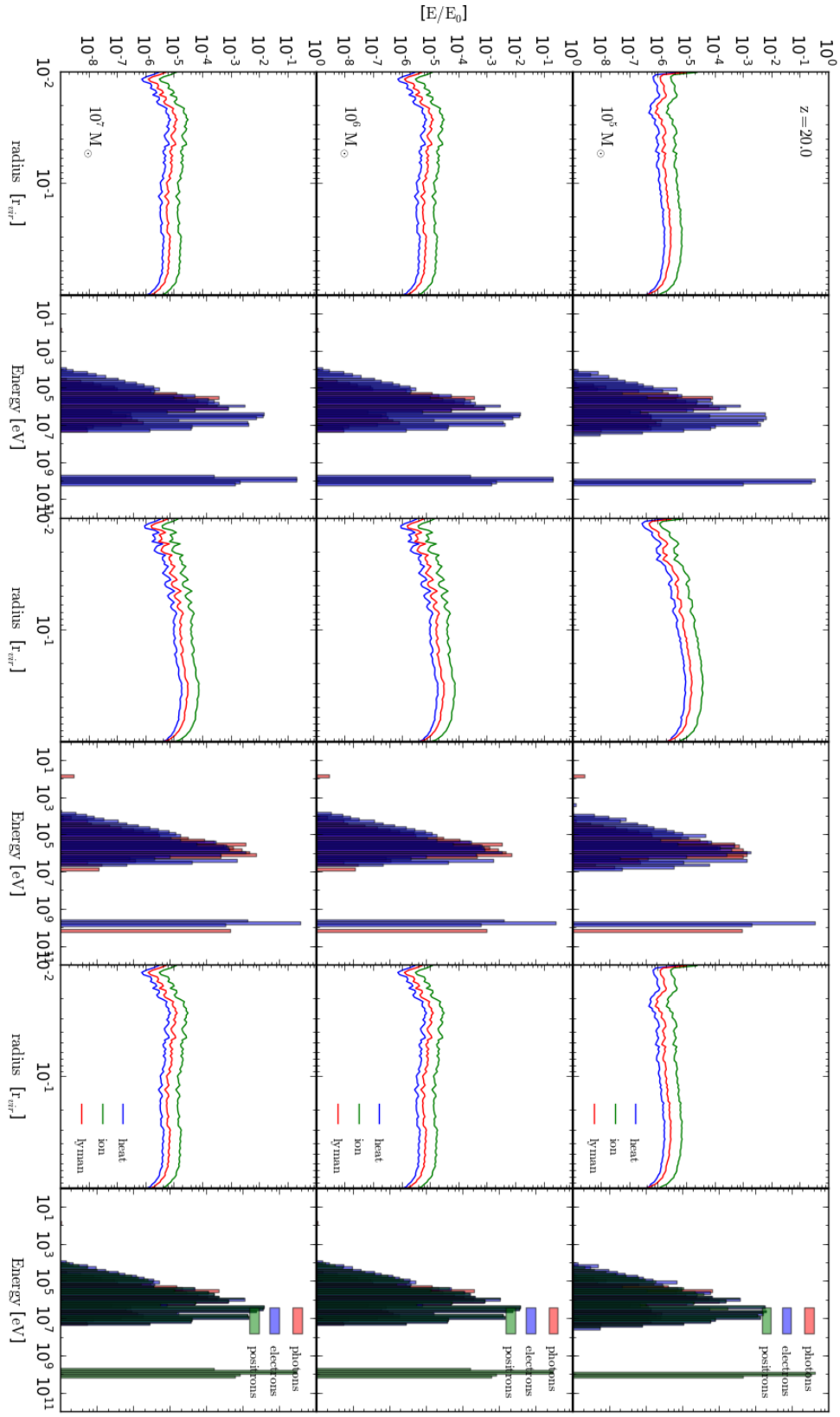

Figure 5.13: Code output for a 10^{10} eV particle injected into 10^5 – $10^7 M_\odot$ halos at redshift 20

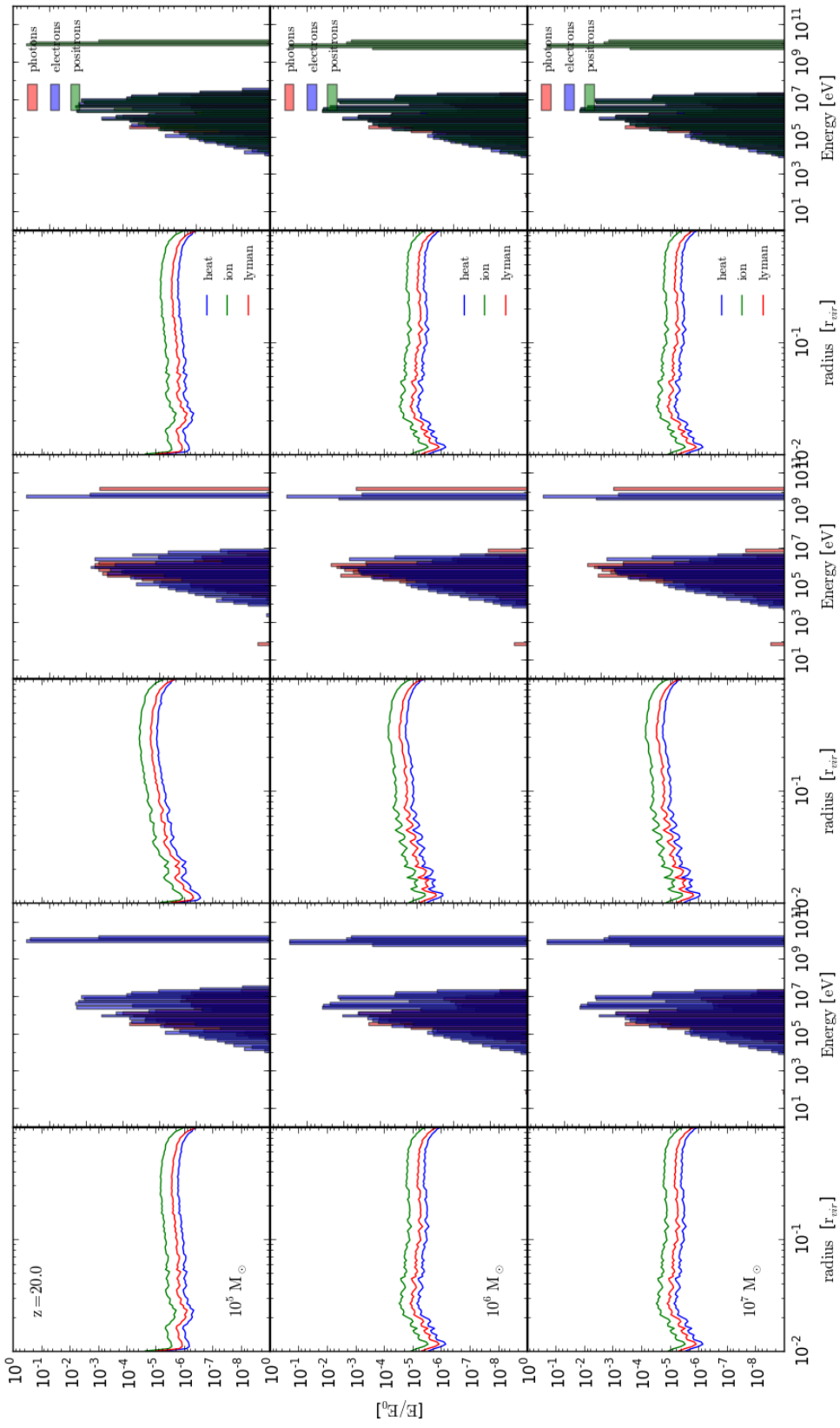

Figure 5.14: Code output for a 10^{10} eV particle injected into 10^5 – $10^7 M_\odot$ halos at redshift 40

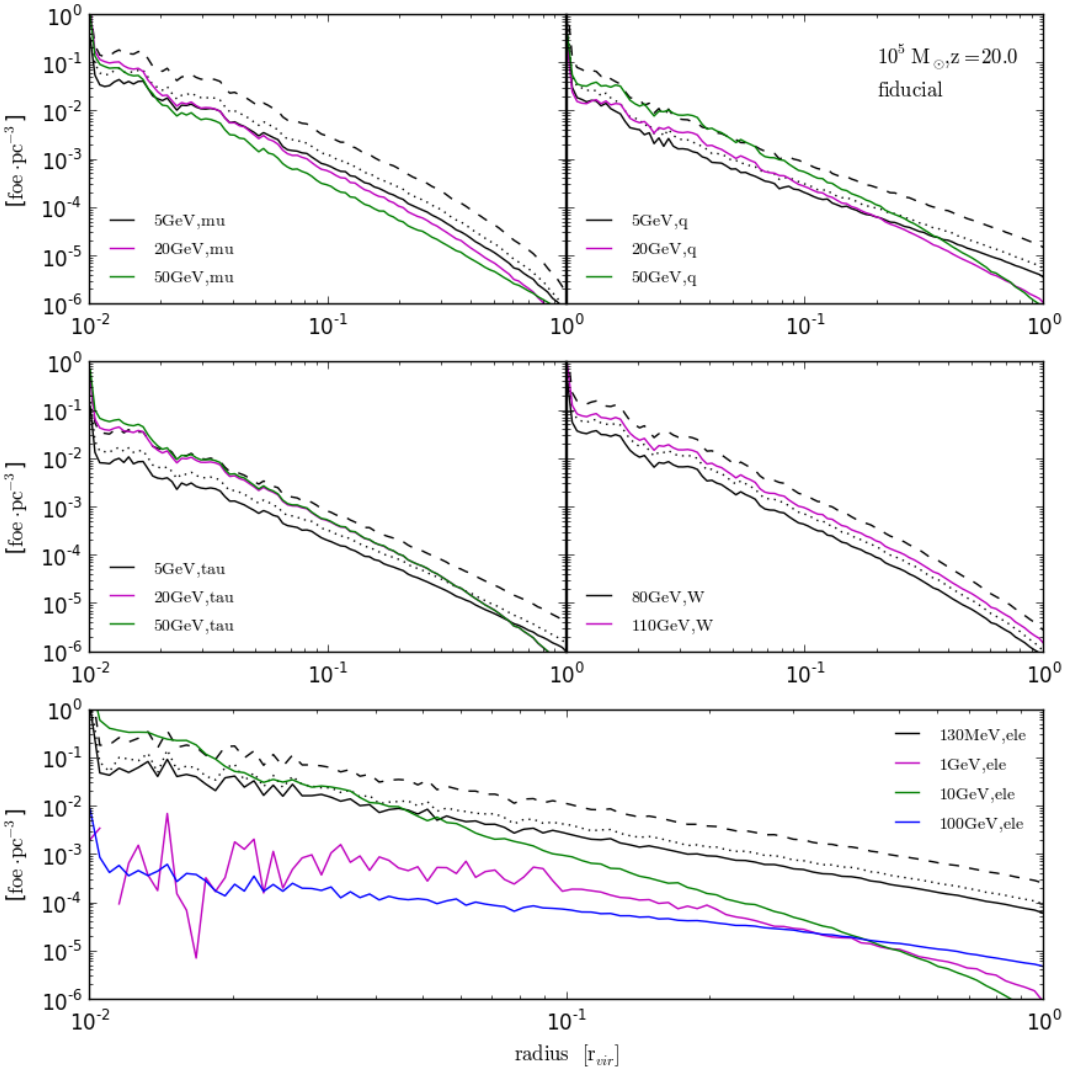

Figure 5.15: Heating, ionisation and Lyman photon production for a fiducial $10^5 M_\odot$ halo at redshift 20 for different dark matter models. Top left shows models annihilating via muons, top right quarks, middle left tau, middle right W boson and bottom via electrons/positrons. Different colours correspond to different dark matter masses and solid lines show energy into heating (for the lightest model in each panel the dashed lines show ionisation and the dotted lines Lyman photon production.)

$\text{foe} \cdot \text{pc}^{-3}$ ($10^{51}\text{erg} \cdot \text{pc}^{-3}$).

In each case the annihilation cross-section is chosen so that the total annihilation power of the halo is the same as for the 130 MeV, $10^{-28}\text{cm}^{-3}\text{s}^{-1}$ case (Where results can be scaled to correspond to different velocity averaged cross-sections.) Comparing the results for different annihilation models in 5.15 shows that both the mass and annihilation channel can make close to an order of magnitude difference in the final energy transfer.

This is particularly evident in the electron/positron model, where the 1 and 100 GeV models are far less efficient at heating the halo than the 130 MeV model, especially near the centre of the halo. Recalling the discussion of IC scattering, the 1 GeV model up-scatters IC photons that readily free stream while the 100 GeV produces electron and positrons via pair-creation for which IC scattering yields IC photons below the Hydrogen ionisation limit which ultimately results in less effective energy transfer. In contrast the 130 MeV is chosen especially to produce IC photons that will readily ionise the surrounding gas, both at the edge and centre of the halo. The 10 GeV model is somewhat of an intermediary case insofar as the IC cascade culminates in electrons and positrons that will readily heat the dense gas at the core of the halo but will tend to the escape the halo when produced close to the edge of the halo.

Figures 5.16 and 5.17 show the same plot with the former showing a $10^6\text{M}_\odot$ halo with a fiducial model profile at redshift 20 whilst the latter is for a $10^5\text{M}_\odot$ Burkert profile at redshift 20. The results for the 10^5 and $10^6\text{M}_\odot$ halo are qualitatively similar, with the larger halo exhibiting a higher heating rate. In contrast the Burkert profile model has a lesser energy transfer rate than then Einasto profile halo. In keeping with the behaviour of cored profiles described earlier, there is also reduced heating of the centre of the halo.

5.3.2 Comparison with Gravitational Binding Energy

The above results allows for the comparison of the halo's gravitational binding energy and the dark matter energy input to be revisited. However unlike the previous chapter the comparison will be made for individual shells rather than the total halo. The energy produced due to dark matter annihilation over the Hubble time t_H, in the spherical shell between r_k and r_{k+1} is

$$U_{dm,shell}(r_k) = \int P_{dm}(r_k)\mathrm{d}S \cdot t_H. \tag{5.6}$$

The gravitational binding energy is given by,

$$U_{G,shell}(r_k) = \frac{GM_{shell}(r_k)M(<r)}{r_k} \tag{5.7}$$

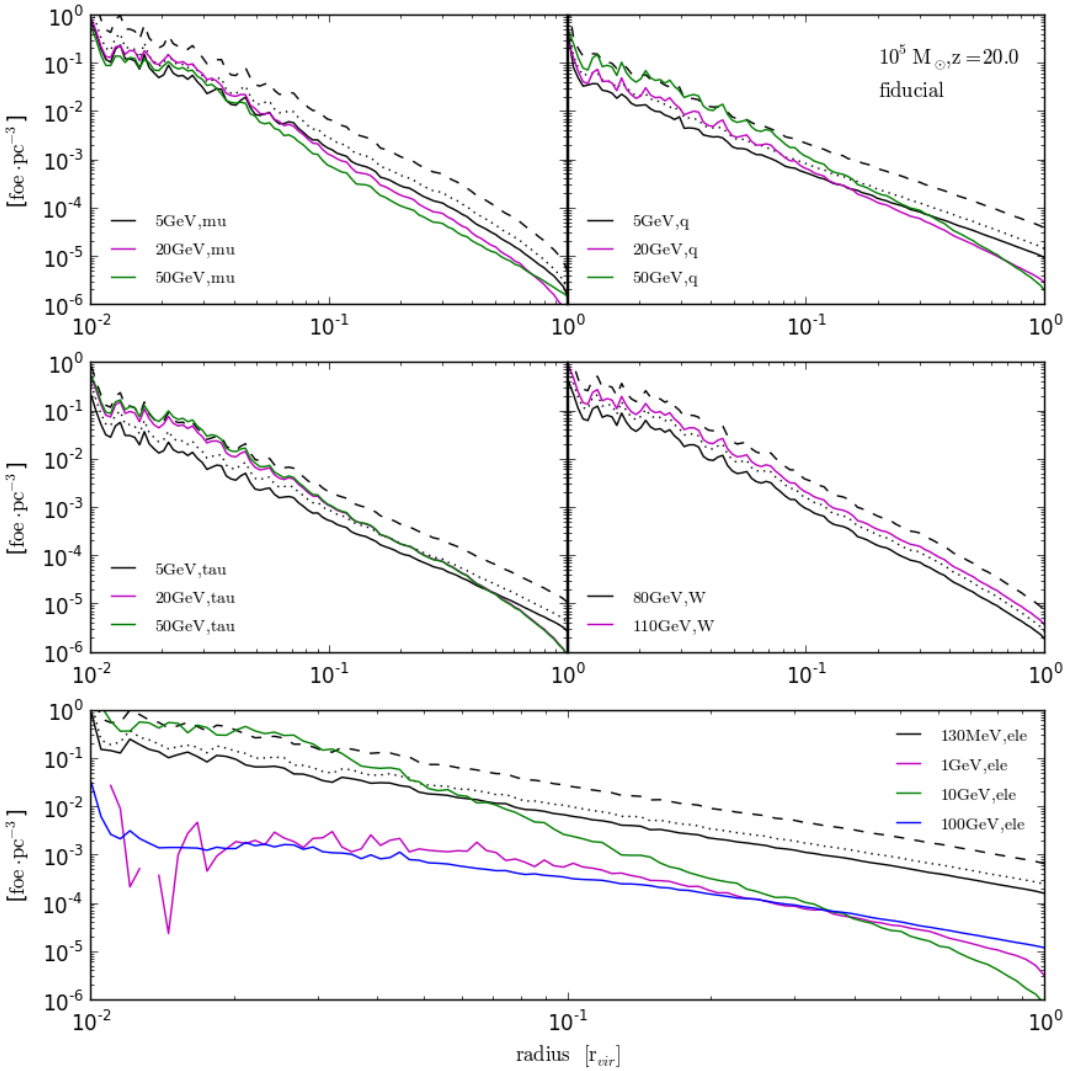

Figure 5.16: Heating, ionisation and Lyman photon production for a Burkert $10^6 M_\odot$ halo at redshift 20 for different dark matter models. Top left shows models annihilating via muons, top right quarks, middle left tau, middle right W boson and bottom via electrons/positrons. Different colours correspond to different dark matter masses and solid lines show energy into heating (for the lightest model in each panel the dashed lines show ionisation and the dotted lines Lyman photon production.)

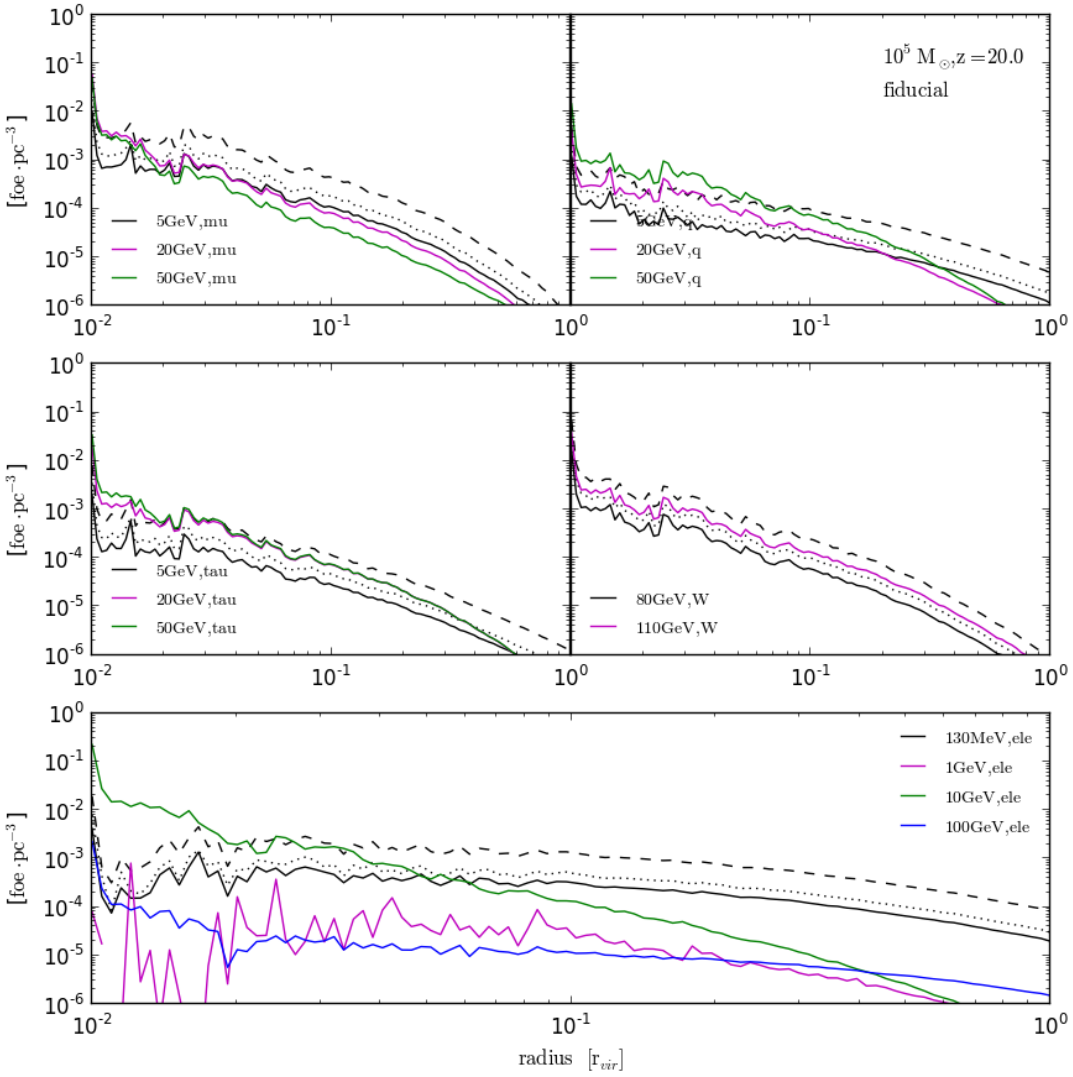

Figure 5.17: Heating, ionisation and Lyman photon production for a Burkert $10^5 M_\odot$ halo at redshift 20 for different dark matter models. Top left shows models annihilating via muons, top right quarks, middle left tau, middle right W boson and bottom via electrons/positrons. Different colours correspond to different dark matter masses and solid lines show energy into heating (for the lightest model in each panel the dashed lines show ionisation and the dotted lines Lyman photon production.)

so that the ratio of the energy going into heating and the gravitational binding energy is

$$R_{shell}(r_k) = \frac{U_{dm,shell}(r_k)}{U_{G,shell}(r_k)} \cdot \mathfrak{H}_k \tag{5.8}$$

where $\mathfrak{H}$ is the heating term previously calculated.

Binding Energy comparison for different $10^5 M_\odot$ and $10^6 M_\odot$ Halo Models

Figure 5.18 shows the ratio of the gravitational binding energy and the energy partitioned into heating over the Hubble time from dark matter annihilation for different halo models. In each plot, the black, magenta, green and blue lines correspond to the fiducial, Einasto-High, Burkert and Burkert-High halo models respectively. Each plot also corresponds to a different dark matter annihilation model, where the column on the left shows annihilation via muon while the column on the right, via electron/positrons. The different rows show different dark matter candidate masses, in the case of the muon channel 5, 20 and 50 GeV and for the electron 130 MeV and 10 and 100 GeV. Also for reference are the grey, dashed lines, which show R_k for the other two fiducial mass models in that column. Figure 5.19 shows the same but for a $10^6 M_\odot$ halo, also at redshift 20.

Examining the plots a number of inferences regarding the potential impact dark annihilation has on the halo can be made. The dark matter halo model first of all sets the total annihilation power, where in general the models with their mass in a more concentrated configuration will produce more energy. For instance in the middle row, the fiducial models behaviour is well replicated by doubling the mass-concentration parameter of the Burkert model with the exception of very close to the centre of the halo where they begin to diverge. In a similar vein, high redshift objects tend to be more efficient at transferring energy courtesy of their increased overall density.

When comparing the energy deposited over the Hubble time to the gravitational binding energy, the ratio favours heating in the shells close to the centre of the halo. In the case of the fiducial $10^5 M_\odot$ halo in Figure 5.18, both the muon and electron annihilation channel models have mass ranges in which the heating due to dark matter annihilation matches, or is in order of magnitude of the binding energy. A notable exception is the 130 MeV electron/positrons model which also effectively heats the outskirts of the halo.

When comparing the 10^5 and $10^6 M_\odot$ halos it becomes apparent that smaller structures are impacted more significantly by dark matter annihilation. This is because while more energy is both produced and deposited inside the halo, in large halos, this is off-set by the greater mass of the structure. As a whole this matches the findings of the work in Chapter 4, albeit with a more realistic estimate of the deposition fractions. Having an additional, not insignificant heating source during the early stages of these

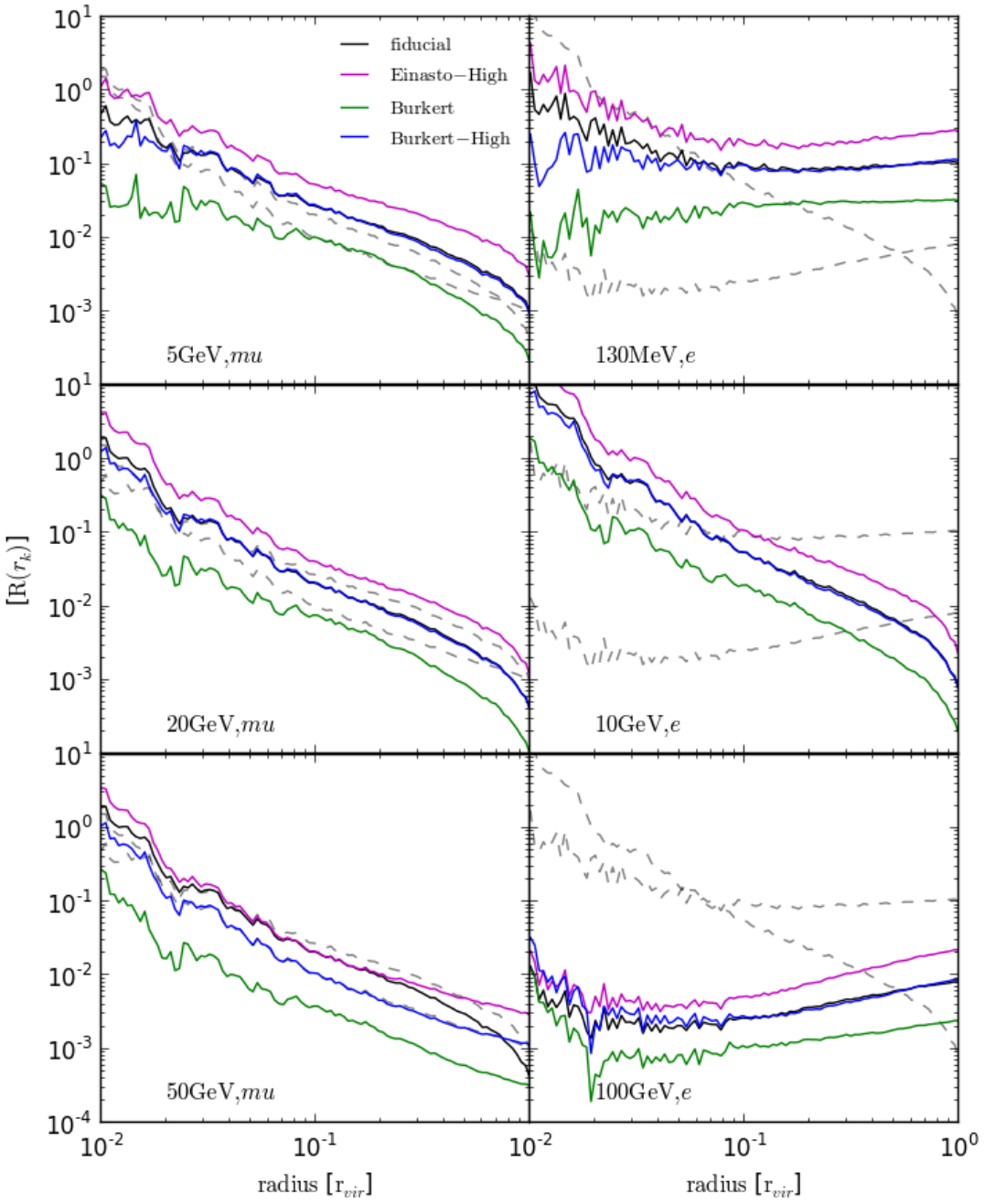

Figure 5.18: Ratio of heating from dark matter annihilation to the gravitational binding energy for a $10^5 M_\odot$ halo at redshift 20 for different dark matter models.

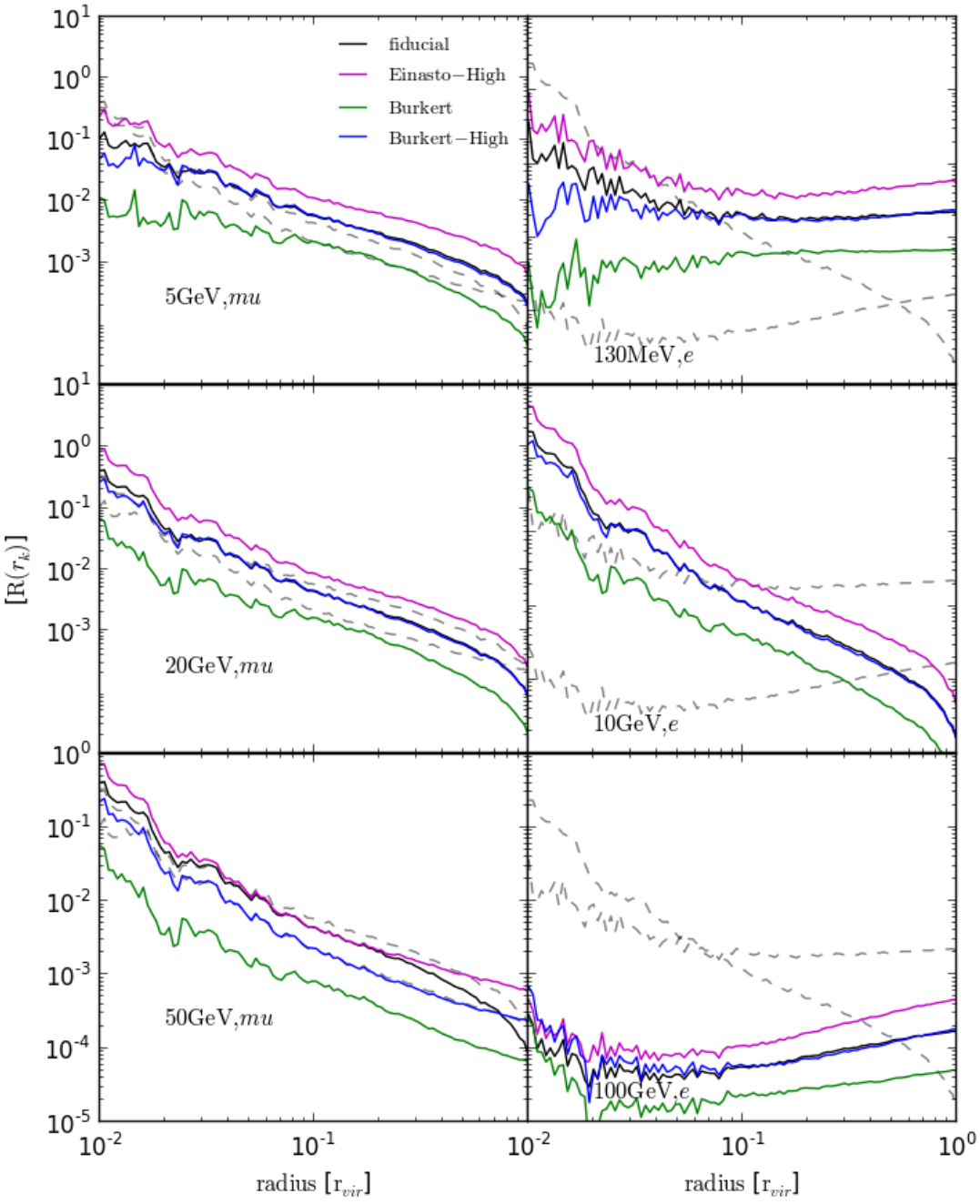

Figure 5.19: Ratio of heating from dark matter annihilation to the gravitational binding energy for a $10^6 M_\odot$ halo at redshift 40 for different dark matter models..

micro-halos' development could result in gas being expelled, or alternatively heated to a degree that prevents/delays star formation. A dynamic model would be required to ascertain how meaningful the heating from dark matter turns out to be. While this is beyond the scope of this work, the heating curves calculated here would be a useful first step towards fully quantifying the impact dark matter annihilation has on early star formation.

Lastly Figure 5.20 compares how, for the same mass, models with different annihilation channels heat the halo. The plots on the left are for halos at redshift 20 and the plots of the right at redshift 40. Plot a) shows a $10^5 M_\odot$ halo and plot b) a $10^7 M_\odot$ halo. In each subfigure, from top to bottom the plots show dark matter annihilated via muons (black), quarks (green) and tau particles (blue). There is more variation in the behaviour for lower mass models than higher as the variance in energy transfer efficiency of the IC scattering process is more marked at lower energies[5]

While it was here shown that energy comparable to that of the binding energy is deposited inside the halo over the Hubble time, most of the injected energy will escape the halo. In the next chapter the results from this calculation are used to determine the changes to the particle distribution of the original annihilation spectrum as a consequence of traversing the halo. These new spectra are then injected into the circumgalactic medium to establish whether there is sufficient heating to curtail the infall of gas onto the halo, and therefore structure formation.

[5]The periodicity in the data close to the halos' centre is due to the choice in injection radius compared to the energy deposition bin spacing.

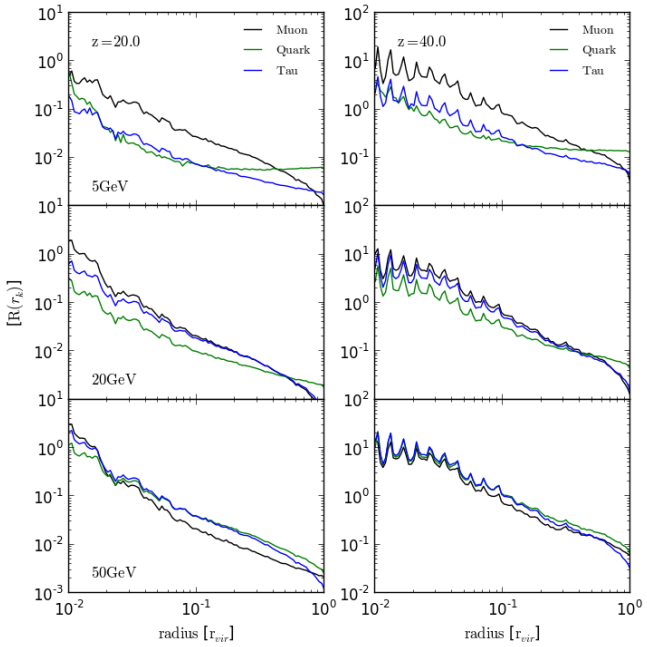

(a) z = $10^5 M_\odot$

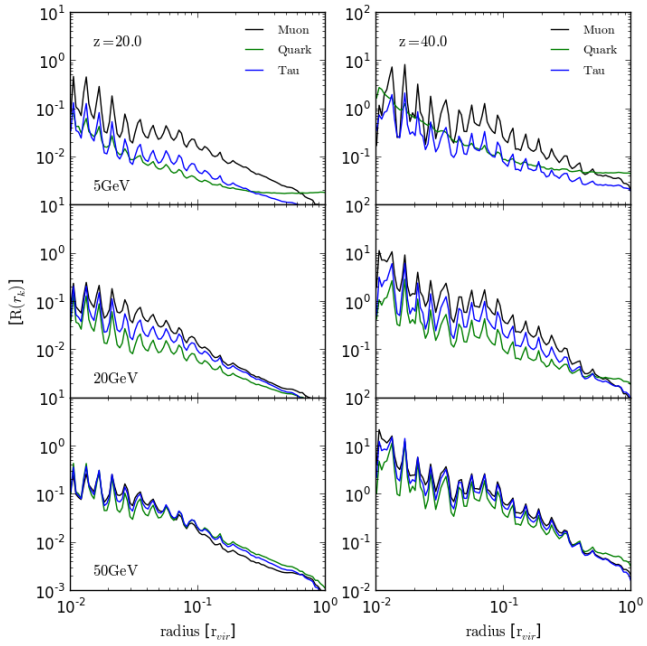

(b) z = $10^7 M_\odot$

Figure 5.20: Comparison of the heating from dark matter annihilation and gravitational binding energy for different annihilation channels. Plot a) shows $10^5 M_\odot$ halos at redshift 20 on the left and redshift 40 on the right. Plot b) shows the same for a $10^7 \odot$ halo.

Chapter 6

Heating of the Circumgalactic Medium

In the previous chapters it was shown that while halos act as partial sinks for the dark matter annihilation energy produced within their confines, a substantial fraction of particles escape the halo. Therefore the circumgalactic medium (CGM) of the halo will be exposed to an elevated level of heating from dark matter annihilation above that from the annihilation from the diffuse dark matter background. Heating the CGM to a sufficient degree can disrupt the evolution of the halo through the suppression of the continuous gas infall required to fuel potential star formation. In the case where the heating effect is pronounced enough it may raise the minimum mass that would allow significant gas accretion onto the halo (Gnedin and Ostriker, 1997; Gnedin, 2000).

6.1 Minimal Baryonic Objects

The emergence of cosmic structure is driven by the growth and eventual gravitational collapse of matter inhomogeneities. Eventually structure formation is believed to become hierarchical, insofar small objects collapse first and then continue to grow through accretion and mergers until they become large halos. When examining the emergence of baryonic structure such as the first populations of stars, it is only natural to ask what determines the mass limit that allows dark matter objects to host baryonic structures. In order for stars and eventually galaxies to begin forming, the halo has to be massive enough for sufficient quantities of gas to collapse onto said halo.

6.1.1 Baryonic Effects

In regimes where dark matter and gas densities are low, pressure felt by the baryons is subdominant to the gravitational dynamics and the two mass components can be approximated as co-evolving. As matter continues to accrue and densities increase dark matter will collapse into halos unimpeded by pressure terms, however the treatments of gas in and surrounding these non-linear dark matter potentials needs to take baryonic effects into account.

Jeans Mass

A valuable first approach is the Jeans mass,

$$M_j = \frac{4\pi}{3}\rho\left(\frac{\lambda_j}{2}\right)^3, \tag{6.1}$$

where λ_j is the Jeans length[1] (Jeans, 1928) and gives the critical mass at which the internal gas pressure can no longer stave of gravitational collapse. In a cosmological setting the Jeans mass can be written in the limit where the gas temperature is decoupled from the CMB temperature (Loeb, 2006) as

$$M_j = 4.54 \times 10^3 \left(\frac{\Omega_m h^2}{0.15}\right)\left(\frac{\Omega_b h^2}{0.022}\right)^{-3/5}\left(\frac{1+z}{10}\right)^{3/2} \mathrm{M}_\odot. \tag{6.2}$$

The above expression does not take into account that when the dark matter and gas distributions start to collapse, shell crossing may occur due to their different dynamics. As such it only holds for the early stages of the collapse process.

Non-linear Potential Approach

An alternative analysis (Loeb, 2006) that gives the resulting baryon overdensity inside collapsed dark matter structure after virialization is as follows. Consider a fully virialized dark matter halo at redshift z_{vir} with a potential $\phi(\mathbf{r})$, such that $\phi(\mathbf{r})$ goes to zero at infinity and $\phi(\mathbf{r}) < 0$ within the halo. One important physical effect neglected in this treatment is the shock-heating of the surrounding gas and resultant entropy production. This becomes important for the larger halos in §6.4 when the modified δ_b due to dark matter annihilation is calculated[2].

Assume that the gas after infall is in hydrostatic equilibrium so that for the pressure p_b and mass density ρ_g of the gas,

$$\nabla p_b = -\rho_b \nabla \phi. \tag{6.3}$$

Once the gas temperature has become decoupled from the CMB (z < 100) and again leaving aside cooling, the pressure evolution is adiabatic:

$$\frac{p_b}{\bar{p}_b} = \left(\frac{\rho_b}{\bar{\rho}_b}\right)^{\frac{5}{3}} \tag{6.4}$$

and barred value indicate the uniform background quantities. Combining equations 6.1

[1] Defined as giving the threshold between exponentially growing and oscillatory modes for density perturbations in a uniform gas field.

[2] A number of additional assumption and approximations underlie this treatment including taking the gas to be stationary and cooling.

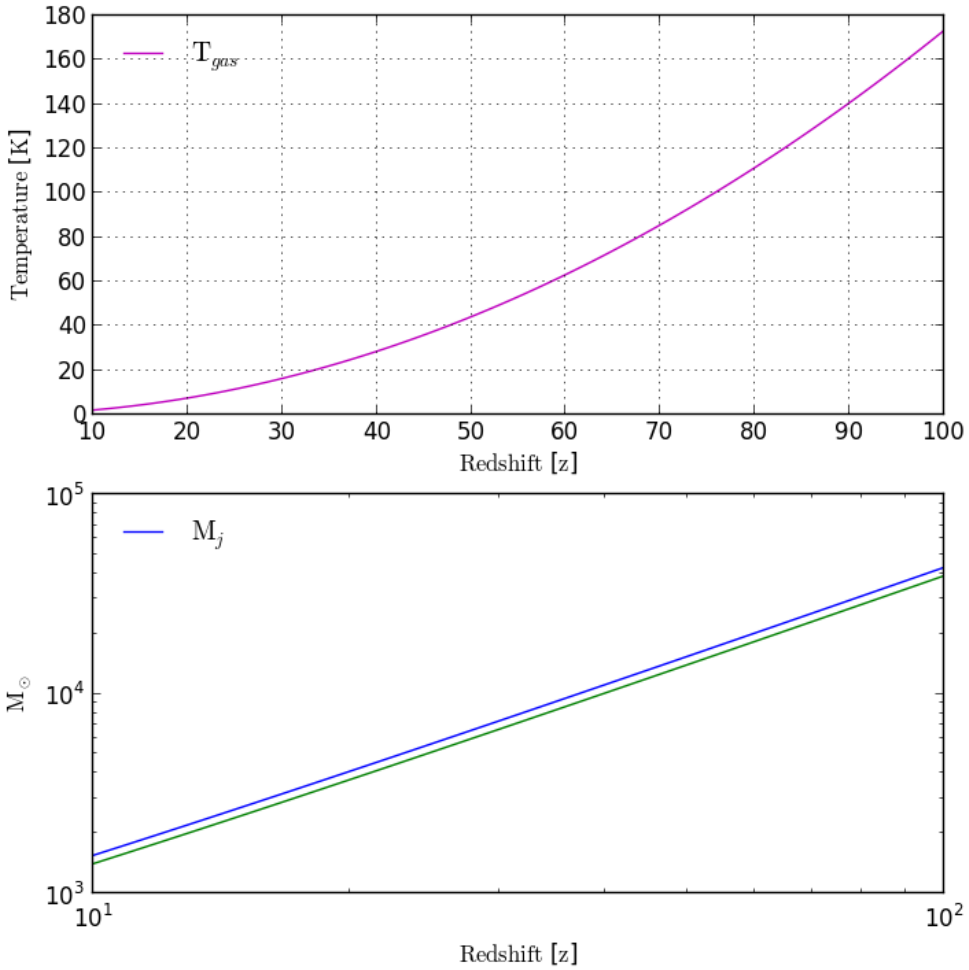

Figure 6.1: The average temperature of the gas in the circumgalactic medium as it varies with redshift is shown in the upper plot. The lower shows both the Jeans mass (blue) and minimal dark matter mass from the non-linear potential calculation (green) with redshift.

and 6.2 and solving yields,

$$\frac{\rho_b}{\bar{\rho}_b} = \left(1 - \frac{2}{5}\frac{\bar{\rho}_b\phi}{\bar{p}_b}\right)^{\frac{3}{2}}. \tag{6.5}$$

Substituting with the temperature of the gas surrounding the halo gives

$$\begin{aligned} \frac{\rho_b}{\bar{\rho}_b} &= \left(1 - \frac{2}{5}\frac{\mu m_p \phi}{k\bar{T}}\right)^{3/2}, \\ \bar{T} &= \frac{\bar{p}_b \mu m_p}{k\bar{\rho}_b}, \end{aligned} \tag{6.6}$$

where μ is the mean molecular weight, k is the Boltzmann constant and m_p the mass of the proton. Let $T_{vir} = -\frac{1}{3}\mu m_p\phi/k$ the virial temperature for the potential $-\phi$, then

$$\delta_b = \frac{\rho_b}{\bar{\rho}_b} - 1 = \left(1 + \frac{6}{5}\frac{T_{vir}}{\bar{T}_g}\right)^{3/2} - 1 \tag{6.7}$$

gives the overdensity of the gas at z_{vir}.

Using the result above, a critical value for δ_b can bet set to indicate the collapse of the gas. This value is to a certain degree arbitrary so for example when $\delta_b > 100$, then $> 50\%$ of the gas that would be present if there were no pressure, accrues onto the halo. Given that the background gas temperature (see Figure 6.1, top panel) can be written as

$$\bar{T}_{gas} \approx 170[(1+z)/100]^2\,\mathrm{K}, \quad \text{for z} < 160, \tag{6.8}$$

then for $\delta_b > 100$, the virial temperature of the halo must exceed

$$T_{vir} > 2.9 \times 10^3 \left[\frac{1+z}{100}\right]^2. \tag{6.9}$$

The virial temperature for a halo that formed at redshift z is defined as,

$$T_{vir} = \frac{\mu m_p G M}{2 k r_{vir}}, \tag{6.10}$$

where r_{vir} is the virial radius of the halo which can be written as,

$$r_{vir} = 0.784\left(\frac{M}{10^8 h^{-1} M_\odot}\right)^{-1/3}\left[\frac{\Omega_m}{\Omega_m^z}\frac{\Delta_c}{18\pi^2}\right]^{-1/3}\left(\frac{1+z}{10}\right)^{-2} h^{-1}\ \mathrm{kpc}. \tag{6.11}$$

In the above expression Δ_c is the collapsed overdensity compared to the critical density as a function of $d \equiv \Omega_m^z - 1$, fitted by Bryan and Norman (1998):

$$\Delta_c = 18\pi^2 + 82d - 39d^2 \tag{6.12}$$

and

$$\Omega_m^z = \frac{\Omega_m(1+z)^3}{\Omega_m(1+z)^3 + \Omega_\Lambda \Omega_k (1+z)^2}. \tag{6.13}$$

At high redshifts $\Omega_m^z \approx 1$ the minimal dark matter halo mass to host baryonic structure is thus given by

$$M_{b,min} = 5.0 \times 10^3 \left(\frac{\Omega_m h^2}{0.15}\right)^{-1/2} \left(\frac{\Omega_b h^2}{0.022}\right)^{-3/5} \left(\frac{1+z}{10}\right)^{3/2} M_\odot. \tag{6.14}$$

Both the Jeans mass and the minimal mass from the non-linear potential treatment are shown in Figure 6.1, bottom panel. As it happens for $\delta_b > 100$ the two expression agree very well with each other. However as δ_b is arbitrarily chosen, the minimal mass in the latter case can vary. Regardless of what δ_b is set to, if the background temperature of the halo $\bar{T}$ is increased, the virial temperature T_{vir} and therefore the total mass of the halo[3] needs to increase along with it to maintain the same δ_b. Having a source of heating of the circumgalactic medium such as dark matter annihilation could, if efficient enough, reduce the amount of gas accreted onto the halo or in even more extreme cases raise the minimal halo mass required for baryonic collapse.

6.2 Modified Dark Matter Annihilation Spectrum

Take the primary source of heating from dark matter annihilation to come from within the halo itself. When considering the actual energy input into the CGM one has to take into consideration that some of the injected energy will have been lost to the halo's gas component, and some will have been down-scattered through the IC induced particle cascades. The modified annihilation spectra are calculated in much the same manner as the total heating and ionisation curves so that the escaped distribution of electrons, photons and positrons for particle α with energy E_i,

$$\mathbf{E}_{jk}^\alpha = \sum_i w_i \mathbf{e}_{ijk}^\alpha, \quad \mathbf{F}_{jk}^\alpha = \sum_i w_i \mathbf{f}_{ijk}^\alpha, \quad \mathbf{P}_{jk}^\alpha = \sum_i w_i \mathbf{p}_{ijk}^\alpha, \tag{6.15}$$

and the total distribution of electrons, photons and positrons for the different annihilation models

$$\begin{aligned} \mathfrak{E}_k &= \sum_\alpha \sum_j f_{j\alpha} \mathbf{E}_{jk}^\alpha, \\ \mathfrak{F}_k &= \sum_\alpha \sum_j f_{j\alpha} \mathbf{F}_{jk}^\alpha, \\ \mathfrak{P}_k &= \sum_\alpha \sum_j f_{j\alpha} \mathbf{P}_{jk}^\alpha, \end{aligned} \tag{6.16}$$

[3]The virial temperature can in general be taken as a proxy for halo mass with an increase in T_{vir} corresponding in an increase in the mass required for the object to collapses.

where w_i and $f_{j\alpha}$ are the same coefficients as in the previous chapter. Figure 6.2 shows both the filtered spectra for individual 5 GeV particles and the entire filtered spectra of a 5 GeV dark matter model annihilating via muons in a $10^6 M_\odot$ halo at redshift 20[4]. As before red, blue and green bars denote photons, electrons and positrons respectively.

Taking this particular annihilation model as an example, the main modifications made to the original distribution of annihilation product can be identified:

Electrons High energy electrons will emerge from the halo having lost a relatively small fraction of their original energy (see narrow distribution of high energy particles in left plot in the top row of Figure 6.2). This means that the full annihilation spectrum will in large part retain its original electron component, but it is broadened towards lower energies There is a second mid-energy range ($10^4 - 10^7$ eV) electron population introduced through pair creation from sufficiently energetic inverse Compton photons which can be seen in both the left hand plots in the top and middle row of Figure 6.2, as well as the middle peak of the full spectrum in the bottom plot. Lastly there is a low energy electron tail due to ionisation from those IC photons that fall below the pair creation limit. The low energy electron population has two peaks corresponding to ionisation from Compton scattering and photo-ionisation.

Photons High energy photons undergo pair-creation to electrons and positrons (see second row of Figure 6.2). The part of the photon annihilation spectrum that lies above the pair creation limit will be severely reduced as is evident when comparing the bottom two rows of Figure 6.2. This is because the mean-free path of pair creation off of the gas field is comparable to the virial radius of the halo for a large fraction of injected photons, and thus only photons injected close to the edge of the halo (these photons make up a small fraction of the total annihilate power due to heightened annihilation rates near the centre) will escape. IC scattering will create an extensive secondary population of photons with those IC photons below the pair-creation limit comprising the prominent mid to low energy tail.

Positrons As a whole, positrons will behave the same way as electrons insofar they both demonstrate a broader original distribution and secondary mid-range

[4]Note that the variability shown in the upper two rows of Figure 6.2 is very similar across different panels. This arises from the hierarchical manner in which the particle deposition library is built up, starting from low energy particles and using those results to augment high energy particle cascades in order to speed up the calculation. In Figure 6.2 both electrons and positrons produce the same spectra of IC photons, while the photon undergoes pair creation to produce an electron/positron pair that will also produce an IC photon spectra comparable to that of the 5GeV particles. The electromagnetic cascade products are all augments from the same low energy results producing similar noise in their escape fraction spectra.

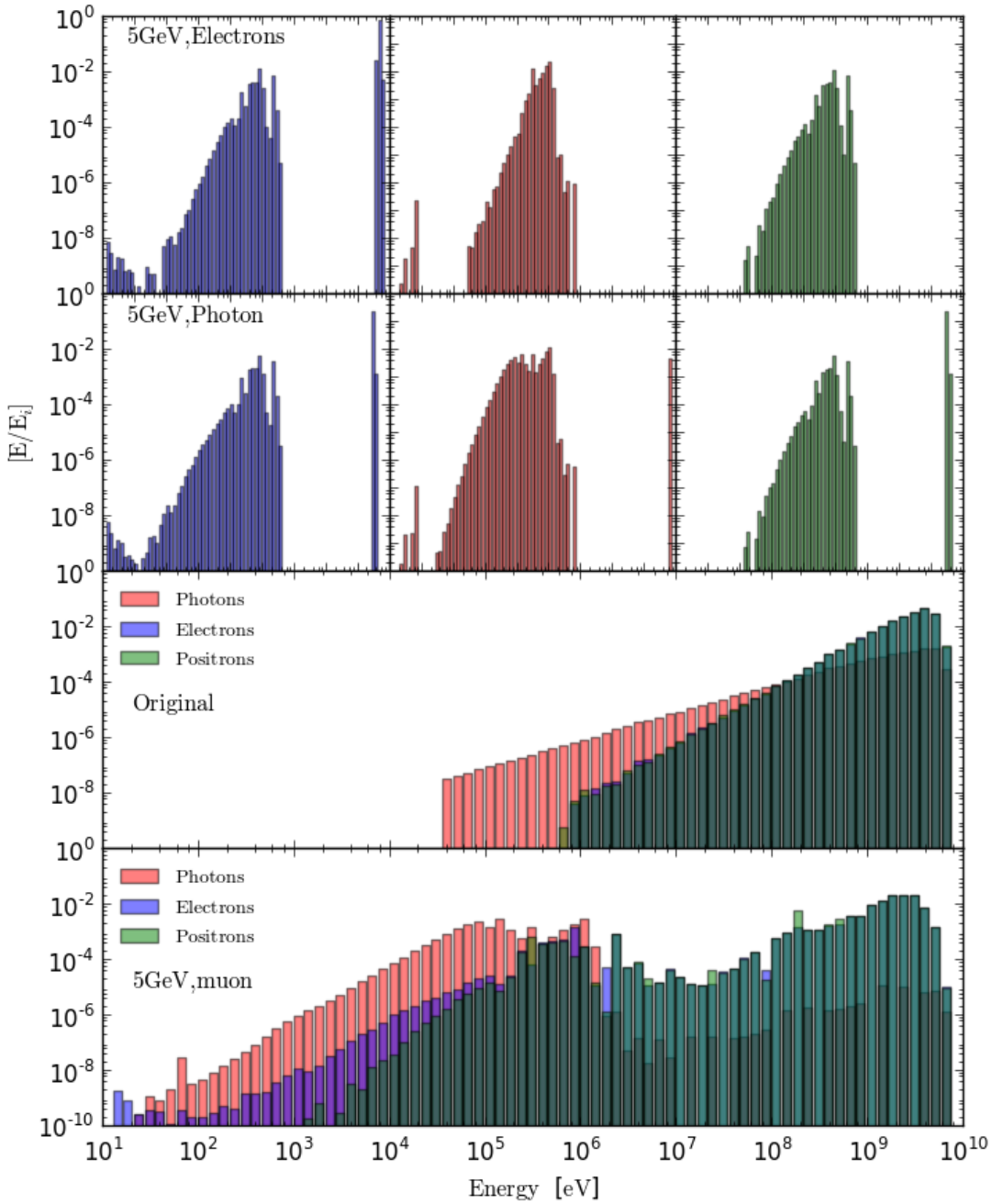

Figure 6.2: The filtered spectra for a 5 GeV electrons and photons (top and middle row) as well as the total spectra for a 5 GeV dark matter model annihilating via muons in a $10^6 M_\odot$ halo at redshift 20, where the original spectrum is shown above the filtered particles. As before red, blue and green denote photons, electrons and positrons respectively.

population due to pair-creation from IC photons. Unlike electrons, positrons don't display a low energy tail as they can't be added to the escaped spectrum through ionisation.

While this analysis pertains specifically to the 5 GeV, muon annihilation model, the same mechanisms driven by IC scattering and pair-creation apply to the other cases with the precise distribution dependent on the original annihilation spectrum.

For the same halo and dark matter annihilation model, Figure 6.3 shows a comparison of the escaped particle spectra of different halo models, similar to Figure 5.8. Where the different panels show the ratio between the High (top), Burkert (middle), Burkert-High (bottom) and the fiducial model. Overall the particle distributions are very similar across all models with the main differences presenting in the high energy photons and $10^3 - 10^4$ eV positrons/electrons. The photon surplus/deficit arises because the only part of the high energy photon distribution that is retained after passing through the halo is that produced in the outermost shells. Therefore highly concentrated halo models such as the Einasto-High case which have their annihilation power production skewed towards the halo's centre will have fewer high energy photons then the fiducial model. In contrast in the Burkert models, more energy is produced at the edge of the halo, so their spectra show more high energy photons than the fiducial case.

A similar argument can be applied to the electron/positron discrepancy. The Burkert profiles produce an excess of $10^3 - 10^4$ eV positrons compared to the fiducial model because these particles are created through pair-production undergone by IC photons off of the halo's gas field. As discussed above these are preferentially injected in the outer parts of the halo for a Burkert profile, and thus the positrons, for which ionisation is just beginning to become inefficient will readily escape. In the more concentrated, fiducial case where more particles are created close to the dense centre of the halo, positrons will still interact with the gas and fewer particles escape. On the other hand the $10^3 - 10^4$ eV electrons are predominantly due to photo- and Compton ionisation which have a larger mean free path compared to both electron/positron pair creation and the virial radius. Therefore the less concentrated Burkert profiles show a deficit of these electrons compared to the fiducial model because they require high densities to be produced.

Lastly it is worth noting that as with the heating curves shown in Chapter 5, the Burkert profile with a higher mass-concentration parameter is qualitatively very similar to the fiducial model. This also holds true for the total annihilation power produced by the two models which means that at least as far as this treatment of dark matter annihilation goes, there maybe a degeneracy between the fiducial Einasto and a more concentrated Burkert case.

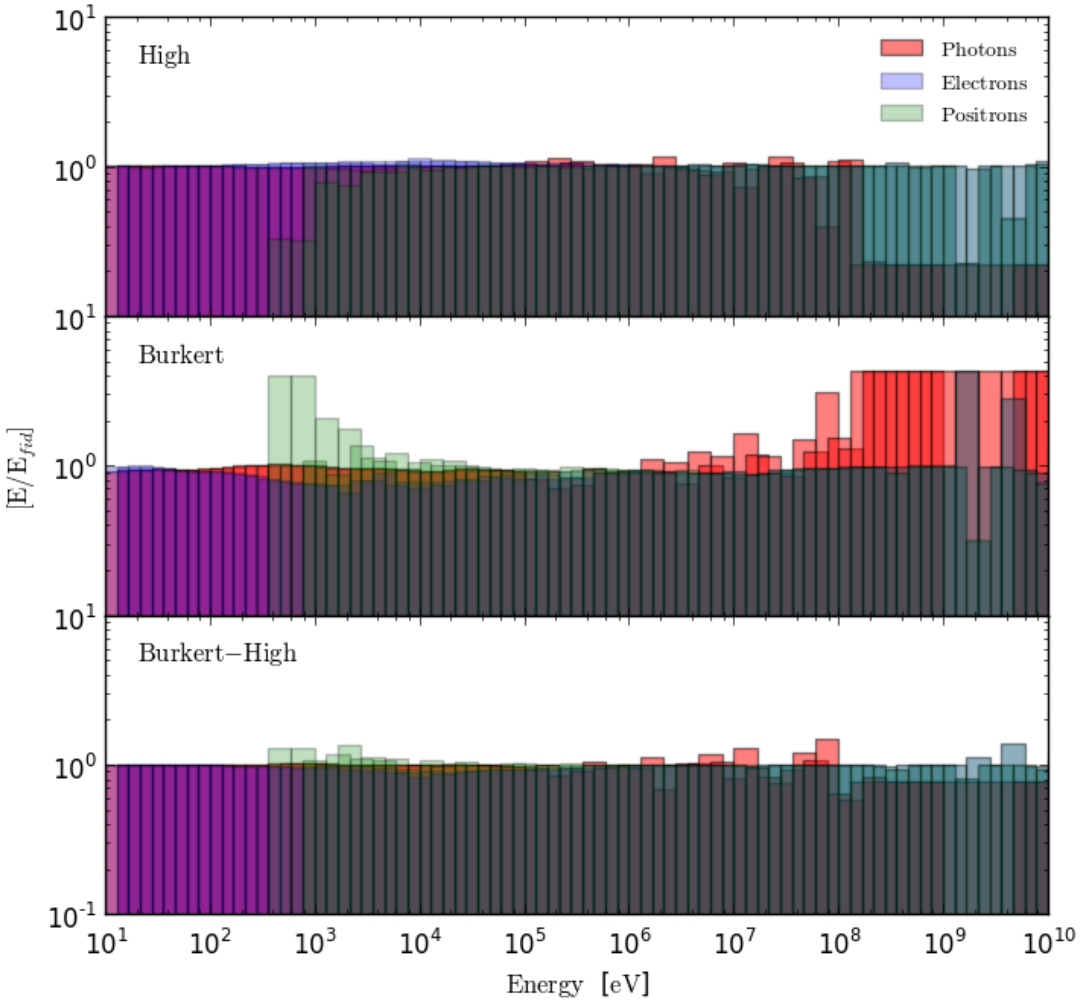

Figure 6.3: Residual of the spectra of escaped particles for different dark matter halo models (from top to bottom Einasto-High, Burkert, Burkert-High) and the fiducial model. All cases show a $10^5 M_\odot$ halo at redshift 40 for a 5 GeV particle annihilating via muons. Red, blue and green columns denote photons, electrons and positrons.

130 MeV, Electrons				
Halo	Photons	Electrons	Positrons	Total
Original	0.000	0.5	0.5	1.0
10^5, z = 20	1.423e−3	0.4985	0.4985	0.9985
10^6, z = 20	2.453e−3	0.4968	0.4968	0.9960
10^7, z = 20	4.293e−3	0.4928	0.4928	0.9899
10^5, z = 40	1.280e−2	0.4887	0.4887	0.9901
10^6, z = 40	2.334e−2	0.4744	0.4744	0.9722
10^7, z = 40	3.582e−2	0.4423	0.4423	0.9204

Table 6.1: Energy breakdown in fractions of the total annihilation power of the escaped spectra for a 130 MeV dark matter model annihilating via electrons/positrons.

6.2.1 Filtered Annihilation Spectra

Following in Figures 6.4-6..8 are plots of the filtered spectra for a selection of the dark matter annihilation models assuming different halo masses and redshifts. In each figure the plot at the top of the figure shows the original annihilation spectrum, while the plots below show the distribution of particles once they've passed through their respective halos. In each case the fiducial dark matter halo model is shown.

There is some noise, especially in the high energy end of the electron/positron spectra for all models. This is in part because due to time constraints fewer iterations were completed for the computationally expensive, high end of the annihilation product spectrum. In addition the energy bins for the escaped particles did not match those of the injected spectra, and some of the noise maybe an artefact of the choice of binning in the data plotted. As the code output is built up hierarchically, noise is also amplified at higher energies as those cascades incorporate results from lower energy particles. Particles with energies below 10^5eV were not augmented so the noise build-up is not an issue for low and mid energy outputs[5].

Also included in tabulated form is the energy breakdown in fractions of the total annihilation power for different escaped particle species (in all cases the neutrino component is not shown). In each table the top row shows the unfiltered spectrum and the subsequent rows the fractions after having passed through the respective, fiducial dark matter halo model. The last column shows how much of the total annihilation power escapes the halo. As expected, high redshift objects are more efficient at absorbing the injected energy, while at a fixed redshift large objects are more effective.

[5]Reducing noise at higher energies and optimising the hierarchical use of results will be a goal for future versions of the energy transfer code

5 GeV, Muons				
Halo	Photons	Electrons	Positrons	Total
Original	3.107e−2	0.4845	0.4842	1.0
10^5, z = 20	4.566e−3	0.4978	0.4968	0.9991
10^6, z = 20	8.622e−2	0.4471	0.4647	0.9960
10^7, z = 20	0.1358	0.4272	0.4230	0.9860
10^5, z = 40	0.1684	0.4124	0.4091	0.9899
10^6, z = 40	0.3218e0	0.3244	0.3177	0.9639
10^7, z = 40	0.5058e0	0.2118	0.2000	0.9176

Table 6.2: Energy breakdown in fractions of the total annihilation power of the escaped spectra for a 5 GeV dark matter model annihilating via muons.

80 GeV, W				
Halo	Photons	Electrons	Positrons	Total
Original	0.5252	0.2374	0.2374	1.0
10^5, z = 20	2.367e−2	0.4882	0.4872	0.9990
10^6, z = 20	4.841e−2	0.4750	0.4737	0.9971
10^7, z = 20	0.1103	0.4570	0.4216	0.9888
10^5, z = 40	0.1213	0.4349	0.4319	0.9911
10^6, z = 40	0.2456	0.3662	0.3577	0.9665
10^7, z = 40	0.3798	0.2723	0.2619	0.9141

Table 6.3: Energy breakdown in fractions of the total annihilation power of the escaped spectra for a 80 GeV dark matter model annihilating via W bosons.

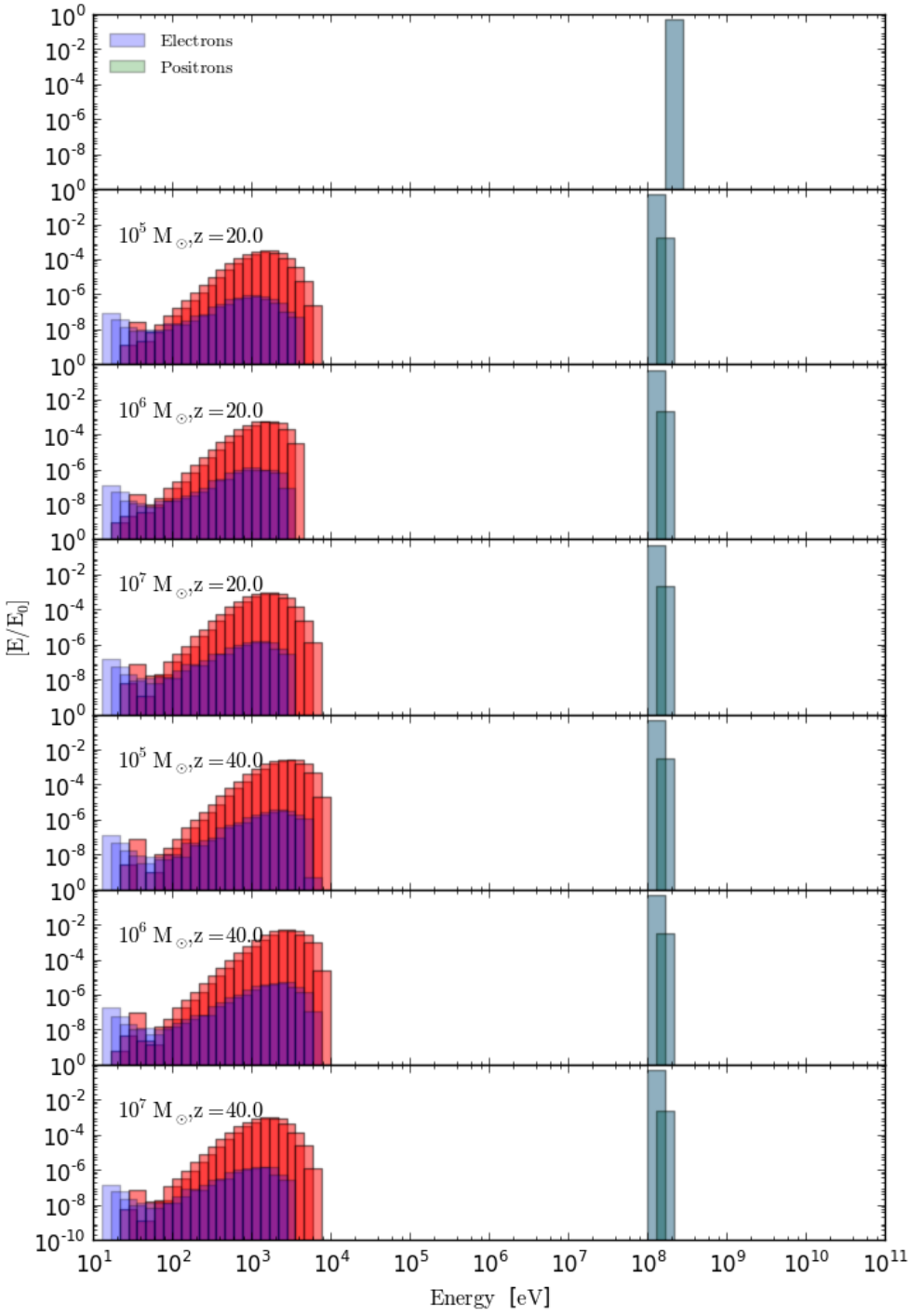

Figure 6.4: The modified spectrum of the 130MeV dark matter model annihilating via the electron/positron channel after having been filtered by the gas component of the halo. The top panel shows the unaltered injected spectrum where blue bars denote electrons, green positrons and red photons. Below are the modified spectra for 10^5, 10^6 and $10^7 M_\odot$ halos at redshift 20 and then for those same halos at redshift 40

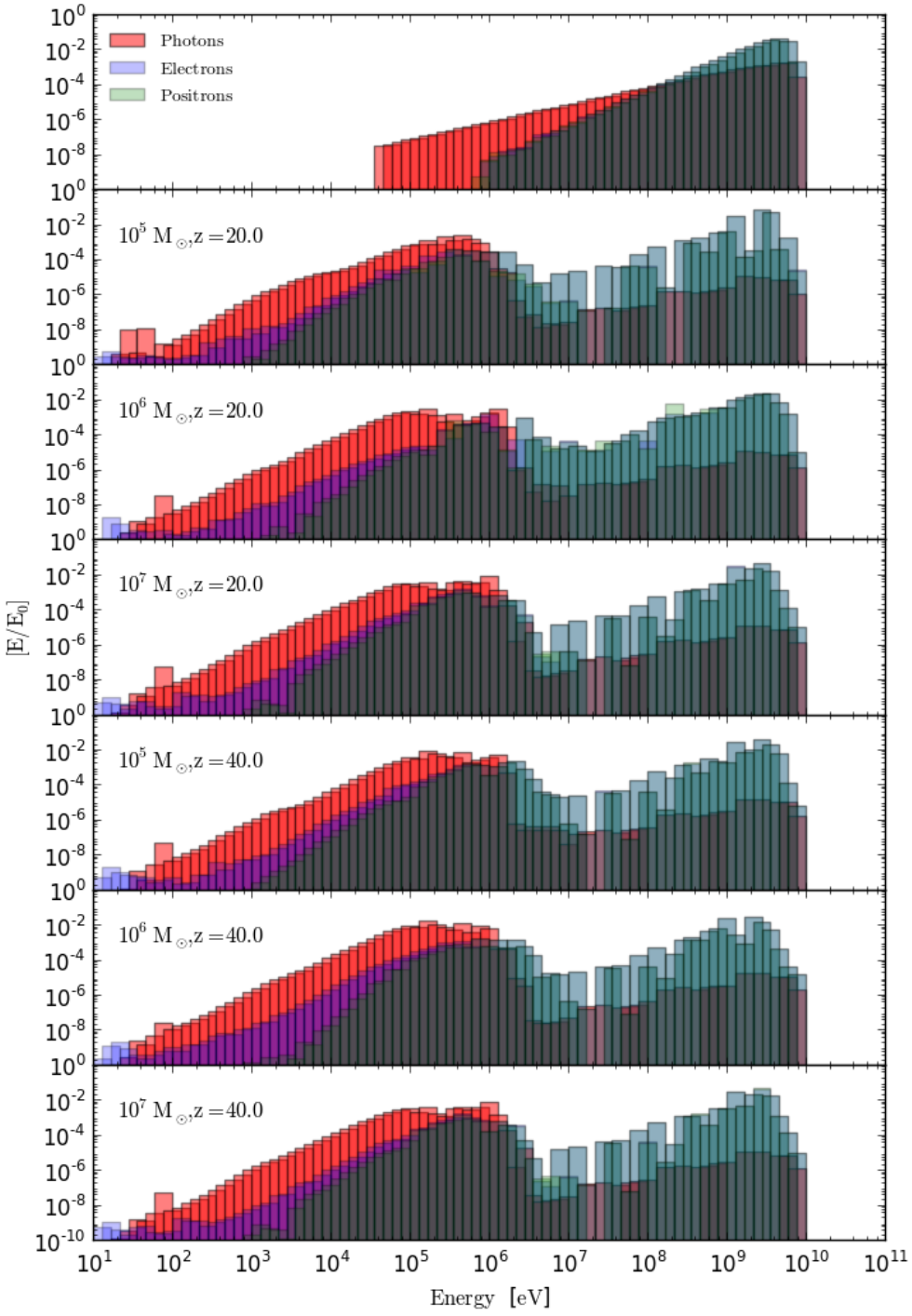

Figure 6.5: The modified spectrum of the 5GeV dark matter model annihilating via the muons channel after having been filtered by the gas component of the halo. The top panel shows the unaltered injected spectrum where blue bars denote electrons, green positrons and red photons. Below are the modified spectra for 10^5, 10^6 and $10^7 M_\odot$ halos at redshift 20 and then for those same halos at redshift 40

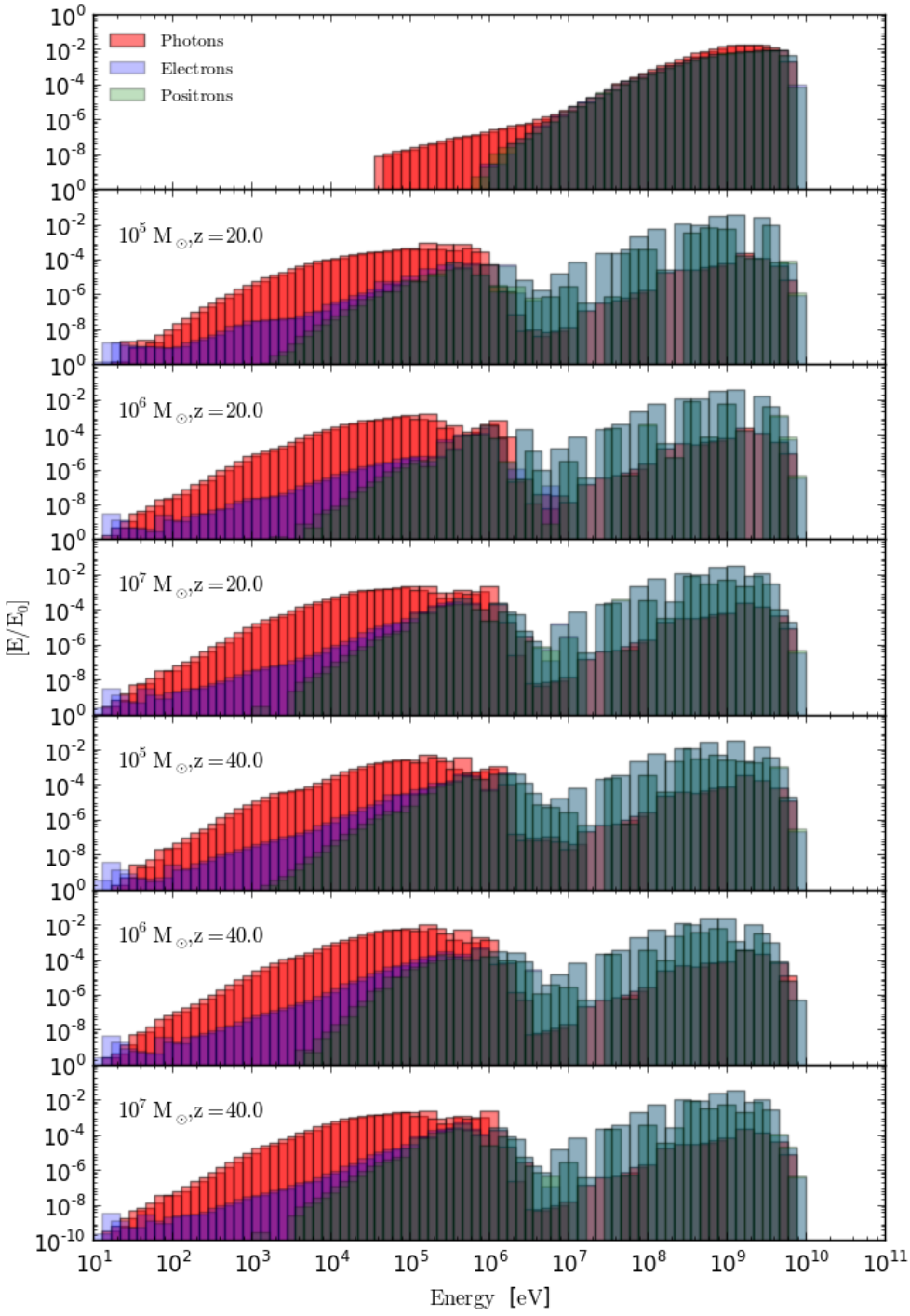

Figure 6.6: The modified spectrum of the 5GeV dark matter model annihilating via the tau channel after having been filtered by the gas component of the halo. The top panel shows the unaltered injected spectrum where blue bars denote electrons, green positrons and red photons. Below are the modified spectra for 10^5, 10^6 and $10^7 M_\odot$ halos at redshift 20 and then for those same halos at redshift 40

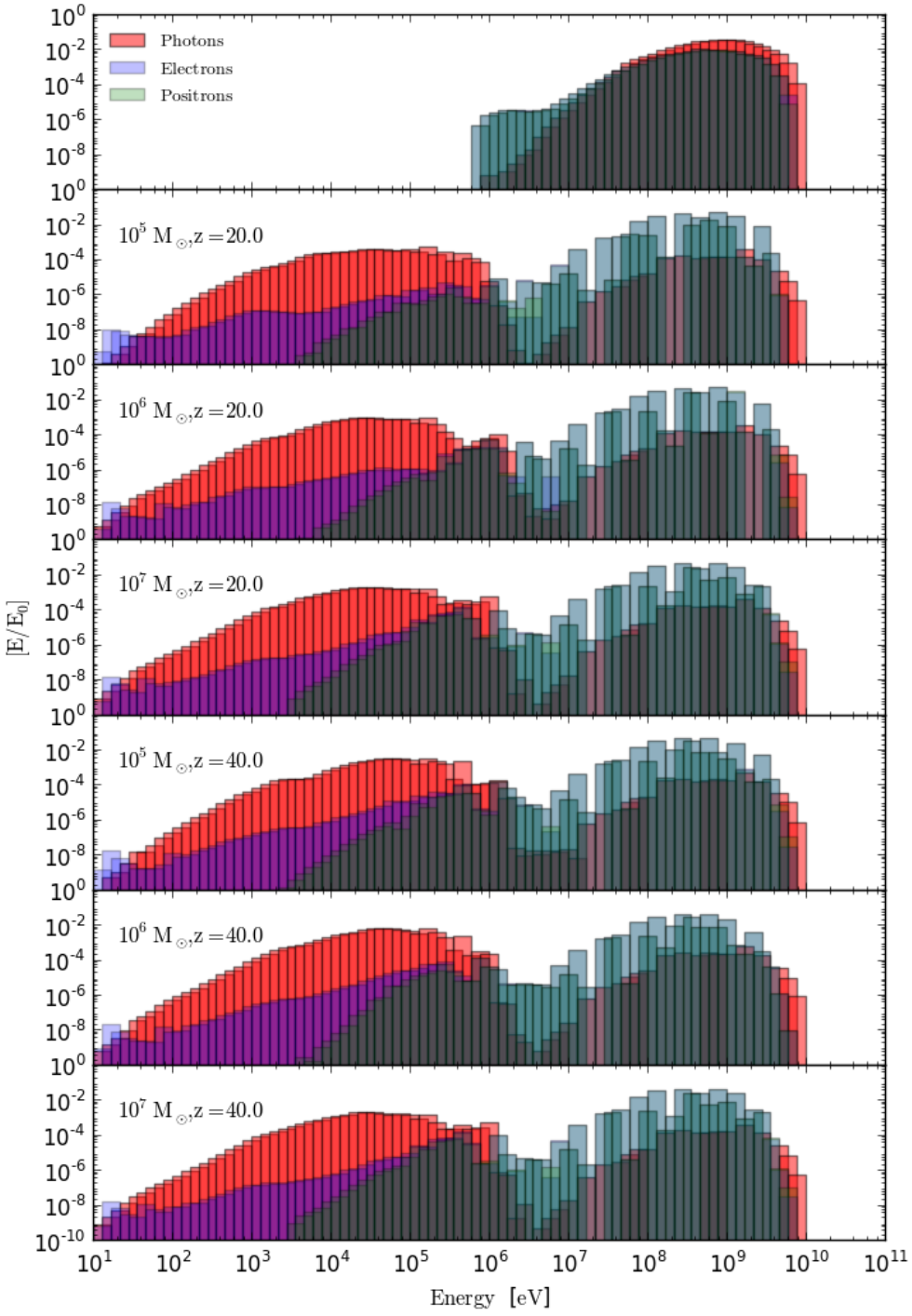

Figure 6.7: The modified spectrum of the 5GeV dark matter model annihilating via the q channel after having been filtered by the gas component of the halo. The top panel shows the unaltered injected spectrum where blue bars denote electrons, green positrons and red photons. Below are the modified spectra for 10^5, 10^6 and $10^7 M_\odot$ halos at redshift 20 and then for those same halos at redshift 40

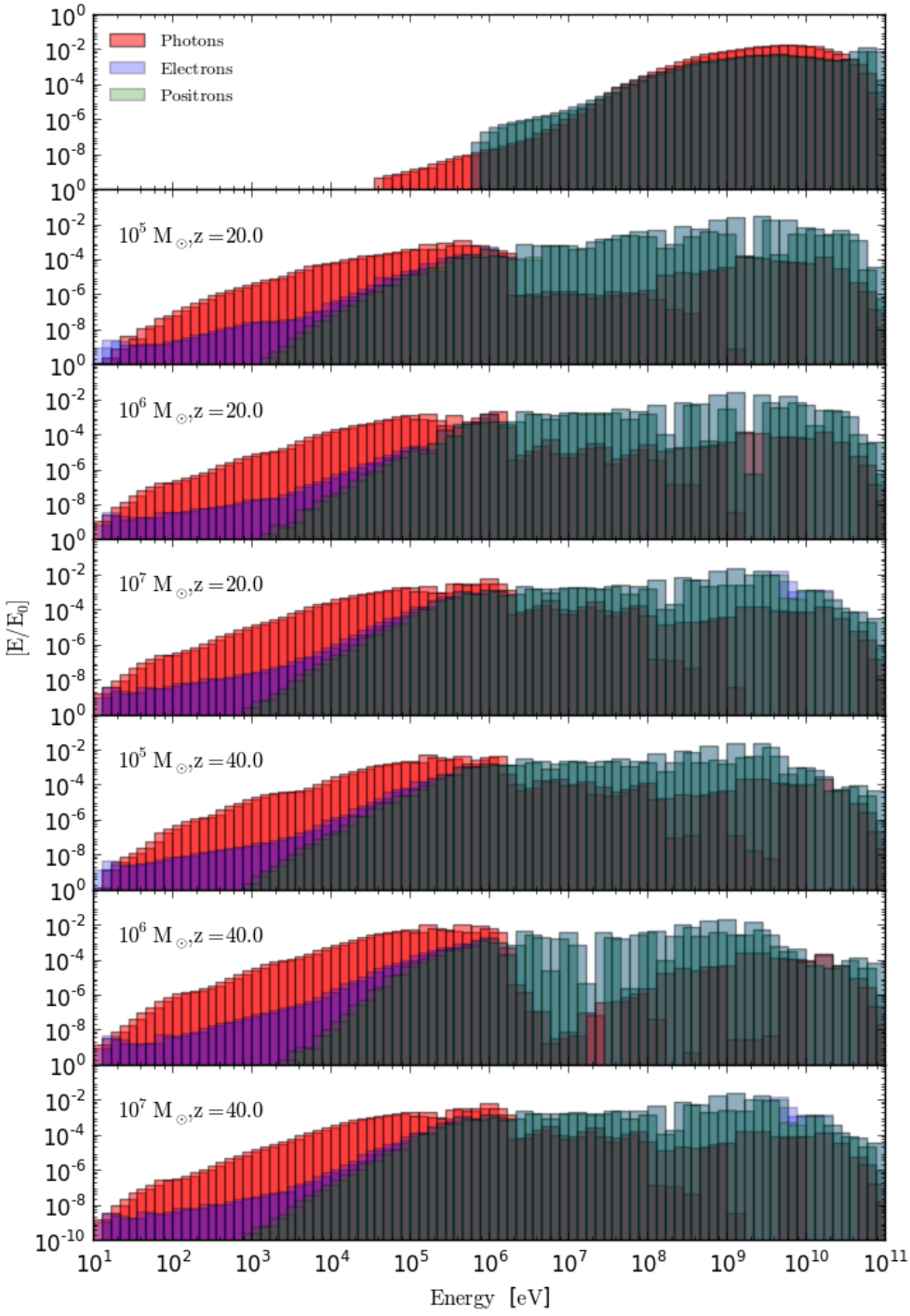

Figure 6.8: The modified spectrum of the 80GeV dark matter model annihilating via the W channel after having been filtered by the gas component of the halo. The top panel shows the unaltered injected spectrum where blue bars denote electrons, green positrons and red photons. Below are the modified spectra for 10^5, 10^6 and $10^7 M_\odot$ halos at redshift 20 and then for those same halos at redshift 40

6.3 Heating of the Circumgalactic Medium

The problem of heating the CGM is approached using the same general approach as that for heating the halo itself. The following section outlines the density model of the gas surrounding the halo, the use of the energy transfer code to calculate the energy transfer to the CGM for particle α with energy E_i and finally the total heating and ionisation of the surrounding gas for different halo and dark matter models.

6.3.1 Gas Distributions

The gas density distribution of the circumgalactic medium is taken from (Bruns et al., 2012) and motivated by an analytic description of gas infall based on the extended Press-Schechter model by Barkana (2004) :

$$\rho_{IGM}(r, r_{vir}) = \begin{cases} 20\bar{\rho}(r/r_{vir})^{-1} & r < 10r_{vir}, \\ \bar{\rho}[1 + \exp(2 - r/5r_{vir})] & r \geq r_{vir}, \end{cases} \tag{6.17}$$

where $\bar{\rho}$ is the average gas density of the IGM and r_{vir} the virial radius. As for the halos, we assume the gas to be un-ionised and to only consist of Hydrogen and Helium[6].

6.3.2 Energy Transfer Code in the CGM

The energy transfer code used to calculate the evolution of particles inside the halo was modified to find the energy loss of particles injected from the edge of the halo into the CGM. There are a number of differences between the inner halo and the CGM problem that are reflected in the changes made to the code:

- The particles are all injected from the virial radius in the direction of the hemisphere away from the halo. There are two boundaries set at r_{vir} and $10\times\mathrm{r}_{vir}$. Even though in order to determine the change in δ_b the main focus is on the heating close to the halo, the second boundary was set a considerable distance beyond it. This is because the CGM is considerably less dense than the halo and therefore a lot of the mean-free paths of the relevant physical processes are an order of magnitude larger than the virial radius[7]. This means that even the secondary particles created a number of virial radii away can contribute to heating the immediate area around the halo. Therefore care must be taken that the original particle is not allowed to "escape" too early to ensure the particles created during the latter parts of the electromagnetic cascade can contribute to the heating of the CGM.

- The downside of allowing the parent particle to travel such an extended distance is the sheer number of secondary, cascade particles it produces, which in turn

[6]Note that there is discontinuity between the density profiles of the gas inside the halo and circumgalactic medium.

[7]The photons created through IC scattering in particular fall into this category.

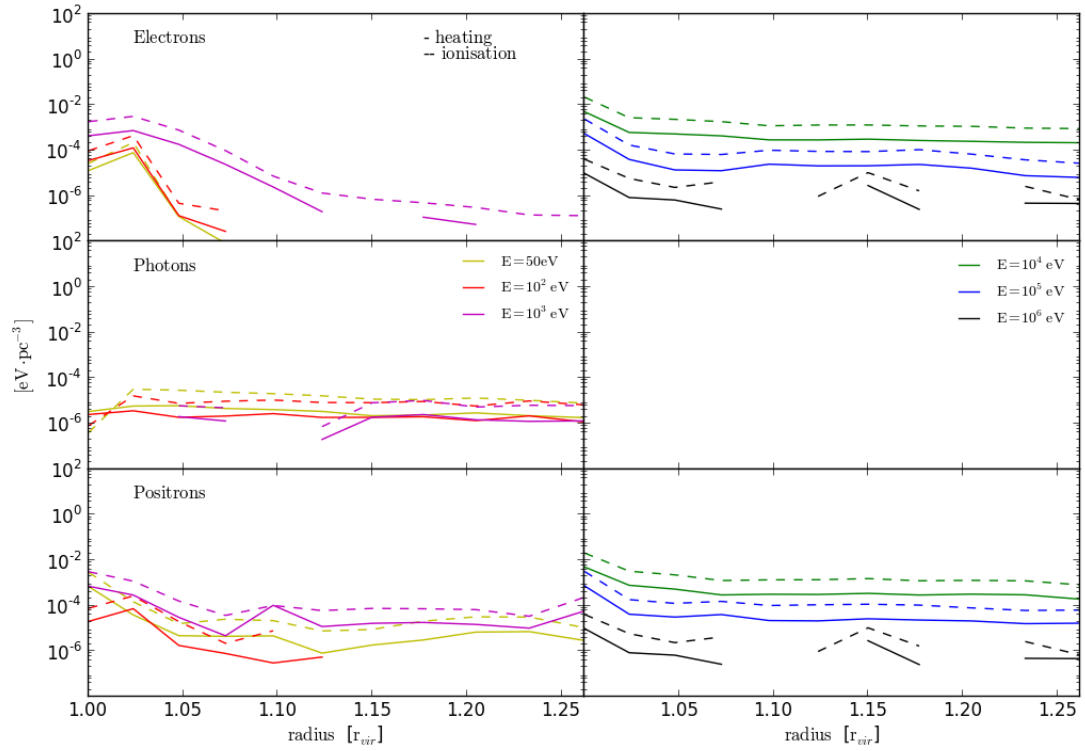

(a) z = 20

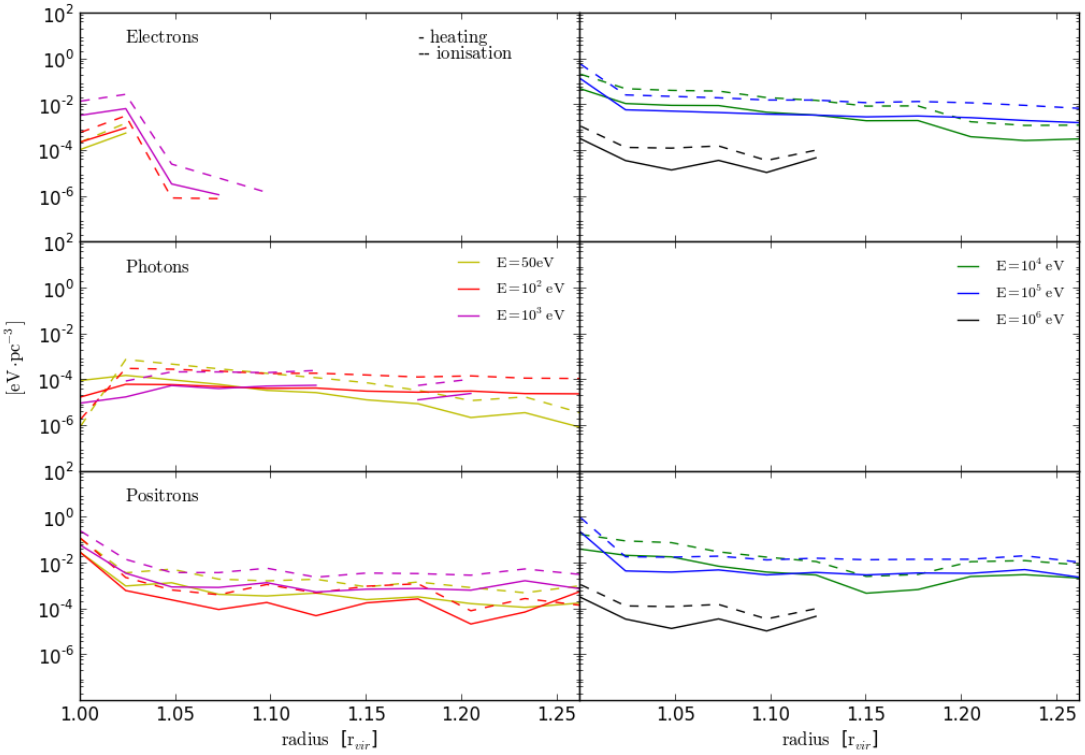

(b) z = 40

Figure 6.9: The energy deposition for low energy particles injected into the CGM around a $10^5 M_\odot$ halo. The top plot shows the halo at redshift 20, the bottom at redshift 40. In each plot, solid lines show the energy going into heating and the dashed into ionisation.

extend the runtime of the code considerably. In the halo environment the number of secondary particles was managed by building up the code outputs hierarchically from low energies up and then using those results to augment the high energy cascades. To replicate this approach for the circumgalactic medium would require running the code to fill the entire $\backsim$10 r_{vir} sphere, which is impractical, especially considering that interest lies predominantly with the heating effect close to the halo. The cascades were still augmented with the results from particles injected from the virial radius, but to further manage run-time, the number of iterations was reduced for each energy bin.

- Having to limit the number of evolutions for the injected particles means that the final heating curves may not be as fully converged as those outputs from inside the halo. However since variation in the spatial distribution of the deposited energy is more pronounced the further the particle travel from its original point of injection, those effects will be lesser for the gas shells of interest, closest to the halo[8].

6.3.3 Code Output

Presented below are the results for the fraction of energy deposited into heating **h** and ionisation χ at radius $\mathbf{r}_k$ for particle type α with energy E_i injected at the virial radius,

$$\mathbf{h}_{ik}^{\alpha}, \quad \chi_{ik}^{\alpha}. \tag{6.18}$$

Low-Energy Example

The energy range of the particles injected into the CGM has been extended to include the low energy tail resulting from interactions of the original annihilation products during their passage through the halo. Despite high energy electrons/positrons still forming the principal component of the distribution, these lower range particles (depending on the annihilation model), can make up a significant fraction of the total energy input. Subsequently their evolution and ability to deposit energy efficiently has important consequences for the overall energy transfer into the CGM.

Figure 6.9 shows the deposition curves for electrons, photons and positrons (top, middle, bottom) with energies between 50 and 10^6 eV for a $10^5 M_\odot$ halo at redshift 20 (Plot a) and 40 (Plot b). In all plots, solid lines denote energy into heating, and dashed lines energy into ionisation. In all panels only the radial distance up to 1.25 r_{vir} is shown.

[8]The spherical symmetry of the CGM environment, the fact that the particles are injected effectively close to the centre of the sphere and that the high energy electrons/positrons diverge very little from their original trajectory also diminishes variation in the radial deposition curves, even with fewer iterations.

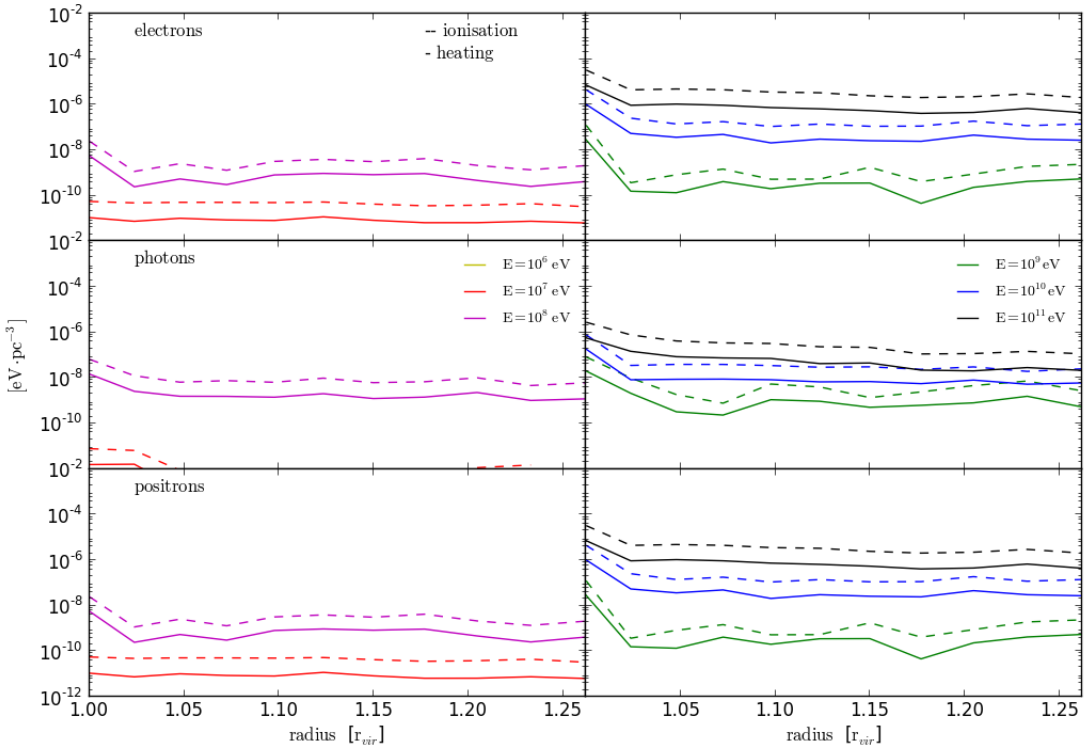

(a) z = 20

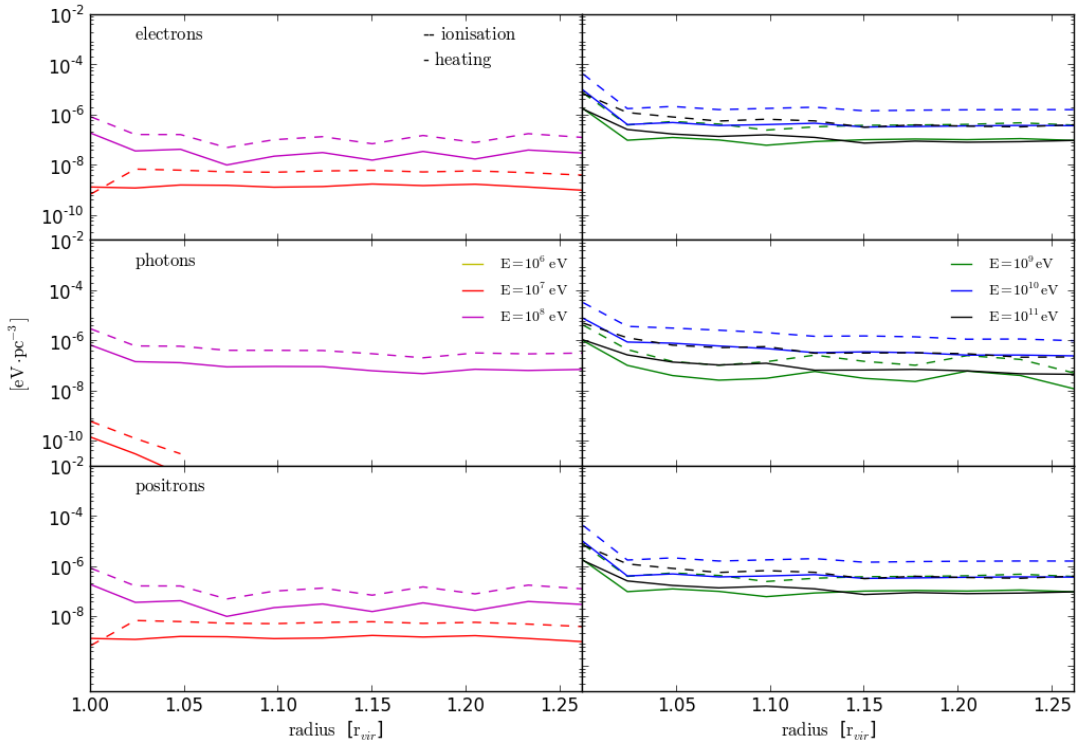

(b) z = 40

Figure 6.10: The energy deposition for high energy particles injected into the CGM around a $10^5 M_\odot$ halo. The top plot shows the halo at redshift 20, the bottom at redshift 40. In each plot, solid lines show the energy going into heating and the dashed into ionisation.

An obvious difference between the CGM and the halo proper is the gas density, and the injected particles' evolution reflects that accordingly. In both Plot a and b, the panels on the left show results for injected particles with energies of 50 (yellow), 100 (red) and 10^3 (magenta) eV. For those cases, electrons and positrons rapidly deposit their entire energy close to the point of injection, with higher energies and lower redshift (both of which correspond to longer mean free paths) leading to more extended deposition curves as expected[9]. In contrast photons even at the low energy limit already transfer energy far beyond the initial site of injection compared to electrons and positions.

The panels on the right show results for injected particles with energies of 10^4, 10^5 and 10^6 eV, (green, blue and black curves respectively). As a whole the behaviour of electrons and positrons is the same, while energy curves continue to extend with the increased energy of the injected particle. Once the threshold between collisional interactions and IC collisions has been reached, energy deposition becomes sporadic due to the up-scattered IC photons lying below the photo-ionisation limit (see black 10^6 eV curve). For photons in this energy range mean free paths have grown sufficiently that no energy transfer near the halo occurs. This indicates the ability of the reduced gas density to suppress the contributions of low energy photons to the overall energy deposition. This will also have consequences for the energy transfer efficiency of high energy leptons for which heating and ionisation of the surrounding gas is predominantly facilitated through IC photons which fall into this energy range.

High-Energy Example

Figure 6.10 shows the same $10^5 M_\odot$ halo as Figure 6.9, with results for particles with energies between 10^6 and 10^{11} eV. Once the energy of the inverse Compton up-scattered photons climbs beyond the photo-ionisation limit, high energy electron and positrons again begin contributing to the heating of the CGM (see red 10^7 eV curve). High energy photons undergo pair-creation and in a similar vein, begin contributing to the energy deposition close to the halo's virial radius once the energy of the electron/positrons pair exceeds 10^7 eV.

Overall high energy electrons and positrons deposit less energy into the CGM compared to their low energy counterparts due to the reduced gas interaction of low energy photons discussed above. However as the initial energy of the particle increases, this is in part offset by the increased multiplicity of the cascades. In particular, where IC photons fall into the energy range in which they undergo pair creation to low energy electrons and positrons, energy deposition efficiency can increase. In general, for low energy particles, energy transfer will be boosted at higher redshifts due to increased gas density. However the accompanying upwards shift in the energy distribution of the

[9]Low energy positrons deposit energy far beyond the reaches of their electron equivalent via the photons created during the positronium-annihilation process.

CMB photon field will ultimately also effect the associated electromagnetic cascade of high energy particles. Therefore the relative energy deposition efficiency for these high energy particles at different redshifts will not only be dependent on the overall density of the interaction medium but also the distribution of the IC photons they produce. For example compare the relative contribution from 10^{10} (blue) and 10^{11} (black) eV electrons at redshifts 20 and 40.

Summary of Outputs

The summary of results for electrons, positrons and photons with energies between 10^7 and 10^9 eV for 10^5 -$10^7 M_\odot$ halos are shown in Figure 6.11 at redshift 20 and at redshift 40 in Figure 6.12. Overall the energy deposition is comparable between the different halo masses since the increase in volume to be heated is in part compensated by the increase in energy transfer efficiency afforded by the same increase in volume.

6.3.4 Heating and Ionisation

The total heating and ionisation fractions are calculated the same way as in the previous chapter. In this case however only summation over the energy and particle type indexes is required, so that

$$\begin{aligned} \mathbf{H}_k &= \sum_\alpha \sum_i f_{\alpha i} \mathbf{h}^\alpha_{ik}, \\ \mathbf{X}_k &= \sum_\alpha \sum_i f_{\alpha i} \chi^\alpha_{ik}. \end{aligned} \tag{6.19}$$

An example of the heating and ionisation fractions at r_k are shown in Figure 6.13 for different halo models (blue corresponding to the fiducial case and magenta to a Burkert profile). The solid, dashed and dotted lines show different dark matter models. While for the 130 MeV (solid line) and 80 GeV via W boson (dotted line) dark matter candidates the underlying halo model does not impact the energy deposition curves, there is a small difference in the case of the 5 GeV via muon (dashed) model. As was shown in Figure 6.3, different dark matter profiles can produce an excess/deficit of particles in parts of the filtered spectrum. If the change in the energy distribution of the injected particles happens to impact those particles that readily interact with the gas, this can translate to variations in the overall energy deposition efficiency. For instance in the case of dark matter models with masses ~ 5 GeV, a considerable portion of the IC photons created fall into the Compton scattering regime. These photons require high gas densities in order to interact over scales comparable to the virial radius of the halos in question here. Halos with concentrated density profiles provide more favourable conditions for Compton ionisation leading to their filtered spectra carrying more of the $10^4 - 10^5$ eV electrons which do interact with the CGM as opposed to the free-streaming

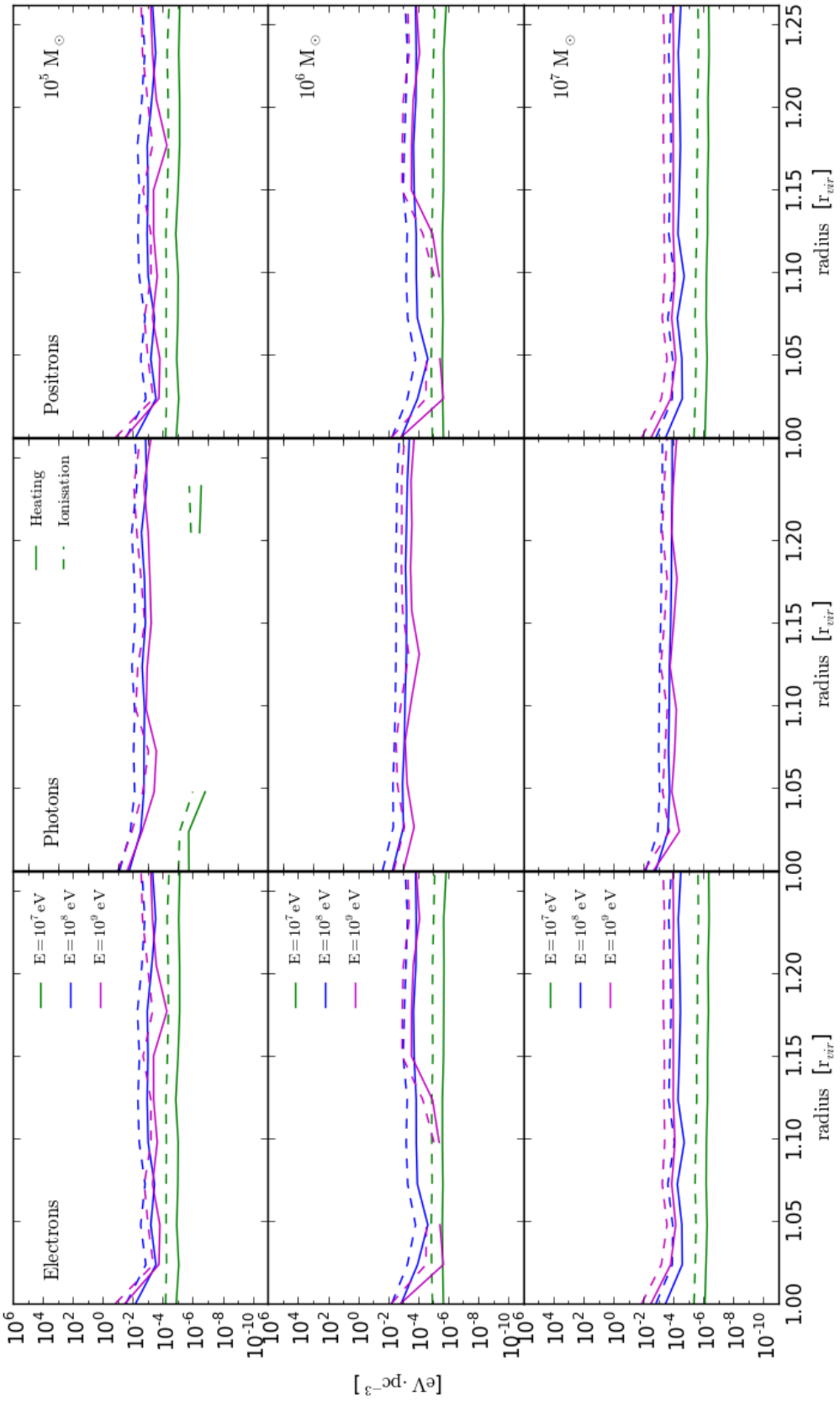

Figure 6.11: Energy transfer code output for 10^7, 10^8 and 10^9 eV particle injected into the CGM surrounding $10^5 - 10^7 M_\odot$ halos at redshift 20

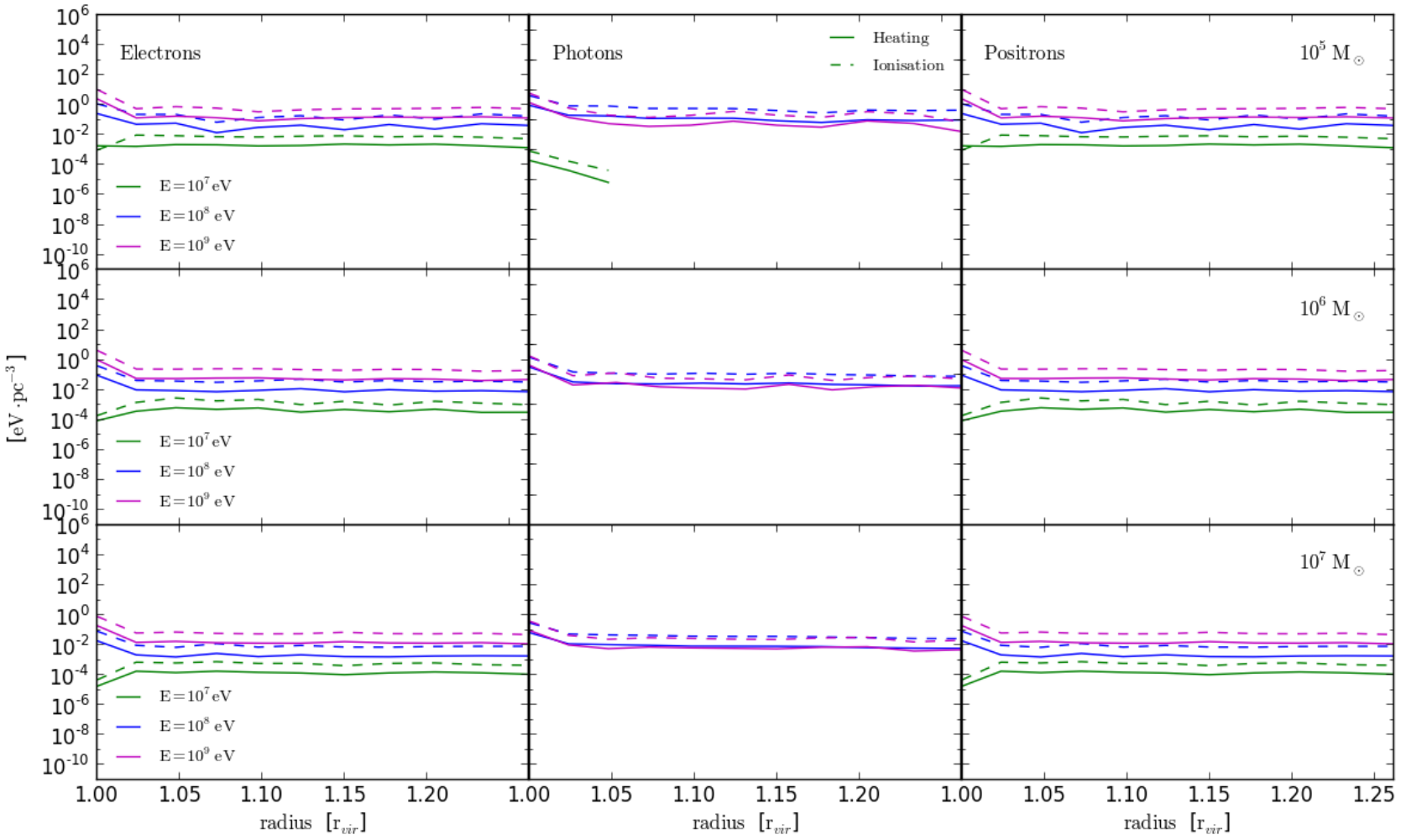

Figure 6.12: Energy transfer code output for 10^7, 10^8 and 10^9 eV particle injected into the CGM surrounding $10^5 - 10^7 M_\odot$ halos at redshift 40

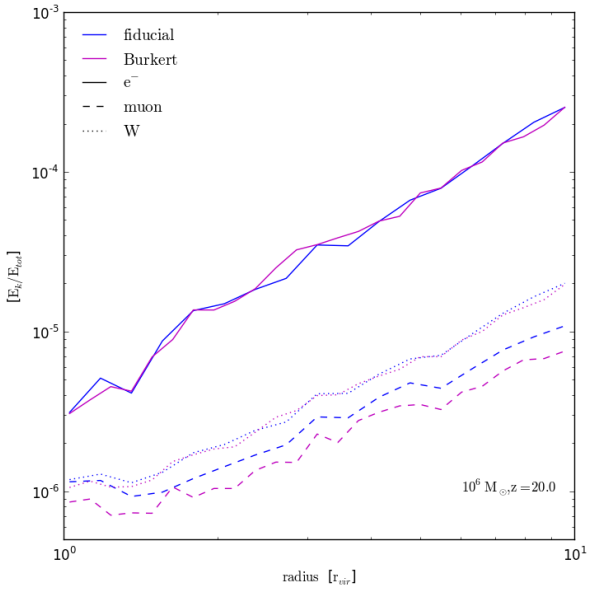

Figure 6.13: Comparison of deposition fractions for different halo models in a $10^6 M_{sol}$ halo at redshift 20. Blue lines show the fiducial and magenta Burkert profiles. The Annihilation models are the 130 MeV via electrons (solid), 5 GeV via muons (dashed) and 110 GeV via W bosons.

IC Compton- energy range photons[10].

Change in Temperature and Ionisation Fraction

The CGM is well approximated by a monatomic, ideal gas for which the internal energy can be written as $U = \frac{3}{2} N k_b T$. Here N denotes the total number of particles and k_b is the Boltzmann constant. Given the total energy produced through dark matter annihilation by the halo over the Hubble time, U_{dm} and the heating $\mathbf{H}_k$ and ionisation $\mathbf{X}_k$ fractions calculated above, the average change in temperature of the shell at $\mathbf{r}_k$ is given by,

$$\Delta T(\mathbf{r}_k) = \frac{2\mathbf{H}_k U_{dm}}{3 N_k k_b}. \tag{6.20}$$

In a similar way the change in ionisation fraction in the shell at $\mathbf{r}_k$ can be written as

$$\Delta X(\mathbf{r}_k) = \frac{\mathbf{X}_k U_{dm}}{\bar{E}_{ion} N_k}. \tag{6.21}$$

Figure 6.14 shows the change in gas temperature (plot a) and ionisation fraction (plot b) for different halo and dark matter models. In both plots halos at redshift 20

[10]The IC photon peak at the Compton interaction range is also why overall 5 GeV dark matter models are less efficient at localised heating and ionisation compared to other models.

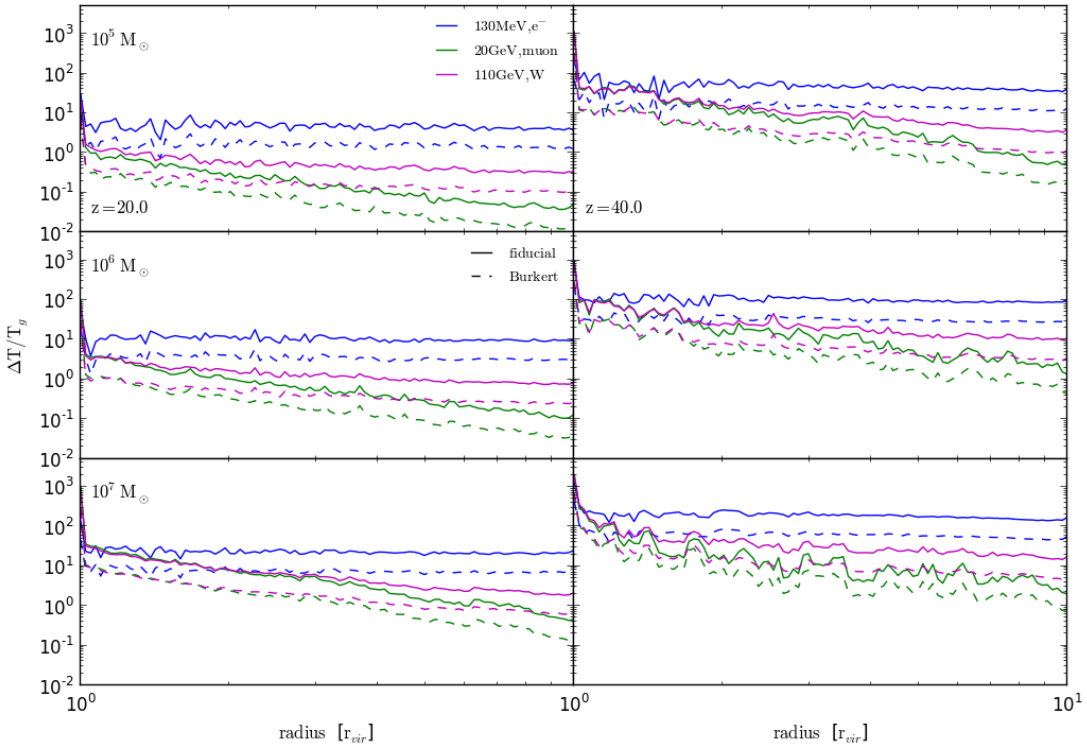

(a) Heating

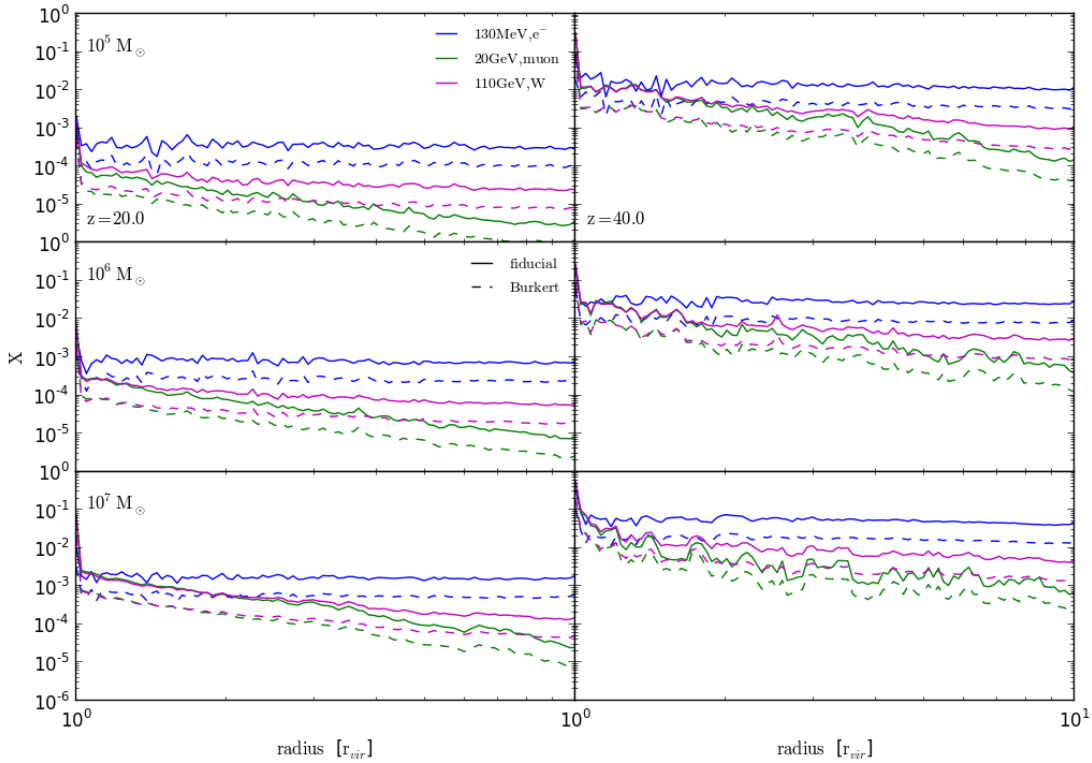

(b) Ionisation

Figure 6.14: The change in temperature, as a fraction of the mean gas temperature (plot a) and the change in the ionisation fraction (plot b) of the CGM due to dark matter annihilation. In each panel solid lines denote fiducial halo models and dashed the Burkert model. Blue, green and magenta lines respectively refer to the 130 MeV via electron/positron, 20 GeV via muons and 110 GeV via W boson annihilation models.

can be found on the left and at redshift 40 on the right. Blue, green and magenta curves respectively show results for 130 MeV via electrons, 20 GeV via muons and 110 GeV via W bosons dark matter models, while solid lines denote the fiducial and dashed the Burkert halo model.

In plot a), the increase in temperature is given as a fraction of the average background gas temperature. The energy input from the different dark matter models is comparable close to the virial radius where the gas density is elevated above the background average and diverges in the outer regions. As with a number of other properties related to the energy transfer efficiency of dark matter annihilation models previously discussed, this behaviour can be explained by considering the mean-free paths and interactions of the secondary cascade particles. While in all cases the filtered spectrum has been modified by the halo and now covers energies all the way down to the photo-ionisation limit, the precise behaviour and distribution of the low energy tail as well as that of the remainder of originally injected particles is still heavily correlated to that of the initial distribution. Therefore the energy peak of the dark matter model's nascent annihilation products remains a useful indicator in determining the relative effectiveness of the model to heat the CGM.

As was the case with heating the halo itself, injected particles will transfer energy to the gas surrounding the halo provided their interaction mean-free paths are comparable to the dimensions of the volume of interest. In addition the process the particle undergoes needs to either result in a collisional interaction with the gas or create a secondary particle to facilitate the energy transfer in that manner. However since the CGM deals with markedly reduced densities and therefore increased mean-free paths compared to the halo proper, the critical energies at which particles can make a meaningful contribution to the heating and ionisation process will differ to those discussed in that scenario. Briefly outlined below are some of the general trends governing the relative heating efficiency of the circumgalactic medium of different dark matter models.

- As can be seen in Figure 6.14 a) the most effective is the 130 MeV dark matter model annihilating via electrons/positrons. $\sim 10^8$ GeV electron/positrons produce IC photons with a energy peak at $\lesssim 10^3$ eV, so that even for the IGM densities photons have a sufficiently short mean free path to undergo photo-ionisation within a small volume around the point of injection. This means that energy is deposited efficiently along the trajectory of the parent particle and results in a near constant change in temperature outwards to 10 r_{vir} with only minimal upturn in the higher density regions near the edge of the halo.

- As the mass of the dark matter model increases the temperature change induced in the CGM decreases compared to the input from the 130 MeV model. This

is because for electrons/positrons with masses ~ 10^9 GeV the IC photon peak is raised to enter the Compton scattering regime. Photons in that energy range were shown in Figure 6.9 to not contribute to the energy deposition close to the edges of the halo. As the mass of the dark matter model is increased above this (to an annihilation product peak ~ 10 GeV) the up-scattered photons eventually become energetic enough to undergo pair-creation. However the secondary electrons and positrons fall into the regime where their respective IC photons sit below the photo-ionisation limit and electro-ionisation has become nigh on negligible so that their energy deposition is far less efficient than that of the 130 MeV cascade particle[11].

- Of course with the exception of the electron/positron channel, all dark matter models considered here produce a distribution of annihilation products so that even in the case of a unfavourable dark matter mass, at least part of the spectrum of injected particles will contribute to energy deposition. The relative effectiveness of the different annihilation channels will thus depend not only on which distribution injects the greatest number of electrons/positrons and photons but also favours energy ranges of particles that effectively interact with the gas.

- If sufficiently massive dark matter models such as the 80 and 110 GeV via W boson example are taken into account then the secondary electron/positrons population approaches the fiducial 10^8 eV energy range. Figure 6.14 a) indeed shows this model to be more effective[12] than the 20 GeV though less so than the actual 130 MeV model since as mentioned above, annihilation via W bosons produces a distribution of particle so that not the entire annihilation power is channeled into the ~ 10^8 eV energy range. The interaction rate of the remainder of the spectrum is enhanced by the increased gas density close to the virial radius and translates to a subtle upturn in the change in temperature, which can also be observed in the 20 GeV model.

- Comparing solid (fiducial) and dashed (Burkert) lines, the heating effect is also reduced for less concentrated halo models. Here however this is predominantly due to the profiles with high density cusps at their centre producing more annihilation power, rather than the variation in energy transfer efficiency of different particle distributions described in Figure 6.13.

[11] In principle there is a intermediate energy for which the associated IC photons pair-create low energy electrons and positrons which readily interact with the low density gas. However in that case a considerable portion of the original photon's energy is channeled into the mass of the resultant particles (M_{ele} = 0.51 MeV) and the overall energy input into the gas is thus reduced.

[12] It is worthy of note here that the difference in the models' heating efficiency only becomes pronounced further removed from the halo, while near the virial radius the two models are close to indistinguishable.

Overall the observations regarding the change in temperature for different dark matter models applies also for the change in ionisation fractions[13]. At redshift 20 the ionisation fraction of the CGM, especially for low mass halos is only increased marginally meaning that the assumption of treating the gas as neutral is valid over the entire Hubble time. On the other hand for halos at redshift 40 ionisation close to the virial radius is sufficient enough to impact the interactions the injected particles would undergo. As the ionisation fraction is increased the energy deposition partition becomes dominated by heating due to the onset of Coulomb scattering as opposed to ionisation for neutral gas. This suggests that the calculation for these halos actually underestimates the change in temperature and the change in δ_b presented in the next section. While this is not explored in this thesis, it provides further motivation for investigating the impact of dark matter annihilation on baryonic structure in a self-consistent manner in future work.

6.4 Raising the Jeans Mass

In the previous section the temperature increase of the circumgalactic medium due to heating from dark matter annihilation was calculated. These results show that this increase is at least comparable to the background gas temperature suggesting that this heating maybe sufficient to impact the accretion of gas onto the halo.

6.4.1 Change in δ_b

Using Equation 6.7 the new δ_b with dark matter annihilation can be calculated so that

$$\delta_{mod} = \frac{\rho_b}{\bar{\rho}_b} - 1 = \left(1 + \frac{6}{5}\frac{T_{vir}}{\bar{T}_g + \Delta T_{DM}}\right)^{3/2} - 1, \tag{6.22}$$

where ΔT_{DM} is the extra heating due to dark matter annihilation. The ΔT_{dm} used here is the average change in temperature taken over the first 5 radial bins from the results in section 6.3.

Figures 6.15 - 6.17 show the modified δ_b for $10^5 M_\odot$ halos at redshifts 20 and 40 and $10^7 M_\odot$ halo at redshift 20. In each figure, the different colours blue, red, green, magenta and black, correspond to the electron/positrons, muon, quark, tau and W boson annihilation channels. The panels, clockwise from the top left show results for the fiducial Einasto, Einasto-high mass concentration, Burkert-high and simple Burkert dark matter halo models. Lastly the different markers indicate the respective dark matter particle masses as indicated by the legend in the bottom left hand plot.

The results for the $10^5 M_\odot$ halos in Figures 6.15 and 6.16 suggests that for a number of dark matter particle and halo models the additional heating from dark matter

[13]On the scales and for the processes considered here, ionisation and heating can be treated as occurring concurrently

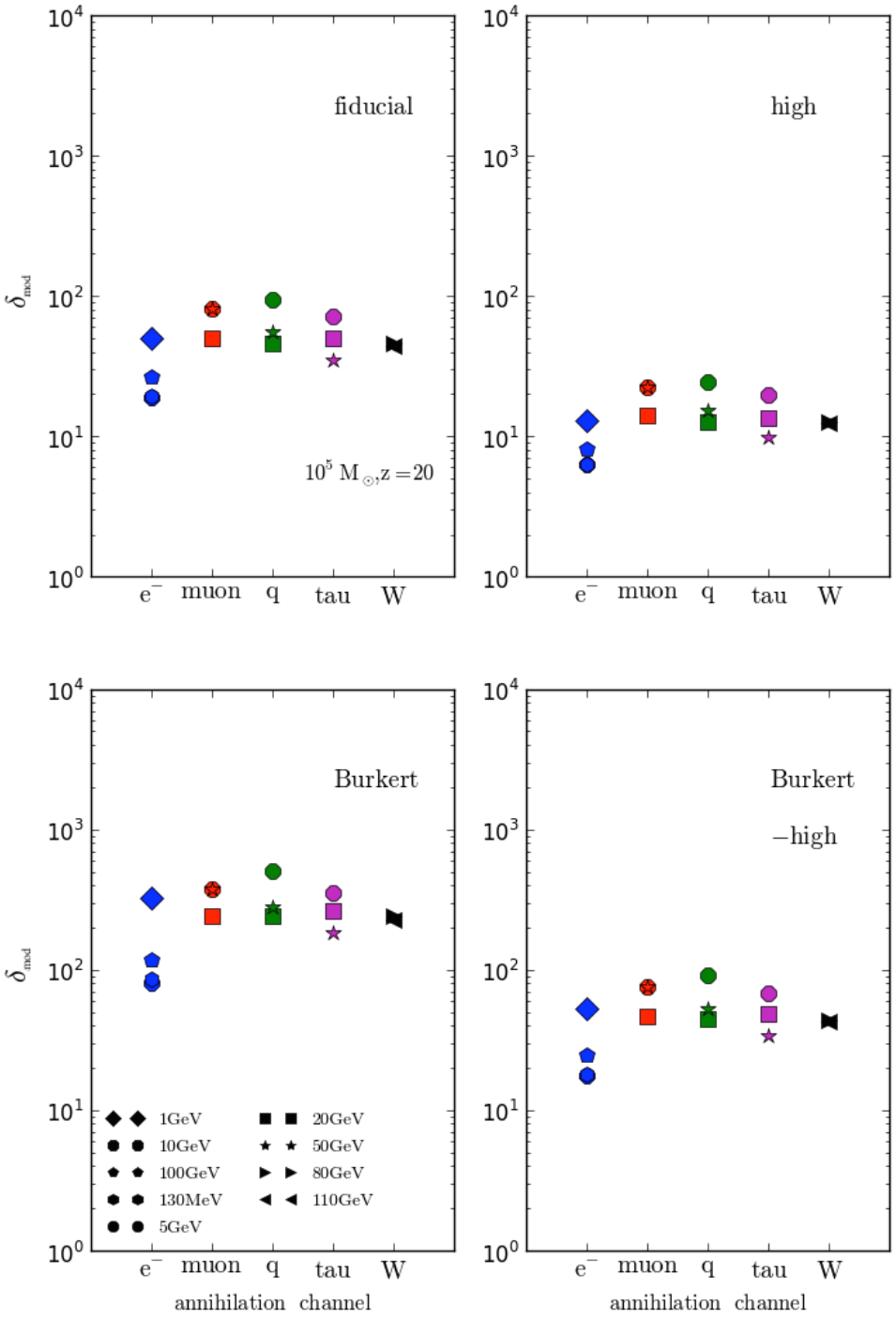

Figure 6.15: Modification of δ_b from dark matter annihilation for a $10^5 M_{sol}$ halo at redshift 20. Different colours correspond to different dark matter, and symbols to different dark matter masses.

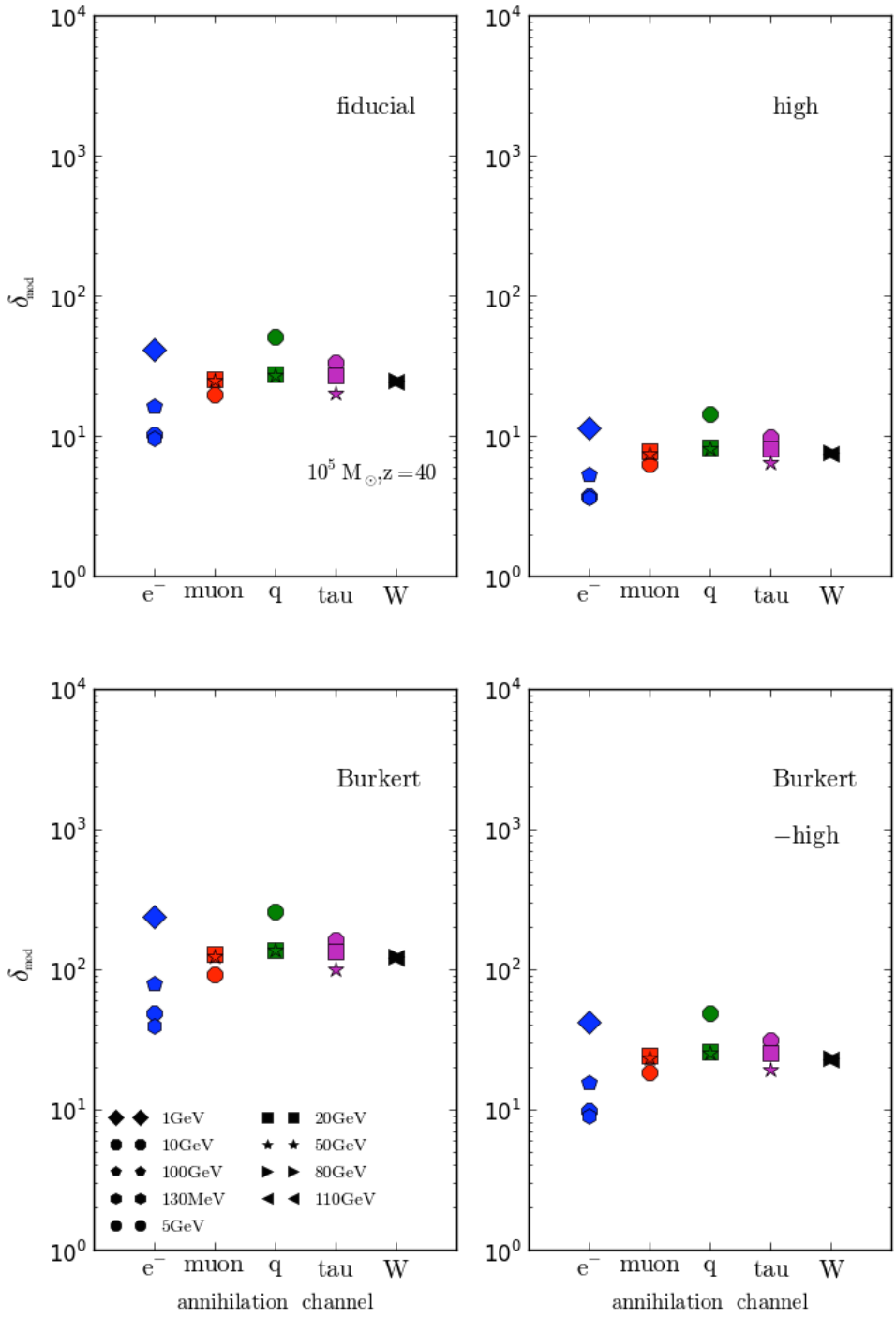

Figure 6.16: Modification of δ_b from dark matter annihilation for a $10^5 M_{sol}$ halo at redshift 40. Different colours correspond to different dark matter, and symbols to different dark matter masses.

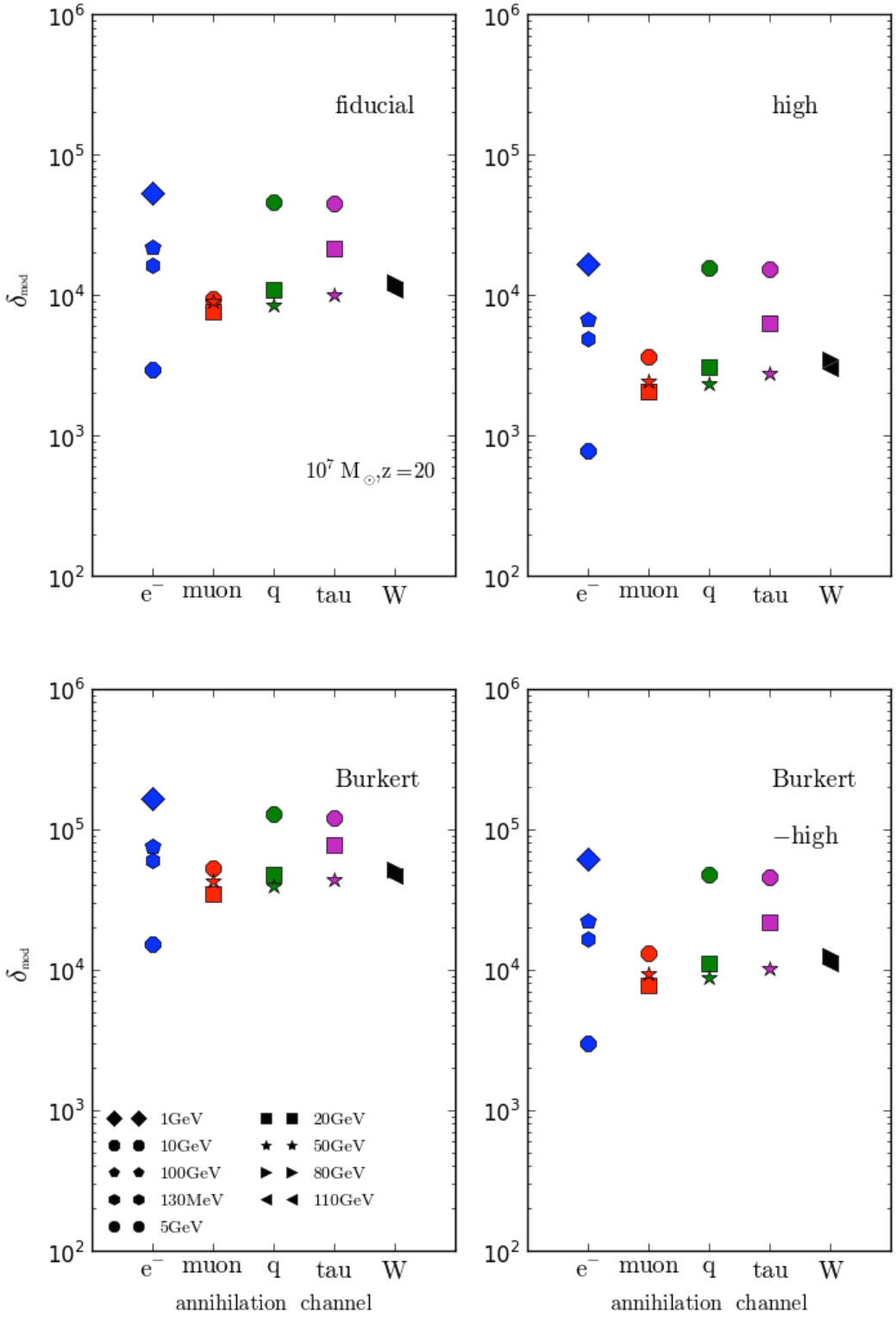

Figure 6.17: Modification of δ_b from dark matter annihilation for a $10^7 M_{sol}$ halo at redshift 20. Different colours correspond to different dark matter, and symbols to different dark matter masses.

annihilation will lower δ_b below 100. As expected this effect is most pronounced for the highly concentrated Einsto-High halo model due to the increase in annihilation power. In comparison results for the standard Burkert model show the impact to be reduced by about an order of magnitude. Understandably the fiducial model falls between the two extremes with the concentrated Burkert profile again producing results comparable to that of the fiducial model.

In terms of dark matter particles, the 130 MeV model annihilating to an electron/positron pair is the most effective in reducing δ_b due to both its efficiency in depositing energy into the gas locally and the fact that none of the annihilation energy is siphoned into neutrinos. Amongst the remaining annihilation channels heavier candidates provide a greater change in δ_b compared to models with masses from $1-5$ GeV. This is in keeping with the previous discussion which showed that electrons and positrons within that energy range produce IC photons which tend to free stream at IGM densities. Results for the halo at redshift 40 are qualitatively similar to those at redshift 20 but with δ_b reduced even further.

Figure 6.17 indicates that δ_b is not significantly impacted for the $10^7 M_\odot$ halo, though again the results are comparable to the lower mass cases in their general behaviour. However as was briefly alluded to earlier, the method of calculating δ_b does not take into account the virialization shocks surrounding the halos and for $10^7 M_\odot$ halos shock heating of the surrounding gas becomes significant. The derivation of δ_{mod} in equation 6.7 however assumes the gas temperature remains at the temperature of the IGM (which gives rise to the large δ_b in Figure 6.17) and therefore the method does not produce reliable results for halos of this mass.

6.4.2 Change in the Minimal Baryonic Mass

If δ_b is sufficiently reduced due to dark matter annihilation in $10^5 M_\odot$ halos at redshifts 20 and 40, what consequences does this suggest for the minimal baryonic objects? Figure 6.18 again shows the annihilation-modified δ_b though this time as a function of halo mass. The top panel shows the results at redshift 20 and the lower panel at redshift 40. In both plots the grey, horizontal line denotes $\delta_b = 100$ which gives the chosen critical value for the collapse of baryonic structures. Different coloured curves show the outputs for different halo/dark matter models.

Given a $\delta_b = 100$, a number of dark matter candidates would reduce the infall of gas onto the halo to a degree that potential baryonic structure formation could be effected. For the dark matter model with the most pronounced impact on δ_b, 130 a MeV particle with a concentrated Einasto profile (black curve), a $10^5 M_\odot$ halo would have to increase in mass by a factor of $2-3$ at redshift 20 and $4-5$ at redshift 40 to recover a δ_b of 100. It is again important to note that the large δ_b produced for halos with mass $>10^6 M_\odot$ arise due to the non-inclusion of shock heating surrounding the halos. However this

does not impact the conclusions drawn for the $10^5 M_\odot$ halos.

6.5 Summary

This chapter explored the heating of the circumgalactic medium due to dark matter annihilation within the halo. In order to understand how the emergence of baryonic structure, such as the formation of the first stars could be impacted by this, the response of the infalling gas to the additional dark matter heating source was calculated via δ_b (see Equation 6.7.) As with the heating of the halo itself, different dark matter density distributions and particles models are compared. In addition, the filtering effect had on the annihilation spectrum due to the injected particles interacting with various media as they travel through the halo, is also incorporated into the calculation.

As expected, more concentrated dark matter halo models will contribute more to the CGM heating due to their elevated annihilation rates caused by the high densities at their centres compared to those with flat-core dark matter profiles. There is also a secondary effect which makes concentrated models more effective as they allow for a greater number of photons to undergo ionisation as their energies reach the Compton regime. The subsequently created electrons are able to deposit energy close to the halo as opposed to the original photons which will free stream through the CGM at background gas densities.

For the models considered in this work, their behaviour and energy transfer efficiency is largely driven by mass of the dark matter particle which sets the peak of the annihilation products' energy distribution. The primary energy loss mechanism for the injected particles is inverse Compton scattering, which means that dark matter models which produce IC photons that readily interact with the CGM will provide greater energy deposition. Models which satisfy this criterium are the 130 MeV models annihilating via electrons/positrons and the more massive candidates ($\gtrsim 50$ GeV) for the other annihilation channels.

In this treatment $\delta_b = 100$ is chosen to set the limit for the collapse of baryonic objects, which indicates $> 50\%$ of the total gas that would have accreted if the gas pressure was neglected. For the dark matter halo and particle models exhibiting the greatest heating effect, a $10^5 M_\odot$ halo would have to increase in mass by a factor of $2-3$ at redshift 20 and $4-5$ at redshift 40 in order to recover $\delta_b = 100$.

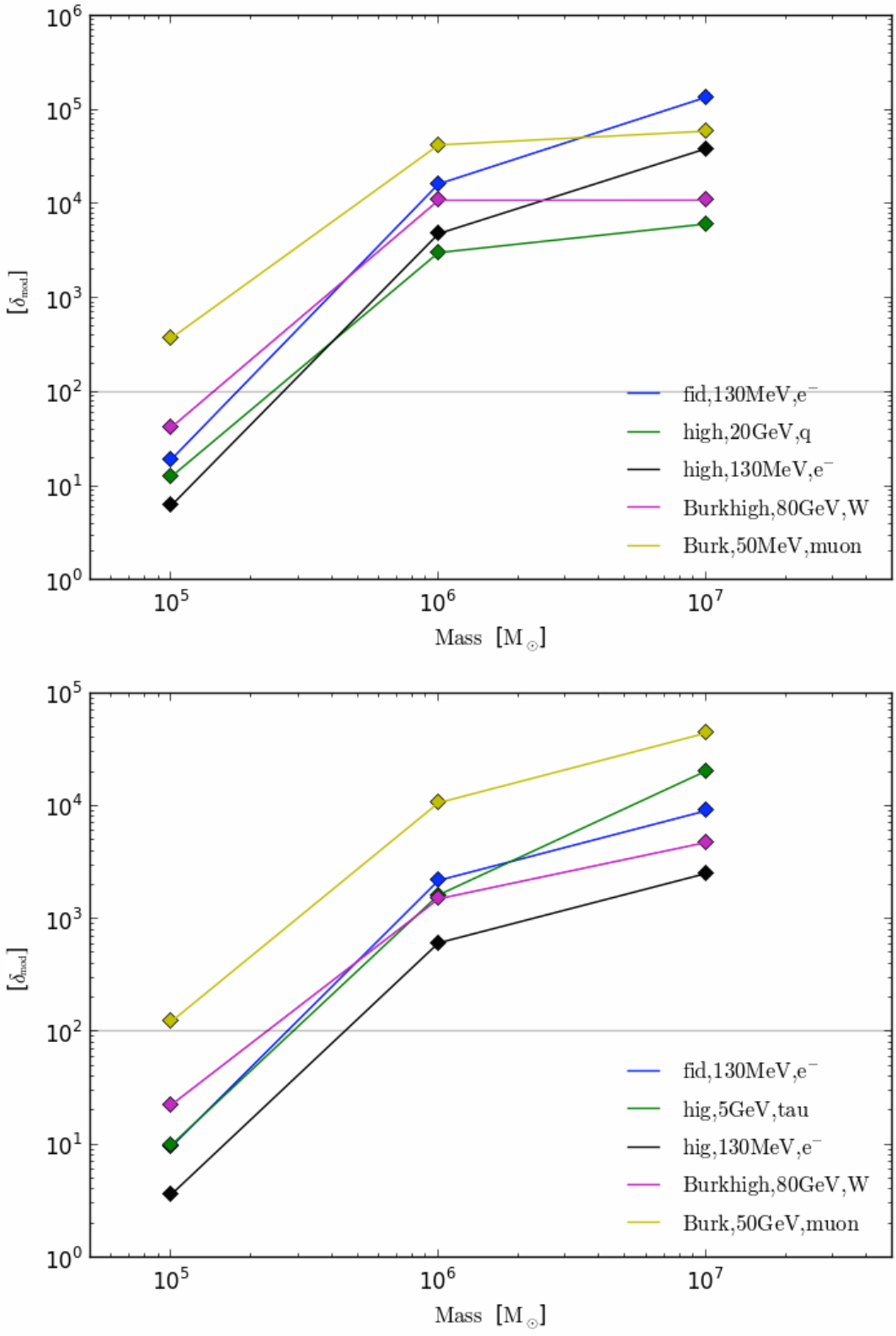

Figure 6.18: Modification of δ_b from dark matter annihilation for different halo masses and dark matter models. The grey horizontal line shows the critical δ_b chosen to indicate sufficient gas accretion onto the halo.

Chapter 7

Halos as non-isolated Objects

Up to this point dark matter halos have been treated as stable, self-contained objects, neglecting any potential impact from both the surrounding structure and annihilation energy coming from the IGM's diffuse dark matter component. Realistically these components will contribute to the heating of the halo and in this chapter the degree to which annihilation in the general environment of the halo encroaches on energy deposition from within the halo will be examined.

Before proceeding, recall how the existence of dark matter halos may directly and indirectly impact on the formation of baryonic structure and the evolution of the intergalactic medium. In particular the existence of secondary dark matter sources of energy deposition in and around halos, and potential complex feedback between annihilating dark matter and baryonic objects could be induced, depending on the relative strengths of these sources.

- Annihilation from the diffuse dark matter background primarily goes into heating and ionising the intergalactic medium. For details see for example Evoli et al. (2014), Slatyer et al. (2009), Furlanetto et al. (2006b), Belikov and Hooper (2009) and Mapelli et al. (2006), which includes discussion of redshifted deposition fractions, limitations due to degeneracies with astrophysical models, as well as the annihilation power boost from collapsed structure. In general the energy produced is assumed to be deposited uniformly, however since halos are dense objects, energy deposition at these sites would differ from the gas in the IGM. The integrated annihilation background thus provides an additional source of heating, especially at the edges of the halo.

- The potential for high redshift halos to heat both themselves and their surroundings was discussed in the chapters prior. In addition to depositing energy into the CGM, the escaped energy from the halo also provides ionisation and heating on top of that from the diffuse background. The precise manner in which dark matter halos ionise the surrounding gas shells would also distinguish itself from those produced by stars[1]. This is of particular relevance because the different

[1] Dark matter candidates tend to have much harder spectra than stars and thus heat gas more evenly.

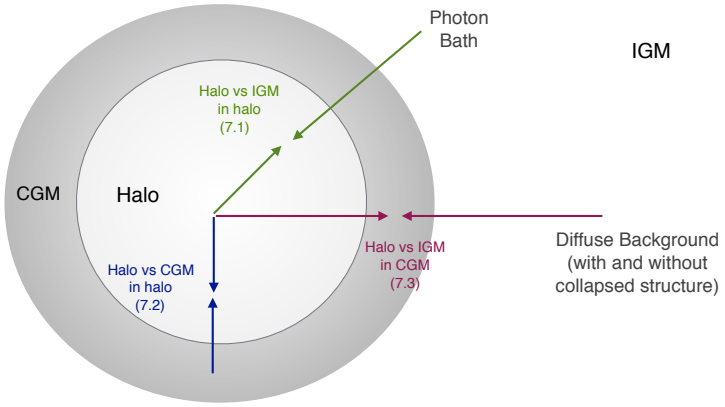

Figure 7.1: Overview of dark matter annihilation in and around high redshift structure.

topologies are imprinted in the 21cm power spectrum and an invaluable tool in characterising high redshift energy sources.

- Lastly, the halo is also subject to additional annihilation power from the dark matter in the immediate surroundings. In principal this process is like the supplementary heating from the diffuse background. Unlike that case however, the injected particles are assumed to be the same/ have the same energy distribution as the original annihilation spectra rather than the modified photon bath resultant from the integrated IC products that characterises the diffuse background (the details of which will be discussed further in the relevant section).

In investigating these secondary interactions it is important to keep in mind that these effects alone will most likely not be prominent enough to be measurable or be able to constrain dark matter models. However it is nonetheless important to establish whether these could instead have an accumulative impact when considered over for example, a self-consistent cosmological simulation, or effectively whether they can be neglected completely when calculating the holistic influence dark matter annihilation has on standard astrophysics. The remainder of this chapter will examine the additional heating of the halo from the CGM as well as the diffuse dark matter photon background, relative to that from the halo proper and is summarised in Figure 7.1.

7.1 Heating from Diffuse Background

First consider the energy input from the uniform dark matter background. Assuming the same self-annihilating type dark matter model as has been implemented up to this point, the power injected per unit volume can be written as

$$\bar{P}_{dm}(z) = \frac{c^2}{m_{dm}}\langle v\sigma\rangle \rho_{dm,0}(1+z)^6 \tag{7.1}$$

where $\rho_{dm,0}$ is the average dark matter density at redshift 0, and m_{dm} and $\langle v\sigma\rangle$ are the dark matter particle mass and velocity averaged annihilation cross-section as utilised previously. As has been shown in the analysis in earlier chapters, the high energy particles produced during the annihilation process do not transfer their entire energy directly to the gas at the point of injection. Instead "photons and e^+e^- injected around the electro-weak scale promptly convert the bulk of their energy into photons with energies lying within a redshift-dependent semi-transparant window where the dominant cooling mechanisms have timescales comparable to a Hubble time" (Slatyer, 2016). Therefore when dealing with the integrated energy input from the diffuse dark matter background, it needs to be taken into account that the effective distribution of this photon bath differs to that of the original annihilation products.

7.1.1 Photon Bath

As has been alluded to consistently throughout this work, the dominant mechanism via which high energy electrons, positrons and photons down-scatter their energy is through numerous inverse Compton scattering and electron/positron pair creation. The energy spectrum of the resultant photon bath however does not only comprise the immediate cascade products injected at that redshift. Given the extensive range of cooling times of the produced particles, there is also an accumulative, appropriately redshifted contribution from previous injections times.

Figure 7.2 shows the energy distribution Q, of the photon bath for (top to bottom) 1, 10 and 100 GeV dark matter candidates annihilating via muons (courtesy of Tracy Slatyer)[2]. Different coloured curves correspond to different redshifts with plots on the left in units of $\mathrm{d}N/\mathrm{d}E/\mathrm{cm}^3$ and plots on the right show the fraction of the total energy input. Regardless of dark matter mass, the distributions peak at $\sim 10^3 - 10^4$ eV since this is the threshold between IC Compton scattering and collisional interactions for electrons and positrons. Once the electromagnetic cascades have down-scattered to this

[2]The photon bath data was calculated using a fixed ionisation history of the universe that did not take heating and ionisation from dark matter annihilation into account. Fortuitously for the redshift parameter space examined in this work, the modification would be minimal. Furthermore the ionisation state of the IGM has less influence over the processes that drive the amassing of the diffuse photon background, (it does however impact the final energy deposition fractions). The photon bath number density used here also incorporated a boost factor from collapsed structure (see Section 7.3.1).

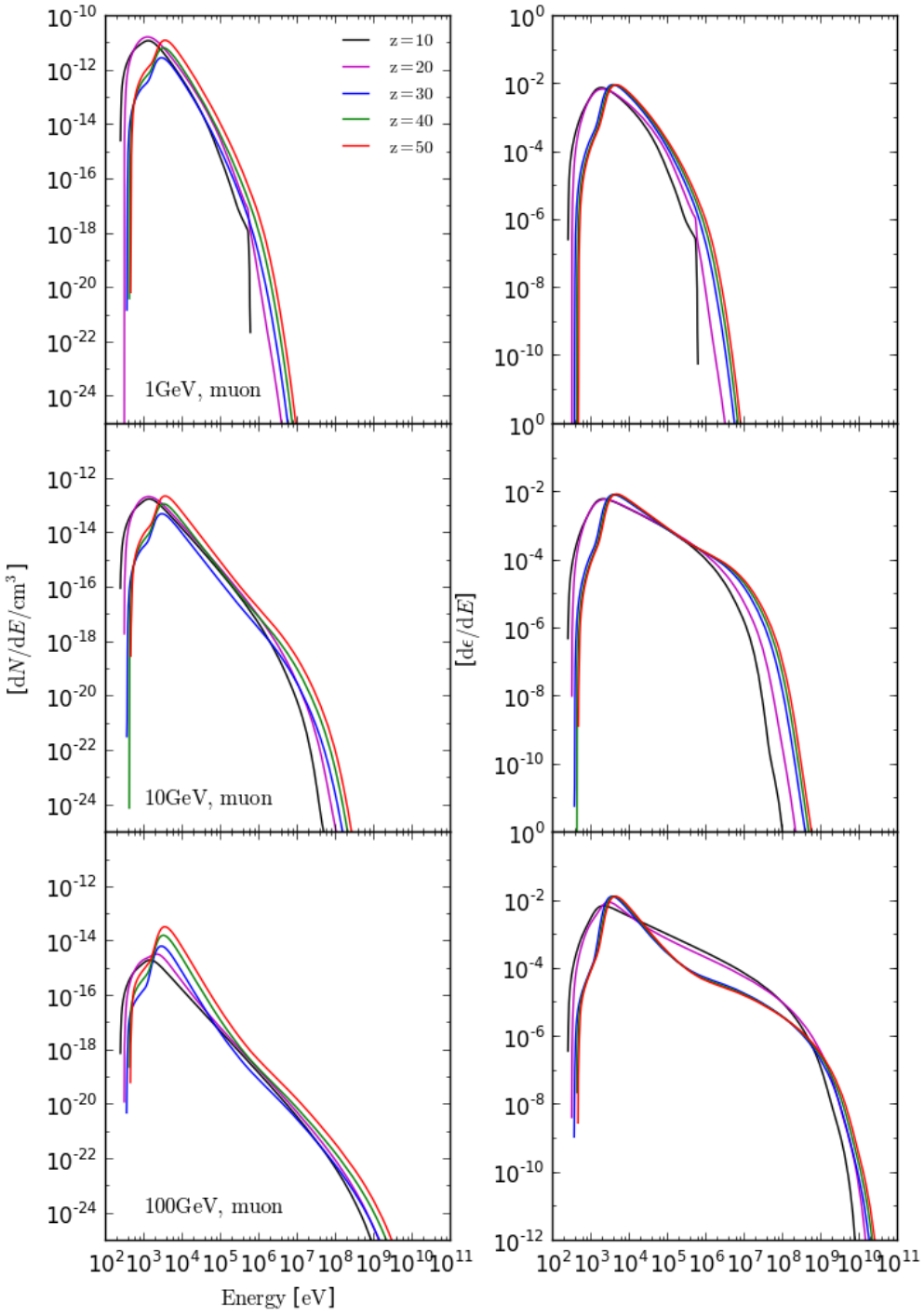

Figure 7.2: The number of photons per energy per unit volume from the diffuse dark matter annihilation background for 10^9, 10^{10} and 10^{11}eV dark matter particles annihilating via the μ channel. The spectrum of photons is shown at redshifts $10, 20, 30, 40$ and 50 in red, green, blue, magenta and black respectively.

point, the remaining particles' energy is rapidly subsumed by the IGM. As the energy of the dark matter particle increases, the photon bath distribution broadens to reflect the accompanying increase in energy of the annihilation products.

7.1.2 Code Outputs

Figure 7.3 shows the code output for the background photon impacting a $10^6 M_\odot$ halo at redshifts 20 (upper plot) and 40 (lower plot). In both plots a and b the top rows show the lower energy results with the high energy results in the bottom rows. Panels on the left plot the fraction of the particle's original energy, E/E_0, deposited at radius r_k while panels on the right show energy deposition in units of eVpc^{-3}.

The, at this point familiar, energy-dependent behaviour is also exhibited in these plots; photons with energy $\lesssim 10^3$ eV deposit all their energy promptly and thus don't propagate beyond the outer shells of the halo while for mid energy range photons energy transfer is sporadic as ionisation becomes inefficient. Once the photons undergo pair-creation, their energy deposition is regulated by the resultant electrons/positrons. When comparing redshifts, the photons at z = 40 will deposit their energy over shorter distances due to the heightened gas density. This is most evident in the ionising photons, and manifests through greater deposition fractions in the high energy photons.

7.1.3 Comparison

In order to compare the energy input from the two sources, the power into the halo from the diffuse dark matter background photon bath must first be calculated. The number density per unit volume of the photons, Q was given in section 7.1.1 so that the total heating from the flux of particles into the halo is given by

$$\mathfrak{H}_\gamma = 4\pi r_{vir}^2 c \sum_i Q_i E_i \mathbf{h}^\gamma_{i,r_{vir}}. \tag{7.2}$$

The ratio of heating from the halo and diffuse background is therefore

$$R_{\gamma,DM} = \frac{\mathfrak{H}_{DM}}{\mathfrak{H}_\gamma} \tag{7.3}$$

where $\mathbf{h}^\gamma_{i,r_{vir}}$ are the heating functions calculated in section 7.1.2 and the heating from the halo proper, $\mathfrak{H}_{DM}$ is taken from section 5.3.1 in Chapter 5. [3] Note that unlike the previous chapters which generally presented the energy input over the Hubble time, the comparison here (and following sections) is between the power from the two sources at

[3] Note there is a small discrepancy between the dark matter masses used for the diffuse background and the muon annihilation channel model used in the actual halo calculation. As the respective annihilation cross-sections are scaled to ensure the same raw power output for all models, the variation in $R_{\gamma,DM}$ is limited to the variation in the radial energy deposition fractions due to the different distributions of the annihilation products. For the differences in mass considered here these do not alter the behaviour at order of magnitude and subsequent conclusions drawn.

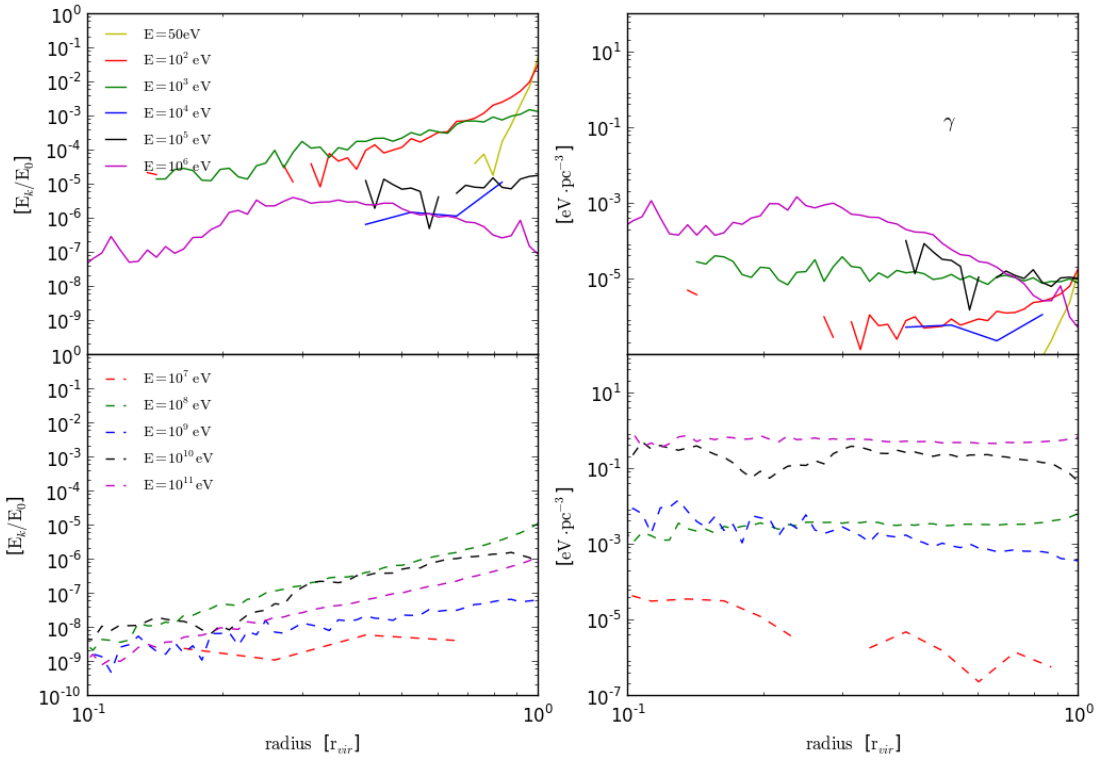

(a) z = 20

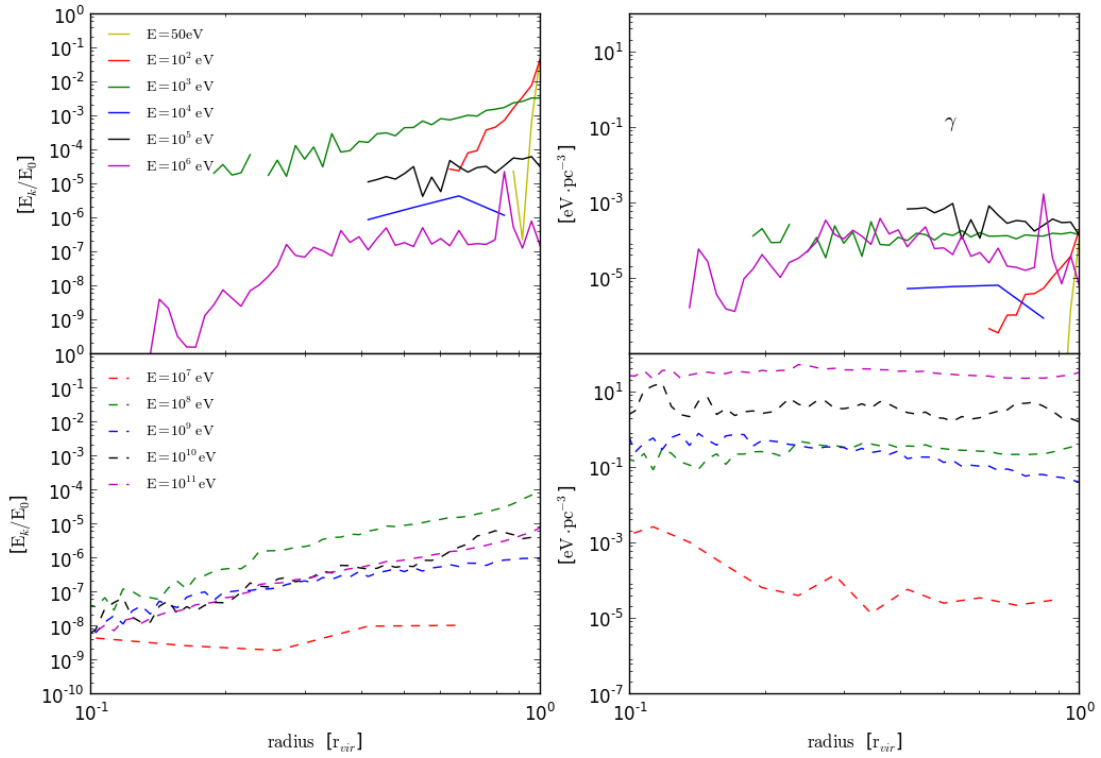

(b) z = 40

Figure 7.3: The energy deposition from photons from the diffuse dark matter background injected into a $10^6 M_\odot$ halo. The top plot shows the halo at redshift 20, the bottom at redshift 40. In all plots, data shows the energy going into heating, for clarity the lines showing ionisation have been omitted.

the relevant redshifts.

Figure 7.4 shows $R_{\gamma,DM}$ for the different halo masses, increasing in size from upper to lower panels. Again, plots on the left show the halos at z = 20 and 40 on the right. In each plot the blue, green and magenta curves correspond to the 1, 10 and 100 GeV dark matter model annihilating via muons. Solid lines show the fiducial halo model and dashed lines the Burkert model with fiducial mass-concentration relation.

For all halos, the heating from the halo proper dominates heating from the diffuse background. At redshift 40 this is by a factor of at least 10^4 and reduced to about 100 at redshift 20. In all cases $R_{\gamma,DM}$ increases towards the halo core since deposition from the diffuse background is mostly occurs close to the virial radius. As was shown in Figure 7.3, the $10^3 - 10^4$ eV photons, which comprise the peak of the photon bath distribution, are not sufficiently energetic to reach far beyond the outer shells, let alone the centre of the halo. While the high energy photons do cross the entire object, they only carry a small fraction of the total photon bath power, as was shown in Figure 7.2. In addition the radial distance at which the photon bath energy transfer is maximal coincides with that for the entire halo which further limits the impact potential of the dark matter annihilation photon background compared to in situ heating.

The decrease of $R_{\gamma,DM}$ with redshift indicates the possibility of the photon bath reaching parity or even surpassing[4] the heating from the halo at later cosmic times, in particular for the case in which halos are less concentrated (see dashed lines indicating the Burkert halo model). It should however be kept in mind that when extrapolating to lower redshifts in general, halos would be expected to host stars and galaxies which would drastically alter the relevant energy scales and thus the potential impact made by dark matter annihilation.

7.2 Heating from the CGM

As a comparison to the calculation of heating from the diffuse photon bath, the contribution from the dark matter in the immediate surroundings of the halo is now examined. While the former gave the accumulated energy input from the total dark matter background, the latter will help determine to what degree the local environment of the halo needs to be taken into consideration when incorporating dark matter annihilation into its evolution.

7.2.1 Code Outputs

The injected particles in this scenario are just the same as the previously presented dark model annihilation products. Figure 7.5 shows the deposition curves for electrons and positrons impacted onto the halo from the virial radius for a $10^6 M_\odot$ halo. Figure 7.3

[4]The reduced average densities at lower redshifts would lessen the self-heating of dark matter halos and also lead to the enhancement of the photon bath due to the increase in cooling times and the continuous build up from dark matter annihilation at preceding redshifts.

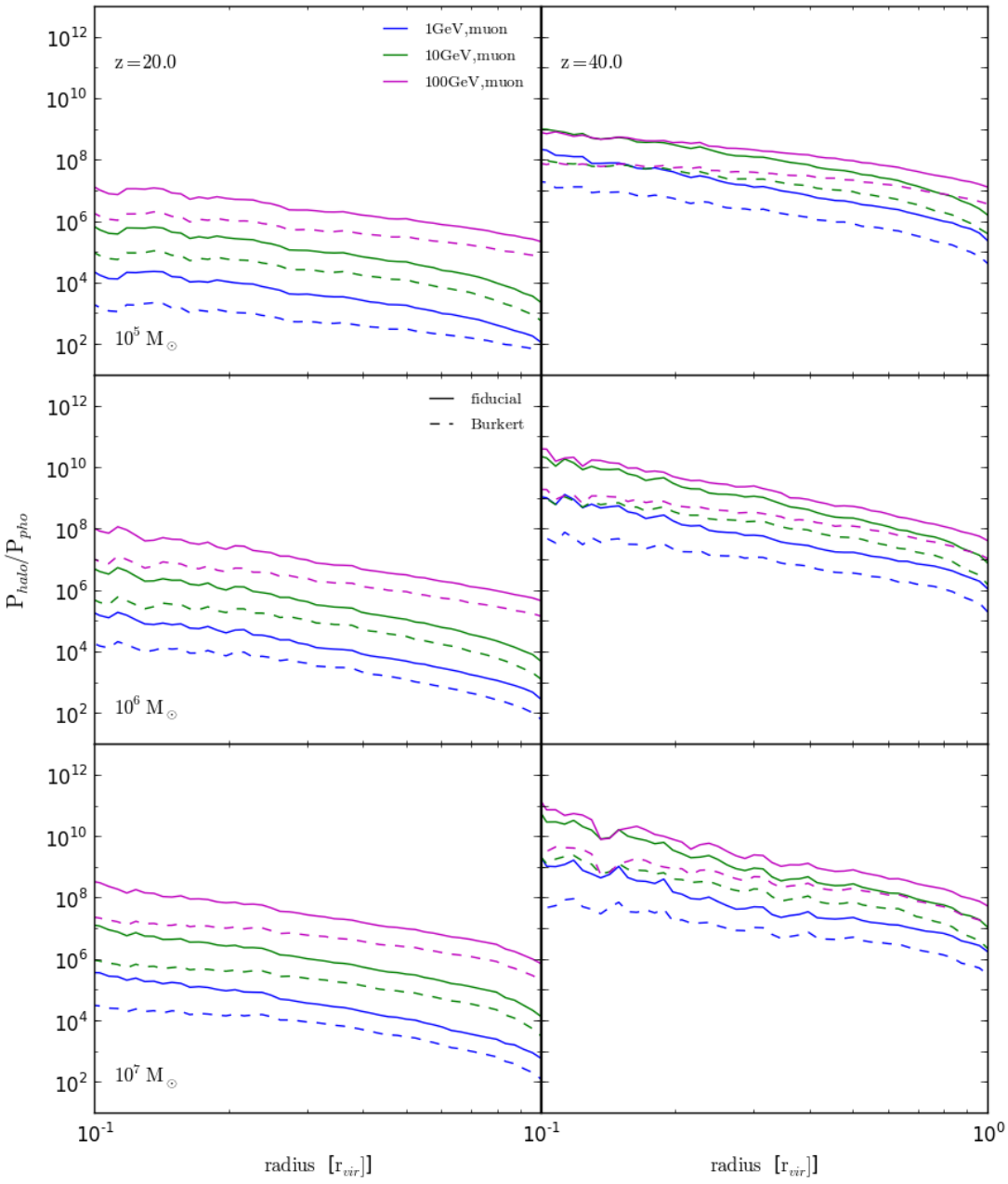

Figure 7.4: Comparison of heating rates of the CGM from the halo and diffuse dark matter background.

shows the equivalent for photons. As before, results for redshift 20 are shown in the upper plot a) and for redshift 40 in the lower plot b). In each plot, the upper panel shows the code outputs for 10^5-10^7 eV and lower 10^8-10^{11} eV particles, while left hand plots the deposition fraction at r_k and the right heating/ionisation in unit of eVpc^{-3}. Solid lines show energy into heating and dashed into ionisation.

The energy-dependent behaviour of the electrons/positrons follows the detailed description in earlier chapters. As was the case with the photons, the ability of the particle to penetrate the halo is limited by collisional processes. Once particles are sufficiently energetic to exclusively undergo IC scattering, the original trajectory is retained and energy can also be deposited in the inner parts of the halo. However for a particle entering from the virial radius, the centre of the halo only subtends a small solid angle meaning that energy transfer even for high energy electrons/positrons remains at the edges and outer parts of the halo.

7.2.2 Comparison

For the heating contribution from the dark matter surrounding the halo, an upper limit can be written as

$$\mathfrak{H}_{CGM} \leq \sum_{i,r_{vir},k}^{\alpha} f_{\alpha,i} \mathbf{h}^{\alpha}_{i,r_{vir},k} \cdot \int_{r_{vir}}^{10 r_{vir}} \bar{P}_{dm}(z) \tag{7.4}$$

where $\bar{P}_{dm}(z)$ is the dark matter annihilation power of the diffuse background per unit volume as defined in Equation 7.1, $f_{\alpha,i}$ the weights for the different dark matter models' annihilation products as per Chapter 5 and $\mathbf{h}^{\alpha}_{i,r_{vir,k}}$ are the deposition fractions for particles injected at the virial radius presented in section 7.2.1. The latter are taken as the upper limit for energy transferred by particles injected at radii further removed from the halo. The ratio comparing the heating from the CGM to that of the halo proper is then

$$R_{CGM,halo} \geq \frac{\mathfrak{H}_{halo}}{\mathfrak{H}_{CGM}} \tag{7.5}$$

with $\mathfrak{H}_{halo}$ the heating from annihilation within the halo for the equivalent dark matter model.

The results are shown in Figure 7.6, where as before halos at redshift 20 are on the left and 40 on the right with panels from upper to lower showing 10^5, 10^6 and $10^7 M_\odot$ halos. Blue curves show the 130 MeV dark matter model annihilating to electron/positron pairs, while green refers to the 5 GeV via muon model. As before solid lines show the fiducial halo model and dashed lines halos with a Burkert profile and the fiducial mass-concentration relation.

At a glance, Figure 7.6 illustrates that heating and ionisation of the halo due to dark matter annihilation in its immediate environment is negligible compared to the annihilation from the halo itself. Otherwise the overall qualitative behaviour is comparable

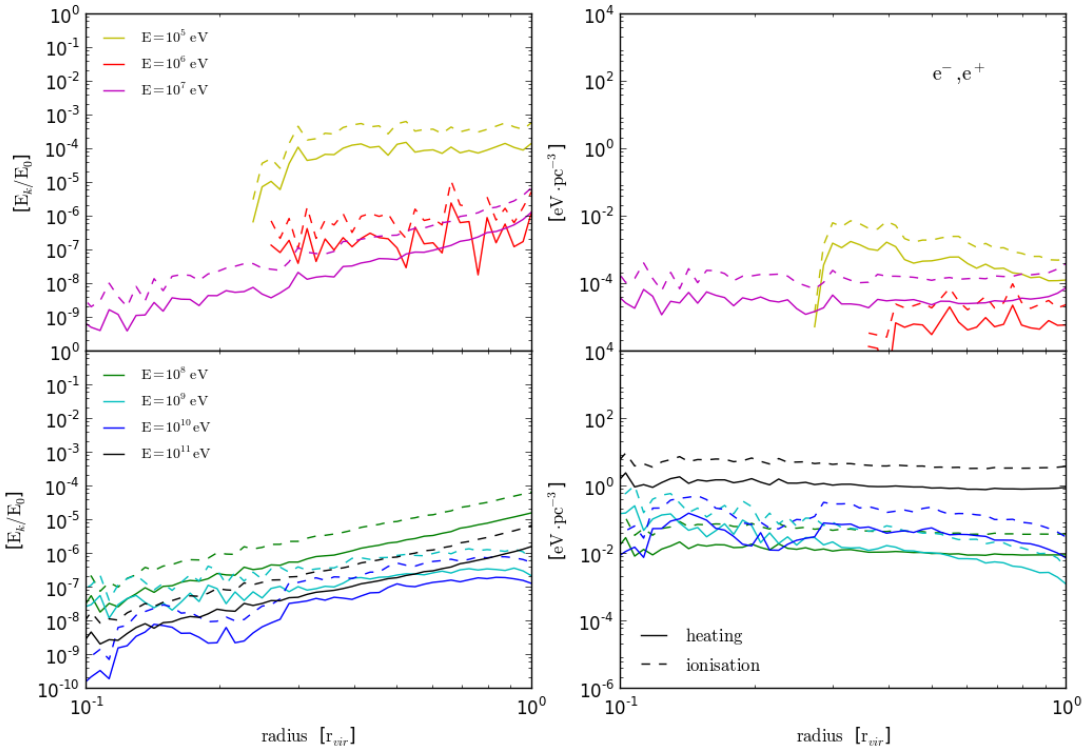

(a) z = 20

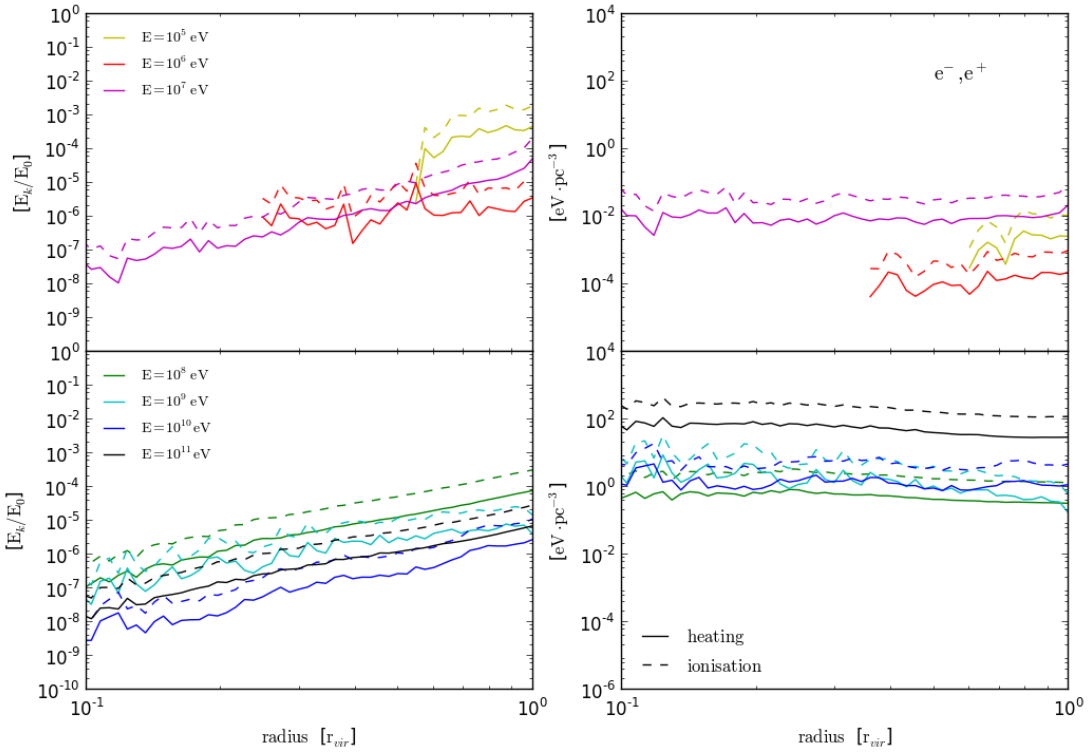

(b) z = 40

Figure 7.5: The energy deposition for electrons/positrons injected from the CGM into a $10^6 M_\odot$ halo. The top plot shows the halo at redshift 20, the bottom at redshift 40. In each plot, solid lines show the energy going into heating and the dashed into ionisation.

to that of the diffuse background in so far as $R_{CGM,halo}$ increases towards the centre underscored by the injected particle's limited coverage of the inner halo. The difference between the two heating sources is also amplified at high redshifts though the contrast is not as severe as for the previous comparison since there is no equivalent accumulation of annihilation particles as there is for the diffuse photon bath.

7.3 Comparison of Heating Sources of the CGM

To conclude this chapter's examination of the prominence of different dark matter annihilation sources, the contribution from the halo and the diffuse background are compared in the context of the circumgalactic medium. The halo driven heating of the CGM for different dark matter models has already been calculated and it remains to present the energy deposition due to the background dark matter distribution which is taken from the literature.

7.3.1 Diffuse Background

Recall Equation 7.1 gives the annihilation power of the diffuse dark matter background, though in general for the high energy annihilation products associated with dark matter annihilation at the electro-weak scale the entirety of the energy produced is not absorbed "on the spot" by the gas. Let the energy deposited into the IGM at redshift z from a particle of type i, created at z' be given by a set of functions $g_i(z, z')$.

$$\mathfrak{H}_{Diff} = \sum_i \int_z^{\sim 1000} g_i(z, z') \mathrm{d}z' \int \bar{P}_{DM}(z) \mathrm{d}V \tag{7.6}$$

in the case were energy deposition is assumed to effectively take place on the temporal spot, the expression simplifies to

$$\mathfrak{H}_{Diff} = \sum_i g_i(z, z') \int \bar{P}_{DM}(z) \mathrm{d}V. \tag{7.7}$$

The heating functions $g_i(z, z')$ are given by a number of authors including Natarajan and Schwarz (2010), Valdes et al. (2010), Evoli et al. (2012) and Slatyer (2016).

Boost Factor

Collapsed structure present a significant enhancement in dark matter annihilation power over that of the diffuse background. The expression for the background power presented in Equation 7.1 however only included the universe's smooth dark matter content. The power from the dark matter in collapsed structure can be written as,

$$P_B(z) = \frac{c^2}{m_{dm}} \langle v\sigma \rangle \int_{M_{min}}^{M_{max}} \left(\frac{\mathrm{d}n}{\mathrm{d}M}(z, M)(1+z)^3 \int_V \rho_{DM}^2(r, M, z) \mathrm{d}V \right) \mathrm{d}M \tag{7.8}$$

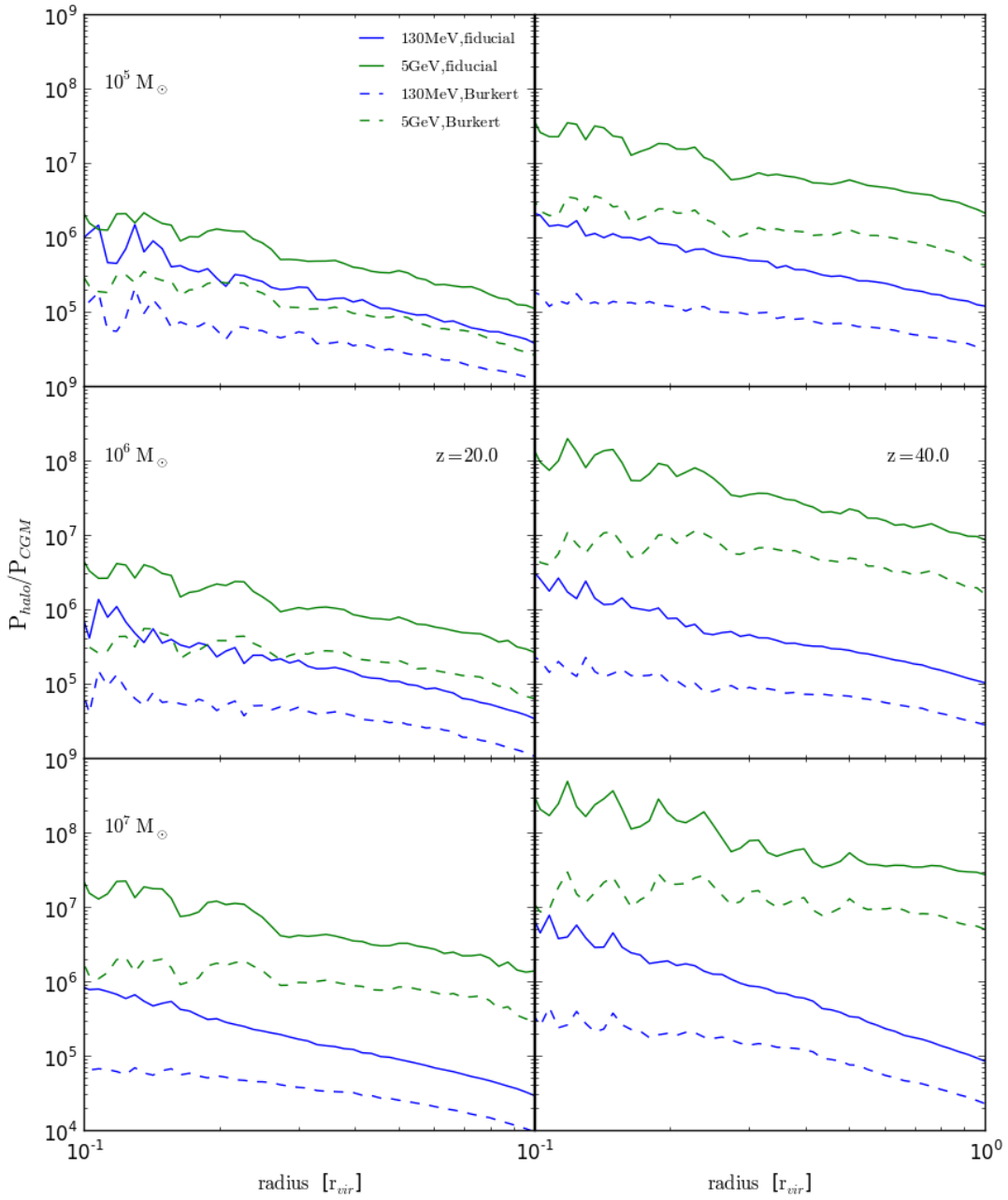

Figure 7.6: Comparison of heating rates within the halo from the halo itself and the CGM

where $\mathrm{d}n/\mathrm{d}M(z, M)(1+z)^3$ is the proper number density of dark matter halos and $\rho^2_{DM}(r, M, z)$ is the density profile of said halos.

In order to incorporate the non-uniform dark matter component, the annihilation power from the fraction of matter in collapsed structure needs to be calculated. However as a very good first order approximation the total annihilation power can simply be written as the sum of the diffuse and collapsed component.

$$\begin{aligned} P_{tot}(z) &\approx \bar{P}_{DM}(z) + P_B(z) \\ &\approx (B(z)+1)\bar{P}_{DM}(z) \end{aligned} \tag{7.9}$$

where a convenient way to express this is via a multiplicative boost factor $B(z)$. Figure 7.7 shows the boost in annihilation power gained from collapsed structure. The black curve shows the power (in units of $\mathrm{eV}s^{-1}$ per atomic nucleus) from the diffuse background alone while the coloured curves show the boost factor from Evoli et al. (2014) for different minimal halo masses. One point of interest is how the choice in M_{min} alone can increase the boost factor by an order of magnitude. In fact which M_{min} is adopted, along with a number of other model parameters, is a major point of contention when it comes to quantising the contribution to the overall annihilation power from collapsed structure.

In general boost factor calculations (Lopez-Honorez et al., 2016; Evoli et al., 2014; Bovy, 2009) extrapolate dark matter halo models down to some chosen representative minimal halo mass. As was already briefly illustrated in Figure 7.7, a major caveat to consider when performing these calculations are the striking variations that arise from inference made about the smallest dark matter halos. Besides the low mass limit, the most pressing question is perhaps whether a halo model intended to describe massive clusters or galaxies is also a valid representation of halos at the other extreme of mass scale. Moreover, uncertainties in the precise density distribution of dark matter halos that already persists at the lower mass range for structure hosting objects, especially at high redshifts. The implications of this can be seen in Figure 6.15 which shows how much dark matter annihilation input dependent results can vary with only moderate changes made to the density profile or mass-concentration relation. Extending these to lower masses will have similar, if not amplified outcomes and boost factor reliant results should be regarded with that in mind. (For further discussion on the topic see Mack (2014)).

7.3.2 Comparison

As before let

$$R_{diff,halo} = \frac{\mathfrak{H}_{halo}}{\mathfrak{H}_{diff}} \tag{7.10}$$

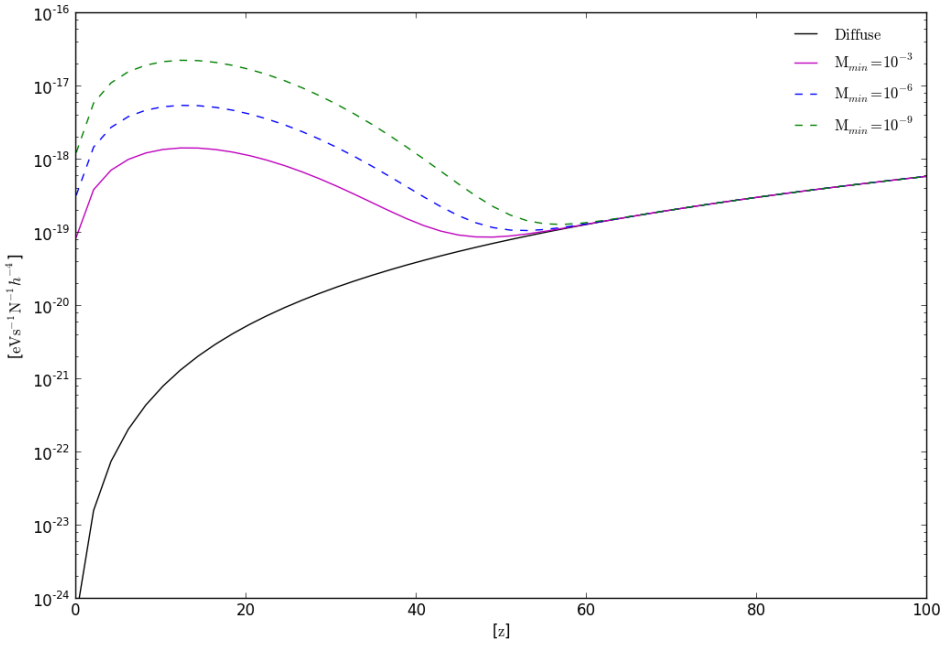

Figure 7.7: Power from dark matter annihilation in the diffuse medium, with and without the boost factor from collapsed structure. Black curve shows the diffuse background alone, and magenta, bus and green curves show the power with boost factor extended to include different minimum halo masses.

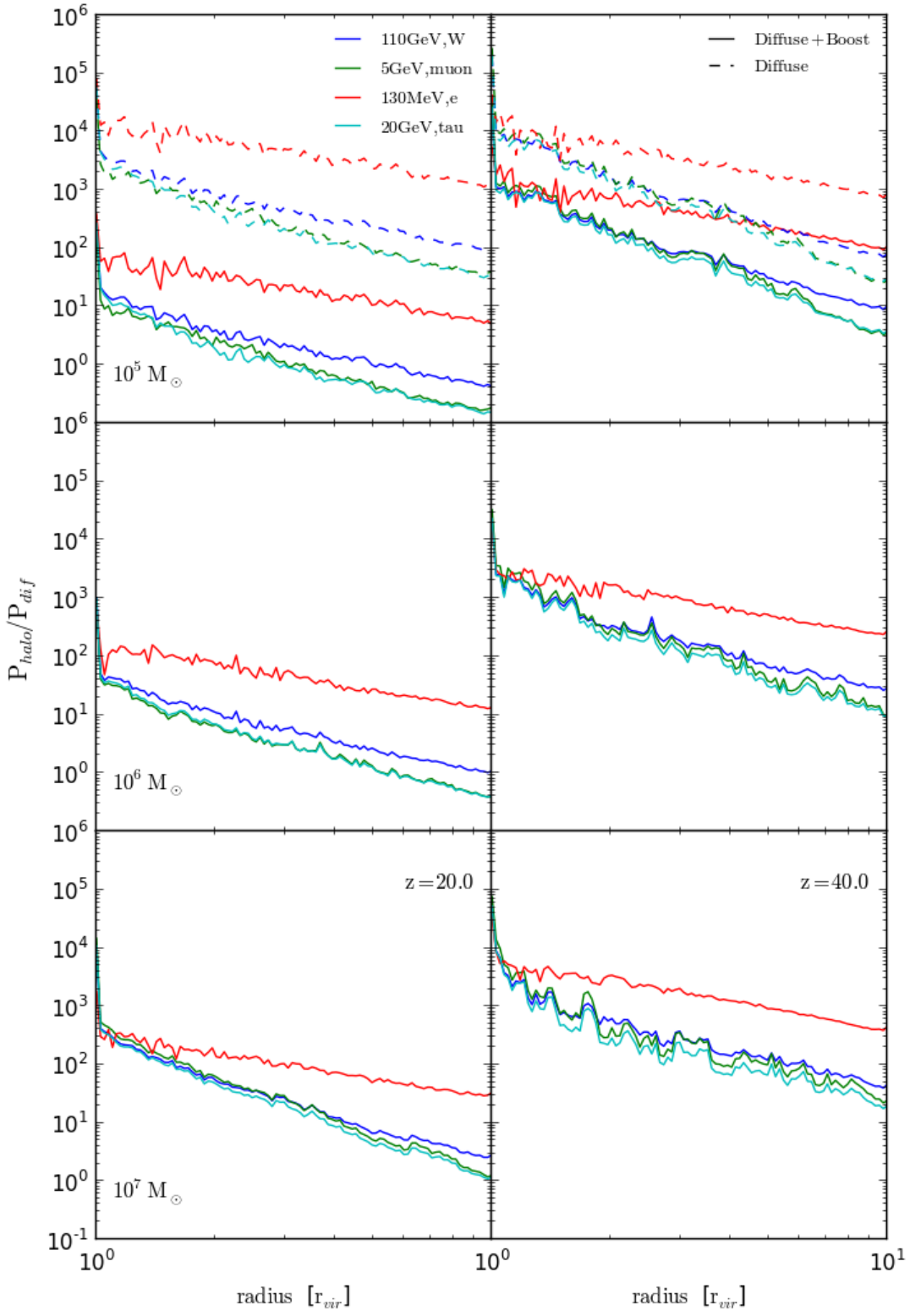

Figure 7.8: Comparison of heating rates of the CGM from the halo and diffuse dark matter background.

give the ratio between heating of the GCM from the halo proper and the diffuse dark matter background. Figure 7.8 shows $R_{diff,halo}$ where the deposition functions $g_i(z, z')$ and boost factor $B(z)$ with $M_{min} = 10^{-3}$ where taken from Evoli et al. (2012) and Evoli et al. (2014). The plots for the different halos are distributed as with the previous comparison figures with different coloured curves showing different dark matter models. Here however, solid lines denote $R_{diff,halo}$ with the boost factor included, while for the $10^5 M_\odot$ halos the diffuse background without collapsed structure is also shown for reference.

At redshift 40 the power from the halo dominates over the diffuse background heating up to $10r_{vir}$, with and without the contribution from collapsed structure. This holds for the range of dark matter models chosen to present the range of masses and different annihilation channels used in this work. The 130 MeV model, as was observed previously, provides more efficient heating further removed from the halo compared to the other models due to the readily interacting, ionising photon it produces through IC scattering.

In contrast at z = 20, and in particular in the case of the $10^5 M_\odot$ halo, the two heating sources become comparable within $10r_{vir}$. While more significant in relation to the input from the halo than that scenario, there is a parallel to the comparison with the diffuse photon bath insofar as they both suggest a more influential role played by the background annihilation as opposed to local structure at lower redshifts. The comparison between the diffuse only (dashed line) and boost factor included terms (solid line) again shows that collapsed structure comes to dominate the total dark matter annihilation input into the IGM .

7.4 Summary

In this chapter secondary heating sources of both the halo and the circumgalactic medium were compared. For the halo proper, additional energy input due to the photon bath from the diffuse dark matter background, as well as the dark matter component in the immediate environment of the halo were calculated. For the CGM the energy input from the halo was compared to the diffuse background heating of the IGM where the boost factor from collapsed structure was also taken into account. In both cases heating and ionisation from the dark matter halo itself presented the dominant source of energy being deposited into the gas, regardless of dark matter particle model used. In all cases the halo dominated behaviour becomes less pronounced at lower redshifts since for the dark matter masses considered here, reduced densities produce environments that are less favourable to energy deposition over scales comparable to the size of halos. In contrast the build up of collapsed structure boosts the annihilation power from the integrated dark matter background.

While these results are somewhat perfunctory in nature, they do have some poten-

tially useful consequences. Both in case of detailed modelling of dark matter annihilation induced modification of baryonic structure in individual halos and the wider integration of dark matter annihilation into cosmic simulations, halos can be treated (at least for the parameter space considered here) as isolated objects insofar as they are predominantly heated by their own dark matter content. In addition, the non-uniform manner in which halos ionise the IGM above that from the diffuse background is of interest as this could provide a qualitatively distinct signature to those from stars in the 21cm power signal. The details of this as well as the observational potential of 21cm physics is discussed further in the next chapter, along with a summary and concluding thoughts on this work.

Chapter 8

Concluding Thoughts

8.1 Summary of Outcomes

Astrophysical settings present new and promising avenues to explore and constrain the fundamental nature of dark matter. With the development of next generation radio telescopes, searches for signatures from dark matter annihilation and decay in global signals such as that from the 21cm hydrogen line have drawn particular interest.

In this thesis, dark matter annihilation in and around high redshift dark matter halos was examined. In particular the work conducted aimed to provide detailed treatment of the energy transfer process, determine the potential for the disruption of baryonic structure formation and compare the relative importance of different sources of annihilation power. Presented below are the key findings of this work as well as some final thoughts on future work and prospects for future detection. Figure 8.1 shows plots representative of the results.

8.1.1 Self-Heating Dark Matter Halos

To gauge the potential for self-heating of collapsed structure due to dark matter annihilation, a simplified energy transfer model was implemented that allowed for a broad parameter space to be investigated (see Chapter 4 and the first plot in row two of Figure 8.1). Variation due to uncertainties in both the underlying dark matter particle and halo models was also accounted for. Different masses (5, 50 and 80 GeV) and annihilation channels (via quarks, muons, tau and W bosons) were compared for the dark matter model. The PYTHIA code was used to simulate a realistic spectrum of annihilation products for the various annihilation channels. The density distribution of small, high redshift halos is not as strongly constrained as their low redshift counterparts, so different dark matter profiles (NFW, Einasto and Burkert) and mass concentration relations were also considered.

- The density concentration of the halos had the greatest impact on the total annihilation power produced with cusp like profiles and high mass-concentration parameters produce up to 10 times more energy than those with flattened and/or less concentrated profiles. In particular, extrapolating the mass-concentration

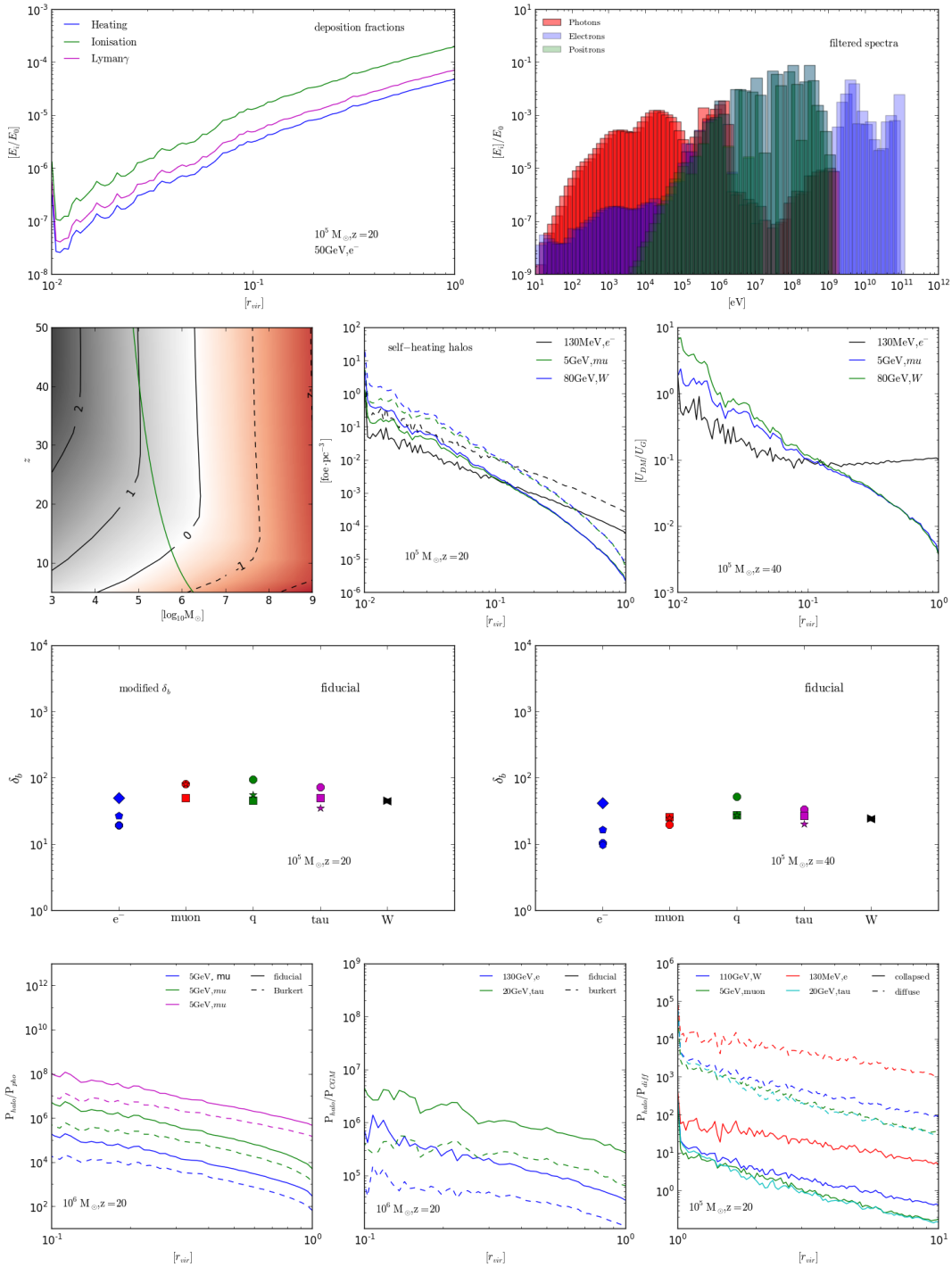

Figure 8.1: Summary Plot

relation to very small, high redshift halos leads to unrealistically concentrated objects.

- For the energy transfer treatment employed in Chapter 4, the most important factors governing efficiency of dark matter models are the particle mass (for a fixed, velocity averaged annihilation cross-section) and the fraction of annihilation power channelled into electrons, positrons and photons as opposed to the non-interacting neutrinos.

- The deposited energy partition into heating, ionisation and Lyman photons was estimated using a secondary particle absorption fraction f_{abs} and the MEDEAII code. (This treatment does not record the spatial distribution of the deposited energy nor the evolution of the secondary particles produced via IC scattering, the dominant energy loss mechanism for the injected particles.)

- The total heating due to dark matter annihilation over the Hubble time and the gravitational binding energy of the halo was then compared. When taking into account molecular cooling, it showed that for halos with mass between 10^5 and $10^6 M_\odot$ halos above redshift 20, the energy input from annihilation dominates and structure formation could potentially be disrupted.

8.1.2 Energy Transfer Code

The first order treatment of particles injected into the halo does not follow the secondary particle created through IC scattering and pair creation off of the gas and CMB photon field, instead using a factor f_{abs} to estimate the final energy transfer. In order to improve on the energy transfer treatment, a Monte Carlo code was created to evolve the full particle cascade (Chapter 3).

- The code also allows for an arbitrary, three dimensional number density distribution of atomic hydrogen, helium, free electrons and CMB photons for the injected particles to interact with. It allows for the fraction and location of energy deposited into heating, ionisation and Lyman photons to be calculated for a predefined volume.

- Interactions taken into account for photons are photo-ionisation, Compton scattering and pair-creation off of the atomic and CMB field.

- Electrons can undergo eletro-ionisation, excitation, Coulomb scattering, recombindation and IC scattering. Annihilation via positronium formation is incorporated for positrons in addition to the electron-interactions.

- The code was used to calculate the radial heating and ionisation of 10^5, 10^6 and $10^7 M_\odot$ halos at redshifts 20 and 40. The code also calculates the energy distribution of the particles escaping from the halos. These results were then used to calculate the heating of the circumgalactic medium as well as in the comparison of different heating sources in and around the halo. (See top row of plots in Figure 8.1.)

8.1.3 Self-heating Dark Matter Halos Revisited

The self-heating of halos in the parameter space of interest identified in previous work was re-examined in Chapter 5 using the updated halo energy transfer code, as well as mass-concentration relation and baryonic density distribution. An additional 130 MeV dark matter model annihilating via electron/positron pairs was also introduced.

- The detailed energy transfer treatment of the secondary cascade particle illustrates how the energy transfer efficiency varies with particle energy. The dominant process via which electrons/positrons lose energy is IC scattering (with photons first undergoing e^-/e^+ pair creation). The mean-free path of the up-scattered IC photons is therefore crucial to energy deposition. An injected particle with sufficient energy leading to the production of a secondary particle with a mean free path less or comparable to the virial radius of the halo will allow for energy to be deposited in the gas.

- In the previous work the choice of annihilation channel influenced outcomes predominantly through the fraction of the total annihilation power partitioned into electrons/positrons and photons, as opposed to the non-interacting neutrinos. Since the updated energy transfer method is sensitive to the energy dependent mean-free path, both the dark matter particle mass (for an annihilation cross section adjusted to give the same total power integrated over the halo) and choice of annihilation channel also impact on the overall energy deposition by changing the energy distribution of annihilation products. (See the second and third plots in the second row of Figure 8.1.)

- Overall the broad conclusions drawn in the earlier calculation are supported in the detailed study, including the comment regarding higher total annihilation power from more concentrated halos and the existence of a parameter space in which dark matter annihilation could modify baryonic structure formation.

- When looking at the radial comparison of the dark matter heating and the gravitational binding, the dark matter effects are more pronounced close to the centre of the halo due to the higher energy transfer fascillitated by both the higher gas

densities and the dark matter annihilation rates. For most dark matter models the energy deposition becomes less efficient in the outer parts of the halo with the exception being the 130 MeV model (or those models producing leptons in that energy range as secondary particles) annihilating via electrons/positrons which was chosen specifically to provide IC photons that interact and is able to provide heating even in the less dense outer regions of the halo.

- Most of the energy produced by dark matter annihilation within the halo escapes, though there is a notable change to the annihilation spectrum due to the injected particles interacting with both the gas and CMB photon field.

8.1.4 The Impact of Dark Matter Annihilation on the CGM

In the detailed study of dark matter annihilation inside high redshift halos, it was shown that the majority of the injected energy escapes into the circumgalactic medium. It was also shown that the energy distribution of the injected particles has been modified through their interaction with both the halo's gas component and the CMB photon field. In Chapter 6, the heating of the CGM due to dark matter annihilation was calculated.

- Similar to the self-heating of the halos, the mean-free paths of the secondary particles play an important role in determining the efficiency with which the halo's surrounding has is heated. Since the gas density of the CGM is notably lower than that of the halo proper, IC photons that would interact through Compton scattering within the halo would free stream in the CGM. Models with masses around 130 MeV and > 50 GeV produce IC photons with energies below the Compton regime and are therefore more effective at depositing energy in the halos' surrounding gas.

- As before more concentrated dark matter profiles produce more annihilation power and therefore more heating of the CGM. In addition, halos with more concentrated density profiles such as Einasto and NFW, produce as small excess of mid energy range electrons compared to halos with a less concentrated Burkert profile. The relative energy transfer efficiency of these electrons provides another subtle enhancement in the heating ability of concentrated density profiles.

- Sufficient increase in temperature of the CGM can lead to the suppression of gas infall onto the halo and formation of baryonic structure. δ_{mod} was calculated for the different dark matter models (see third row of Figure 8.1). At redshifts 20 and 40, a $10^5 M_\odot$ halo would have to increase in mass by a factor $2-3$ and $4-5$ respectively to recover the $\delta_b = 100$ threshold for baryonic collapse. An important caveat is that the method used in the chapter breaks down for the more massive

halos analysed here as it does not take into account shock heating which results in a inflated value of δ_b.

8.1.5 Comparison of Heating Sources

Lastly the relative importance of different dark matter annihilation sources was investigated for both the halo proper and the circumgalactic medium and these results were presented in Chapter 7. Some of the results are shown in the lowest row of plots in Figure 8.1.

- **Photon Bath vs Halo** dark matter candidates at the electroweak scale rapidly convert most their energy to photons. The diffuse dark matter background produces a photon bath that saturate the IGM and provides a secondary heating source for the halos.

- **CGM vs Halo** The dark matter annihilating in the CGM also provides an additional heating source for the inner halo.

- **Halo vs Diffuse Background** The heating of the circumgalactic medium from the halo was previously discussed. The energy input from the halo was compared to the uniform heating from the integrated background. Both a contribution from a uniform dark matter background and one in which collapsed structure provided a boost to the total annihilation power were presented.

At redshifts 20 and 40, the comparison in all of the above cases showed that the heating from the halo dominated over the secondary sources regardless of dark matter particle model. However there is a trend suggesting that background heating sources become more prominent at lower redshifts. This is because at lower redshifts the reduced densities are less favourable to energy transfer over halo scale distances for the particle injected at the energy scales proposed here. Additionally an increasing fraction of matter is contained in collapsed structure which further boost the annihilation power of the diffuse background.

8.2 Future Applications and Final Thoughts

In this thesis the impact of dark matter annihilation on early structure formation is explored. It was shown that while the resultant self-heating of dark matter halos and their immediate environment has the potential to lead to a modified evolution of the first stars and galaxies, the high redshifts at which these objects occur present significant challenges for attempts at direct observation. Nonetheless dark matter annihilation may still provide an identifiable signature by modifying the progression of reionisation both through direct heating and ionisation of the IGM and modification of baryonic

structure which canonically drives the process. The treatment of dark matter annihilation is complicated by the emergence of structure, both by the dynamic nature of its evolution and the complex feedback mechanisms that exist between halos and both the standard and additional dark matter background. In addition the energy transfer of the relativistic standard model particles injected by dark matter annihilation is highly non-trivial, especially within structure. The latter in particular, makes in situ incorporation of dark matter annihilation into cosmological simulations very challenging.

The work completed here aims to contribute to the identification of the parameter space in which dark matter annihilation impacts early structure formation as well as developing tools to assist with the rigorous treatment of energy transfer in non-homogeneous density fields. It also looks to determine the relative importance of different sources of dark matter annihilation and by extension which processes take precedent in the inclusion in cosmological simulations. While the analysis of a single halo cannot predict the accumulative effect dark matter annihilation has on hierarchical structure formation over time, it does aid in the formulation of models that will be compatible with simulations and allow for testable predictions to be made.

The exploration of the Epoch of Reionisation is one of the key frontiers of astrophysics. Observations by radio telescopes of the 21-cm line over the next decade will hopefully provide unprecedented insight into the early Universe and have the potential to shed light onto altogether new phenomena. In order to identify a signal indicative of new physics, careful modelling is required to account for both uncertainties in the dark matter and astrophysical models. It is crucial that predictions of a dark matter modified 21cm signal integrates dark matter annihilation into the emergence of structure. A number of challenges remain before the latter can be fully realised but the prospective comparisons to be made with future observations will provide valuable constraints to guide the ongoing quest to uncover the fundamental nature of dark matter.

Bibliography

T. Abel, P. Anninos, Y. Zhang, and M. L. Norman. Modeling primordial gas in numerical cosmology. *New Astronomy*, 2:181–207, August 1997. doi: 10.1016/S1384-1076(97)00010-9.

T. Abel, G. L. Bryan, and M. L. Norman. The Formation of the First Star in the Universe. *Science*, 295:93–98, January 2002. doi: 10.1126/science.295.5552.93.

E. S. Abers and B. W. Lee. Gauge Theories. *Physics Report*, 9:1–141, 1973. doi: 10.1016/0370-1573(73)90027-6.

F. A. Agaronyan, A. M. Atoyan, and A. M. Nagapetyan. Photoproduction of Electron-Positron Pairs in Compact X-Ray Sources. *Astrophysics*, 19:187–194, April 1983. doi: 10.1007/BF01005624.

S. Agostinelli, J. Allison, K. Amako, J. Apostolakis, H. Araujo, P. Arce, M. Asai, D. Axen, S. Banerjee, G. Barrand, F. Behner, L. Bellagamba, J. Boudreau, L. Broglia, A. Brunengo, H. Burkhardt, S. Chauvie, J. Chuma, R. Chytracek, G. Cooperman, G. Cosmo, P. Degtyarenko, A. Dell'Acqua, G. Depaola, D. Dietrich, R. Enami, A. Feliciello, C. Ferguson, H. Fesefeldt, G. Folger, F. Foppiano, A. Forti, S. Garelli, S. Giani, R. Giannitrapani, D. Gibin, J.J. GÃşmez Cadenas, I. GonzÃąlez, G. Gracia Abril, G. Greeniaus, W. Greiner, V. Grichine, A. Grossheim, S. Guatelli, P. Gumplinger, R. Hamatsu, K. Hashimoto, H. Hasui, A. Heikkinen, A. Howard, V. Ivanchenko, A. Johnson, F.W. Jones, J. Kallenbach, N. Kanaya, M. Kawabata, Y. Kawabata, M. Kawaguti, S. Kelner, P. Kent, A. Kimura, T. Kodama, R. Kokoulin, M. Kossov, H. Kurashige, E. Lamanna, T. LampÃľn, V. Lara, V. Lefebure, F. Lei, M. Liendl, W. Lockman, F. Longo, S. Magni, M. Maire, E. Medernach, K. Minamimoto, P. Mora de Freitas, Y. Morita, K. Murakami, M. Nagamatu, R. Nartallo, P. Nieminen, T. Nishimura, K. Ohtsubo, M. Okamura, S. O'Neale, Y. Oohata, K. Paech, J. Perl, A. Pfeiffer, M.G. Pia, F. Ranjard, A. Rybin, S. Sadilov, E. Di Salvo, G. Santin, T. Sasaki, N. Savvas, Y. Sawada, S. Scherer, S. Sei, V. Sirotenko, D. Smith, N. Starkov, H. Stoecker, J. Sulkimo, M. Takahata, S. Tanaka, E. Tcherniaev, E. Safai Tehrani, M. Tropeano, P. Truscott, H. Uno, L. Urban, P. Urban, M. Verderi, A. Walkden, W. Wander, H. Weber, J.P. Wellisch, T. Wenaus, D.C. Williams, D. Wright, T. Yamada, H. Yoshida, and D. Zschiesche. Geant4âĂŤa simulation toolkit. *Nuclear Instruments and Methods in Physics Research Section A: Accelerators, Spectrometers, Detectors and Associated Equipment*, 506(3):250 – 303, 2003. ISSN 0168-9002. doi: http://dx.doi.org/10.1016/S0168-9002(03)01368-8. URL `http://www.sciencedirect.com/science/article/pii/S0168900203013688`.

D. S. Akerib, H. M. Araújo, X. Bai, A. J. Bailey, J. Balajthy, S. Bedikian, E. Bernard, A. Bernstein, A. Bolozdynya, A. Bradley, D. Byram, S. B. Cahn, M. C. Carmona-Benitez, C. Chan,

J. J. Chapman, A. A. Chiller, C. Chiller, K. Clark, T. Coffey, A. Currie, A. Curioni, S. Dazeley, L. de Viveiros, A. Dobi, J. Dobson, E. M. Dragowsky, E. Druszkiewicz, B. Edwards, C. H. Faham, S. Fiorucci, C. Flores, R. J. Gaitskell, V. M. Gehman, C. Ghag, K. R. Gibson, M. G. D. Gilchriese, C. Hall, M. Hanhardt, S. A. Hertel, M. Horn, D. Q. Huang, M. Ihm, R. G. Jacobsen, L. Kastens, K. Kazkaz, R. Knoche, S. Kyre, R. Lander, N. A. Larsen, C. Lee, D. S. Leonard, K. T. Lesko, A. Lindote, M. I. Lopes, A. Lyashenko, D. C. Malling, R. Mannino, D. N. McKinsey, D.-M. Mei, J. Mock, M. Moongweluwan, J. Morad, M. Morii, A. S. J. Murphy, C. Nehrkorn, H. Nelson, F. Neves, J. A. Nikkel, R. A. Ott, M. Pangilinan, P. D. Parker, E. K. Pease, K. Pech, P. Phelps, L. Reichhart, T. Shutt, C. Silva, W. Skulski, C. J. Sofka, V. N. Solovov, P. Sorensen, T. Stiegler, K. O'Sullivan, T. J. Sumner, R. Svoboda, M. Sweany, M. Szydagis, D. Taylor, B. Tennyson, D. R. Tiedt, M. Tripathi, S. Uvarov, J. R. Verbus, N. Walsh, R. Webb, J. T. White, D. White, M. S. Witherell, M. Wlasenko, F. L. H. Wolfs, M. Woods, C. Zhang, and LUX Collaboration. First Results from the LUX Dark Matter Experiment at the Sanford Underground Research Facility. *Physical Review Letters*, 112(9):091303, March 2014. doi: 10.1103/PhysRevLett.112.091303.

J. Albiński and F. Michel. Quantum calculation of the barrier and internal wave contributions to light- and heavy-ion elastic scattering. *Physical Review D*, 25:213–225, Jan 1982. doi: 10.1103/PhysRevC.25.213. URL `https://link.aps.org/doi/10.1103/PhysRevC.25.213`.

C. Alcock, C. W. Akerlof, R. A. Allsman, T. S. Axelrod, D. P. Bennett, S. Chan, K. H. Cook, K. C. Freeman, K. Griest, S. L. Marshall, H.-S. Park, S. Perlmutter, B. A. Peterson, M. R. Pratt, P. J. Quinn, A. W. Rodgers, C. W. Stubbs, and W. Sutherland. Possible gravitational microlensing of a star in the Large Magellanic Cloud. *Nature*, 365:621–623, October 1993. doi: 10.1038/365621a0.

Y. Ali-Haïmoud and M. Kamionkowski. Cosmic microwave background limits on accreting primordial black holes. *Physical Review D*, 95(4):043534, February 2017. doi: 10.1103/PhysRevD.95.043534.

J. Allison, K. Amako, J. Apostolakis, H. Araujo, P. Arce Dubois, M. Asai, G. Barrand, R. Capra, S. Chauvie, R. Chytracek, G. A. P. Cirrone, G. Cooperman, G. Cosmo, G. Cuttone, G. G. Daquino, M. Donszelmann, M. Dressel, G. Folger, F. Foppiano, J. Generowicz, V. Grichine, S. Guatelli, P. Gumplinger, A. Heikkinen, I. Hrivnacova, A. Howard, S. Incerti, V. Ivanchenko, T. Johnson, F. Jones, T. Koi, R. Kokoulin, M. Kossov, H. Kurashige, V. Lara, S. Larsson, F. Lei, O. Link, F. Longo, M. Maire, A. Mantero, B. Mascialino, I. McLaren, P. Mendez Lorenzo, K. Minamimoto, K. Murakami, P. Nieminen, L. Pandola, S. Parlati, L. Peralta, J. Perl, A. Pfeiffer, M. G. Pia, A. Ribon, P. Rodrigues, G. Russo, S. Sadilov, G. Santin, T. Sasaki, D. Smith, N. Starkov, S. Tanaka, E. Tcherniaev, B. Tome, A. Trindade, P. Truscott, L. Urban, M. Verderi, A. Walkden, J. P. Wellisch, D. C. Williams, D. Wright, and H. Yoshida. Geant4 developments and applications. *IEEE Transactions on Nuclear Science*, 53(1):270–278, Feb 2006. ISSN 0018-9499. doi: 10.1109/TNS.2006.869826.

B. Andersson, G. Gustafson, and C. Peterson. A semiclassical model for quark jet fragmentation. *Zeitschrift fur Physik C Particles and Fields*, 1:105–116, March 1979. doi: 10.1007/BF01450386.

B. Andersson, G. Gustafson, and B. Söderberg. A general model for jet fragmentation.

Zeitschrift fur Physik C Particles and Fields, 20:317–329, December 1983. doi: 10.1007/BF01407824.

Paul W. Angel, Gregory B. Poole, Aaron D. Ludlow, Alan R. Duffy, Paul M. Geil, Simon J. Mutch, Andrei Mesinger, and J. Stuart B. Wyithe. Dark-ages reionization and galaxy formation simulation âĂŞ ii. spin and concentration parameters for dark matter haloes during the epoch of reionization. *MNRAS*, 459(2):2106–2117, 2016. doi: 10.1093/mnras/stw737. URL `http://mnras.oxfordjournals.org/content/459/2/2106.abstract`.

G. Angloher, M. Bauer, I. Bavykina, A. Bento, C. Bucci, C. Ciemniak, G. Deuter, F. von Feilitzsch, D. Hauff, P. Huff, C. Isaila, J. Jochum, M. Kiefer, M. Kimmerle, J.-C. Lanfranchi, F. Petricca, S. Pfister, W. Potzel, F. Pröbst, F. Reindl, S. Roth, K. Rottler, C. Sailer, K. Schäffner, J. Schmaler, S. Scholl, W. Seidel, M. v. Sivers, L. Stodolsky, C. Strandhagen, R. Strauß, A. Tanzke, I. Usherov, S. Wawoczny, M. Willers, and A. Zöller. Results from 730 kg days of the CRESST-II Dark Matter search. *European Physical Journal C*, 72:1971, April 2012. doi: 10.1140/epjc/s10052-012-1971-8.

E. Aprile, M. Alfonsi, K. Arisaka, F. Arneodo, C. Balan, L. Baudis, B. Bauermeister, A. Behrens, P. Beltrame, K. Bokeloh, E. Brown, G. Bruno, R. Budnik, J. M. R. Cardoso, W.-T. Chen, B. Choi, D. Cline, A. P. Colijn, H. Contreras, J. P. Cussonneau, M. P. Decowski, E. Duchovni, S. Fattori, A. D. Ferella, W. Fulgione, F. Gao, M. Garbini, C. Ghag, K.-L. Giboni, L. W. Goetzke, C. Grignon, E. Gross, W. Hampel, F. Kaether, A. Kish, J. Lamblin, H. Landsman, R. F. Lang, M. Le Calloch, C. Levy, K. E. Lim, Q. Lin, S. Lindemann, M. Lindner, J. A. M. Lopes, K. Lung, T. Marrodán Undagoitia, F. V. Massoli, A. J. Melgarejo Fernandez, Y. Meng, A. Molinario, E. Nativ, K. Ni, U. Oberlack, S. E. A. Orrigo, E. Pantic, R. Persiani, G. Plante, N. Priel, A. Rizzo, S. Rosendahl, J. M. F. dos Santos, G. Sartorelli, J. Schreiner, M. Schumann, L. Scotto Lavina, P. R. Scovell, M. Selvi, P. Shagin, H. Simgen, A. Teymourian, D. Thers, O. Vitells, H. Wang, M. Weber, and C. Weinheimer. Dark Matter Results from 225 Live Days of XENON100 Data. *Physical Review Letters*, 109(18):181301, November 2012. doi: 10.1103/PhysRevLett.109.181301.

M. Arnaud and R. Rothenflug. An updated evaluation of recombination and ionization rates. *Astron. and Astrophys. Supp. Series*, 60:425–457, June 1985.

E. Aubourg, P. Bareyre, S. Bréhin, M. Gros, M. Lachièze-Rey, B. Laurent, E. Lesquoy, C. Magneville, A. Milsztajn, L. Moscoso, F. Queinnec, J. Rich, M. Spiro, L. Vigroux, S. Zylberajch, R. Ansari, F. Cavalier, M. Moniez, J.-P. Beaulieu, R. Ferlet, P. Grison, A. Vidal-Madjar, J. Guibert, O. Moreau, F. Tajahmady, E. Maurice, L. Prévôt, and C. Gry. Evidence for gravitational microlensing by dark objects in the Galactic halo. *Nature*, 365:623–625, October 1993. doi: 10.1038/365623a0.

W. Baade. The Resolution of Messier 32, NGC 205, and the Central Region of the Andromeda Nebula. *Astrophysical Journal*, 100:137, September 1944. doi: 10.1086/144650.

H. W. Babcock. The rotation of the Andromeda Nebula. *Lick Observatory Bulletin*, 19:41–51, 1939. doi: 10.5479/ADS/bib/1939LicOB.19.41B.

H. Baer, C. Balázs, A. Belyaev, T. Krupovnickas, and X. Tata. Updated reach of CERN LHC and constraints from relic density, brightarrowsgamma and a_{mu} in the mSUGRA model. *Journal of High Energy Physics*, 6:054, June 2003. doi: 10.1088/1126-6708/2003/06/054.

J. A. Bagger. Weak-Scale Supersymmetry: Theory and Practice. *ArXiv High Energy Physics - Phenomenology e-prints*, April 1996.

V. Barger, M. S. Berger, and P. Ohmann. Supersymmetric particle spectrum. *Phys. Rev. D*, 49: 4908–4930, May 1994. doi: 10.1103/PhysRevD.49.4908. URL `http://link.aps.org/doi/10.1103/PhysRevD.49.4908`.

R. Barkana. A model for infall around virialized haloes. *MNRAS*, 347:59–66, January 2004. doi: 10.1111/j.1365-2966.2004.07177.x.

Rennan Barkana. Studying the sources of cosmic reionization with 21-cm fluctuations. *Monthly Notices of the Royal Astronomical Society*, 397(3):1454–1463, 2009. ISSN 1365-2966. doi: 10.1111/j.1365-2966.2009.14929.x. URL `http://dx.doi.org/10.1111/j.1365-2966.2009.14929.x`.

M. C. Begelman, M. Volonteri, and M. J. Rees. Formation of supermassive black holes by direct collapse in pre-galactic haloes. *Monthly Notices of the Royal Astronomical Society*, 370:289–298, July 2006. doi: 10.1111/j.1365-2966.2006.10467.x.

K. G. Begeman, A. H. Broeils, and R. H. Sanders. Extended rotation curves of spiral galaxies - Dark haloes and modified dynamics. *MNRAS*, 249:523–537, April 1991. doi: 10.1093/mnras/249.3.523.

J. Bekenstein and M. Milgrom. Does the missing mass problem signal the breakdown of Newtonian gravity? *The Astrophysical Journal*, 286:7–14, November 1984. doi: 10.1086/162570.

J. D. Bekenstein. Phase coupling gravitation: Symmetries and gauge fields. *Physics Letters B*, 202:497–500, March 1988. doi: 10.1016/0370-2693(88)91851-5.

J. D. Bekenstein. Relativistic gravitation theory for the modified Newtonian dynamics paradigm. *Physics Review D*, 70(8):083509, October 2004. doi: 10.1103/PhysRevD.70.083509.

J. D. Bekenstein and R. H. Sanders. Gravitational lenses and unconventional gravity theories. *The Astrophysical Journal*, 429:480–490, July 1994. doi: 10.1086/174337.

A. V. Belikov and D. Hooper. How dark matter reionized the Universe. *Physical Review D*, 80 (3):035007, August 2009. doi: 10.1103/PhysRevD.80.035007.

A. Benson, A. Venkatesan, and J. M. Shull. The Escape Fraction of Ionizing Radiation from Galaxies. *Astrophysical Journal*, 770:76, June 2013. doi: 10.1088/0004-637X/770/1/76.

A. J. Benson. Galaxy formation theory. *Physics Report*, 495:33–86, October 2010. doi: 10.1016/j.physrep.2010.06.001.

L. Bergström. Non-baryonic dark matter: observational evidence and detection methods. *Reports on Progress in Physics*, 63:793–841, May 2000. doi: 10.1088/0034-4885/63/5/2r3.

R. Bernabei, P. Belli, F. Cappella, R. Cerulli, F. Montechia, F. Nozzoli, A. Incicchitti, D. Prosperi, C. J. Dai, H. H. Kuang, J. M. Ma, and Z. P. Ye. Dark Matter search. *Nuovo Cimento Rivista Serie*, 26(1):1–74, January 2003.

R. Bernabei, P. Belli, F. Cappella, R. Cerulli, C. J. Dai, A. D'Angelo, H. L. He, A. Incicchitti, H. H. Kuang, J. M. Ma, F. Montecchia, F. Nozzoli, D. Prosperi, X. D. Sheng, and Z. P. Ye. First results from DAMA/LIBRA and the combined results with DAMA/NaI. *European*

Physical Journal C, 56:333, August 2008. doi: 10.1140/epjc/s10052-008-0662-y.

R. Bernabei, P. Belli, F. Cappella, R. Cerulli, C. J. Dai, A. D'Angelo, H. L. He, A. Incicchitti, H. H. Kuang, X. H. Ma, F. Montecchia, F. Nozzoli, D. Prosperi, X. D. Sheng, R. G. Wang, and Z. P. Ye. New results from DAMA/LIBRA. *European Physical Journal C*, 67:39–49, May 2010. doi: 10.1140/epjc/s10052-010-1303-9.

G. Bertone and D. Hooper. A History of Dark Matter. *ArXiv e-prints*, May 2016.

G. Bertone, D. Hooper, and J. Silk. Particle dark matter: evidence, candidates and constraints. *Phys. Rep.*, 405:279–390, January 2005. doi: 10.1016/j.physrep.2004.08.031.

J. Binney and S. Tremaine. *Galactic dynamics*. Princeton, NJ, Princeton University Press, 1987, 747 p., 1987.

G. R. Blumenthal and R. J. Gould. Bremsstrahlung, synchrotron radiation, and compton scattering of high-energy electrons traversing dilute gases. *Rev. Mod. Phys.*, 42:237–270, Apr 1970. doi: 10.1103/RevModPhys.42.237. URL `http://link.aps.org/doi/10.1103/RevModPhys.42.237`.

A. Bosma. *The distribution and kinematics of neutral hydrogen in spiral galaxies of various morphological types*. PhD thesis, PhD Thesis, Groningen Univ., (1978), 1978.

J. Bovy. Substructure boosts to dark matter annihilation from Sommerfeld enhancement. *Physical Review D*, 79(8):083539, April 2009. doi: 10.1103/PhysRevD.79.083539.

Michael Boylan-Kolchin, Volker Springel, Simon D. M. White, Adrian Jenkins, and Gerard Lemson. Resolving cosmic structure formation with the millennium-ii simulation. *MNRAS*, 398(3):1150–1164, 2009. doi: 10.1111/j.1365-2966.2009.15191.x. URL `http://mnras.oxfordjournals.org/content/398/3/1150.abstract`.

B H Bransden and C J Noble. Electron impact excitation of atomic hydrogen and hydrogenic ions. *Journal of Physics B: Atomic and Molecular Physics*, 9(9):1507, 1976. URL `http://stacks.iop.org/0022-3700/9/i=9/a=016`.

V. Bromm and A. Loeb. Formation of the First Supermassive Black Holes. *Astrophysical Journal*, 596:34–46, October 2003. doi: 10.1086/377529.

V. Bromm, N. Yoshida, L. Hernquist, and C. F. McKee. The formation of the first stars and galaxies. *Nature*, 459:49–54, May 2009. doi: 10.1038/nature07990.

Loren R. Bruns, J. Stuart B. Wyithe, Joss Bland-Hawthorn, and Mark Dijkstra. Clustering of lyÎś emitters around luminous quasars at z= 2âĂŞ3: an alternative probe of reionization on galaxy formation. *Monthly Notices of the Royal Astronomical Society*, 421(3):2543–2552, 2012. doi: 10.1111/j.1365-2966.2012.20479.x. URL `http://mnras.oxfordjournals.org/content/421/3/2543.abstract`.

G. L. Bryan and M. L. Norman. Statistical Properties of X-Ray Clusters: Analytic and Numerical Comparisons. *Astrophysical Journal*, 495:80–99, March 1998. doi: 10.1086/305262.

A. Burkert. The Structure of Dark Matter Halos in Dwarf Galaxies. *ApJl*, 447:L25, July 1995. doi: 10.1086/309560.

S. Burles, K. M. Nollett, and M. S. Turner. Big Bang Nucleosynthesis Predictions for Precision Cosmology. *The Astrophysical Journal*, 552:L1–L5, May 2001. doi: 10.1086/320251.

B. J. Carr and S. W. Hawking. Black holes in the early Universe. *Monthly Notices of the Royal Astronomical Society*, 168:399–416, August 1974. doi: 10.1093/mnras/168.2.399.

K. Chang and S. Refsdal. Flux variations of QSO 0957+561 A, B and image splitting by stars near the light path. *Nature (Londong)*, 282:561–564, December 1979. doi: 10.1038/282561a0.

E. Chapman, F. B. Abdalla, G. Harker, V. Jelić, P. Labropoulos, S. Zaroubi, M. A. Brentjens, A. G. de Bruyn, and L. V. E. Koopmans. Foreground removal using FASTICA: a showcase of LOFAR-EoR. *Monthly Notices of the Royal Astronomical Society*, 423:2518–2532, July 2012. doi: 10.1111/j.1365-2966.2012.21065.x.

X. Chen and M. Kamionkowski. Particle decays during the cosmic dark ages. *Phys. Rev. D*, 70 (4):043502, August 2004. doi: 10.1103/PhysRevD.70.043502.

Leonid Chuzhoy and Paul R. Shapiro. Heating and cooling of the early intergalactic medium by resonance photons. *The Astrophysical Journal*, 655(2):843, 2007. URL `http://stacks.iop.org/0004-637X/655/i=2/a=843`.

D. Clowe, A. Gonzalez, and M. Markevitch. Weak-Lensing Mass Reconstruction of the Interacting Cluster 1E 0657-558: Direct Evidence for the Existence of Dark Matter. *The Astrophysical Journal*, 604:596–603, April 2004. doi: 10.1086/381970.

D. Clowe, M. Bradač, A. H. Gonzalez, M. Markevitch, S. W. Randall, C. Jones, and D. Zaritsky. A Direct Empirical Proof of the Existence of Dark Matter. *The Astrophysical Journal*, 648: L109–L113, September 2006. doi: 10.1086/508162.

T. Cohen, M. Lisanti, T. R. Slatyer, and J. G. Wacker. Illuminating the 130 GeV gamma line with continuum photons. *Journal of High Energy Physics*, 10:134, October 2012. doi: 10.1007/JHEP10(2012)134.

S. Cole. Modeling galaxy formation in evolving dark matter halos. *Astrophysical Journal*, 367: 45–53, January 1991. doi: 10.1086/169600.

Sidney Coleman and Jeffrey Mandula. All possible symmetries of the s matrix. *Phys. Rev.*, 159: 1251–1256, Jul 1967. doi: 10.1103/PhysRev.159.1251. URL `http://link.aps.org/doi/10.1103/PhysRev.159.1251`.

Julia M. Comerford and Priyamvada Natarajan. The observed concentrationâĂŞmass relation for galaxy clusters. *MNRAS*, 379(1):190–200, 2007. doi: 10.1111/j.1365-2966.2007.11934.x. URL `http://mnras.oxfordjournals.org/content/379/1/190.abstract`.

C. A. Correa, J. S. B. Wyithe, J. Schaye, and A. R. Duffy. The accretion history of dark matter haloes - III. A physical model for the concentration-mass relation. *MNRAS*, 452:1217–1232, September 2015. doi: 10.1093/mnras/stv1363.

D. J. Croton, V. Springel, S. D. M. White, G. De Lucia, C. S. Frenk, L. Gao, A. Jenkins, G. Kauffmann, J. F. Navarro, and N. Yoshida. The many lives of active galactic nuclei: cooling flows, black holes and the luminosities and colours of galaxies. *Monthly Notices of the Royal Astronomical Society*, 365:11–28, January 2006. doi: 10.1111/j.1365-2966.2005.09675.x.

C. Csáki, J. Hubisz, G. D. Kribs, P. Meade, and J. Terning. Big corrections from a little Higgs. *Physics Review D*, 67(11):115002, June 2003. doi: 10.1103/PhysRevD.67.115002.

M. Davis, J. Huchra, D. W. Latham, and J. Tonry. A survey of galaxy redshifts. II - The large scale space distribution. *The Astrophysical Journal*, 253:423–445, February 1982. doi: 10.1086/159646.

S. Dimopoulos, S. Raby, and Frank Wilczek. Supersymmetry and the scale of unification. *Phys. Rev. D*, 24:1681–1683, Sep 1981. doi: 10.1103/PhysRevD.24.1681. URL `http://link.aps.org/doi/10.1103/PhysRevD.24.1681`.

S. Dodelson and M. Liguori. Can Cosmic Structure Form without Dark Matter? *Physical Review Letters*, 97(23):231301, December 2006. doi: 10.1103/PhysRevLett.97.231301.

S. Dodelson and L. M. Widrow. Sterile neutrinos as dark matter. *Physical Review Letters*, 72: 17–20, January 1994a. doi: 10.1103/PhysRevLett.72.17.

S. Dodelson and L. M. Widrow. Sterile neutrinos as dark matter. *Physical Review Letters*, 72: 17–20, January 1994b. doi: 10.1103/PhysRevLett.72.17.

A. G. Doroshkevich, Y. B. Zeldovich, R. A. Syunyaev, and M. Y. Khlopov. Astrophysical implications of the neutrino rest mass. II - The density-perturbation spectrum and small-scale fluctuations in the microwave background. III - Nonlinear growth of perturbations and the missing mass. *Pisma v Astronomicheskii Zhurnal*, 6:457–469, August 1980a.

A. G. Doroshkevich, Y. B. Zeldovich, R. A. Syunyaev, and M. Y. Khlopov. Astrophysical Implications of the Neutrino Rest Mass - Part Two - the Density Perturbation Spectrum and Small-Scale Fluctuations in the MICROWAVE_ Background. *Soviet Astronomy Letters*, 6: 252–259, April 1980b.

M. Drees and M. M. Nojiri. Neutralino relic density in minimal N=1 supergravity. *Physical Review D*, 47:376–408, January 1993. doi: 10.1103/PhysRevD.47.376.

H. Dreiner, D. Schmeier, and J. Tattersall. Contact interactions probe effective dark-matter models at the lhc. *EPL (Europhysics Letters)*, 102(5):51001, 2013. URL `http://stacks.iop.org/0295-5075/102/i=5/a=51001`.

Alan R. Duffy, Joop Schaye, Scott T. Kay, Claudio Dalla Vecchia, Richard A. Battye, and C. M. Booth. Impact of baryon physics on dark matter structures: a detailed simulation study of halo density profiles. *MNRAS*, 405(4):2161–2178, 2010. doi: 10.1111/j.1365-2966.2010.16613.x. URL `http://mnras.oxfordjournals.org/content/405/4/2161.abstract`.

EDELWEISS Collaboration, E. Armengaud, C. Augier, A. Benoît, L. Bergé, J. Blümer, A. Broniatowski, V. Brudanin, B. Censier, G. Chardin, M. Chapellier, F. Charlieux, P. Coulter, G. A. Cox, X. Defay, M. de Jesus, Y. Dolgorouki, J. Domange, L. Dumoulin, K. Eitel, D. Filosofov, N. Fourches, J. Gascon, G. Gerbier, J. Gironnet, M. Gros, S. Henry, S. Hervé, A. Juillard, H. Kluck, V. Kozlov, H. Kraus, V. A. Kudryavtsev, P. Loaiza, S. Marnieros, X.-F. Navick, C. Nones, E. Olivieri, P. Pari, L. Pattavina, B. Paul, M. Robinson, S. Rozov, V. Sanglard, B. Schmidt, S. Scorza, S. Semikh, A. S. Torrento-Coello, L. Vagneron, M.-A. Verdier, R. J. Walker, and E. Yakushev. Final results of the EDELWEISS-II WIMP search using a 4-kg array of cryogenic germanium detectors with interleaved electrodes. *Physics Letters B*, 702:329–335, August 2011. doi: 10.1016/j.physletb.2011.07.034.

J. Einasto and U. Haud. Galactic models with massive corona. I - Method. II - Galaxy. *Astronomy and Astrophysics*, 223:89–106, October 1989.

Mohamed M. El Kheishen, Ahmed A. Shafik, and Amr A. Aboshousha. Analytic formulas for the neutralino masses and the neutralino mixing matrix. *Phys. Rev. D*, 45:4345–4348, Jun 1992. doi: 10.1103/PhysRevD.45.4345. URL http://link.aps.org/doi/10.1103/PhysRevD.45.4345.

C. Evoli, M. ValdÃľs, A. Ferrara, and N. Yoshida. Energy deposition by weakly interacting massive particles: a comprehensive study. *MNRAS*, 422(1):420–433, 2012. doi: 10.1111/j.1365-2966.2012.20624.x. URL http://mnras.oxfordjournals.org/content/422/1/420.abstract.

C. Evoli, A. Mesinger, and A. Ferrara. Unveiling the nature of dark matter with high redshift 21 cm line experiments. *Journal of Cosmology and Astroparticle Physics*, 11:024, November 2014. doi: 10.1088/1475-7516/2014/11/024.

B. Famaey and S. S. McGaugh. Modified Newtonian Dynamics (MOND): Observational Phenomenology and Relativistic Extensions. *Living Reviews in Relativity*, 15:10, September 2012. doi: 10.12942/lrr-2012-10.

Glennys R. Farrar and Pierre Fayet. Phenomenology of the production, decay, and detection of new hadronic states associated with supersymmetry. *Physics Letters B*, 76(5):575 – 579, 1978. ISSN 0370-2693. doi: http://dx.doi.org/10.1016/0370-2693(78)90858-4. URL http://www.sciencedirect.com/science/article/pii/0370269378908584.

E. Feenberg and H. Primakoff. Interaction of cosmic-ray primaries with sunlight and starlight. *Phys. Rev.*, 73:449–469, Mar 1948. doi: 10.1103/PhysRev.73.449. URL http://link.aps.org/doi/10.1103/PhysRev.73.449.

J. E. Felten and P. Morrison. Omnidirectional Inverse Compton and Synchrotron Radiation from Cosmic Distributions of Fast Electrons and Thermal Photons. *Astrophysical Journal*, 146:686, December 1966. doi: 10.1086/148946.

J. L. Feng. MPIK Webpages, Research: dark matter, 2016. URL https://www.mpi-hd.mpg.de/lin/research_DM.en.html. [Online; accessed 5-August-2016].

J. L. Feng, M. Kaplinghat, and H.-B. Yu. Sommerfeld enhancements for thermal relic dark matter. *Physical Review D*, 82(8):083525, October 2010. doi: 10.1103/PhysRevD.82.083525.

C. Ferrigno, P. Blasi, and D. de Marco. High energy gamma ray counterparts of astrophysical sources of ultra-high energy cosmic rays. *Nuclear Physics B Proceedings Supplements*, 136:191–197, November 2004. doi: 10.1016/j.nuclphysbps.2004.10.031.

G. B. Field. The Time Relaxation of a Resonance-Line Profile. *Astrophysical Journal*, 129:551, May 1959. doi: 10.1086/146654.

Vladimir I. Fisher, Yuri V. Ralchenko, Vladimir A. Bernshtam, Alexander Goldgirsh, Yitzhak Maron, Leonid A. Vainshtein, Igor Bray, and Helen Golten. Electron-impact-excitation cross sections of hydrogenlike ions. *Phys. Rev. A*, 55:329–334, Jan 1997. doi: 10.1103/PhysRevA.55.329. URL http://link.aps.org/doi/10.1103/PhysRevA.55.329.

H. Fritzsch, Murray Gell-Mann, and H. Leutwyler. Advantages of the Color Octet Gluon Picture. *Phys. Lett.*, 47B:365–368, 1973. doi: 10.1016/0370-2693(73)90625-4.

M. Fukugita, C. J. Hogan, and P. J. E. Peebles. The Cosmic Baryon Budget. *The Astrophysical Journal*, 503:518–530, August 1998. doi: 10.1086/306025.

S. R. Furlanetto, S. P. Oh, and F. H. Briggs. Cosmology at low frequencies: The 21 cm transition and the high-redshift Universe. *Physics Report*, 433:181–301, October 2006a. doi: 10.1016/j.physrep.2006.08.002.

S. R. Furlanetto, S. P. Oh, and E. Pierpaoli. Effects of dark matter decay and annihilation on the high-redshift 21cm background. *Physical Review D*, 74(10):103502, November 2006b. doi: 10.1103/PhysRevD.74.103502.

Steven R. Furlanetto and Samuel Johnson Stoever. Secondary ionization and heating by fast electrons. *MNRAS*, 404(4):1869–1878, 2010. doi: 10.1111/j.1365-2966.2010.16401.x. URL `http://mnras.oxfordjournals.org/content/404/4/1869.abstract`.

S. Genel, M. Vogelsberger, V. Springel, D. Sijacki, D. Nelson, G. Snyder, V. Rodriguez-Gomez, P. Torrey, and L. Hernquist. Introducing the Illustris project: the evolution of galaxy populations across cosmic time. *MNRAS*, 445:175–200, November 2014. doi: 10.1093/mnras/stu1654.

S. L. Glashow, J. Iliopoulos, and L. Maiani. Weak Interactions with Lepton-Hadron Symmetry. *Physical Review*, D2:1285–1292, 1970. doi: 10.1103/PhysRevD.2.1285.

N. Y. Gnedin. Cosmological Reionization by Stellar Sources. *Astrophysical Journal*, 535:530–554, June 2000. doi: 10.1086/308876.

N. Y. Gnedin and J. P. Ostriker. Reionization of the Universe and the Early Production of Metals. *Astrophysical Journal*, 486:581–598, September 1997.

A. W. Graham, D. Merritt, B. Moore, J. Diemand, and B. Terzić. Empirical Models for Dark Matter Halos. III. The Kormendy Relation and the $\log\rho_e$-$\log R_e$ Relation. *AJ*, 132:2711–2716, December 2006. doi: 10.1086/508992.

N. Guessoum, P. Jean, and W. Gillard. Positron annihilation on polycyclic aromatic hydrocarbon molecules in the interstellar medium. *MNRAS*, 402(2):1171–1178, 2010. doi: 10.1111/j.1365-2966.2009.15954.x. URL `http://mnras.oxfordjournals.org/content/402/2/1171.abstract`.

J. F. Gunion and H. E. Haber. Higgs bosons in supersymmetric models. *Nuclear Physics B*, 272:567–568, August 1986. doi: 10.1016/0550-3213(93)90653-7.

Z. Haiman, M. J. Rees, and A. Loeb. Destruction of Molecular Hydrogen during Cosmological Reionization. *Astrophysical Journal*, 476:458–463, February 1997.

W. Heitler. *Quantum Theory of Radiation*. Oxford University (Clarendon Press), Oxford, 1954. ISBN 0198512120.

C. M. Hirata. Wouthuysen-Field coupling strength and application to high-redshift 21-cm radiation. *MNRAS*, 367:259–274, March 2006. doi: 10.1111/j.1365-2966.2005.09949.x.

E. Hubble. A Relation between Distance and Radial Velocity among Extra-Galactic Nebulae. *Proceedings of the National Academy of Science*, 15:168–173, March 1929. doi: 10.1073/pnas.15.3.168.

E. P. Hubble. Extragalactic nebulae. *ApJ*, 64, December 1926. doi: 10.1086/143018.

J. H. Jeans. The motions of stars in a kapteyn-universe. *Monthly Notices of the Royal Astronomical Society*, 82(3):122–132, 1922. doi: 10.1093/mnras/82.3.122. URL `http:`

//mnras.oxfordjournals.org/content/82/3/122.short.

J. H. Jeans. *Astronomy and cosmogony*. Cambridge [Eng.] The University press, 1928., 1928.

Frank C. Jones. Calculated spectrum of inverse-compton-scattered photons. *Physical Review*, 167:1159–1169, Mar 1968. doi: 10.1103/PhysRev.167.1159. URL http://link.aps.org/doi/10.1103/PhysRev.167.1159.

J. Joseph and F. Rohrlich. Pair production and bremsstrahlung in the field of free and bound electrons. *Rev. Mod. Phys.*, 30:354–368, Apr 1958. doi: 10.1103/RevModPhys.30.354. URL http://link.aps.org/doi/10.1103/RevModPhys.30.354.

G. Jungman, M. Kamionkowski, and K. Griest. Supersymmetric dark matter. *Phys. Rept.*, 267:195–373, March 1996. doi: 10.1016/0370-1573(95)00058-5.

F. D. Kahn and L. Woltjer. Intergalactic Matter and the Galaxy. *Astrophysical Journal*, 130: 705, November 1959. doi: 10.1086/146762.

Theodor Kaluza. On the Problem of Unity in Physics. *Sitzungsber. Preuss. Akad. Wiss. Berlin (Math. Phys.)*, 1921:966–972, 1921.

I. Kant. *Allgemeine Naturgeschichte und Theorie des Himmels, Part I*. J. F. Peterson, Königsberg un Leipzig, 1755. ISBN 0198512120.

J. C. Kapteyn. First Attempt at a Theory of the Arrangement and Motion of the Sidereal System. *Astrophysical Journal*, 55:302, May 1922. doi: 10.1086/142670.

W. J. Karzas and R. Latter. Electron Radiative Transitions in a Coulomb Field. *ApJs*, 6:167, May 1961. doi: 10.1086/190063.

H. I. Kim, C. H. Lee, and J. H. MacGibbon. Diffuse γ-ray background and primordial black hole constraints on the spectral index of density fluctuations. *Physical Review D*, 59(6):063004, March 1999. doi: 10.1103/PhysRevD.59.063004.

Yong-Ki Kim and M. Eugene Rudd. Binary-encounter-dipole model for electron-impact ionization. *Phys. Rev. A*, 50:3954–3967, Nov 1994. doi: 10.1103/PhysRevA.50.3954. URL http://link.aps.org/doi/10.1103/PhysRevA.50.3954.

A. A. Klypin, S. Trujillo-Gomez, and J. Primack. Dark Matter Halos in the Standard Cosmological Model: Results from the Bolshoi Simulation. *ApJ*, 740:102, October 2011. doi: 10.1088/0004-637X/740/2/102.

E. Komatsu, J. Dunkley, M. R. Nolta, C. L. Bennett, B. Gold, G. Hinshaw, N. Jarosik, D. Larson, M. Limon, L. Page, D. N. Spergel, M. Halpern, R. S. Hill, A. Kogut, S. S. Meyer, G. S. Tucker, J. L. Weiland, E. Wollack, and E. L. Wright. Five-Year Wilkinson Microwave Anisotropy Probe Observations: Cosmological Interpretation. *The Astrophysical Journal Supplement*, 180:330–376, February 2009. doi: 10.1088/0067-0049/180/2/330.

M. R. Krumholz and J. C. Tan. Slow Star Formation in Dense Gas: Evidence and Implications. *Astrophysical Journal*, 654:304–315, January 2007. doi: 10.1086/509101.

T. Lasserre, C. Afonso, J. N. Albert, J. Andersen, R. Ansari, É. Aubourg, P. Bareyre, F. Bauer, J. P. Beaulieu, G. Blanc, A. Bouquet, S. Char, X. Charlot, F. Couchot, C. Coutures, F. Derue, R. Ferlet, J. F. Glicenstein, B. Goldman, A. Gould, D. Graff, M. Gros, J. Haissinski, J. C. Hamilton, D. Hardin, J. de Kat, A. Kim, É. Lesquoy, C. Loup, C. Magneville, B. Man-

soux, J. B. Marquette, É. Maurice, A. Milsztajn, M. Moniez, N. Palanque-Delabrouille, O. Perdereau, L. Prévot, N. Regnault, J. Rich, M. Spiro, A. Vidal-Madjar, L. Vigroux, S. Zylberajch, and EROS Collaboration. Not enough stellar mass Machos in the Galactic halo. *Astronomy and Astrophysics*, 355:L39–L42, March 2000.

A. Loeb. First Light. *ArXiv Astrophysics e-prints*, March 2006.

L. Lopez-Honorez, O. Mena, Á. Moliné, S. Palomares-Ruiz, and A. C. Vincent. The 21 cm signal and the interplay between dark matter annihilations and astrophysical processes. *Journal of Cosmology and Astropartic l Physics*, 8:004, August 2016. doi: 10.1088/1475-7516/2016/08/004.

A. D. Ludlow, S. Bose, R. E. Angulo, L. Wang, W. A. Hellwing, J. F. Navarro, S. Cole, and C. S. Frenk. The mass-concentration-redshift relation of cold and warm dark matter haloes. *MNRAS*, 460:1214–1232, August 2016. doi: 10.1093/mnras/stw1046.

Jane H. MacGibbon. Can Planck-mass relics of evaporating black holes close the universe? *Nature*, 329:308–309, 1987. doi: 10.1038/329308a0.

K. J. Mack. Known unknowns of dark matter annihilation over cosmic time. *MNRAS*, 439: 2728–2735, April 2014. doi: 10.1093/mnras/stu129.

M. Maltoni, T. Schwetz, M. A. Tórtola, and J. W. Valle. Status of three-neutrino oscillations after the SNO-salt data. *Physical Review D*, 68(11):113010, December 2003. doi: 10.1103/PhysRevD.68.113010.

M. Mapelli, A. Ferrara, and E. Pierpaoli. Impact of dark matter decays and annihilations on reionization. *MNRAS*, 369:1719–1724, July 2006. doi: 10.1111/j.1365-2966.2006.10408.x.

M. Markevitch. Chandra Observation of the Most Interesting Cluster in the Universe. In A. Wilson, editor, *The X-ray Universe 2005*, volume 604 of *ESA Special Publication*, page 723, January 2006.

M. Markevitch, A. H. Gonzalez, D. Clowe, A. Vikhlinin, W. Forman, C. Jones, S. Murray, and W. Tucker. Direct Constraints on the Dark Matter Self-Interaction Cross Section from the Merging Galaxy Cluster 1E 0657-56. *The Astrophysical Journal*, 606:819–824, May 2004. doi: 10.1086/383178.

S. P. Martin. *A Supersymmetry Primer*, pages 1–98. World Scientific Publishing Co, 1998. doi: 10.1142/9789812839657_0001.

C. F. McKee and E. C. Ostriker. Theory of Star Formation. *Annual Review of Astronomy and Astrophysics*, 45:565–687, September 2007. doi: 10.1146/annurev.astro.45.051806.110602.

G. Mellema, L. V. E. Koopmans, F. A. Abdalla, G. Bernardi, B. Ciardi, S. Daiboo, A. G. de Bruyn, K. K. Datta, H. Falcke, A. Ferrara, I. T. Iliev, F. Iocco, V. Jelić, H. Jensen, R. Joseph, P. Labroupoulos, A. Meiksin, A. Mesinger, A. R. Offringa, V. N. Pandey, J. R. Pritchard, M. G. Santos, D. J. Schwarz, B. Semelin, H. Vedantham, S. Yatawatta, and S. Zaroubi. Reionization and the Cosmic Dawn with the Square Kilometre Array. *Experimental Astronomy*, 36:235–318, August 2013. doi: 10.1007/s10686-013-9334-5.

D. Merritt, J. F. Navarro, A. Ludlow, and A. Jenkins. A Universal Density Profile for Dark and Luminous Matter? *ApJ*, 624:L85–L88, May 2005. doi: 10.1086/430636.

A. Mesinger, A. Ewall-Wice, and J. Hewitt. Reionization and beyond: detecting the peaks of the cosmological 21 cm signal. *Monthly Notices of the Royal Astronomical Society*, 439: 3262–3274, April 2014. doi: 10.1093/mnras/stu125.

M. Milgrom. A modification of the Newtonian dynamics as a possible alternative to the hidden mass hypothesis. *The Astrophysical Journal*, 270:365–370, July 1983a. doi: 10.1086/161130.

M. Milgrom. A modification of the Newtonian dynamics - Implications for galaxies. *The Astrophysical Journal*, 270:371–389, July 1983b. doi: 10.1086/161131.

M. Milgrom. A Modification of the Newtonian Dynamics - Implications for Galaxy Systems. *The Astrophysical Journal*, 270:384, July 1983c. doi: 10.1086/161132.

M. Milgrom and R. H. Sanders. MOND predictions of 'halo' phenomenology in disc galaxies. *Monthly Notices of the Royal Astronomical Society*, 357:45–48, February 2005. doi: 10.1111/j.1365-2966.2004.08578.x.

M. Milgrom and R. H. Sanders. Modified Newtonian Dynamics Rotation Curves of Very Low Mass Spiral Galaxies. *The Astrophysical Journal*, 658:L17–L20, March 2007. doi: 10.1086/513695.

S. Mitra, A. Ferrara, and T. R. Choudhury. The escape fraction of ionizing photons from high-redshift galaxies from data-constrained reionization models. *MNRAS*, 428:L1–L5, January 2013. doi: 10.1093/mnrasl/sls001.

J. W. Motz, Haakon A. Olsen, and H. W. Koch. Pair production by photons. *Rev. Mod. Phys.*, 41:581–639, Oct 1969. doi: 10.1103/RevModPhys.41.581. URL `http://link.aps.org/doi/10.1103/RevModPhys.41.581`.

S. G. Murray, C. Power, and A. S. G. Robotham. HMFcalc: An online tool for calculating dark matter halo mass functions. *Astronomy and Computing*, 3:23–34, November 2013. doi: 10.1016/j.ascom.2013.11.001.

Y. Nagashima. *Elementary Particle Physics:Foundations of the Standard Model*. Wiley, 2013.

A. Natarajan and D. J. Schwarz. Distinguishing standard reionization from dark matter models. *Physical Review D*, 81(12):123510, June 2010. doi: 10.1103/PhysRevD.81.123510.

J. F. Navarro, C. S. Frenk, and S. D. M. White. The Structure of Cold Dark Matter Halos. *ApJ*, 462:563, May 1996. doi: 10.1086/177173.

S. F. Novaes. Standard Model: An Introduction. *ArXiv High Energy Physics - Phenomenology e-prints*, January 2000.

J. H. Oort. The force exerted by the stellar system in the direction perpendicular to the galactic plane and some related problems. *Bulletin of the Astronomical Institutes of the Netherlands*, 6:249, August 1932.

J. H. Oort. Some Problems Concerning the Structure and Dynamics of the Galactic System and the Elliptical Nebulae NGC 3115 and 4494. *Astrophysical Journal*, 91:273, April 1940. doi: 10.1086/144167.

B. Paczynski. Gravitational microlensing by the galactic halo. *The Astrophysical Journal*, 304: 1–5, May 1986. doi: 10.1086/164140.

P. J. E. Peebles. PRIMEVAL ADIABATIC PERTURBATIONS: EFFECT OF MASSIVE

NEUTRINOS. *The Astrophysical Journal*, 258:415–424, 1982. doi: 10.1086/160094.

M. E. Peskin. *Supersymmetry in Elementary Particle Physics*, page 609. World Scientific, 2008.

A. Pich. The Standard Model of Electroweak Interactions. *ArXiv e-prints*, May 2007.

Planck Collaboration, P. A. R. Ade, N. Aghanim, M. Arnaud, M. Ashdown, J. Aumont, C. Baccigalupi, A. J. Banday, R. B. Barreiro, J. G. Bartlett, and et al. Planck 2015 results. XIII. Cosmological parameters. *ArXiv e-prints*, February 2015.

Planck Collaboration, P. A. R. Ade, N. Aghanim, M. Arnaud, M. Ashdown, J. Aumont, C. Baccigalupi, A. J. Banday, R. B. Barreiro, J. G. Bartlett, and et al. Planck 2015 results. XIII. Cosmological parameters. *Astronomy and Astrophysics*, 594:A13, September 2016. doi: 10.1051/0004-6361/201525830.

J. C. Pober, A. R. Parsons, J. E. Aguirre, Z. Ali, R. F. Bradley, C. L. Carilli, D. DeBoer, M. Dexter, N. E. Gugliucci, D. C. Jacobs, P. J. Klima, D. MacMahon, J. Manley, D. F. Moore, I. I. Stefan, and W. P. Walbrugh. Opening the 21 cm Epoch of Reionization Window: Measurements of Foreground Isolation with PAPER. *Astrophysical Journal*, 768:L36, May 2013. doi: 10.1088/2041-8205/768/2/L36.

Gregory B. Poole, Paul W. Angel, Simon J. Mutch, Chris Power, Alan R. Duffy, Paul M. Geil, Andrei Mesinger, and Stuart B. Wyithe. Dark-ages reionization and galaxy formation simulation âĂŞ i. the dynamical lives of high-redshift galaxies. *MNRAS*, 459(3):3025–3039, 2016. doi: 10.1093/mnras/stw674. URL `http://mnras.oxfordjournals.org/content/459/3/3025.abstract`.

V. Poulin, P. D. Serpico, and J. Lesgourgues. Dark Matter annihilations in halos and high-redshift sources of reionization of the universe. *Journal of Cosmology and Astroparticle Physics*, 12:041, December 2015. doi: 10.1088/1475-7516/2015/12/041.

P. Renton. *Electroweak Interactions: An Introduction to the Physics of Quarks and Leptons*. 1990. ISBN 9780521366922. URL `http://www.cambridge.org/uk/catalogue/catalogue.asp?isbn=0521266033`.

E. Ripamonti, M. Mapelli, and A. Ferrara. The impact of dark matter decays and annihilations on the formation of the first structures. *Monthly Notices of the Royal Astronomical Society*, 375(4):1399–1408, 2007. doi: 10.1111/j.1365-2966.2006.11402.x.

E. Ripamonti, F. Iocco, A. Ferrara, R. Schneider, A. Bressan, and P. Marigo. First star formation with dark matter annihilation. *Monthly Notices of the Royal Astronomical Society*, 406(4):2605–2615, 2010. doi: 10.1111/j.1365-2966.2010.16854.x. URL `http://mnras.oxfordjournals.org/content/406/4/2605.abstract`.

M. S. Roberts and A. H. Rots. Comparison of Rotation Curves of Different Galaxy Types. *Astronomy and Astrophysics*, 26:483–485, August 1973.

M. Roos. Astrophysical and Cosmological Probes of Dark Matter. *Journal of Modern Physics*, 3:1152–1171, 2012. doi: 10.4236/jmp.2012.329150.

L. J. Rosenberg and K. A. van Bibber. Searches for invisible axions. *Phys. Rept.*, 325:1–39, 2000. doi: 10.1016/S0370-1573(99)00045-9.

V. C. Rubin and W. K. Ford, Jr. Rotation of the Andromeda Nebula from a Spectroscopic

Survey of Emission Regions. *ApJ*, 159:379, February 1970. doi: 10.1086/150317.

V. C. Rubin, N. Thonnard, and W. K. Ford, Jr. Extended rotation curves of high-luminosity spiral galaxies. IV - Systematic dynamical properties, SA through SC. *ApJl*, 225:L107–L111, November 1978. doi: 10.1086/182804.

V. C. Rubin, W. K. J. Ford, and N. . Thonnard. Rotational properties of 21 SC galaxies with a large range of luminosities and radii, from NGC 4605 /R = 4kpc/ to UGC 2885 /R = 122 kpc/. *ApJ*, 238:471–487, June 1980. doi: 10.1086/158003.

N. Sakai and Tsutomu Yanagida. Proton decay in a class of supersymmetric grand unified models. *Nuclear Physics B*, 197(3):533 – 542, 1982. ISSN 0550-3213. doi: http://dx.doi.org/10.1016/0550-3213(82)90457-6. URL `//www.sciencedirect.com/science/article/pii/0550321382904576`.

Abdus Salam. Weak and Electromagnetic Interactions. *Conf. Proc.*, C680519:367–377, 1968.

R. H. Sanders. The Published Extended Rotation Curves of Spiral Galaxies: Confrontation with Modified Dynamics. *The Astrophysical Journal*, 473:117, December 1996. doi: 10.1086/178131.

R. H. Sanders. A Stratified Framework for Scalar-Tensor Theories of Modified Dynamics. *The Astrophysical Journal*, 480:492–502, May 1997. doi: 10.1086/303980.

R. H. Sanders. Clusters of galaxies with modified Newtonian dynamics. *Monthly Notices of the Royal Astronomical Society*, 342:901–908, July 2003. doi: 10.1046/j.1365-8711.2003.06596.x.

R. H. Sanders. Neutrinos as cluster dark matter. *Monthly Notices of the Royal Astronomical Society*, 380:331–338, September 2007. doi: 10.1111/j.1365-2966.2007.12073.x.

D. N. Schramm and G. Steigman. Relic Neutrinos and the Density of the Universe. *The Astrophysical Journal*, 243:1, January 1981. doi: 10.1086/158559.

M.D. Schwartz. *Quantum Field Theory and the Standard Model*. Cambridge University Press, 2013.

Julian Schwinger. The theory of quantized fields. i. *Phys. Rev.*, 82:914–927, Jun 1951. doi: 10.1103/PhysRev.82.914. URL `https://link.aps.org/doi/10.1103/PhysRev.82.914`.

G. Servant and T. M. P. Tait. Is the lightest Kaluza-Klein particle a viable dark matter candidate? *Nuclear Physics B*, 650:391–419, February 2003. doi: 10.1016/S0550-3213(02)01012-X.

M B Shah, D S Elliott, and H B Gilbody. Pulsed crossed-beam study of the ionisation of atomic hydrogen by electron impact. *Journal of Physics B: Atomic and Molecular Physics*, 20(14):3501, 1987. URL `http://stacks.iop.org/0022-3700/20/i=14/a=022`.

M B Shah, D S Elliott, P McCallion, and H B Gilbody. Single and double ionisation of helium by electron impact. *Journal of Physics B: Atomic, Molecular and Optical Physics*, 21(15):2751, 1988. URL `http://stacks.iop.org/0953-4075/21/i=15/a=019`.

H. Shapley and H. D. Curtis. The Scale of the Universe. *Bulletin of the National Research Council, Vol. 2, Part 3, No. 11, p. 171-217*, 2:171–217, May 1921.

R. K. Sheth, H. J. Mo, and G. Tormen. Ellipsoidal collapse and an improved model for the number and spatial distribution of dark matter haloes. *MNRAS*, 323:1–12, May 2001. doi:

10.1046/j.1365-8711.2001.04006.x.

J. M. Shull. Heating and ionization by X-ray photoelectrons. *Astrophysical Journal*, 234: 761–764, December 1979. doi: 10.1086/157553.

J. M. Shull and M. E. van Steenberg. X-ray secondary heating and ionization in quasar emission-line clouds. *ApJ*, 298:268–274, November 1985. doi: 10.1086/163605.

T. Sjöstrand, S. Mrenna, and P. Skands. PYTHIA 6.4 physics and manual. *Journal of High Energy Physics*, 5:026, May 2006. doi: 10.1088/1126-6708/2006/05/026.

T. Sjöstrand, S. Mrenna, and P. Skands. A brief introduction to PYTHIA 8.1. *Computer Physics Communications*, 178:852–867, June 2008. doi: 10.1016/j.cpc.2008.01.036.

C. Skordis. Generalizing tensor-vector-scalar cosmology. *Physical Review D*, 77(12):123502, June 2008. doi: 10.1103/PhysRevD.77.123502.

C. Skordis, D. F. Mota, P. G. Ferreira, and C. Bœhm. Large Scale Structure in Bekenstein's Theory of Relativistic Modified Newtonian Dynamics. *Physical Review Letters*, 96(1):011301, January 2006. doi: 10.1103/PhysRevLett.96.011301.

T. R. Slatyer. Indirect dark matter signatures in the cosmic dark ages. II. Ionization, heating, and photon production from arbitrary energy injections. *Physical Review D*, 93(2):023521, January 2016. doi: 10.1103/PhysRevD.93.023521.

Tracy R. Slatyer. Indirect dark matter signatures in the cosmic dark ages. i. generalizing the bound on s-wave dark matter annihilation from planck results. *Phys. Rev. D*, 93:023527, Jan 2016. doi: 10.1103/PhysRevD.93.023527. URL `http://link.aps.org/doi/10.1103/PhysRevD.93.023527`.

Tracy R. Slatyer, Nikhil Padmanabhan, and Douglas P. Finkbeiner. Cmb constraints on wimp annihilation: Energy absorption during the recombination epoch. *Phys. Rev. D*, 80:043526, Aug 2009. doi: 10.1103/PhysRevD.80.043526. URL `http://link.aps.org/doi/10.1103/PhysRevD.80.043526`.

L. Spitzer, Jr. and E. H. Scott. Heating of H i Regions by Energetic Particles. II. Interaction Between Secondaries and Thermal Electrons. *ApJ*, 158:161, October 1969. doi: 10.1086/150180.

Douglas Spolyar, Katherine Freese, and Paolo Gondolo. Dark matter and the first stars: A new phase of stellar evolution. *Phys. Rev. Lett.*, 100:051101, Feb 2008. doi: 10.1103/PhysRevLett.100.051101. URL `http://link.aps.org/doi/10.1103/PhysRevLett.100.051101`.

V. Springel, S. D. M. White, A. Jenkins, C. S. Frenk, N. Yoshida, L. Gao, J. Navarro, R. Thacker, D. Croton, J. Helly, J. A. Peacock, S. Cole, P. Thomas, H. Couchman, A. Evrard, J. Colberg, and F. Pearce. Simulations of the formation, evolution and clustering of galaxies and quasars. *Nature*, 435:629–636, June 2005. doi: 10.1038/nature03597.

P. M. Stone, Y. K. Kim, and J. P. Desclaux. Electron-impact cross sections for dipole- and spin-allowed excitation of hydrogen, helium and lithium. *J Res. Natl. Inst. Stand. Technol.*, 4:327, July 2002. doi: 10.1086/168325.

R. Svensson and A. Zdziarski. Photon-photon scattering of gamma rays at cosmological distances. *ApJ*, 349:415–428, February 1990. doi: 10.1086/168325.

S. J. Tingay, R. Goeke, J. D. Bowman, D. Emrich, S. M. Ord, D. A. Mitchell, M. F. Morales, T. Booler, B. Crosse, R. B. Wayth, C. J. Lonsdale, S. Tremblay, D. Pallot, T. Colegate, A. Wicenec, N. Kudryavtseva, W. Arcus, D. Barnes, G. Bernardi, F. Briggs, S. Burns, J. D. Bunton, R. J. Cappallo, B. E. Corey, A. Deshpande, L. Desouza, B. M. Gaensler, L. J. Greenhill, P. J. Hall, B. J. Hazelton, D. Herne, J. N. Hewitt, M. Johnston-Hollitt, D. L. Kaplan, J. C. Kasper, B. B. Kincaid, R. Koenig, E. Kratzenberg, M. J. Lynch, B. Mckinley, S. R. Mcwhirter, E. Morgan, D. Oberoi, J. Pathikulangara, T. Prabu, R. A. Remillard, A. E. E. Rogers, A. Roshi, J. E. Salah, R. J. Sault, N. Udaya-Shankar, F. Schlagenhaufer, K. S. Srivani, J. Stevens, R. Subrahmanyan, M. Waterson, R. L. Webster, A. R. Whitney, A. Williams, C. L. Williams, and J. S. B. Wyithe. The Murchison Widefield Array: The Square Kilometre Array Precursor at Low Radio Frequencies. *Publications of the Astronomical Society of Australia*, 30:e007, January 2013. doi: 10.1017/pasa.2012.007.

P. Tisserand, L. Le Guillou, C. Afonso, J. N. Albert, J. Andersen, R. Ansari, É. Aubourg, P. Bareyre, J. P. Beaulieu, X. Charlot, C. Coutures, R. Ferlet, P. Fouqué, J. F. Glicenstein, B. Goldman, A. Gould, D. Graff, M. Gros, J. Haissinski, C. Hamadache, J. de Kat, T. Lasserre, É. Lesquoy, C. Loup, C. Magneville, J. B. Marquette, É. Maurice, A. Maury, A. Milsztajn, M. Moniez, N. Palanque-Delabrouille, O. Perdereau, Y. R. Rahal, J. Rich, M. Spiro, A. Vidal-Madjar, L. Vigroux, S. Zylberajch, and EROS-2 Collaboration. Limits on the Macho content of the Galactic Halo from the EROS-2 Survey of the Magellanic Clouds. *Astronomy and Astrophysics*, 469:387–404, July 2007. doi: 10.1051/0004-6361:20066017.

M. Valdes, A. Ferrara, M. Mapelli, and E. Ripamonti. Constraining dark matter through 21-cm observations. *Monthly Notices of the Royal Astronomical Society*, 377(1):245–252, 2007. doi: 10.1111/j.1365-2966.2007.11594.x.

M. Valdes, C. Evoli, and A. Ferrara. Particle energy cascade in the intergalactic medium. *Monthly Notices of the Royal Astronomical Society*, 404(3):1569–1582, 2010. doi: 10.1111/j.1365-2966.2010.16387.x.

D. A. Verner, G. J. Ferland, K. T. Korista, and D. G. Yakovlev. Atomic Data for Astrophysics. II. New Analytic FITS for Photoionization Cross Sections of Atoms and Ions. *ApJ*, 465:487, July 1996. doi: 10.1086/177435.

R. R. Volkas. Prospects for mass unification at low energy scales. *Phys. Rev. D*, 53:2681–2698, Mar 1996. doi: 10.1103/PhysRevD.53.2681. URL `https://link.aps.org/doi/10.1103/PhysRevD.53.2681`.

Steven Weinberg. A Model of Leptons. *Physics Review Letters*, 19:1264–1266, 1967. doi: 10.1103/PhysRevLett.19.1264.

S. D. M. White and C. S. Frenk. Galaxy formation through hierarchical clustering. *Astrophysical Journal*, 379:52–79, September 1991. doi: 10.1086/170483.

S. D. M. White, C. S. Frenk, and M. Davis. Clustering in a neutrino-dominated universe. *The Astrophysical Journal*, 274:L1–L5, November 1983. doi: 10.1086/184139.

J. H. Wise, M. J. Turk, and T. Abel. Resolving the Formation of Protogalaxies. II. Central Gravitational Collapse. *Astrophysical Journal*, 682:745-757, August 2008. doi: 10.1086/588209.

S. A. Wouthuysen. On the excitation mechanism of the 21-cm (radio-frequency) interstellar hydrogen emission line. *Astronomical Journal*, 57:31–32, 1952. doi: 10.1086/106661.

E. L. Wright. A Cosmology Calculator for the World Wide Web. *The Publications of the Astronomical Society of the Pacific*, 118:1711–1715, December 2006. doi: 10.1086/510102.

W.-M. Yao, C. Amsler, D. Asner, R.M. Barnett, J. Beringer, P.R. Burchat, C.D. Carone, C. Caso, O. Dahl, G. D'Ambrosio, A. DeGouvea, M. Doser, S. Eidelman, J.L. Feng, T. Gherghetta, M. Goodman, C. Grab, D.E. Groom, A. Gurtu, K. Hagiwara, K.G. Hayes, J.J. Hernández-Rey, K. Hikasa, H. Jawahery, C. Kolda, Kwon Y., M.L. Mangano, A.V. Manohar, A. Masoni, R. Miquel, K. Mönig, H. Murayama, K. Nakamura, S. Navas, K.A. Olive, L. Pape, C. Patrignani, A. Piepke, G. Punzi, G. Raffelt, J.G. Smith, M. Tanabashi, J. Terning, N.A. Törnqvist, T.G. Trippe, P. Vogel, T. Watari, C.G. Wohl, R.L. Workman, P.A. Zyla, B. Armstrong, G. Harper, V.S. Lugovsky, P. Schaffner, M. Artuso, K.S. Babu, H.R. Band, E. Barberio, M. Battaglia, H. Bichsel, O. Biebel, P. Bloch, E. Blucher, R.N. Cahn, D. Casper, A. Cattai, A. Ceccucci, D. Chakraborty, R.S. Chivukula, G. Cowan, T. Damour, T. DeGrand, K. Desler, M.A. Dobbs, M. Drees, A. Edwards, D.A. Edwards, V.D. Elvira, J. Erler, V.V. Ezhela, W. Fetscher, B.D. Fields, B. Foster, D. Froidevaux, T.K. Gaisser, L. Garren, H.-J. Gerber, G. Gerbier, L. Gibbons, F.J. Gilman, G.F. Giudice, A.V. Gritsan, M. Grünewald, H.E. Haber, C. Hagmann, I. Hinchliffe, A. Höcker, P. Igo-Kemenes, J.D. Jackson, K.F. Johnson, D. Karlen, B. Kayser, D. Kirkby, S.R. Klein, K. Kleinknecht, I.G. Knowles, R.V. Kowalewski, P. Kreitz, B. Krusche, Yu.V. Kuyanov, O. Lahav, P. Langacker, A. Liddle, Z. Ligeti, T.M. Liss, L. Littenberg, L. Liu, K.S. Lugovsky, S.B. Lugovsky, T. Mannel, D.M. Manley, W.J. Marciano, A.D. Martin, D. Milstead, M. Narain, P. Nason, Y. Nir, J.A. Peacock, S.A. Prell, A. Quadt, S. Raby, B.N. Ratcliff, E.A. Razuvaev, B. Renk, P. Richardson, S. Roesler, G. Rolandi, M.T. Ronan, L.J. Rosenberg, C.T. Sachrajda, S. Sarkar, M. Schmitt, O. Schneider, D. Scott, T. Sjöstrand, G.F. Smoot, P. Sokolsky, S. Spanier, H. Spieler, A. Stahl, T. Stanev, R.E. Streitmatter, T. Sumiyoshi, N.P. Tkachenko, G.H. Trilling, G. Valencia, K. van Bibber, M.G. Vincter, D.R. Ward, B.R. Webber, J.D. Wells, M. Whalley, L. Wolfenstein, J. Womersley, C.L. Woody, A. Yamamoto, O.V. Zenin, J. Zhang, and R.-Y. Zhu. Review of Particle Physics. *Journal of Physics G*, 33:1+, 2006. URL `http://pdg.lbl.gov`.

W. M. Yao et al. Review of Particle Physics. *Journal of Physics G*, G33:1–1232, 2006. doi: 10.1088/0954-3899/33/1/001.

Jun'ichi Yokoyama. Cosmological constraints on primordial black holes produced in the near-critical gravitational collapse. *Physical Review D*, 58:107502, Oct 1998. doi: 10.1103/PhysRevD.58.107502. URL `https://link.aps.org/doi/10.1103/PhysRevD.58.107502`.

A. A. Zdziarski and R. Svensson. Absorption of X-rays and gamma rays at cosmological distances. *ApJ*, 344:551–566, September 1989. doi: 10.1086/167826.

A. Zee. *Quantum field theory in a nutshell*. 2003.

Ya. B. Zeldovich, A. A. Klypin, M. Yu. Khlopov, and V. M. Chechetkin. Astrophysical constraints on the mass of heavy stable neutral leptons. *Soviet Journal of Nuclear Physics*, 31: 664–669, 1980. [Yad. Fiz.31,1286(1980)].

F. Zwicky. Die Rotverschiebung von extragalaktischen Nebeln. *Helvetica Physica Acta*, 6:

110–127, 1933.

F. Zwicky. On the Masses of Nebulae and of Clusters of Nebulae. *ApJ*, 86:217, October 1937. doi: 10.1086/143864.

Appendix A

The lightest neutralino in minimal SUSY

A.1 MSSM Model

As an illustrative example, a brief introduction to the minimal supersymmetric model (Dimopoulos et al., 1981) (MSSM) is presented. While collider experiments have as of yet failed to provide any evidence for the theory, giving weight to calls to look beyond the supersymmetric framework, the construction of the model, as well as identification of suitable dark matter candidates, is applicable to other dark matter models. Despite containing the fewest additional supersymmetric elements that allows for the recovery of the Standard Model, the MSSM comes with a great number of free parameters[1]. The abundance of free parameters also allows for some flexibility in terms of the mass and cross-section of the prospective dark matter particle.

Below are outlined the key ingredients going into the MSSM, as well as the derivation of the mass for the lightest neutralino and annihilation cross-section.

A.1.1 Supersymmetric Fields

The first step is the assignment of the necessary supersymmetric doubles to the Standard Model particles. All fermions are assigned scalar counterparts where the *slepton*[2] is the super-partner of the lepton and the *squark* refers to that of the quark. The fermion counterparts to the SM bosons are the *gluino* ($\tilde{g}$), *wino* ($\tilde{W}^i$) and *bino* ($\tilde{B}$). Lastly to avoid mathematical anomalies related to symmetry breaking, an additional Higgs field is added and both are associated with the spin 1/2 *Higgsino*. The SM and new SUSY fields are summarized in Table A.1.

A.1.2 Lagrangian

The Lagrangian of the MSSM is given by

$$\mathcal{L}_{SUSY} = -\frac{1}{2}(W^{ij}\psi_i\psi_j + W^*_{ij}\psi^{i\dagger}\psi^{j\dagger}) - W^i W^*_j \tag{A.1}$$

[1] Most of these set the particle masses and mixing angles.

[2] The unfortunate naming convention of super-particles stipulates an s to be added to the name of SM particles.

SUSY Field	SM	Spin	SUSY	Spin
Q	u_L, d_L	1/2	$\tilde{u}_L, \tilde{d}_L$	0
U^c	$\bar{u}_R$	1/2	$\bar{u}^*_R$	0
D^c	$\bar{d}_R$	1/2	$\bar{d}^*_R$	0
L	μ_L, e_L	1/2	$\tilde{\mu}_L, \tilde{e}_L$	0
E^c	$\bar{e}_R$	1/2	$\bar{e}^*_R$	0
H_1	H_1	0	$\tilde{H}_1$	1/2
H_2	H_2	0	$\tilde{H}_2$	1/2
G^a	g	1	$\tilde{g}$	1/2
W_i	W_i	1	$\tilde{W}_i$	1/2
B	B	1	$\tilde{B}$	1/2

Table A.1: Summary of MSSM fields

where

$$W^i \equiv \partial W/\partial\phi_i, \quad W^*_i \equiv \partial W/\partial\phi^{i*}, \quad W^{ij} \equiv \partial^2 W/\partial\phi_i\partial\phi_j.$$

and ϕ_i and ψ_i are the scalar and fermion fields. W is the potential of the MSSM and can be thought of as the supersymmetric equivalent of the Standard Yukawa coupling with modifications to accommodate the additional Higgs fields.

$$W = \epsilon_{ij}[y_e H^j_1 L^i E^c + y_d H^j_1 Q^i D^c + y_u H^i_2 Q^J U^c] + \epsilon_{ij}\mu H^i_1 H^j_2 \tag{A.2}$$

A.1.3 R-Parity

In the Standard Model both the baryon number B and lepton number L are additively conserved quantum numbers. This however is no longer the case for all couplings in the MSSM and new multiplicative quantum number, R-parity, is added to the theory

$$R \equiv (-1)^{3B+L+2s} \tag{A.3}$$

where B, L and s are the familiar baryon, lepton and spin quantum numbers. While originally introduced to suppress undesirable properties of MSSM such as proton decay (Farrar and Fayet, 1978; Sakai and Yanagida, 1982) conservation of R-parity also leads to the presence of promising dark matter candidates. Within the MSSM, SM particles have $R = 1$ and the *sparticles* have $R = -1$ forming a $\mathbb{Z}_2$ symmetry. In other words to conserve R-parity, a decaying sparticle can only decay into an odd number of sparticles (with arbitrary number of SM particles) thus implying that the lightest supersymmetric particle is stable.

SUSY Dark Matter Candidates

This stability criterion makes the lightest supersymmetric particle (LSP) an attractive dark matter candidate. In addition, astrophysical observations stipulate that dark mat-

ter should carry neither electric or colour charge which narrows down the list of potential candidates to neutral MSSM particles. Furthermore, supersymmetry stipulates that the SUSY particles have the same mass as their SM counterparts. However since no such particles have been observed, SUSY must in fact manifest as a broken symmetry. The manner in which the symmetry is broken (Barger et al., 1994) is not unique, though physical motivation such as the preservation of the Planck/electroweak scale hierarchy does provide some constraints.

Within MSSM a number of potential candidates exist including the sneutrino, axino, gravitino and the neutralino. In context of this thesis the neutralino is of greatest interest as it falls into the category of self-annihilating dark matter particle investigated here[3] and in the following section some of the properties of the neutralino are derived.

A.1.4 The Lightest Neutralino

Neutralinos are the mass eigenstates of the linear superposition of binos, winos and Higgsinos.

$$\tilde{\chi}_i^0 = a_{i1}\tilde{B} + a_{i2}\tilde{W}_3 + a_{i3}\tilde{H}_1^0 + a_{i4}\tilde{H}_2^0 \tag{A.4}$$

The lightest of these, denoted $\tilde{H}_1^0$, is the neutralino dark matter candidate. Furthermore, neutralinos are fermionic Majorana particles meaning they self-annihilate and recalling R-parity conservation, annihilate to SM particles.

Mass

The mass eigenstates of the neutralino can be derived by diagonalising their corresponding mass matrix

$$\mathcal{Y}_\chi = \begin{pmatrix} M_1 & 0 & -M_z\cos\beta\sin\theta_W & M_z\sin\beta\sin\theta_W \\ 0 & M_2 & M_z\cos\beta\cos\theta_W & -M_z\cos\beta\cos\theta_W \\ -M_z\cos\beta\sin\theta_W & M_z\cos\beta\cos\theta_W & 0 & -\mu \\ M_z\sin\beta\sin\theta_W & -M_z\sin\beta\cos\theta_W & -\mu & 0 \end{pmatrix} \tag{A.5}$$

here M_1, M_2 and μ are free mass parameters corresponding to the bino, wino and higgsinos. θ_W is the Weinberg angle and $\tan\beta = v_2/v_1$ where v_2/v_1 is the ratio of the vacuum expectation value of the Higgs fields. For the MSSM neutralino, mass eigenstates can be found analytically (El Kheishen et al., 1992) by diagonalising the mass matrix such that

$$N^*\mathcal{Y}_\chi N^{-1} = N_D, \tag{A.6}$$

[3]Neutralinos also avoid a number of undesirable qualities such as potential overproduction in the early universe for the gravitino or a scattering cross section off nuclei that has been ruled out by direct detection experiments for sneutrinos.

where N is a unitary matrix and N_D is the diagonal neutralino matrix. In general N will be imaginary however under CP invariance there is a real matrix A (Gunion and Haber, 1986) such that

$$\begin{aligned} A\mathcal{Y}_\chi A^{-1} &= \mathrm{Diag}(\epsilon_1\tilde{M}_1^0, \epsilon_2\tilde{M}_2^0, \epsilon_3\tilde{M}_3^0, \epsilon_4\tilde{M}_4^0) = \mathcal{M}_D \\ Z^\dagger Z &= 1 \end{aligned} \tag{A.7}$$

and $\epsilon_i = \pm 1$. Rearranging Equation A.7 to solve for a_{ij} and the eigenvalues gives

$$A\mathcal{Y}_\chi - \mathcal{M}_D A = 0 \tag{A.8}$$

which upon expansion gives

$$\begin{aligned} &[Y_{11} - \epsilon_i M_{\chi_i^0}]a_{i1} + Y_{21}a_{i2} + Y_{31}a_{i3} + Y_{41}a_{i4} = 0 \\ &Y_{12}a_{i1} + [Y_{22} - \epsilon_i M_{\chi_i^0}]a_{i2} + Y_{32}a_{i3} + Y_{42}a_{i4} = 0 \\ &Y_{13}a_{i1} + Y_{23}a_{i2} + [Y_{33} - \epsilon_i M_{\chi_i^0}]a_{i3} + Y_{43}a_{i4} = 0 \\ &Y_{14}a_{i1} + Y_{24}a_{i2} + Y_{34}a_{i3} + [Y_{44} - \epsilon_i M_{\chi_i^0}]a_{i4} = 0 \end{aligned} \tag{A.9}$$

Using the eigenvalue condition $|\mathbf{B} - \lambda\mathbf{I}| = 0$ to give the characteristic polynomial

$$\begin{aligned} &\mathcal{E}_1 + \mathcal{E}_2 + \mathcal{E}_3 = 0 \\ &\mathcal{E}_1 = (\epsilon_i M_{\chi_i^0})^4 - (M_1 + M_2)(\epsilon_i M_{\chi_i^0})^3 + (M_1 M_2 - M_z^2 - \mu^2)(\epsilon_i M_{\chi_i^0})^2 \\ &\mathcal{E}_2 = [(M_1 + M_2\mu^2(M_1\cos\theta_W + M_2\sin\theta_W)M_z^2 - \mu M_z^2\sin 2\beta)]\epsilon_i M_{\chi_i^0} \\ &\mathcal{E}_3 = (M_1\cos^2\theta_W + M_2\sin^2\theta_W)\mu M_z^2\sin 2\beta - M_1 M_2\mu^2 \end{aligned} \tag{A.10}$$

These have an analytic solution yielding the eigenvalues and therefore masses of the neutralinos as functions of M_1, M_2 and μ

$$\begin{aligned} \epsilon_1 M_{\chi_1^0} &= -(\frac{1}{2}b - \frac{1}{6}C_2)^{1/2} + \left[\frac{1}{2}b - \frac{1}{3}C_2 + \frac{C_3}{(8b - \frac{8}{3}C_2)^{1/2}}\right]^{1/2} + \frac{1}{4}(M_1 + M_2) \\ \epsilon_2 M_{\chi_2^0} &= +(\frac{1}{2}b - \frac{1}{6}C_2)^{1/2} - \left[\frac{1}{2}b - \frac{1}{3}C_2 + \frac{C_3}{(8b - \frac{8}{3}C_2)^{1/2}}\right]^{1/2} + \frac{1}{4}(M_1 + M_2) \\ \epsilon_3 M_{\chi_3^0} &= -(\frac{1}{2}b - \frac{1}{6}C_2)^{1/2} + \left[\frac{1}{2}b - \frac{1}{3}C_2 + \frac{C_3}{(8b - \frac{8}{3}C_2)^{1/2}}\right]^{1/2} - \frac{1}{4}(M_1 + M_2) \\ \epsilon_4 M_{\chi_4^0} &= +(\frac{1}{2}b - \frac{1}{6}C_2)^{1/2} + \left[\frac{1}{2}b - \frac{1}{3}C_2 + \frac{C_3}{(8b - \frac{8}{3}C_2)^{1/2}}\right]^{1/2} + \frac{1}{4}(M_1 + M_2) \end{aligned} \tag{A.11}$$

where

$$
\begin{aligned}
C_2 &= (M_1 M_2 - M_z^2 - \mu^2) - \frac{3}{8}(M_1 + M_2)^2 \\
C_3 &= \frac{1}{8}(M_1 + M_2)^3 + \frac{1}{2}(M_1 + M_2)(M_1 M_2 - M_z^2 - \mu^2) \\
&\quad + (M_1 + M_2)\mu^2 + (M_1 \cos^2\theta_W + M_2 \sin^2\theta_W) M_z^2 + \mu M_z^2 \sin 2\beta \\
C_4 &= -(M_1 \cos^2\theta_W + M_2 \sin^2\theta_W) M_z^2 \mu \sin 2\beta - M_1 M_2 \mu^2 \\
&\quad + \frac{1}{4}(M_1 + M_2)[(M_1 + M_2)\mu^2 + (M_1 \cos^2\theta_W + M_2 \sin^2\theta_W) M_z^2 + \mu M_z^2 \sin 2\beta] \\
&\quad + \frac{1}{16}(M_1 M_2 - M_z^2 - \mu^2)(M_1 + M_2)^2 - \frac{3}{256}(M_1 + M_2)^4 \\
b &= \frac{1}{2^{1/3}} \Re[-S + i(D/27)^{1/2}]^{1/3} \\
D &= -4U3 - 27S^2, \quad U = -\frac{1}{3}C_2^2 - 4C_4, \quad S = -C_3^2 - \frac{2}{27}C_2^3 + \frac{8}{3}C_2 C_4.
\end{aligned}
$$

After dividing by a_{i1} and using the results for the neutralino mass, Equations A.9 becomes

$$
\begin{aligned}
Y_{21}\frac{a_{i2}}{a_{i1}} + Y_{31}\frac{a_{i3}}{a_{i1}} + Y_{41}\frac{a_{i4}}{a_{i1}} &= -[Y_{11} - \epsilon_i M_{\chi_i^0}] \\
[Y_{22} - \epsilon i M_{\chi_i^0}]\frac{a_{i2}}{a_{i1}} + Y_{32}\frac{a_{i3}}{a_{i1}} + Y_{42}\frac{a_{i4}}{a_{i1}} &= -Y_{21} \\
Y_{23}\frac{a_{i2}}{a_{i1}} + [Y_{33}\epsilon_i M_{\chi_i^0}]\frac{a_{i3}}{a_{i1}} + Y_{43}\frac{a_{i4}}{a_{i1}} &= -Y_{13} \\
Y_{23}\frac{a_{i2}}{a_{i1}} + Y_{34}\frac{a_{i3}}{a_{i1}} + [Y_{44} - \epsilon_i M_{\chi_i^0}]\frac{a_{i4}}{a_{i1}} &= -Y_{14}
\end{aligned}
\tag{A.12}
$$

with solutions

$$
\begin{aligned}
\frac{a_{i2}}{a_{i1}} &= \frac{1}{\tan\theta_W}\frac{M_1 - \epsilon_i M_{\chi_i^0}}{M_2 - \epsilon_i M_{\chi_i^0}} \\
\frac{a_{i3}}{a_{i1}} &= \frac{-\mu[M_2 - \epsilon_i M_{\chi_i^0}][M_1 - \epsilon_i M_{\chi_i^0}] - M_z^2 \sin\beta\cos\beta[(M_1 - M_2)\cos^2\theta_W + M_2 - \epsilon M_{\chi_i^0}]}{M_z[M_2 - \epsilon_i M_{\chi_i^0}]\sin\theta_W[-\mu\cos\beta + \epsilon_i M_{\chi_i^0}\sin\beta]} \\
\frac{a_{i4}}{a_{i1}} &= \frac{\epsilon_i M_{\chi_i^0}[M_2 - \epsilon_i M_{\chi_i^0}][M_1 - \epsilon_i M_{\chi_i^0}] - M_z^2 \cos^2\beta[(M_1 - M_2)\cos^2\theta_W + M_2 - \epsilon_i M_{\chi_i^2}]}{M_z[M_2 - \epsilon_i M_{\chi_i^0}]\sin\theta_W[\mu\cos\beta + \epsilon_i M_{\chi_i^0}\sin\beta]}.
\end{aligned}
\tag{A.13}
$$

From the unitary condition imposed on A,

$$
a_{i1}^2 + a_{i2}^2 + a_{i3}^2 + a_{i4}^2 = 1
$$

which gives the required coefficients for the lightest neutralino mass state

$$a_{i1} = \left[1 + \left(\frac{a_{i2}}{a_{i1}}\right)^2 + \left(\frac{a_{i3}}{a_{i1}}\right)^2 + \left(\frac{a_{i4}}{a_{i1}}\right)^2\right]^{-1/2}. \tag{A.14}$$

In general the mass eigenstates are difficult to solve analytically and must be found using numerical methods.

Annihilation Cross-section

For detection purposes the interaction cross-sections of greatest interest are those for annihilation and direct scattering off nuclei. Dark matter in the present cosmological era is assumed to be cold, that is the particles are taken to be non-relativistic. The annihilation cross-section is therefore often taken to be constant and discarding higher order velocity terms so that

$$\sigma_{DM} v = \alpha_0 \tag{A.15}$$

The cross-sections are then calculated via tree-level Feynman diagrams where neutralinos annihilate to Higgs and gauge boson as well as fermions (in general favouring the heavier quarks and leptons). An appealing feature of the SUSY paradigm is that its dark matter candidates are weakly interacting as dark matter particles and an annihilation cross-section around the weak scale will produce the correct relic density observed today. When calculating the annihilation cross-section at high redshift the non-relativistic approximation breaks down and the velocity dependence needs to be taken into account see Drees and Nojiri (1993) or Jungman et al. (1996) for further details on the higher order calculations.

Appendix B

Derivation of the IC photon spectrum

Inverse Compton scattering is the dominant mechanism via which energy carried by the relativistic, annihilation products is down-scattered. Actual energy transfer is only facilitated by the collisional interaction between the down-scattered cascade products and the gas. Therefore the distribution of IC photons is an important factor in determining the overall energy deposition efficiency of different dark matter models, especially for finite volumes where energy transfer is strongly dependent on the interaction mean-free path. Below the derivation (following the notation of (Jones, 1968; Blumenthal and Gould, 1970)) of the approximate IC photon spectrum produced by electrons/positrons scattering off of the CMB photon field is presented.

B.1 Derivation in the Relativistic Limit

Assume an isotropic, mono-energetic distribution of photons. Let the a_1 and a be the energy of the photon before and after the collision and let γ denote the energy of the incoming electron/positron with all energies given in units of the electron rest mass $m_e c^2$. The electron velocity is given in the usual manner as $\beta = \mathbf{v}/c$. Un-primed quantities are given in the lab frame and dashed quantities denote those in the rest-frame of the leptons.

B.1.1 Relativistic Kinematics during IC Scattering

The key approximation made in this derivation pertains to the angular distribution of the IC scattered photons for relativistic electrons and positrons. Consider a relativistic electron moving along the x-axis and undergoing IC scattering with the aforementioned isotropic, mono-energetic photon field. In the laboratory frame the photons make an angle θ_1 with the x-axis which is

$$\tan(\theta_1') = \frac{\sin(\theta_1)}{\gamma(\cos\theta_1 - \beta)} \tag{B.1}$$

in the rest frame of the electron. The energy of the photon in that frame is

$$a_1' = \gamma a_1(1 - \beta\cos(\theta)) \tag{B.2}$$

where it is assumed that the energy of the up scattered photon remains small compared to that of the incoming electrons and that the IC scattering can be treated as continuous rather than discrete. In the relativistic limit where $1 << \gamma$ the approximation

$$\beta \approx 1 - \frac{1}{2\gamma^2}$$

can be made. As $\beta \to 1$

$$\tan(\theta_1') \longrightarrow \frac{\cot(\theta_1/2)}{\gamma} \tag{B.3}$$

It therefore becomes evident that in the rest frame of the relativistic electron, incident photons are well approximated by a narrow beam running in parallel with the x-axis. This observation allows for the three dimensional IC scattering problem to be greatly simplified. Let θ_{IC}' and ϕ' be the polar and azimuthal angles the photon scatters through during the IC process and let the plane defined by the incoming photon and electron/positron coincide with $\phi' = 0$. If the electron or positron is energetic enough to assume $\theta_1' \approx 0$ then $\theta_{IC}' = \theta'$. Furthermore the Klein-Nishina cross-section is independent of χ' so that the angular component of the derivation can be reduced to a single variable.

B.1.2 IC Spectrum in Relativistic Limit

Now to derive the energy spectrum of the photons travelling in the beam incident parallel with the path of the electron. Making use of the angle simplifying result above, let

$$y \equiv \cos\chi'$$

so that $-1 \le y \le 1$. Then in the laboratory frame, and integrating over y, the differential photon density is given by

$$\mathrm{d}n = n(a_1, y)\mathrm{d}a_1\mathrm{d}y = \frac{1}{2}n(a_1)\mathrm{d}a_1\mathrm{d}y. \tag{B.4}$$

Using the fact that $\mathrm{d}n/a_1$ is invariant (see Felten and Morrison (1966); Feenberg and Primakoff (1948) for detailed proof) and making use of the Jacobian $|\mathrm{d}a_1'/\mathrm{d}y| = \gamma\beta a_1 \to \gamma a_1$ from equation B.2

$$\frac{1}{a_1'}\mathrm{d}n'(a_1'; a_1)\mathrm{d}a_1' = \frac{1}{2}a_1^{-1}n(a_1)\mathrm{d}a_1\mathrm{d}y \tag{B.5}$$

Here $\mathrm{d}n'(a_1'; a_1)\mathrm{d}a_1'$ is the total differential photon density of the incident beam in the rest frame of the electron within $\mathrm{d}a_1'$ due to photons in $\mathrm{d}a_1$. Before undergoing IC scattering, the energy distribution of incident photons is therefore given by

$$n'(a_1')\mathrm{d}a_1' = \frac{a_1'}{2\gamma a_1^2}S(a_1'; a_1/2\gamma, a_1 2\gamma)\mathrm{d}a_1' \tag{B.6}$$

where for relativistic γ, $S(x;a,b)$ is the characteristic function over the interval $[a,b]$ such that

$$S(x;a,b) = \begin{cases} 1 & a \leq x \geq b \\ 0 & x < a, x > b. \end{cases}$$

The latter is included to signify the range of a_1'. The Compton scattering Klein-Nishina cross-section is

$$\sigma(a',a_1',y') = \frac{r_0^2(1+y'^2)}{2[1+a_1'(1-y')]}\left\{\frac{a_1'^2(1-y')^2}{(1+y'^2)[1+a_1'(-y')]}\right\}\delta(a'-f(a_1',y')) \tag{B.7}$$

where

$$f(a_1',y') = \frac{a_1}{1+a_1'(-y')}$$

and

$$r_0 \equiv \frac{e^2}{mc^2}$$

is the classical electron radius. Since $\mathrm{d}t = \gamma \mathrm{d}t'$,

$$\frac{\mathrm{d}N}{\mathrm{d}t} = \frac{1}{\gamma}\frac{\mathrm{d}N}{\mathrm{d}t'} \tag{B.8}$$

which when combined with the interaction rate, $n'c\sigma(a',a_1',y')\mathrm{d}t'$, gives

$$\begin{aligned}\frac{\mathrm{d}^4N}{\mathrm{d}t\mathrm{d}a_1'\mathrm{d}a'\mathrm{d}y'} = \Bigg\{&\frac{\pi r_0^2 c}{2a_1^2\gamma^2}\frac{1+y'^2}{1+a_1'(1-y')^2} \\ &\times\left(1+\frac{a_1'^2(1-y')^2}{(1+y'^2)[+a_1'(1-y')]}\right) \\ &\times a_1'\delta(a'-f(a_1',y'))S(a_1';a_1/2\gamma,a_1 2\gamma)\Bigg\}\end{aligned} \tag{B.9}$$

after integration over ϕ'. Using the expression for $f(a_1',a_1)$ above yields

$$\mathrm{d}a'\mathrm{d}a_1'\mathrm{d}y' = [1+a_1'(-y')]\mathrm{d}a'\mathrm{d}a_1'\mathrm{d}f$$

which allows (B.5) to be directly integrated over f giving

$$\begin{aligned}\frac{\mathrm{d}^3N}{\mathrm{d}t'\mathrm{d}a'\mathrm{d}y'} = &\frac{\pi r_0^2 c}{2a_1'^2\gamma^2}\left[(1+y'^2)+\frac{a'^2(1-y')2}{1-a'(-y')}\right] \\ &\times\frac{a'}{1-a'(-y')}S\left[\frac{a'}{-a'(1-y')};a_1/2\gamma,a_1 2\gamma\right].\end{aligned} \tag{B.10}$$

Using the Doppler-shift formula and new variable η

$$a' = \frac{a}{\gamma(1-\beta y')} \tag{B.11}$$

$$\eta = (1-\beta y') \tag{B.12}$$

allows B.10 to be recast as

$$\frac{\mathrm{d}^3N}{\mathrm{d}t\mathrm{d}a\mathrm{d}\eta} = \frac{\pi r_0^2 ca}{2\gamma^4 a_1^2(1-a/\gamma)}\left[\eta^2 - 2\eta + \frac{(a/\gamma)^2}{(1-a\gamma)}\right]\frac{S(\eta;\eta_1,\eta_2)}{\eta^2} \tag{B.13}$$

where

$$\eta_1 = \frac{a}{2a_1\gamma^2(1-a/\gamma)},$$

$$\eta_2 = \frac{2a}{a_1(1=a/\gamma)}$$

and the approximation $1-y' \approx \eta$ was used. The integral performed over η yields

$$\left[\eta - 2\ln\eta - \frac{2}{\eta} - \frac{(a/\gamma)^2}{(1-a/\gamma)\eta}\right]_L^U \tag{B.14}$$

Here the limits U and L are dependent on the region of integration. In the case where $a_1/4\gamma^2 \le a \le a_1$, then $\eta_1 \le 1/\gamma^2$ and $1/\gamma^2 \le \eta_2 \le 2$ then

$$\frac{\mathrm{d}^2N}{\mathrm{d}t\mathrm{d}a} \approx \frac{\pi r_0^2 c}{2\gamma^4 a_1}\left(\frac{4\gamma^2 a}{a_1} - 1\right) \tag{B.15}$$

where higher order terms were neglected. In contrast for $a_1 \le a \le 4a_1\gamma^2/(1+4a_1\gamma)$, $\eta_1 \ge 2$ and $1/2\gamma^2 \le \eta_2 \le 2$ which gives the final result

$$\begin{aligned}\frac{\mathrm{d}^2N}{\mathrm{d}t\mathrm{d}a} \approx \frac{2\pi r_0^2 c}{a_1\gamma^2}\Bigg[&2q''\ln q'' + (1+2q'')(1-q'') \\ &+ \frac{1}{2}\frac{(4a_1\gamma q'')^2}{(1+4a_1\gamma q'')}(1-q'')\Bigg]\end{aligned} \tag{B.16}$$

where

$$q'' = \frac{a}{4a_1\gamma(1-a/\gamma)}. \tag{B.17}$$

B.1.3 Limitations

There are two key assumptions that go into the derivation of the IC photon spectrum. The first is that the electron is sufficiently relativistic to allow the incident photon in the rest frame of the electron to be treated as a narrow beam and secondary that the energy gained by the up-scattered photon is small compared to that of the electron. When

considering astrophysical applications these limits must be taken into consideration. However, for the purposes of this thesis the approximations made are sufficient since

- Annihilation products for the dark matter masses considered here are injected at highly relativistic energies. Moreover, while crossing the halos and cirucmgalactic medium only a very small fraction of the injected particle's energy is lost and the particle remains relativistic.

- The energy loss due to IC scattering is small compared to the electron/positron energy for the dark matter masses used here. For models at the TeV scale and beyond however, the expression of the IC spectrum would have to be re-derived in the ultra-relativistic limit. Similarly at higher redshifts than considered here, the energy of the CMB photons would increase and the continuous energy loss approximation would eventually break down.

Appendix C

Additional Results and Code Outputs

Figures C.1 to C.4 show the summary outputs of the halo energy transfer code for energies not shown in Chapter 5, that is for 10^5, 10^7, 10^9 and 10^{11} eV. In each figure, the upper plots show outputs at redshift 20 and the lower at 40. As before the first two columns show the results for electrons, the middle photons and the last positrons. In each column the plots on the left show the deposition fractions summed radially over the halo, with blue, green and red curves denoting heating, lyman photons and ionisation respectively. The bar plots on the right show the spectrum of particles having escaped from the halo with electrons, positrons and photons being shown in blue, green and red. From top to bottom, rows show the outputs for 10^5, 10^6 and $10^7 M_\odot$ halos.

Similar results were also obtained for energies placed at 10 logspaced bins between those energy values shown here and in Chapter 5. These were then used as the basis to produce the total deposition curves and filtered energy spectra discussed throughout the thesis.

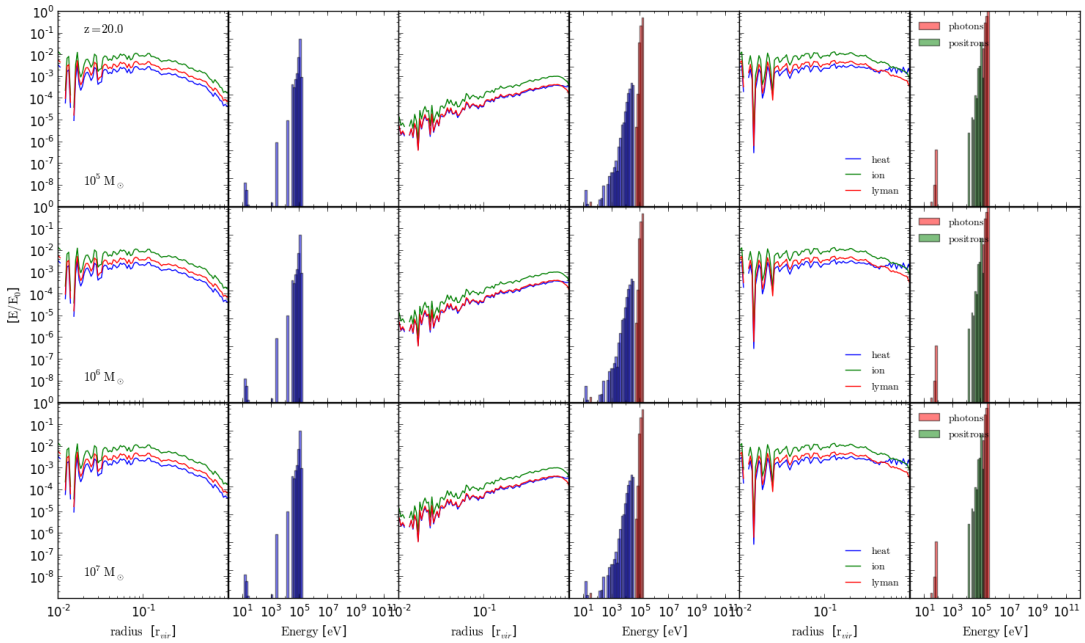

(a) z = 20

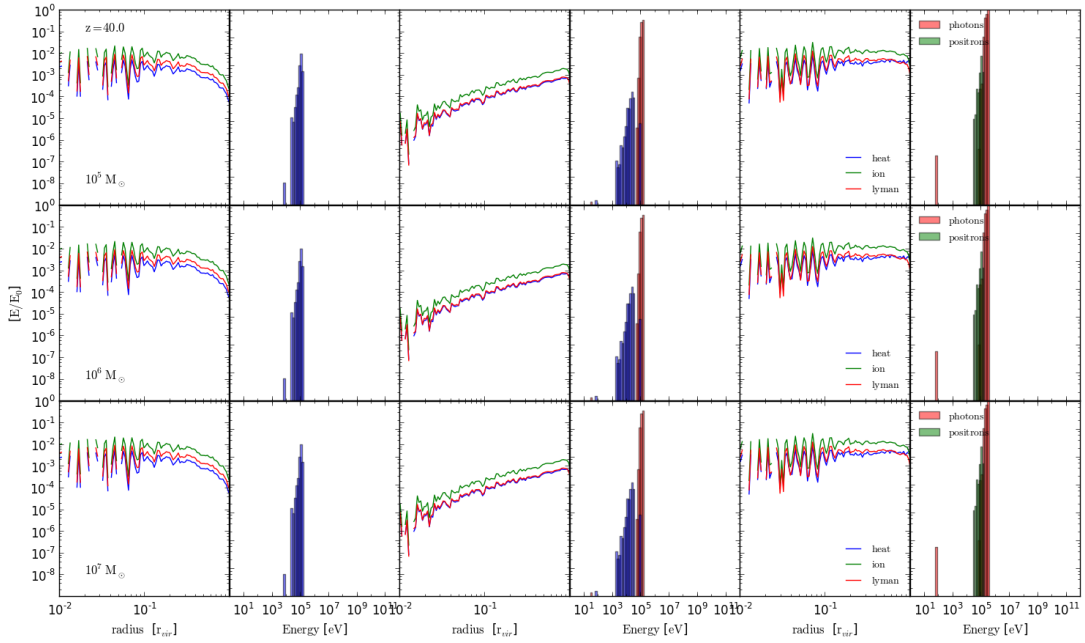

(b) z = 40

Figure C.1: Summary of halo energy transfer code outputs for $10^5 M_\odot$ halos

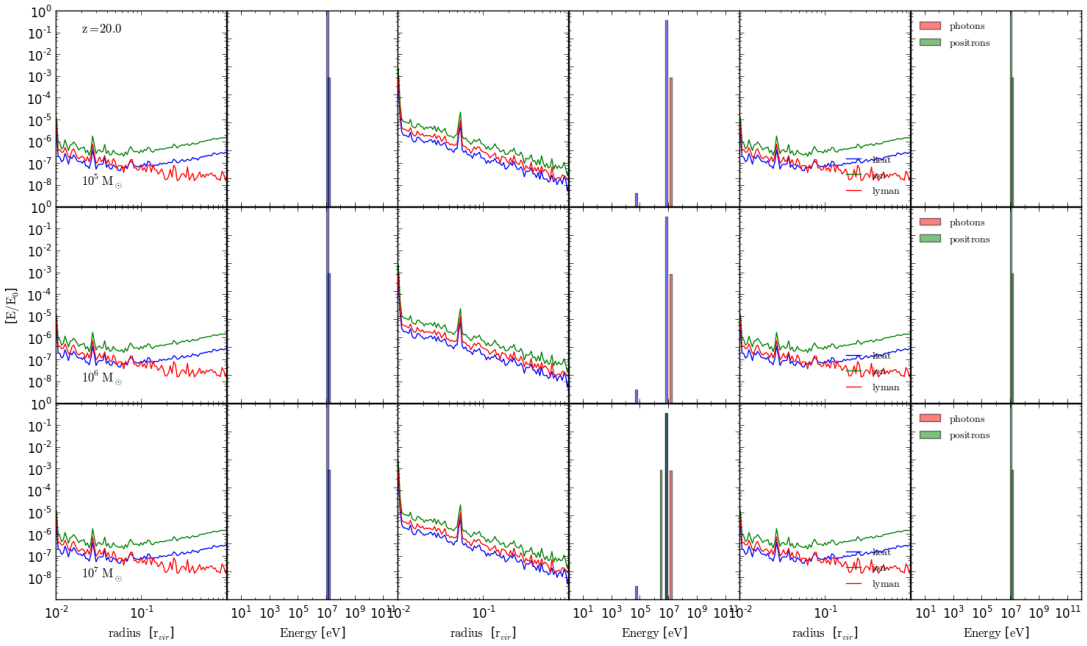

(a) z = 20

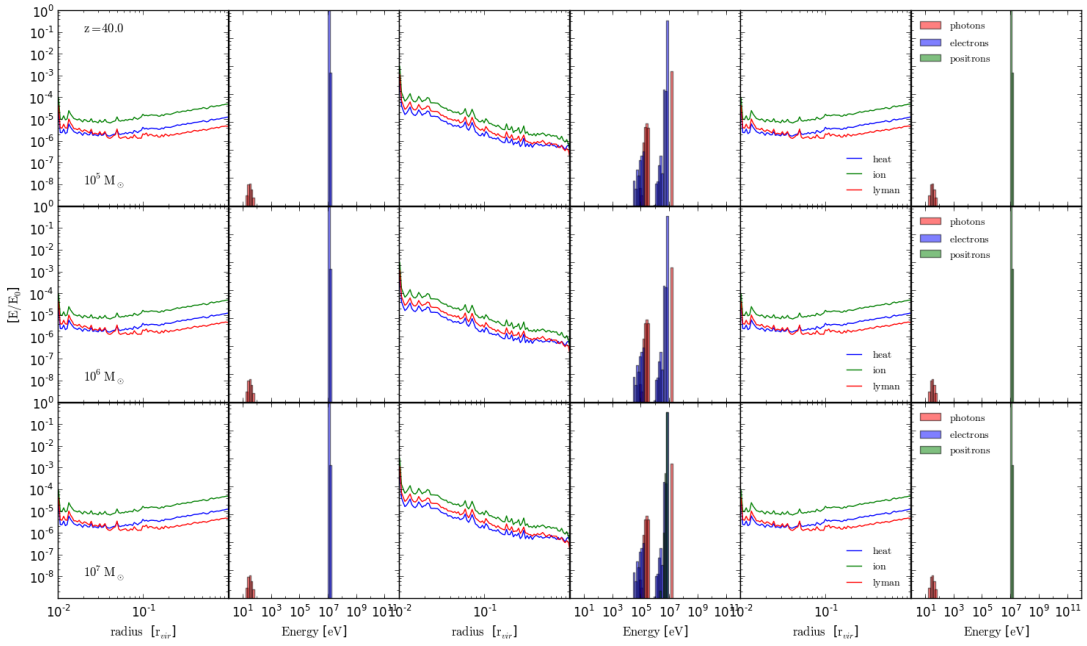

(b) z = 40

Figure C.2: Summary of halo energy transfer code outputs for $10^7 M_\odot$ halos

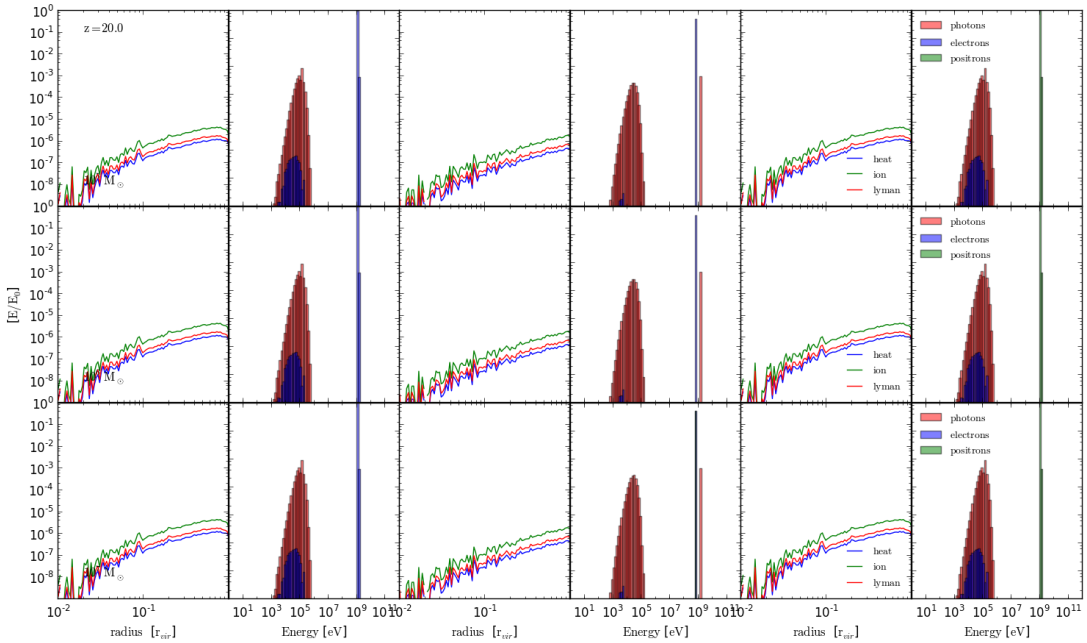

(a) z = 20

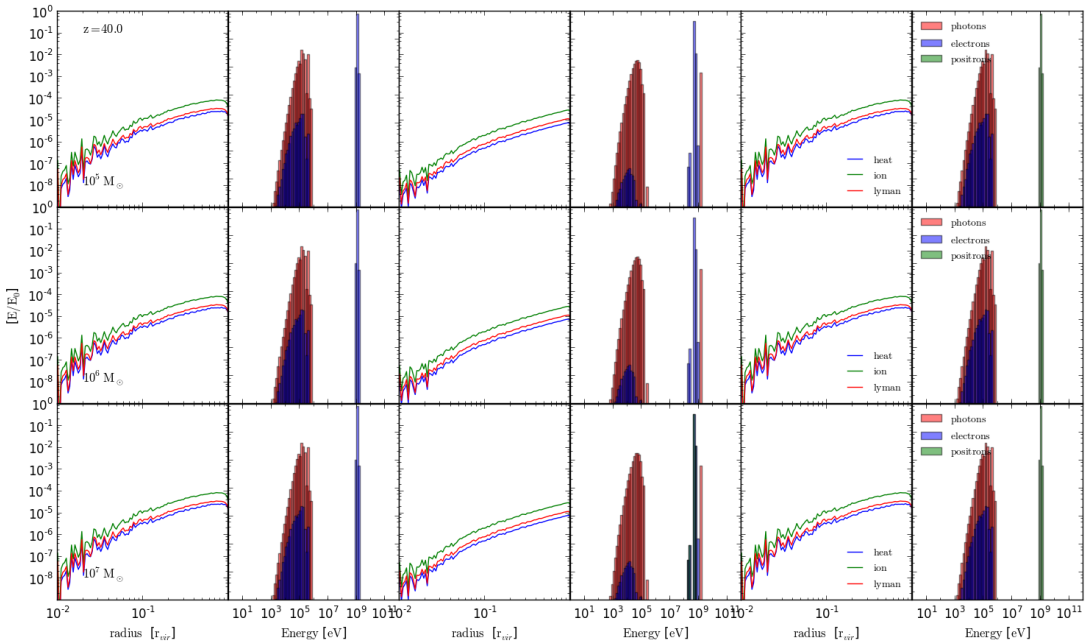

(b) z = 40

Figure C.3: Summary of halo energy transfer code outputs for $10^9 M_\odot$ halos

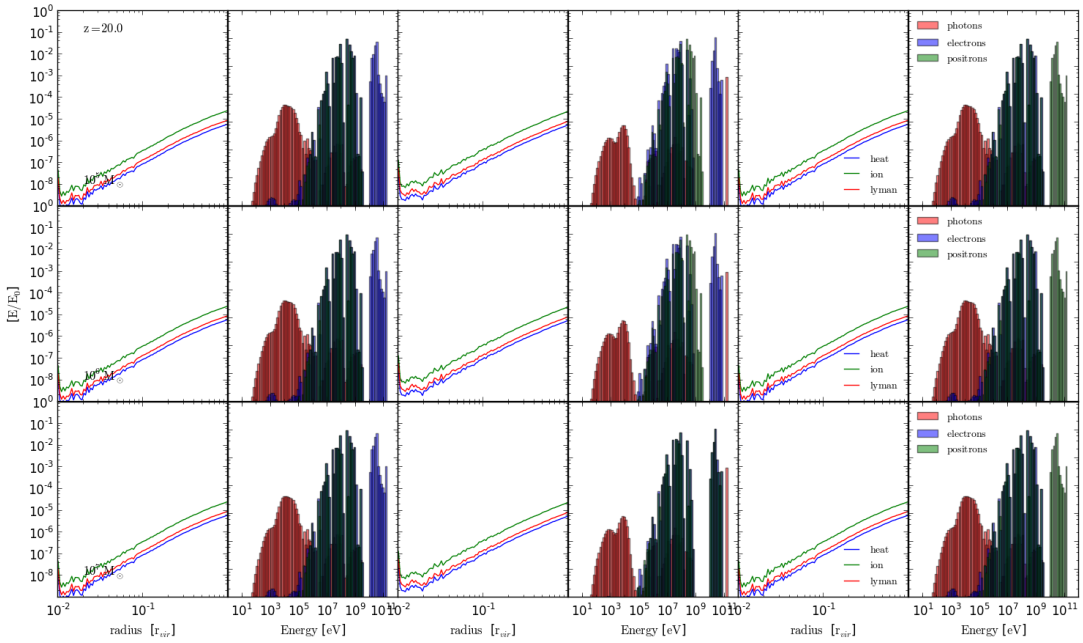

(a) z = 20

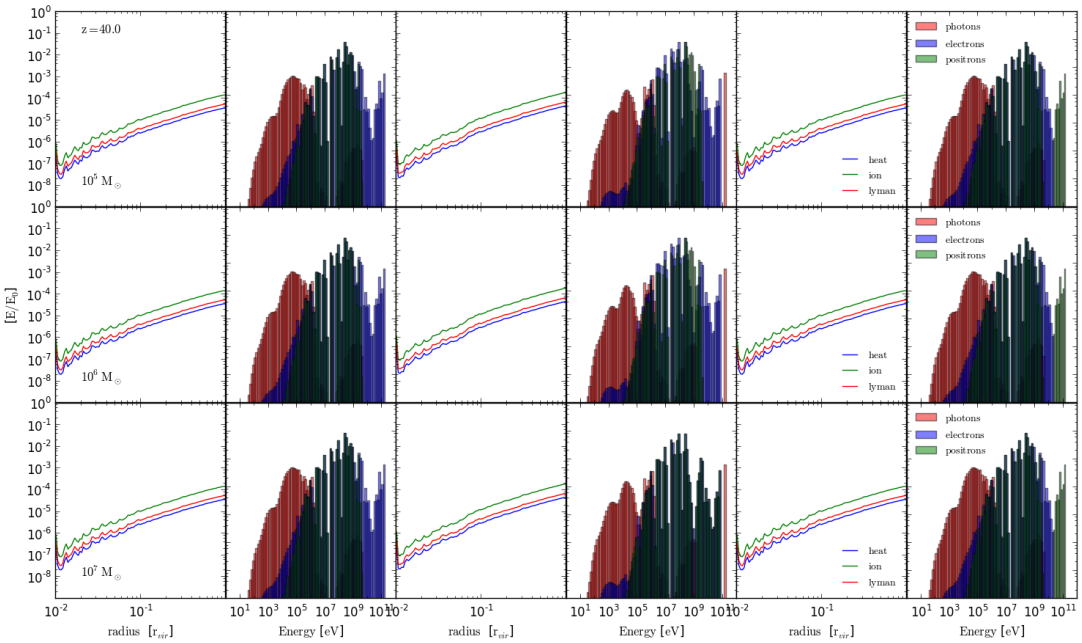

(b) z = 40

Figure C.4: Summary of halo energy transfer code outputs for $10^{11}M_{\odot}$ halos